

Failure Mechanism of Wet Shotcrete Support in Underground Space

Lead Guest Editor: Guoming Liu

Guest Editors: Lianjun Chen, Shengqiang Jiang, Cheng-Long Wang, and Peter Koteš





Failure Mechanism of Wet Shotcrete Support in Underground Space

Advances in Civil Engineering

Failure Mechanism of Wet Shotcrete Support in Underground Space

Lead Guest Editor: Guoming Liu

Guest Editors: Lianjun Chen, Shengqiang Jiang,
Cheng-Long Wang, and Peter Koteš



Copyright © 2022 Hindawi Limited. All rights reserved.

This is a special issue published in "Advances in Civil Engineering." All articles are open access articles distributed under the Creative Commons Attribution License, which permits unrestricted use, distribution, and reproduction in any medium, provided the original work is properly cited.






Chief Editor

Cumaraswamy Vipulanandan, USA










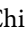



Associate Editors

Chiara Bedon , Italy
Constantin Chalioris , Greece
Ghassan Chehab , Lebanon
Ottavia Corbi, Italy
Mohamed ElGawady , USA
Husnain Haider , Saudi Arabia
Jian Ji , China
Jiang Jin , China
Shazim A. Memon , Kazakhstan
Hossein Moayedi , Vietnam
Sanjay Nimbalkar, Australia
Giuseppe Oliveto , Italy
Alessandro Palmeri , United Kingdom
Arnaud Perrot , France
Hugo Rodrigues , Portugal
Victor Yepes , Spain
Xianbo Zhao , Australia

Academic Editors

José A.F.O. Correia, Portugal
Glenda Abate, Italy
Khalid Abdel-Rahman , Germany
Ali Mardani Aghabaglou, Turkey
José Aguiar , Portugal
Afaq Ahmad , Pakistan
Muhammad Riaz Ahmad , Hong Kong
Hashim M.N. Al-Madani , Bahrain
Luigi Aldieri , Italy
Angelo Aloisio , Italy
Maria Cruz Alonso, Spain
Filipe Amarante dos Santos , Portugal
Serji N. Amirkhania, USA
Eleftherios K. Anastasiou , Greece
Panagiotis Ch. Anastasopoulos , USA
Mohamed Moafak Arbili , Iraq
Farhad Aslani , Australia
Siva Avudaiappan , Chile
Ozgur BASKAN , Turkey
Adewumi Babafemi, Nigeria
Morteza Bagherpour, Turkey
Qingsheng Bai , Germany
Nicola Baldo , Italy
Daniele Baraldi , Italy

Eva Barreira , Portugal
Emilio Bastidas-Arteaga , France
Rita Bento, Portugal
Rafael Bergillos , Spain
Han-bing Bian , China
Xia Bian , China
Huseyin Bilgin , Albania
Giovanni Biondi , Italy
Hugo C. Biscaia , Portugal
Rahul Biswas , India
Edén Bojórquez , Mexico
Giosuè Boscato , Italy
Melina Bosco , Italy
Jorge Branco , Portugal
Bruno Briseghella , China
Brian M. Broderick, Ireland
Emanuele Brunesi , Italy
Quoc-Bao Bui , Vietnam
Tan-Trung Bui , France
Nicola Buratti, Italy
Gaochuang Cai, France
Gladis Camarini , Brazil
Alberto Campisano , Italy
Qi Cao, China
Qixin Cao, China
Iacopo Carnacina , Italy
Alessio Cascardi, Italy
Paolo Castaldo , Italy
Nicola Cavalagli , Italy
Liborio Cavaleri , Italy
Anush Chandrappa , United Kingdom
Wen-Shao Chang , United Kingdom
Muhammad Tariq Amin Chaudhary, Kuwait
Po-Han Chen , Taiwan
Qian Chen , China
Wei Tong Chen , Taiwan
Qixiu Cheng, Hong Kong
Zhanbo Cheng, United Kingdom
Nicholas Chileshe, Australia
Prinya Chindaprasirt , Thailand
Corrado Chisari , United Kingdom
Se Jin Choi , Republic of Korea
Heap-Yih Chong , Australia
S.H. Chu , USA
Ting-Xiang Chu , China

Zhaofei Chu , China
Wonseok Chung , Republic of Korea
Donato Ciampa , Italy
Gian Paolo Cimellaro, Italy
Francesco Colangelo, Italy
Romulus Costache , Romania
Liviu-Adrian Cotfas , Romania
Antonio Maria D'Altri, Italy
Bruno Dal Lago , Italy
Amos Darko , Hong Kong
Arka Jyoti Das , India
Dario De Domenico , Italy
Gianmarco De Felice , Italy
Stefano De Miranda , Italy
Maria T. De Risi , Italy
Tayfun Dede, Turkey
Sadik O. Degertekin , Turkey
Camelia Delcea , Romania
Cristoforo Demartino, China
Giuseppe Di Filippo , Italy
Luigi Di Sarno, Italy
Fabio Di Trapani , Italy
Aboelkasim Diab , Egypt
Thi My Dung Do, Vietnam
Giulio Dondi , Italy
Jiangfeng Dong , China
Chao Dou , China
Mario D'Aniello , Italy
Jingtao Du , China
Ahmed Elghazouli, United Kingdom
Francesco Fabbrocino , Italy
Flora Faleschini , Italy
Dingqiang Fan, Hong Kong
Xueping Fan, China
Qian Fang , China
Salar Farahmand-Tabar , Iran
Ilenia Farina, Italy
Roberto Fedele, Italy
Guang-Liang Feng , China
Luigi Fenu , Italy
Tiago Ferreira , Portugal
Marco Filippo Ferrotto, Italy
Antonio Formisano , Italy
Guoyang Fu, Australia
Stefano Galassi , Italy

Junfeng Gao , China
Meng Gao , China
Giovanni Garcea , Italy
Enrique García-Macías, Spain
Emilio García-Taengua , United Kingdom
DongDong Ge , USA
Khaled Ghaedi, Malaysia
Khaled Ghaedi , Malaysia
Gian Felice Giaccu, Italy
Agathoklis Giaralis , United Kingdom
Ravindran Gobinath, India
Rodrigo Gonçalves, Portugal
Peilin Gong , China
Belén González-Fonteboa , Spain
Salvatore Grasso , Italy
Fan Gu, USA
Erhan Güneyisi , Turkey
Esra Mete Güneyisi, Turkey
Pingye Guo , China
Ankit Gupta , India
Federico Gusella , Italy
Kemal Hacıefendioğlu, Turkey
Jianyong Han , China
Song Han , China
Asad Hanif , Macau
Hadi Hasanzadehshooiili , Canada
Mostafa Fahmi Hassanein, Egypt
Amir Ahmad Hedayat , Iran
Khandaker Hossain , Canada
Zahid Hossain , USA
Chao Hou, China
Biao Hu, China
Jiang Hu , China
Xiaodong Hu, China
Lei Huang , China
Cun Hui , China
Bon-Gang Hwang, Singapore
Jijo James , India
Abbas Fadhil Jasim , Iraq
Ahad Javanmardi , China
Krishnan Prabhakan Jaya, India
Dong-Sheng Jeng , Australia
Han-Yong Jeon, Republic of Korea
Pengjiao Jia, China
Shaohua Jiang , China

MOUSTAFA KASSEM , Malaysia
Mosbeh Kaloop , Egypt
Shankar Karuppannan , Ethiopia
John Kechagias , Greece
Mohammad Khajehzadeh , Iran
Afzal Husain Khan , Saudi Arabia
Mehran Khan , Hong Kong
Manoj Khandelwal, Australia
Jin Kook Kim , Republic of Korea
Woosuk Kim , Republic of Korea
Vaclav Koci , Czech Republic
Loke Kok Foong, Vietnam
Hailing Kong , China
Leonidas Alexandros Kouris , Greece
Kyriakos Kourousis , Ireland
Moacir Kripka , Brazil
Anupam Kumar, The Netherlands
Emma La Malfa Ribolla, Czech Republic
Ali Lakirouhani , Iran
Angus C. C. Lam, China
Thanh Quang Khai Lam , Vietnam
Luciano Lamberti, Italy
Andreas Lampropoulos , United Kingdom
Raffaele Landolfo, Italy
Massimo Latour , Italy
Bang Yeon Lee , Republic of Korea
Eul-Bum Lee , Republic of Korea
Zhen Lei , Canada
Leonardo Leonetti , Italy
Chun-Qing Li , Australia
Dongsheng Li , China
Gen Li, China
Jiale Li , China
Minghui Li, China
Qingchao Li , China
Shuang Yang Li , China
Sunwei Li , Hong Kong
Yajun Li , China
Shun Liang , China
Francesco Liguori , Italy
Jae-Han Lim , Republic of Korea
Jia-Rui Lin , China
Kun Lin , China
Shibin Lin, China

Tzu-Kang Lin , Taiwan
Yu-Cheng Lin , Taiwan
Hexu Liu, USA
Jian Lin Liu , China
Xiaoli Liu , China
Xuemei Liu , Australia
Zaobao Liu , China
Zhuang-Zhuang Liu, China
Diego Lopez-Garcia , Chile
Cristiano Loss , Canada
Lyan-Ywan Lu , Taiwan
Jin Luo , USA
Yanbin Luo , China
Jianjun Ma , China
Junwei Ma , China
Tian-Shou Ma, China
Zhongguo John Ma , USA
Maria Macchiaroli, Italy
Domenico Magisano, Italy
Reza Mahinroosta, Australia
Yann Malecot , France
Prabhat Kumar Mandal , India
John Mander, USA
Iman Mansouri, Iran
André Dias Martins, Portugal
Domagoj Matesan , Croatia
Jose Matos, Portugal
Vasant Matsagar , India
Claudio Mazzotti , Italy
Ahmed Mebarki , France
Gang Mei , China
Kasim Mermerdas, Turkey
Giovanni Minafò , Italy
Masoomah Mirrashid , Iran
Abbas Mohajerani , Australia
Fadzli Mohamed Nazri , Malaysia
Fabrizio Mollaioli , Italy
Rosario Montuori , Italy
H. Naderpour , Iran
Hassan Nasir , Pakistan
Hossein Nassiraei , Iran
Satheeskumar Navaratnam , Australia
Ignacio J. Navarro , Spain
Ashish Kumar Nayak , India
Behzad Nematollahi , Australia

Chayut Ngamkhanong , Thailand
Trung Ngo, Australia
Tengfei Nian, China
Mehdi Nikoo , Canada
Youjun Ning , China
Olugbenga Timo Oladinrin , United Kingdom
Oladimeji Benedict Olalusi, South Africa
Timothy O. Olawumi , Hong Kong
Alejandro Orfila , Spain
Maurizio Orlando , Italy
Siti Aminah Osman, Malaysia
Walid Oueslati , Tunisia
SUVASH PAUL , Bangladesh
John-Paris Pantouvakis , Greece
Fabrizio Paolacci , Italy
Giuseppina Pappalardo , Italy
Fulvio Parisi , Italy
Dimitrios G. Pavlou , Norway
Daniele Pellegrini , Italy
Gatheeshgar Perampalam , United Kingdom
Daniele Perrone , Italy
Giuseppe Piccardo , Italy
Vagelis Plevris , Qatar
Andrea Pranno , Italy
Adolfo Preciado , Mexico
Chongchong Qi , China
Yu Qian, USA
Ying Qin , China
Giuseppe Quaranta , Italy
Krishanu ROY , New Zealand
Vlastimir Radonjanin, Serbia
Carlo Rainieri , Italy
Rahul V. Ralegaonkar, India
Raizal Saifulnaz Muhammad Rashid, Malaysia
Alessandro Rasulo , Italy
Chonghong Ren , China
Qing-Xin Ren, China
Dimitris Rizos , USA
Geoffrey W. Rodgers , New Zealand
Pier Paolo Rossi, Italy
Nicola Ruggieri , Italy
JUNLONG SHANG, Singapore



Nikhil Saboo, India
Anna Saetta, Italy
Juan Sagaseta , United Kingdom
Timo Saksala, Finland
Mostafa Salari, Canada
Ginevra Salerno , Italy
Evangelos J. Sapountzakis , Greece
Vassilis Sarhosis , United Kingdom
Navaratnarajah Sathiparan , Sri Lanka
Fabrizio Scozzese , Italy
Halil Sezen , USA
Payam Shafigh , Malaysia
M. Shahria Alam, Canada
Yi Shan, China
Hussein Sharaf, Iraq
Mostafa Sharifzadeh, Australia
Sanjay Kumar Shukla, Australia
Amir Si Larbi , France
Okan Sirin , Qatar
Piotr Smarzewski , Poland
Francesca Sollecito , Italy
Rui Song , China
Tian-Yi Song, Australia
Flavio Stochino , Italy
Mayank Sukhija , USA
Piti Sukontasukkul , Thailand
Jianping Sun, Singapore
Xiao Sun , China
T. Tafsirojjan , Australia
Fujiao Tang , China
Patrick W.C. Tang , Australia
Zhi Cheng Tang , China
Weerachart Tangchirapat , Thailand
Xiixin Tao, China
Piergiorgio Tataranni , Italy
Elisabete Teixeira , Portugal
Jorge Iván Tobón , Colombia
Jing-Zhong Tong, China
Francesco Trentadue , Italy
Antonello Troncone, Italy
Majbah Uddin , USA
Tariq Umar , United Kingdom
Muahmmad Usman, United Kingdom
Muhammad Usman , Pakistan
Mucteba Uysal , Turkey

Ilaria Venanzi , Italy
Castorina S. Vieira , Portugal
Valeria Vignali , Italy
Claudia Vitone , Italy
Liwei WEN , China
Chunfeng Wan , China
Hua-Ping Wan, China
Roman Wan-Wendner , Austria
Chaohui Wang , China
Hao Wang , USA
Shiming Wang , China
Wayne Yu Wang , United Kingdom
Wen-Da Wang, China
Xing Wang , China
Xiuling Wang , China
Zhenjun Wang , China
Xin-Jiang Wei , China
Tao Wen , China
Weiping Wen , China
Lei Weng , China
Chao Wu , United Kingdom
Jiangyu Wu, China
Wangjie Wu , China
Wenbing Wu , China
Zhixing Xiao, China
Gang Xu, China
Jian Xu , China
Panpan , China
Rongchao Xu , China
HE YONGLIANG, China
Michael Yam, Hong Kong
Hailu Yang , China
Xu-Xu Yang , China
Hui Yao , China
Xinyu Ye , China
Zhoujing Ye, China
Gürol Yildirim , Turkey
Dawei Yin , China
Doo-Yeol Yoo , Republic of Korea
Zhanping You , USA
Afshar A. Yousefi , Iran
Xinbao Yu , USA
Dongdong Yuan , China
Geun Y. Yun , Republic of Korea

Hyun-Do Yun , Republic of Korea
Cemal YİĞİT , Turkey
Paolo Zampieri, Italy
Giulio Zani , Italy
Mariano Angelo Zanini , Italy
Zhixiong Zeng , Hong Kong
Mustafa Zeybek, Turkey
Henglong Zhang , China
Jiupeng Zhang, China
Tingting Zhang , China
Zengping Zhang, China
Zetian Zhang , China
Zhigang Zhang , China
Zhipeng Zhao , Japan
Jun Zhao , China
Annan Zhou , Australia
Jia-wen Zhou , China
Hai-Tao Zhu , China
Peng Zhu , China
QuanJie Zhu , China
Wenjun Zhu , China
Marco Zucca, Italy
Haoran Zuo, Australia
Junqing Zuo , China
Robert Černý , Czech Republic
Süleyman İpek , Turkey

Contents



Construction and Application of Relationship Model between Development of Mining Industry and Carbon Emission of Energy Consumption

Lili Wei , Guangyu Jia , Xiaohui Xu, and Lingyun Zhao
Research Article (23 pages), Article ID 5143501, Volume 2022 (2022)



Preparation, Encapsulation, and Performance Evaluation of Ternary Phase Change Materials for Building Envelope

Hongzhi Zhu, Bin Guo , and Zhi Li
Research Article (7 pages), Article ID 8246365, Volume 2022 (2022)


Optimization of the Stirring Blade Structure of the Pumping Unit Based on the Improvement of Concrete Suction Efficiency

Shengqiang Jiang , Hong Wan, Guodong Cao , Yuanqiang Tan, Jingang Liu, Shiping Yang, Xiangwu Xiao, Zhenggang Tong, and Quanxu Yu
Research Article (17 pages), Article ID 1255348, Volume 2022 (2022)



Numerical Simulation Research on Cutting Rock with a PDC Cutter Assisted by an Impact Force

Yong Wang , Hongjian Ni , Ruihe Wang, Bin Huang, Shubin Liu, and Heng Zhang
Research Article (9 pages), Article ID 8282104, Volume 2022 (2022)

Quantitative Characterization of Overburden Rock Development Pattern in the Goaf at Different Key Stratum Locations Based on DEM

Xiaoqiang Zhang , Bolin Hu, Jiaying Zou, Chuandong Liu, and Yuanfan Ji
Research Article (18 pages), Article ID 8011350, Volume 2021 (2021)

Analysis of Plastic Zone and Pressure Variance Features of Surrounding Rock of High-Altitude Macker Tunnel: A Case Study in Jiangluling Macker Tunnel in Qinghai

Xiaojun Ma, Hongyan Guo , Juyi Hu, Shuang Cai , Liang Cheng, and Danfeng Zhang
Research Article (11 pages), Article ID 3632826, Volume 2021 (2021)

Research Article

Construction and Application of Relationship Model between Development of Mining Industry and Carbon Emission of Energy Consumption

Lili Wei , Guangyu Jia , Xiaohui Xu, and Lingyun Zhao

School of Business, Shandong Jianzhu University, Jinan 250101, China

Correspondence should be addressed to Guangyu Jia; jiagy@sdjzu.edu.cn

Received 4 March 2022; Accepted 11 April 2022; Published 8 June 2022

Academic Editor: Guoming Liu

Copyright © 2022 Lili Wei et al. This is an open access article distributed under the Creative Commons Attribution License, which permits unrestricted use, distribution, and reproduction in any medium, provided the original work is properly cited.

With the world's consensus on low-carbon emission reduction, all walks of life have formulated low-carbon development goals. As a high-energy consumption industry, it is urgent for mining industry to implement the development strategy of low-carbon emission reduction. Therefore, this study tries to provide reasonable suggestions and references for the low-carbon development of the mining industry. Firstly, this study analyzes the industry development, energy consumption, and carbon emission of mining industry from 2000 to 2020. Then, using the Tapio theory, this study constructs the analysis model of decoupling between carbon emission of mining industry and industry growth. The analysis method of decoupling state assignment is proposed for the first time in the model. At the same time, the energy efficiency decoupling index and energy structure decoupling index are introduced to explain the causes of carbon emission decoupling. The research shows that the carbon emission of energy consumption in China's mining industry peaked in 2013, and the energy efficiency decoupling in 2001–2014 is the main driver of carbon emission decoupling. The sharp growth of industrial output value leads to the decoupling of energy efficiency. At present, the improvement of energy efficiency of China's mining industry faces great resistance. At the same time, the inhibition effect of energy efficiency on carbon emissions is limited, and the energy structure will be the main factor to inhibit carbon emissions.

1. Introduction and Literature Review

China is not only the country with the largest energy production and consumption in the world but also the country with the largest carbon emissions [1]. In 2020, China's carbon emissions are 9.9 billion tons. Since 2006, China has been the world's largest carbon emitter [2]. In September 2020, China promised the world that it would achieve carbon peak by 2030 and carbon neutrality by 2060 [3]. The proposal of “double carbon target” puts forward higher requirements for China's mining carbon emission reduction and low-carbon development [4]. As a high-energy consumption industry, it is of great significance to study the carbon emission of energy consumption in China's mining industry and its relationship with the growth of industrial output value and analyze its reasons for the green and low-carbon development of mining industry.

The decoupling theory was originally used in physics to study the comparison of the change trends of two variables. Later, OECD [5] put forward the concept and model of “decoupling” in the economic sense for the first time in the report of *Indicators for Measuring the Decoupling Relationship between Economic Growth and Environmental Impact* and discussed how to reduce or even block the correlation between economic growth and environmental pollution. At present, research mainly focuses on energy conservation and emission reduction, and the decoupling method is applied to different levels, including industry level, regional level, and national level. The later research involves the influencing factors of carbon emission and further refines the decoupling indicators into primary decoupling and secondary decoupling [6]. Primary decoupling is the decoupling between economic growth and natural resources, while the decoupling between economic growth and environmental pollution is called secondary

decoupling. Tapio constructed a complete decoupling index system and studied the decoupling between the development of the European transportation industry and transportation volume and CO₂ [7]. Then, Gray et al. [8], Diakoulaki and Mandaraka [9], Freitas and Kaneko [10], Cserekyei and Stern [11], and Conte Grand [12] applied the Tapio decoupling model to analyze the decoupling relationship between economic growth and carbon emissions at the national and industrial levels. In the field of energy conservation, Zhao et al. [13] and Wang [14] used the decoupling theory to study the correlation between China's economic growth and energy consumption. In the field of emission reduction, Peng et al. [15] and Wang et al. [16] studied the decoupling relationship and degree between China's economic growth and energy carbon emissions by constructing the decoupling analysis model of economy and energy carbon emissions and analyzed the temporal and spatial evolution trend of their decoupling development. Yue and Li [17] studied the decoupling relationship between economic growth and carbon emissions in some provinces from a regional perspective. Subsequently, Ren et al. [18], Lu et al. [19], and Wang and Yang [20] constructed the influencing factor model of carbon dioxide emission.

The main methods to measure the decoupling relationship between carbon emissions and economic growth are the elasticity coefficient proposed by Tapio and the decoupling factor proposed by OECD. In contrast, Tapio is better able to eliminate the error in the selection of base period [7, 21]. Therefore, this study uses the Tapio index to measure the relationship between environmental pressure represented by economic growth and carbon emission. The analysis of relevant literature found that the research on the decoupling of carbon emissions from mining energy consumption is less and not in-depth. Combined with the particularity of China's mining industry, this study constructs the decoupling model of carbon emission in mining industry using the Tapio theory. In the model, the analysis method of assigning value to the decoupling state is proposed for the first time. The original decoupling model cannot directly reflect the change law of carbon emission decoupling state when analyzing the characteristics of time evolution. To better analyze the causes of carbon emission decoupling, two intermediate variables, energy efficiency decoupling index and energy structure decoupling index, are introduced. Because there are great differences among the subsectors of the mining industry, this study not only studies the decoupling relationship between the carbon emissions and the growth of the whole mining industry but also studies the five subsectors.

2. Research Methods and Data Sources

2.1. Introduction to Decoupling Theory. The decoupling theory is a basic theory to describe the relationship between economic growth and resource consumption or environmental pollution. Decoupling analysis has become a research hotspot in the field of resources and environment. At present, speed decoupling analysis mainly includes OECD model and Tapio decoupling model [22]. The decoupling factor method of

OECD model is based on the initial value and the final value. It is sensitive to the selection of values, and the calculation results are prone to deviation [5]. The Tapio decoupling model can not only analyze the impact of various factors on decoupling indicators by constructing a causal chain but also integrate two types of indicators: total amount change and relative amount change. It adopts the elastic analysis method with the period as the time scale to reflect the decoupling relationship between variables, which effectively alleviates the calculation deviation caused by the high sensitivity or extreme value selected at the beginning and end of the OECD index model. It further improves the objectivity and accuracy of decoupling relationship measurement and analysis [7]. Therefore, this study adopts the Tapio decoupling analysis model. The calculation formula is as follows:

$$e = \frac{\% \Delta C}{\% \Delta GDP}, \quad (1)$$

where e represents the decoupling index between economic growth and carbon emissions; GDP represents output value; C represents carbon emissions; and $\% \Delta C$ and $\% \Delta GDP$ represent the change rates of C and GDP, respectively.

The decoupling degree is determined according to the decoupling index. The Tapio decoupling model takes 0, 0.8, and 1.2 as the critical values of decoupling index and divides the decoupling relationship into three states: negative decoupling, decoupling, and connection [7]. According to the positive and negative change rate of carbon emission and GDP, the decoupling relationship is further divided into eight decoupling states: weak negative decoupling, strong negative decoupling, expansion negative decoupling, decline decoupling, strong decoupling, weak decoupling, recession connection, and expansion connection, as shown in Table 1.

2.2. Construction of Decoupling Analysis Model of Carbon Emission in Mining Industry

2.2.1. Construction of Carbon Emission Decoupling Analysis Model. According to the decoupling theory introduced above, the calculation formula of carbon emission decoupling index is transformed as follows:

$$e = \frac{\% \Delta C}{\% \Delta G} = \frac{(C^t - C^{t-1})/C^{t-1}}{(G^t - G^{t-1})/G^{t-1}} = \frac{\Delta C/C^{t-1}}{\Delta G/G^{t-1}}, \quad (2)$$

where e refers to the decoupling index between carbon emissions and industrial output value; $\% \Delta C$ and $\% \Delta G$ represent the change rate of carbon emission and industrial output value, respectively, C^t and G^t represent carbon emissions and industrial output value in period t ; C^{t-1} and G^{t-1} represent carbon emissions and industrial output value in $t-1$ period, ΔC refers to the difference between carbon emissions in phase t and phase $t-1$, and ΔG represents the difference between the industrial output value of phase t and the industrial output value of phase $t-1$.

According to formula (2), the calculation formula of carbon emission decoupling index of mining industry and its subsectors is as follows:

TABLE 1: Classification of the decoupling status by the Tapio model.

State	% ΔC	% ΔGDP	e
Strong decoupling	<0	>0	$e < 0$
Weak decoupling	>0	>0	$0 < e < 0.8$
Decline decoupling	<0	<0	$e > 1.2$
Expansion connection	>0	>0	$0.8 \leq e \leq 1.2$
Recession connection	<0	<0	$0.8 \leq e \leq 1.2$
Expansion negative decoupling	>0	>0	$e > 1.2$
Weak negative decoupling	<0	<0	$0 < e < 0.8$
Strong negative decoupling	>0	<0	$e < 0$

$$e_i = \frac{\% \Delta C_i}{\% \Delta G_i}, \quad (3)$$

where e_i refers to the decoupling index between the carbon emissions and the output value of i sector; $\% \Delta C_i$ and $\% \Delta G_i$ represent the change rate of the carbon emission and output value of i sector, respectively; and $e, e_1, e_2, e_3, e_4,$ and $e_5,$ respectively, represent the carbon emission decoupling index of mining industry (all sectors), coal sector, petroleum and natural gas sector, ferrous metal sector, nonferrous metal sector, and nonmetal sector.

Formula (2) can be abbreviated as follows:

$$e = \frac{\Delta C/C^{t-1}}{\Delta G/G^{t-1}} = \frac{\Delta C/C}{\Delta G/G}. \quad (4)$$

Next, formulas (2)–(4) are decomposed as follows:

$$e = \frac{\Delta C/C}{\Delta G/G} = \frac{\Delta C/C}{\Delta E/E} \times \frac{\Delta E/E}{\Delta G/G}, \quad (5)$$

where e represents the decoupling index between carbon emissions and industrial output value; $\Delta C/C = \% \Delta C$ represents the change rate of carbon emissions of the industry; $\Delta G/G = \% \Delta G$ represents the change rate of industrial output value; and $\Delta E/E = \% \Delta E$ represents the change rate of energy consumption in the industry.

$$\text{Let } e_K = \frac{\Delta C/C}{\Delta E/E} = \frac{\% \Delta C}{\% \Delta E}, \quad (6)$$

where e_K refers to the decoupling index between carbon emissions and energy consumption, which is called the decoupling index of energy structure. $\% \Delta C$ and $\% \Delta E,$ respectively, represent the change rate of carbon emission and energy consumption. This index reflects the relationship between the change in carbon emission and the change in energy consumption. Generally, it is mainly determined by the proportion of all kinds of energy consumed, that is, by the structure of energy consumption.

According to formula (6), the calculation formula of decoupling index of energy structure of mining industry and its subindustries is as follows:

$$e_{Ki} = \frac{\% \Delta C_i}{\% \Delta E_i}, \quad (7)$$

where e_{ki} represents the decoupling index of carbon emission and energy consumption of i sector; $\% \Delta C_i$ and $\% \Delta E_i$ represent the change rate of carbon emission and output

value of i sector, respectively; and $e_k, e_{k1}, e_{k2}, e_{k3}, e_{k4},$ and $e_{k5},$ respectively, represent the decoupling index of energy structure of mining industry (all sectors), coal sector, petroleum and natural gas sector, ferrous metal sector, nonferrous metal sector, and nonmetal sector.

$$\text{Let } e_T = \frac{\Delta E/E}{\Delta G/G} = \frac{\% \Delta E}{\% \Delta G}, \quad (8)$$

where e_T represents the decoupling index between energy consumption and industrial output value, which is called the energy efficiency decoupling index. This index reflects the energy consumption per unit output value. Generally, it is mainly related to energy-saving technologies and energy-saving and emission reduction measures.

According to formula (8), the calculation formula of energy efficiency decoupling index of mining industry and its subindustries is as follows:

$$e_{Ti} = \frac{\% \Delta E_i}{\% \Delta G_i}, \quad (9)$$

where e_{Ti} represents the decoupling index of energy consumption and output value of i sector; $\% \Delta E_i$ and $\% \Delta G_i,$ respectively, represent the change rate of energy consumption and industrial output value of i sector; and $e_T, e_{T1}, e_{T2}, e_{T3}, e_{T4},$ and $e_{T5},$ respectively, represent the energy efficiency decoupling index of mining industry (all sectors), coal sector, petroleum and natural gas sector, ferrous metal sector, nonferrous metal sector, and nonmetal sector.

The following formula can be obtained from formulas (5), (6), and (8):

$$e = e_K \times e_T. \quad (10)$$

Formula (10) shows that the carbon emission decoupling index is the product of energy structure index and energy efficiency index [15]. Therefore, to further understand the reasons for the decoupling between output growth and carbon emission, based on logical causality, the carbon emission decoupling index can be decomposed into two intermediate variables. The intermediate variables are the decoupling index between output growth and energy consumption and the decoupling index between energy consumption and carbon emission.

2.2.2. Analysis Model of Decoupling State of Carbon Emission. According to the previous description, among the decoupling states of carbon emissions, the most ideal state is the strong decoupling state, indicating that the economic growth is positive and the carbon emission growth is negative. The strong negative decoupling is the most unsatisfactory state, indicating that the economic growth is negative while the environmental pressure is increasing. When the economic aggregate maintains continuous growth ($\Delta GDP > 0$), the smaller the GDP elasticity of energy carbon emissions, the more significant the decoupling, that is, the higher the decoupling degree.

To intuitively reflect the decoupling state of carbon emissions in each period, a two-dimensional coordinate

diagram can be used to reflect the decoupling state and its formation mechanism, as shown in Figure 1 [7, 23]. To facilitate the presentation of the decoupling state, each decoupling state is corresponding to a symbol with a positive and negative sign. The symbol with “+” indicates the decoupling state, which means that the environmental pressure decreases and is conducive to carbon emission reduction; the symbol with “-” indicates the negative decoupling state, which means that the environmental pressure increases, as shown in Table 2. To further visually show the decoupling states according to the time series in the figure for comparison and analysis, each decoupling state is now corresponding to different values, and the values from large to small are corresponding to the ideal and unsatisfactory decoupling states, as shown in Table 2. In other words, strong decoupling state “+I,” the most ideal state, corresponds to “3,” and strong negative decoupling state “-I,” the least ideal state, corresponds to “-3.”

According to the above analysis theory, the energy structure decoupling analysis model and energy efficiency decoupling analysis model have the same theory of the carbon emission decoupling analysis model. The decoupling analysis model of energy structure is given, as shown in Table 3; the energy efficiency decoupling analysis model is shown in Table 4.

2.3. Data Source and Data Processing

2.3.1. Research Object and Data Scope. The research object is the mining industry and its subsectors from 2000 to 2020. The subsectors include mining and washing of coal, extraction of petroleum and natural gas, mining and processing of ferrous metal ores, mining and processing of nonferrous metal ores, and mining and processing of nonmetal ores. In addition to five sectors, China’s mining industry also includes “Professional and support activities for mining” and “Mining of other ores.” Because the output value of “Mining of other ores” accounts for less than 0.1%, “Professional and support activities for mining” only appeared in 2012, and the proportion of output value is also very low. Therefore, the research object of this study is the five main subsectors of China’s mining industry.

In this study, energy is divided into four categories: coal products, petroleum products, natural gas, and secondary energy. Among them, coal products include raw coal, cleaned coal, other coal washing, coke, coke oven gas, blast furnace gas, other gas, and other coking products. Petroleum products include crude oil, gasoline, diesel oil, kerosene, fuel oil, liquefied petroleum gas, refinery dry gas, naphtha, and other petroleum products. Natural gas includes natural gas and liquefied natural gas. Secondary energy includes electricity and heat.

2.3.2. Data Sources. The industrial output value comes from *China Statistical Yearbook* [24]. The specific sources of data are as follows: the industrial output value data from 2000 to 2004 adopt the product sales revenue of industrial

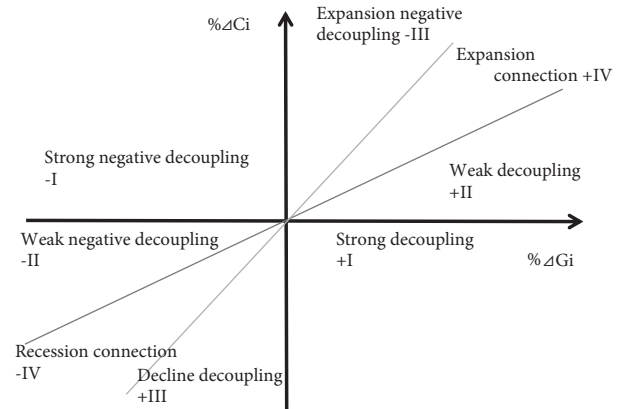


FIGURE 1: Framework for decoupling judgments.

enterprises above designated size in the Statistical Yearbook; the industrial output value data from 2005 to 2017 adopt the main business income of industrial enterprises above designated size in the Statistical Yearbook; and the industrial output value data from 2018 to 2020 adopt the business income of industrial enterprises above designated size in the Statistical Yearbook.

The industrial energy consumption data are from the end energy consumption of industrial subindustries in the *China Energy Statistics Yearbook* from 2000 to 2020 [25]. To avoid repeated calculation and unclear conversion coefficient of standard coal, standard coal equivalent in Statistical Yearbook is adopted. Due to the partial lack of industry end energy consumption data in 2020, it is estimated according to the changes in industrial output value and summary of Statistical Yearbook in 2020.

2.3.3. Data Processing. To avoid the impact of inflation on the annual output value, the industrial output value is treated to eliminate inflation, and the output value from 2001 to 2020 is treated as the base period based on the ex-factory price index of industrial producers in 2000.

The five subsectors are abbreviated as coal sector, petroleum and natural gas sector, ferrous metal sector, nonferrous metal sector, and nonmetal sector. For the calculation method and process of carbon emissions of mining industry and subindustries involved in this study, Wei’s et al.’s research is referred [26].

The carbon emission decoupling index, energy structure decoupling index, and energy efficiency decoupling index of mining industry are expressed as e , e_K , and e_T , respectively. The carbon emission decoupling index of coal sector, petroleum and natural gas sector, ferrous metal sector, nonferrous metal sector, and nonmetal sector is expressed as e_1 , e_2 , e_3 , e_4 , and e_5 , respectively. The decoupling index of energy structure of coal sector, petroleum and natural gas sector, ferrous metal sector, nonferrous metal sector, and nonmetal sector is expressed as e_{k1} , e_{k2} , e_{k3} , e_{k4} , and e_{k5} , respectively. The energy efficiency decoupling index of coal sector, petroleum and natural gas sector, ferrous metal sector, nonferrous metal sector, and nonmetal sector is expressed as e_{T1} , e_{T2} , e_{T3} , e_{T4} , and e_{T5} , respectively.

TABLE 2: Analysis model of decoupling state of carbon emission.

State	State symbol	State value	$\% \Delta C_i$	$\% \Delta G_i$	e_i
Strong decoupling	+I	3	<0	>0	$e < 0$
Weak decoupling	+II	2	>0	>0	$0 < e < 0.8$
Decline decoupling	+III	1	<0	<0	$e > 1.2$
Expansion connection	+IV	0	>0	>0	$0.8 \leq e \leq 1.2$
Recession connection	-IV	0	<0	<0	$0.8 \leq e \leq 1.2$
Expansion negative decoupling	-III	-1	>0	>0	$e > 1.2$
Weak negative decoupling	-II	-2	<0	<0	$0 < e < 0.8$
Strong negative decoupling	-I	-3	>0	<0	$e < 0$

TABLE 3: Analysis model of decoupling state of energy structure.

State	State symbol	State value	$\% \Delta C_i$	$\% \Delta E_i$	e_{K_i}
Strong decoupling	+I	3	<0	>0	$e < 0$
Weak decoupling	+II	2	>0	>0	$0 < e < 0.8$
Decline decoupling	+III	1	<0	<0	$e > 1.2$
Expansion connection	+IV	0	>0	>0	$0.8 \leq e \leq 1.2$
Recession connection	-IV	0	<0	<0	$0.8 \leq e \leq 1.2$
Expansion negative decoupling	-III	-1	>0	>0	$e > 1.2$
Weak negative decoupling	-II	-2	<0	<0	$0 < e < 0.8$
Strong negative decoupling	-I	-3	>0	<0	$e < 0$

TABLE 4: Analysis model of decoupling state of energy efficiency.

State	State symbol	State value	$\% \Delta E_i$	$\% \Delta G_i$	e_{T_i}
Strong decoupling	+I	3	<0	>0	$e < 0$
Weak decoupling	+II	2	>0	>0	$0 < e < 0.8$
Decline decoupling	+III	1	<0	<0	$e > 1.2$
Expansion connection	+IV	0	>0	>0	$0.8 \leq e \leq 1.2$
Recession connection	-IV	0	<0	<0	$0.8 \leq e \leq 1.2$
Expansion negative decoupling	-III	-1	>0	>0	$e > 1.2$
Weak negative decoupling	-II	-2	<0	<0	$0 < e < 0.8$
Strong negative decoupling	-I	-3	>0	<0	$e < 0$

3. Analysis of Calculation Results of Energy Consumption and Carbon Emission of Mining Industry

3.1. *Growth Analysis of Mining Industry and Its Subsectors.* According to the collected data, the fixed base output value of mining industry and its five subindustries is obtained, as shown in Table 5.

As a basic industry, mining belongs to the traditional industry sector and its development is greatly affected by the macroeconomic environment and has obvious cyclical characteristics. China's mining industry has grown rapidly since 2003. In 2008, the total output value of mining industry exceeded trillion, reaching 1178.138 billion CNY. By 2014, the output value had reached 2659.354 billion CNY, the highest in history, as shown in Figure 2. From 2002 to 2014, the total output value increased by 10.52% annually. On the contrary, the output value has been declining from 2015 to 2019, and the output value fell to 163.1195 billion CNY in 2019. During the whole period, except for the petroleum and natural gas sector, the change in output value of other subsectors is almost consistent with the change in total

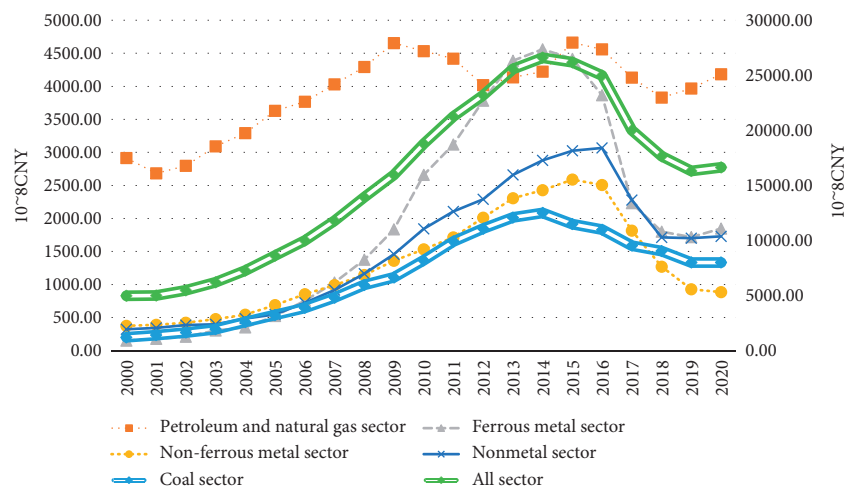
output value, and there is a trend of first rising and then falling. The output value of the petroleum and natural gas sector has fluctuated unstable, as shown in Figure 2.

3.2. *Analysis of Mining Energy Consumption.* According to the collected data, the energy consumption of mining industry and its five subindustries is obtained, as shown in Table 6.

The total energy consumption of China's mining industry has been rising steadily from 2000 to 2013. In 2013, the energy consumption reached a peak of 119.7685 million tons of standard coal, which is consistent with the increasing trend of mining output value. From 2014 to 2016, the energy consumption decreased significantly to 83.9234 million tons of standard coal, and there is little change in energy consumption from 2017 to 2020. From the perspective of energy consumption of each subsector, the energy consumption of coal sector has always been the highest, accounting for more than 40%, followed by petroleum and natural gas sector. The energy consumption of other sectors accounts for less, but shows an upward trend, exceeding 20% by 2020, as shown in Figure 3.

TABLE 5: Fixed base output value of mining industry and its subsectors from 2000 to 2020.

Year	Coal sector (10 ⁸ CNY)	Petroleum and natural gas sector (10 ⁸ CNY)	Ferrous metal sector (10 ⁸ CNY)	Nonferrous metal sector (10 ⁸ CNY)	Nonmetal sector (10 ⁸ CNY)	All sectors (10 ⁸ CNY)
2000	1213.77	2914.99	152.84	375.18	323.20	4979.98
2001	1411.41	2682.46	178.36	390.09	343.84	5006.16
2002	1650.30	2798.88	211.21	421.02	385.50	5466.91
2003	1946.62	3091.59	306.48	476.55	397.35	6218.60
2004	2598.28	3290.07	351.75	545.35	485.83	7271.29
2005	3232.01	3630.00	525.16	689.63	549.55	8626.35
2006	3884.37	3768.48	754.65	855.58	725.67	9988.75
2007	4811.45	4029.57	1030.07	992.26	918.04	11781.38
2008	5968.44	4292.88	1375.24	1144.09	1163.43	13944.08
2009	6646.81	4654.25	1837.04	1359.72	1460.52	15958.34
2010	8208.45	4534.22	2658.26	1533.11	1843.55	18777.59
2011	9910.69	4418.75	3119.56	1712.76	2104.92	21266.70
2012	11080.22	4016.41	3782.20	2013.20	2291.45	23183.47
2013	12091.39	4137.20	4387.27	2305.65	2658.62	25580.13
2014	12502.30	4221.89	4561.09	2428.21	2880.06	26593.54
2015	11489.95	4660.90	4415.80	2588.11	3024.87	26179.64
2016	10979.68	4561.11	3863.83	2505.52	3067.20	24977.34
2017	9539.57	4131.47	2232.24	1816.75	2278.61	19998.65
2018	9037.60	3829.75	1799.28	1271.38	1712.77	17650.79
2019	7999.75	3965.62	1716.35	927.27	1702.95	16311.95
2020	8007.05	4181.83	1846.01	883.60	1727.68	16646.17

FIGURE 2: Changes in output value of China's mining industry and its subsectors from 2000 to 2020. *Note.* In Figure 2, the values of coal sector and all sectors correspond to the right coordinate axis, and the values of other subsectors correspond to the left coordinate axis.

The proportion of secondary energy in China's mining energy consumption structure continues to increase. The proportion of secondary energy increased from 20.57% in 2009 to 22.84% in 2010. After that, the proportion of secondary energy consumption continued to increase to 39.28% in 2020, reaching an all-time high. While increasing the consumption of secondary energy, the consumption of coal products is reduced. For example, the proportion of coal in the history of 2009 decreased from 52.62% to 24.38% in 2020. The proportion of natural gas consumption has increased significantly since 2014, which is mainly due to the continuous increase in natural gas consumption in the petroleum and natural gas sector. By 2020, the proportion of natural gas in the energy consumption of the petroleum and

natural gas sector reached 60%, as shown in Figure 4, but statistics show that the proportion of coal energy in primary energy consumption has been very high, reaching 66.59% in 2012 and 40.15% in 2020, as shown in Figure 4.

Mining activities need to consume a lot of energy, which is the main source of carbon emissions. Low-carbon, green, and sustainable development requires industrial activities to reduce energy consumption and pollutant emissions [27]. From 2001 to 2016, China's mining energy intensity continued to decline, from 1.26 tce/10⁴CNY to 0.34 tce/10⁴CNY, increased slightly in 2017, and reached 0.54 tce/10⁴CNY in 2020, as shown in Figure 3. In terms of comparison of various subsectors, the energy intensity of the coal sector decreased the fastest, from 2.06 tce/10⁴CNY in 2000 to 0.29 tce/10⁴CNY in

TABLE 6: Energy consumption of mining industry and its subsectors from 2000 to 2020.

Year	Coal sector (10 ⁴ tce)	Petroleum and natural gas sector (10 ⁴ tce)	Ferrous metal sector (10 ⁴ tce)	Nonferrous metal sector (10 ⁴ tce)	Nonmetal sector (10 ⁴ tce)	All sectors (10 ⁴ tce)
2000	2504.00	2645.84	157.43	192.59	423.37	5923.23
2001	2656.52	2837.84	165.36	208.27	462.02	6330.01
2002	2899.91	2938.14	262.23	247.68	534.57	6882.53
2003	3511.94	3017.35	276.26	271.60	598.25	7675.40
2004	4226.67	2579.36	307.61	278.80	532.44	7924.88
2005	4240.53	2643.75	401.76	290.55	575.64	8152.23
2006	4163.68	2681.31	450.45	307.74	586.39	8189.57
2007	4580.79	2747.59	524.33	345.37	611.44	8809.51
2008	4016.09	2998.69	833.35	468.19	911.75	9228.07
2009	6080.10	2975.44	572.21	380.67	746.11	10754.53
2010	5959.84	3120.18	711.85	429.78	726.40	10948.05
2011	6245.63	2917.73	853.01	527.06	735.44	11278.87
2012	6453.00	2895.21	1053.81	586.30	979.72	11968.04
2013	6310.61	3096.36	1088.31	598.28	883.29	11976.85
2014	3653.96	3184.60	1047.70	598.00	911.24	9395.50
2015	4229.60	3149.46	820.27	561.94	864.22	9625.49
2016	3507.90	2867.48	677.91	519.28	819.77	8392.34
2017	4058.21	2872.61	697.57	524.23	737.72	8890.34
2018	3716.41	2850.63	714.70	578.67	838.03	8698.44
2019	3872.12	2904.64	729.61	575.42	835.22	8917.01
2020	3875.65	3063.00	784.73	548.32	847.35	9119.05

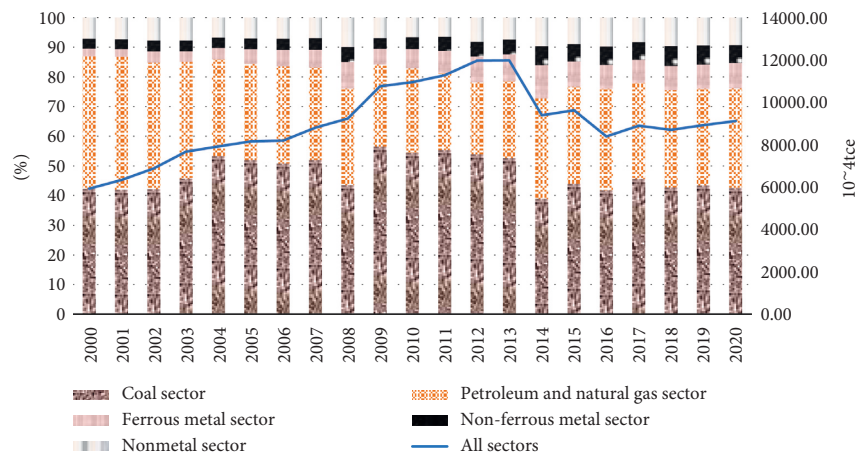


FIGURE 3: Comparative analysis of energy consumption of China’s mining industry and its subsectors from 2000 to 2020. *Note.* In Figure 3, the value of “all sectors” corresponds to the left coordinate, and other values correspond to the right coordinate.

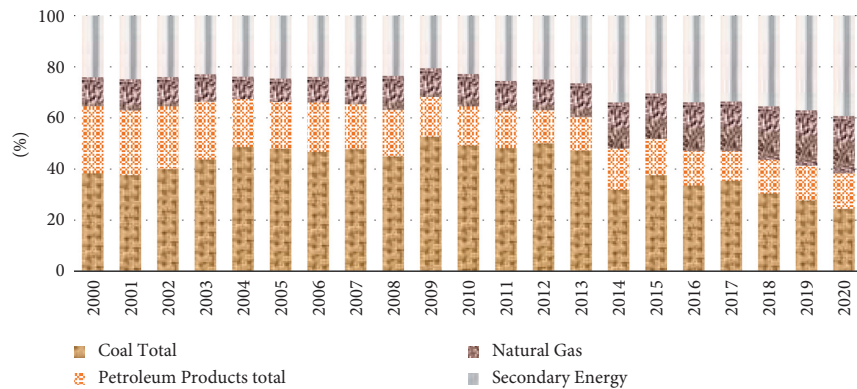


FIGURE 4: Comparative analysis of energy consumption structure of mining industry from 2000 to 2020.

2014, with a decrease rate of 85.92%, and rebounded to $0.49 \text{ tce}/10^4 \text{ CNY}$ in 2020 in the later stage. At the same time, the energy intensity of ferrous metal sector and nonmetal ores sector has also decreased significantly. On the contrary, the energy intensity of nonferrous metal ores sector first decreased and then increased to $0.62 \text{ tce}/10^4 \text{ CNY}$ in 2020, becoming the highest in history. The energy intensity of petroleum and natural gas sector is $0.73 \text{ tce}/10^4 \text{ CNY}$ in 2020, which has become the sector with the highest energy consumption per unit output value, as shown in Figure 5.

3.3. Analysis of Calculation Results of Carbon Emission of Energy Consumption in Mining Industry. The calculation process of carbon emission of energy consumption in mining industry and its subdivisions refers to the research of Wei et al. [26], and the specific calculation results are shown in Table 7.

From 2000 to 2020, the change trend of carbon emissions from energy consumption of China's mining industry is to rise for a long time, then decline sharply, and finally stabilize, as shown in Figure 6. The lowest carbon emission in 2000 was 179.4723 million tons, and the carbon peak in 2013 was 388.740300 million tons. From 2014 to 2016, carbon emissions decreased rapidly to 278.6806 million tons, a decrease of 28.31% compared with 2013. The highest carbon emission of the coal sector was 205.9115 million tons in 2013, and the carbon emission of the sector changed steadily. The highest value of the petroleum and natural gas sector is 76.9346 million tons in 2015, and the change in carbon emission in the sector is unstable. The highest carbon emission of ferrous metal sector is 51.0265 million tons in 2013, and the change in carbon emission of the sector is relatively stable. The highest carbon emission of nonferrous metal sector is 26.1781 million tons in 2019, and the carbon emission variable of the sector is unstable. The highest carbon emission of nonmetal sector is 34.5513 million tons in 2012, and the change in carbon emission of the sector is basically stable, as shown in Figure 6.

From the perspective of carbon emissions of various industries, the coal sector accounts for the largest proportion of carbon emissions, accounting for more than 40% from 2000 to 2020. Followed by the petroleum and natural gas sector, the proportion fluctuated greatly. The carbon emission of ferrous metal sector is the third, but the change is very large. The nonmetal sector ranks fourth, with a very stable proportion. The nonferrous metal sector accounts for the smallest proportion and the industry scale is small, but it has maintained growth, as shown in Figure 7.

4. Empirical Analysis on the Decoupling Relationship between Carbon Emission and Industrial Growth in Mining Industry

Due to the great differences in the production of each subsector, this study not only studies the decoupling of the carbon emission of the mining industry, but also studies the decoupling states of carbon emissions in five subsectors, respectively.

4.1. Decoupling Analysis of Carbon Emissions from the Coal Sector. According to the collected data of the coal sector from 2000 to 2020, this part calculates the carbon emission change rate $\% \Delta C_1$, the energy consumption change rate $\% \Delta E_1$, and the industrial output value change rate $\% \Delta G_1$ and then calculates the carbon emission decoupling index e_1 , the energy structure decoupling index e_{K1} , and the energy efficiency decoupling index e_{T1} using formulas (3), (7), and (9). The decoupling state of carbon emission is judged according to the decoupling model, as shown in Table 2; the decoupling state of energy structure is judged according to the decoupling model, as shown in Table 3; and the decoupling state of energy efficiency is judged according to the decoupling model, as shown in Table 4. All calculation results are shown in Table 8.

According to Figure 8, in the 20 years from 2001 to 2020, there are 13 times of decoupling between carbon emission and output value growth of the coal sector, including 4 times of strong decoupling, 8 times of weak decoupling, and 1 time of recession decoupling. There are 6 times of negative decoupling, including 3 times of strong negative decoupling, 2 times of weak negative decoupling, and 1 time of expansion negative decoupling. The expansion connection occurred 1 time. From the whole research period, most of the carbon emissions are decoupled from the output value growth, which proves that the carbon emission reduction in the coal sector is effective.

As shown in Figure 9, from the perspective of time evolution characteristics, the decoupling state of the coal sector is consistent. The period from 2001 to 2020 can be divided into two stages. The first is 2001–2014, which is the decoupling state between carbon emission and output value growth of the coal sector. In addition to the weak negative decoupling affected by the financial storm in 2009, this period shows the rapid growth of output value, but the growth of carbon emission is slow or even negative; this period is not only the golden decade of rapid development of the mining industry but also the stage of rapid development of China's economy. Finally, 2015–2020 is the negative decoupling stage between carbon emission and output value growth of the coal sector, which is reflected in the negative growth of output value, but the slow reduction or even increase in carbon emission. During this period, the market demand for coal products decreased, because China's economic development slowed down and the country put forward macro-policies such as supply-side reform and industrial structure optimization. At the same time, as China's main petrochemical energy, the development of coal sector is restricted by environmental factors.

To further analyze the reasons for the decoupling between energy carbon emission and output value growth in the coal sector, the carbon emission decoupling index e_1 is decomposed into two intermediate variables: energy efficiency decoupling e_{T1} and energy structure decoupling e_{K1} . The relationship between intermediate variables and carbon emission decoupling index is shown in Figure 10. According to Figure 10, the fluctuation of carbon emission decoupling index and energy efficiency decoupling index in the coal sector is almost identical, indicating that the decoupling

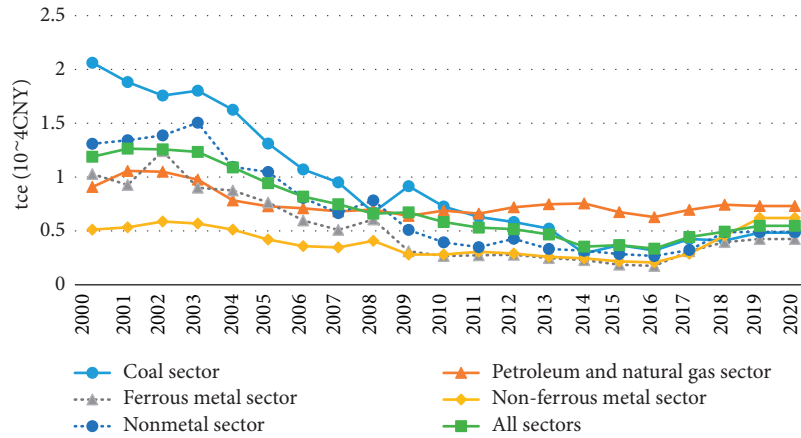


FIGURE 5: Comparative analysis of energy intensity of mining industry and its subsectors from 2000 to 2020.

TABLE 7: Carbon emissions of mining industry and its subsectors from 2000 to 2020.

Year	Coal sector (10 ⁴ t)	Petroleum and natural gas sector (10 ⁴ t)	Ferrous metal sector (10 ⁴ t)	Nonferrous metal sector (10 ⁴ t)	Nonmetal sector (10 ⁴ t)	All sectors (10 ⁴ t)
2000	8264.86	6630.87	754.94	806.89	1489.67	17947.23
2001	8821.33	7224.24	796.31	869.51	1630.07	19341.46
2002	9472.94	7442.95	941.15	929.14	1739.59	20525.77
2003	11393.53	7609.33	1246.00	1194.46	2036.44	23479.75
2004	13451.44	6712.31	1389.39	1183.82	1829.99	24566.95
2005	13544.54	6919.98	1870.04	1260.67	1911.92	25507.15
2006	13329.34	6661.88	2187.24	1361.47	1980.72	25520.66
2007	14594.01	6704.67	2589.68	1560.68	2097.78	27546.82
2008	13127.86	7113.56	3466.87	1916.14	2903.04	28527.48
2009	18966.27	7104.76	2584.34	1659.99	2486.78	32802.14
2010	18781.23	7394.48	3301.66	1912.25	2499.19	33888.80
2011	19769.17	7105.40	4047.41	2304.65	2640.93	35867.57
2012	20540.05	7084.64	4636.35	2510.34	3455.13	38226.50
2013	20591.15	7465.77	5102.65	2605.86	3108.61	38874.03
2014	13015.30	7671.99	4995.94	2596.87	3189.36	31469.46
2015	14309.50	7693.46	3865.09	2415.69	3005.72	31289.45
2016	12169.03	7173.64	3385.83	2245.97	2893.60	27868.06
2017	13773.09	7112.47	3436.50	2313.86	2683.12	29319.03
2018	13002.64	6918.40	3538.35	2610.47	3001.20	29071.06
2019	13396.44	7051.19	3780.76	2617.81	3001.36	29847.56
2020	13408.66	7435.62	4066.37	2494.52	3044.95	30450.11

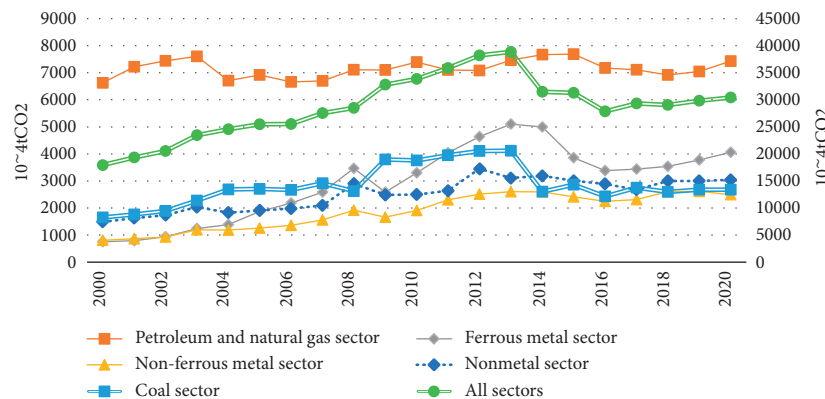


FIGURE 6: Carbon emissions of China’s mining industry and subsectors from 2000 to 2020. *Note.* In Figure 6, the value of coal sector and all sectors adopts the right longitudinal axis coordinates, and the other values are the left longitudinal axis coordinates.

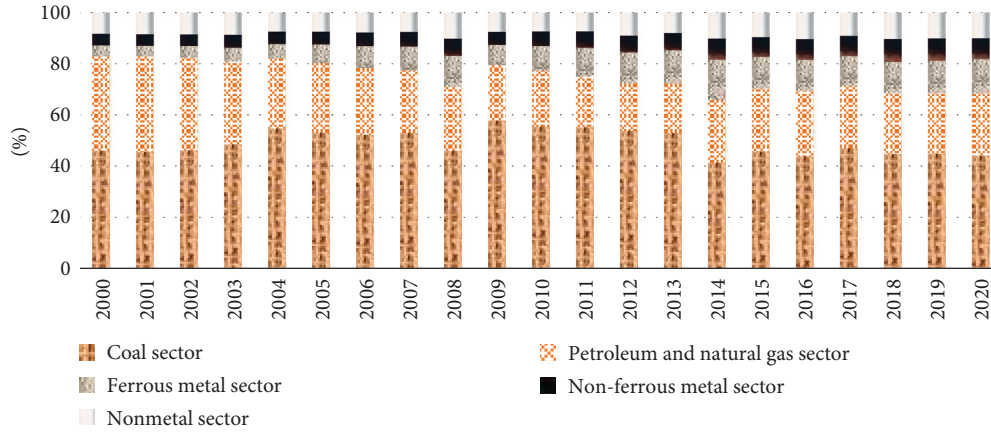


FIGURE 7: Analysis on the proportion of carbon emissions of various sectors from 2000 to 2020.

TABLE 8: Decoupling index and decoupling relationship of the coal sector from 2001 to 2020.

Year	$\% \Delta E_1$	$\% \Delta G_1$	$\% \Delta C_1$	e_{T1}	e_{T1} state	e_{K1}	e_{K1} state	e_1	e_1 state
2001	0.06	0.16	0.07	0.37	+II 2	1.11	+IV 0	0.41	+II 2
2002	0.09	0.17	0.07	0.54	+II 2	0.81	+IV 0	0.44	+II 2
2003	0.21	0.18	0.20	1.18	+IV 0	0.96	+IV 0	1.13	+IV 0
2004	0.20	0.33	0.18	0.61	+II 2	0.89	+IV 0	0.54	+II 2
2005	0.00	0.24	0.01	0.01	+II 2	2.11	-III -1	0.03	+II 2
2006	-0.02	0.20	-0.02	-0.09	+I 3	0.88	-IV 0	-0.08	+I 3
2007	0.10	0.24	0.09	0.42	+II 2	0.95	+IV 0	0.40	+II 2
2008	-0.12	0.24	-0.10	-0.51	+I 3	0.81	+IV 0	-0.42	+I 3
2009	0.51	0.11	0.44	4.52	-III -1	0.87	+IV 0	3.91	-III -1
2010	-0.02	0.23	-0.01	-0.08	+I 3	0.49	-II -2	-0.04	+I 3
2011	0.05	0.21	0.05	0.23	+II 2	1.10	+IV 0	0.25	+II 2
2012	0.03	0.12	0.04	0.28	+II 2	1.17	+IV 0	0.33	+II 2
2013	-0.02	0.09	0.00	-0.24	+I 3	-0.11	-I -3	0.03	+II 2
2014	-0.42	0.03	-0.37	-12.39	+I 3	0.87	-IV 0	-10.83	+I 3
2015	0.16	-0.08	0.10	-1.95	-I -3	0.63	+II 2	-1.23	-I -3
2016	-0.17	-0.04	-0.15	3.84	+III 1	0.88	-IV 0	3.37	+III 1
2017	0.16	-0.13	0.13	-1.20	-I -3	0.84	+IV 0	-1.00	-I -3
2018	-0.08	-0.05	-0.06	1.60	+III 1	0.66	-II -2	1.06	-II -2
2019	0.04	-0.11	0.03	-0.36	-I -3	0.72	+II 2	-0.26	-I -3
2020	-0.03	+0.00	0.00	-1.00	-II -2	1.00	-IV 0	1.00	-II -2

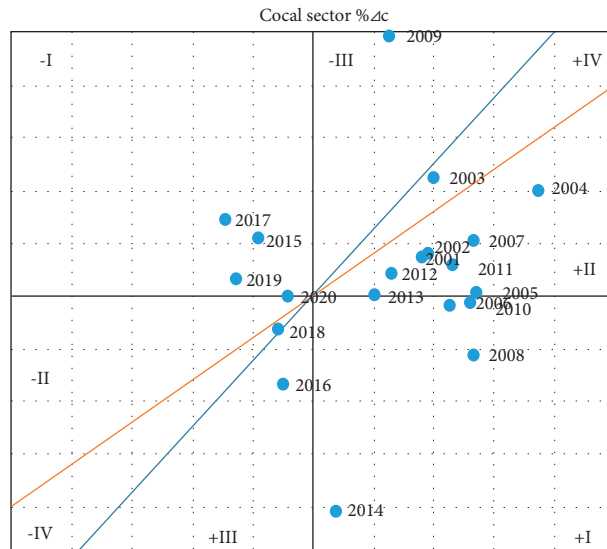


FIGURE 8: Carbon emission decoupling states of energy consumption in coal sector from 2001 to 2020.

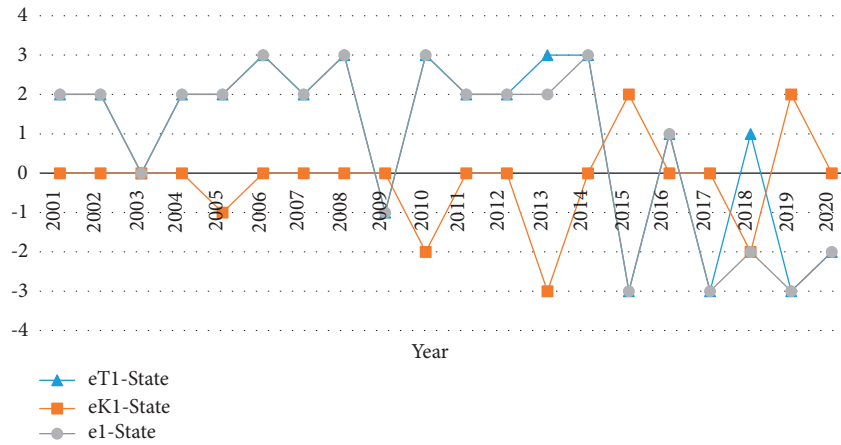


FIGURE 9: Decoupling of energy efficiency, energy structure, and carbon emission in coal sector from 2001 to 2020.

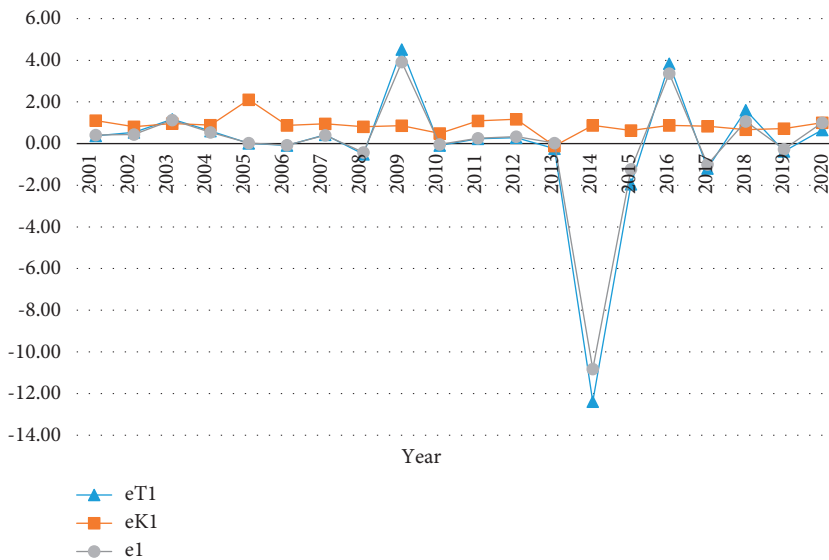


FIGURE 10: Relationship between carbon emission decoupling index and intermediate variables in coal sector from 2001 to 2020.

state of carbon emission is determined by the energy efficiency decoupling index. That is to say, the main driving factor of carbon emission reduction in the coal sector is energy efficiency. Energy efficiency is mainly affected by energy-saving measures and improving the level of energy utilization technology. Therefore, these two aspects are very important for carbon emission reduction in the coal sector. At the same time, in-depth analysis found that the positive and substantial growth of output value will lead to strong decoupling of carbon emissions. For example, the growth rate of output value from 2004 to 2012 exceeded 20%, which corresponds to strong decoupling or weak decoupling of carbon emissions. On the contrary, the growth of output value from 2015 to 2019 is negative, resulting in strong negative decoupling or weak negative decoupling of carbon emissions, as shown in Figure 9. Through this phenomenon, this study believes that at present, the adjustable range of production capacity of the coal sector is very limited, and the coal supply lacks elasticity; that is, the industry is still in the stage of economies of scale. When the coal output is reduced,

the corresponding energy consumption and operating costs cannot be reduced.

According to Figures 9 and 10, it can be seen that the decoupling index of energy structure has a little impact on the decoupling state of carbon emissions during the whole period. The decoupling of energy structure has been getting better and better since 2014, and the decoupling state has occurred many times, which has an increasing inhibitory effect on carbon emissions. The decoupling of energy efficiency has a great inhibitory effect on carbon emissions from 2001 to 2014, but its inhibitory effect has decreased and even promoted carbon emissions since 2015. It can be seen from Figure 9 that the effect of energy conservation and emission reduction in the coal sector from 2001 to 2014 is very prominent, and the energy intensity has been declining. It is obvious that the energy efficiency of the coal sector has stabilized or even rebounded since 2015. It can be seen that the energy efficiency of the coal sector has tended to the limit, and its inhibitory effect on carbon emissions has begun to decrease. At the same time, according to the previous

TABLE 9: Decoupling index and decoupling relationship of the petroleum and natural gas sector from 2001 to 2020.

Year	$\% \Delta E_2$	$\% \Delta G_2$	$\% \Delta C_2$	e_{T2}	e_{T2} state	e_{K2}	e_{K2} state	e_2	e_2 state			
2001	0.07	-0.08	0.09	-0.91	-I	-3	1.23	-III	-1	-1.12	-I	-3
2002	0.04	0.04	0.03	0.81	+IV	0	0.86	+IV	0	0.70	+II	2
2003	0.03	0.10	0.02	0.26	+II	2	0.83	+IV	0	0.21	+II	2
2004	-0.15	0.06	-0.12	-2.26	+I	3	0.81	-IV	0	-1.84	+I	3
2005	0.02	0.10	0.03	0.24	+II	2	1.24	-III	-1	0.30	+II	2
2006	0.01	0.04	-0.04	0.37	+II	2	-2.63	+I	3	-0.98	+I	3
2007	0.02	0.07	0.01	0.36	+II	2	0.26	+II	2	0.09	+II	2
2008	0.09	0.07	0.06	1.40	-III	-1	0.67	+II	2	0.93	+IV	0
2009	-0.01	0.08	0.00	-0.09	+I	3	0.16	-II	-2	-0.01	+I	3
2010	0.05	-0.03	0.04	-1.89	-I	-3	0.84	+IV	0	-1.58	-I	-3
2011	-0.06	-0.03	-0.04	2.55	+III	1	0.60	-II	-2	1.54	+III	1
2012	-0.01	-0.09	0.00	0.08	-II	-2	0.38	-II	-2	0.03	-II	-2
2013	0.07	0.03	0.05	2.31	-III	-1	0.77	+II	2	1.79	-III	-1
2014	0.03	0.02	0.03	1.39	-III	-1	0.97	+IV	0	1.35	-III	-1
2015	-0.01	0.10	0.00	-0.11	+I	3	-0.25	-I	-3	0.03	+II	2
2016	-0.09	-0.02	-0.07	4.18	+III	1	0.75	+II	2	3.16	+III	1
2017	+0.00	-0.09	-0.01	-0.02	-I	-3	-4.77	+I	3	0.09	-II	-2
2018	-0.01	-0.07	-0.03	0.10	-II	-2	3.57	+III	1	0.37	-II	-2
2019	0.02	0.04	0.02	0.53	+II	2	1.01	+IV	0	0.54	+II	2
2020	-0.02	0.06	0.05	-0.33	+I	3	-2.86	-I	-3	0.95	+IV	0

analysis, with the development of new energy, the future energy structure should be the main factor to curb carbon emissions from coal sector.

4.2. *Decoupling Analysis of Carbon Emissions from the Petroleum and Natural Gas Sector.* According to the collected data of the petroleum and natural gas sector from 2000 to 2020, this part calculates the carbon emission change rate $\% \Delta C_2$, the energy consumption change rate $\% \Delta E_2$, and the industrial output value change rate $\% \Delta G_2$ and then calculates the carbon emission decoupling index e_2 , the energy structure decoupling index e_{K2} , and the energy efficiency decoupling index e_{T2} using formulas (3), (7), and (9). The decoupling state of carbon emission is judged according to the decoupling model, as shown in Table 2; the decoupling state of energy structure is judged according to the decoupling model, as shown in Table 3; and the decoupling state of energy efficiency is judged according to the decoupling model, as shown in Table 4. All calculation results are shown in Table 9.

According to Figure 11, from 2001 to 2020, there are 11 times of decoupling between carbon emission and output value growth of the petroleum and natural gas sector, including 3 times of strong decoupling, 6 times of weak decoupling, and 2 times of recession decoupling. There are 7 times of negative decoupling, including 2 times of strong negative decoupling, 3 times of weak negative decoupling, and 2 times of expansion negative decoupling. There are 2 times of expansion connection. From the whole research period, most of the carbon emissions are decoupled from the growth of output value, which proves that the energy conservation and emission reduction in the petroleum and natural gas sector have a certain effect, but the effect is not good.

As shown in Figure 12, from the perspective of time evolution characteristics, the decoupling state of carbon

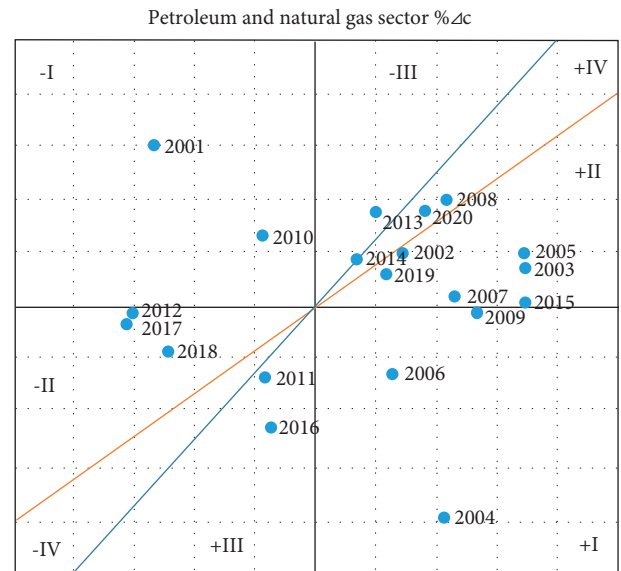


FIGURE 11: Carbon emission decoupling states of energy consumption in the petroleum and natural gas sector from 2001 to 2020.

emissions in the petroleum and natural gas sector showed phased changes from 2001 to 2020, which is divided into three stages according to the decoupling index. The first stage from 2001 to 2009 is the decoupling state of carbon emissions. In addition to the strong negative decoupling state in 2001, the following eight years are almost the decoupling state. In particular, observing the decoupling index, it can be considered that this stage is more inclined to the strong decoupling state. The output value has been increasing steadily from 2002 to 2009, but the carbon emissions have decreased. This stage is the period with the best emission reduction effect in the petroleum and natural

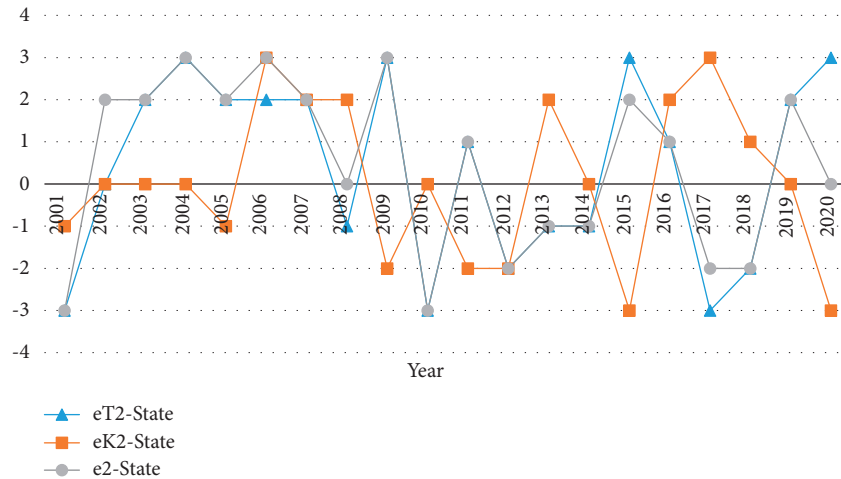


FIGURE 12: Decoupling of energy efficiency, energy structure, and carbon emission in the petroleum and natural gas sector from 2001 to 2020.

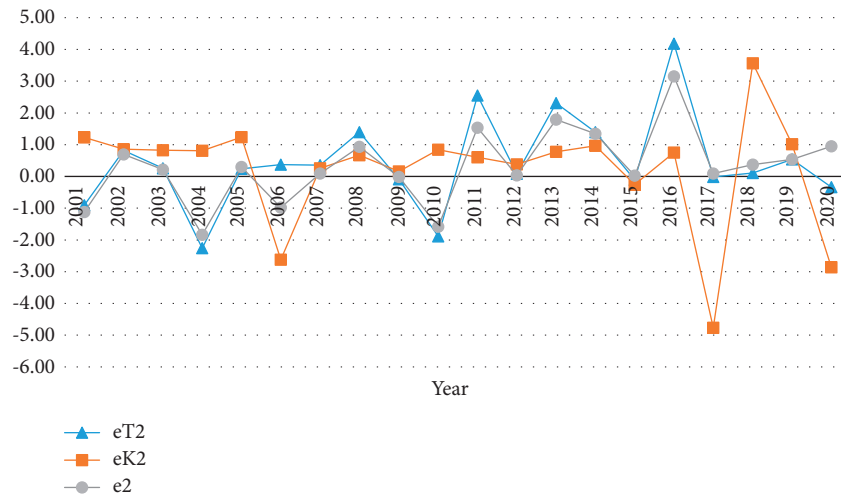


FIGURE 13: Relationship between carbon emission decoupling index and intermediate variables of the petroleum and natural gas sector from 2001 to 2020.

gas sector. The second stage is from 2010 to 2014, which is basically in the state of negative decoupling, except for recession decoupling in 2011; the output value has been decreasing or increasing slightly during this period. The third stage is 2015–2020. The negative decoupling state of carbon emissions fluctuates greatly in this period. The decoupling state and negative decoupling state appear alternately and are closely related to the increase in output value.

To further analyze the reasons for the decoupling between energy carbon emission and output value growth in the petroleum and natural gas sector, the carbon emission decoupling index e_2 is decomposed into energy efficiency decoupling index e_{T2} and energy structure decoupling index e_{K2} . The relationship between intermediate variables and carbon emission decoupling index is shown in Figure 13. According to Figures 12 and 13, it can be seen that the decoupling of carbon emissions in the petroleum and natural gas sector is mainly affected by energy efficiency, and the

decoupling of carbon emissions by energy structure is small. From 2002 to 2009, energy efficiency basically inhibited carbon emissions, and from 2010 to 2014, energy efficiency basically promoted carbon emissions. From 2015 to 2020, the energy structure has an increasing impact on the decoupling of carbon emissions. In particular, the energy structure in 2016–2019 has an inhibitory effect on carbon emissions. The analysis of the energy structure data of subdivided sectors also confirms this conclusion, because the petroleum and natural gas sector has been increasing the consumption of natural gas in recent years; the consumption of natural gas accounts for nearly 60% in 2020, as shown in Figure 3.

4.3. Decoupling Analysis of Carbon Emission from the Ferrous Metal Sector. According to the collected data of the ferrous metal sector from 2000 to 2020, this part calculates the carbon emission change rate $\% \Delta C_3$, the energy consumption

TABLE 10: Decoupling index and decoupling relationship of the ferrous metal sector from 2001 to 2020.

Year	$\% \Delta E_3$	$\% \Delta G_3$	$\% \Delta C_3$	e_{T3}	e_{T3} state	e_{K3}	e_{K3} state	e_3	e_3 state			
2001	0.05	0.17	0.05	0.30	+II	2	1.09	+IV	0	0.33	+II	2
2002	0.59	0.18	0.18	3.18	-III	-1	0.31	+II	2	0.99	+IV	0
2003	0.05	0.45	0.32	0.12	+II	2	6.05	-III	-1	0.72	+II	2
2004	0.11	0.15	0.12	0.77	+II	2	1.01	+IV	0	0.78	+II	2
2005	0.31	0.49	0.35	0.62	+II	2	1.13	+IV	0	0.70	+II	2
2006	0.12	0.44	0.17	0.28	+II	2	1.40	-III	-1	0.39	+II	2
2007	0.16	0.36	0.18	0.45	+II	2	1.12	+IV	0	0.50	+II	2
2008	0.59	0.34	0.34	1.76	-III	-1	0.57	+II	2	1.01	+IV	0
2009	-0.31	0.34	-0.25	-0.93	+I	3	0.81	-IV	0	-0.76	+I	3
2010	0.24	0.45	0.28	0.55	+II	2	1.14	+IV	0	0.62	+II	2
2011	0.20	0.17	0.23	1.14	+IV	0	1.14	+IV	0	1.30	-III	-1
2012	0.24	0.21	0.15	1.11	+IV	0	0.62	+II	2	0.69	+II	2
2013	0.03	0.16	0.10	0.20	+II	2	3.07	-III	-1	0.63	+II	2
2014	-0.04	0.04	-0.02	-0.94	+I	3	0.56	-II	-2	-0.53	+I	3
2015	-0.22	-0.03	-0.23	6.81	+III	1	1.04	-IV	0	7.11	+III	1
2016	-0.17	-0.12	-0.12	1.39	+III	1	0.71	-II	-2	0.99	-IV	0
2017	0.03	-0.42	0.01	-0.07	-I	-3	0.52	+II	2	-0.04	-I	-3
2018	0.02	-0.19	0.03	-0.13	-I	-3	1.21	-III	-1	-0.15	-I	-3
2019	0.02	-0.05	0.07	-0.45	-I	-3	3.28	-III	-1	-1.49	-I	-3
2020	-0.05	0.02	0.08	-2.20	+I	3	-1.60	-I	-3	3.51	+I	3

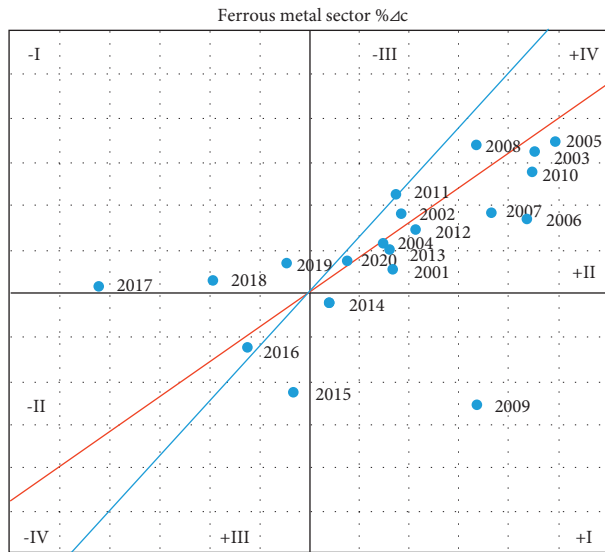


FIGURE 14: Carbon emission decoupling states of energy consumption in the ferrous metal sector from 2001 to 2020.

change rate $\% \Delta E_3$, and the industrial output value change rate $\% \Delta G_3$ and then calculates the carbon emission decoupling index e_3 , the energy structure decoupling index e_{K3} , and the energy efficiency decoupling index e_{T3} using formulas (3), (7), and (9). The decoupling state of carbon emission is judged according to the decoupling model, as shown in Table 2; the decoupling state of energy structure is judged according to the decoupling model, as shown in Table 3; and the decoupling state of energy efficiency is judged according to the decoupling model, as shown in Table 4. All calculation results are shown in Table 10.

According to Figure 14, during 2001–2020, there are 13 decoupling states between carbon emission and output value

growth of the ferrous metal sector, including 3 strong decoupling states, 9 weak decoupling states, and 1 recession decoupling. There are 4 times of negative decoupling, including 3 times of strong negative decoupling and 1 time of expansion negative decoupling. There are three connection states, including expansion connection twice and recession connection once. From the whole research period, most of the carbon emissions are decoupled from the growth of output value, which proves that the energy conservation and emission reduction effect of ferrous metal sector is very effective.

As shown in Figure 15, from the perspective of time evolution characteristics, the change in carbon emission decoupling state of the ferrous metal sector from 2001 to 2020 is stable, which can be basically divided into three stages. The first stage is from 2001 to 2016. The carbon emissions are decoupled. Except for the weak negative decoupled state in 2011, others are basically in the weak decoupled state and connected state. During this period, the output value has maintained a large increase. 2003–2010 is the stage of rapid development of the ferrous metal sector, reaching a growth rate of 49% in 2005, as shown in Table 8. The second stage is 2017–2019. The decoupling state of carbon emission is strong negative decoupling, which shows that the output value decreases, but the carbon emission keeps increasing. The third stage is 2020. The carbon emission is in a strong decoupling state. The strong negative decoupling state in the early stage is immediately reversed to a strong decoupling state, which shows that the output value increases, but the carbon emission decreases.

To further analyze the reasons for the decoupling between energy carbon emission and output value growth in the ferrous metal sector, the relationship between carbon emission decoupling index e_3 and energy efficiency decoupling index e_{T3} and energy structure decoupling index e_{K3} is shown

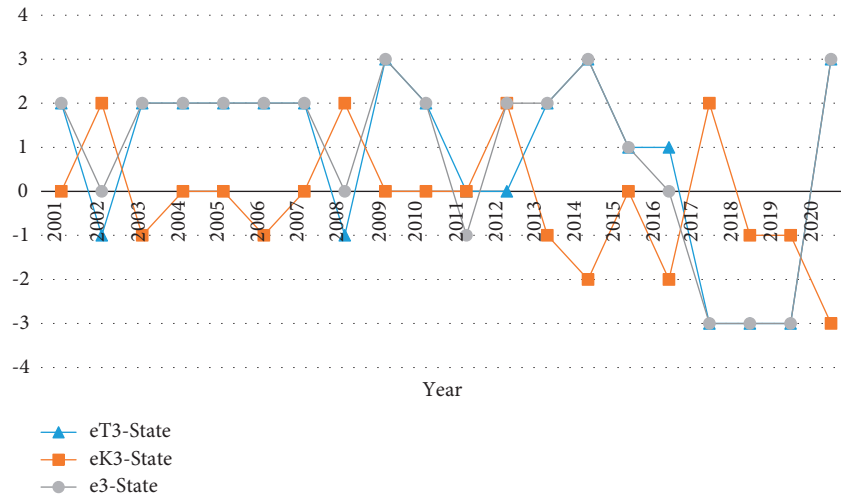


FIGURE 15: Decoupling of energy efficiency, energy structure, and carbon emission of the ferrous metal sector from 2001 to 2020.

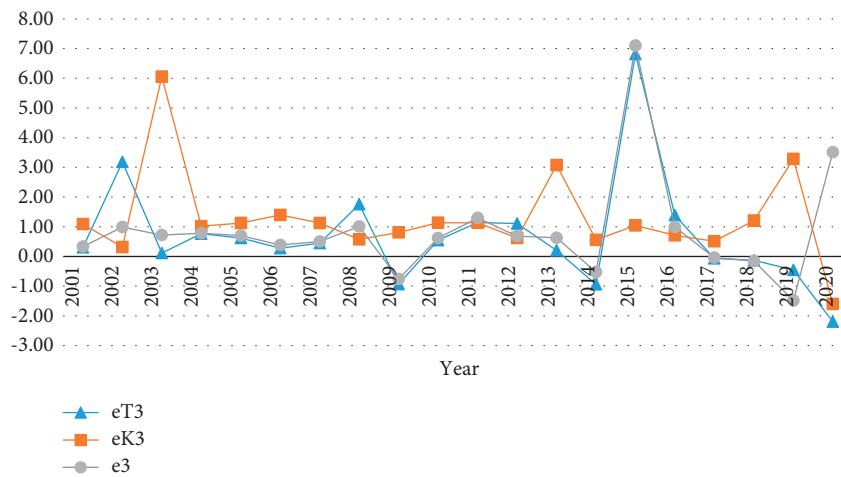


FIGURE 16: Relationship between carbon emission decoupling index and intermediate variables of the ferrous metal sector from 2001 to 2020.

in Figure 16. According to Figures 15 and 16, the fluctuation of carbon emission decoupling index of the ferrous metal sector is basically consistent with that of energy efficiency decoupling index, indicating that the decoupling state of carbon emission is determined by energy efficiency decoupling index. That is to say, the main driving factor of carbon emission of ferrous metal sector is energy efficiency. Energy efficiency is mainly affected by energy-saving measures and improving the level of energy utilization technology. Therefore, these two aspects are very important for carbon emission reduction in the ferrous metal sector. At the same time, the in-depth analysis found that the positive and substantial growth of output value has brought about the decoupling of carbon emissions. For example, the average increase rate of output value from 2003 to 2010 was more than 35%, which corresponds to the weak decoupling of carbon emissions and the weak decoupling of energy efficiency. When there is a negative change rate of output value from 2015 to 2019, the corresponding carbon emission is strongly negative decoupling. The energy structure of the sector

cannot inhibit carbon emissions, as shown in Figure 15. To sum up, the energy efficiency and energy structure of the ferrous metal industry have great potential to curb carbon emissions. At present, the sector is heavily dependent on economic scale, and the fluctuation of output value has a great impact on the efficiency of production factors.

4.4. Decoupling Analysis of Carbon Emission from the Non-ferrous Metal Sector. According to the collected data of the nonferrous metal from 2000 to 2020, this part calculates the carbon emission change rate $\% \Delta C_3$, the carbon emission change rate $\% \Delta C_4$, the energy consumption change rate $\% \Delta E_4$, and the industrial output value change rate $\% \Delta G_4$ and then calculates the carbon emission decoupling index e_4 , the energy structure decoupling index e_{K_4} , and the energy efficiency decoupling index e_{T_4} using formulas (3), (7) and (9). The decoupling state of carbon emission is judged according to the decoupling model, as shown in Table 2; the decoupling state of energy structure is judged according to the

TABLE 11: Decoupling index and decoupling relationship of the nonferrous metal sector from 2001 to 2020.

Year	$\% \Delta E_4$	$\% \Delta G_4$	$\% \Delta C_4$	e_{T4}	e_{T4} state	e_{K4}	e_{K4} state	e_4	e_4 state			
2001	0.08	0.04	0.08	2.05	-III	-1	0.95	+IV	0	1.95	-III	-1
2002	0.19	0.08	0.07	2.39	-III	-1	0.36	+II	2	0.86	+IV	0
2003	0.10	0.13	0.29	0.73	+II	2	2.96	-III	-1	2.16	-III	-1
2004	0.03	0.14	-0.01	0.18	+II	2	-0.34	+I	3	-0.06	+I	3
2005	0.04	0.26	0.06	0.16	+II	2	1.54	-III	-1	0.25	+II	2
2006	0.06	0.24	0.08	0.25	+II	2	1.35	-III	-1	0.33	+II	2
2007	0.12	0.16	0.15	0.77	+II	2	1.20	+IV	0	0.92	+IV	0
2008	0.36	0.15	0.23	2.32	-III	-1	0.64	+II	2	1.49	-III	-1
2009	-0.19	0.19	-0.13	-0.99	+I	3	0.72	-II	-2	-0.71	+I	3
2010	0.13	0.13	0.15	1.01	+IV	0	1.18	+IV	0	1.19	+IV	0
2011	0.23	0.12	0.21	1.93	-III	-1	0.91	+IV	0	1.75	-III	-1
2012	0.11	0.18	0.09	0.64	+II	2	0.79	+II	2	0.51	+II	2
2013	0.02	0.15	0.04	0.14	+II	2	1.86	-III	-1	0.26	+II	2
2014	-0.00	0.05	0.00	-0.01	+I	3	7.37	+III	1	-0.06	+I	3
2015	-0.06	0.07	-0.07	-0.92	+I	3	1.16	+IV	0	-1.06	+I	3
2016	-0.08	-0.03	-0.07	2.38	+III	1	0.93	+IV	0	2.20	+III	1
2017	0.01	-0.27	0.03	-0.03	-I	-3	3.17	-III	-1	-0.11	-I	-3
2018	0.10	-0.30	0.13	-0.35	-I	-3	1.23	-III	-1	-0.43	-I	-3
2019	-0.01	-0.27	+0.00	0.02	-II	-2	-0.50	-I	-3	-0.01	-I	-3
2020	-0.02	-0.08	-0.05	0.29	-II	-2	2.08	+III	-2	0.61	-II	-2

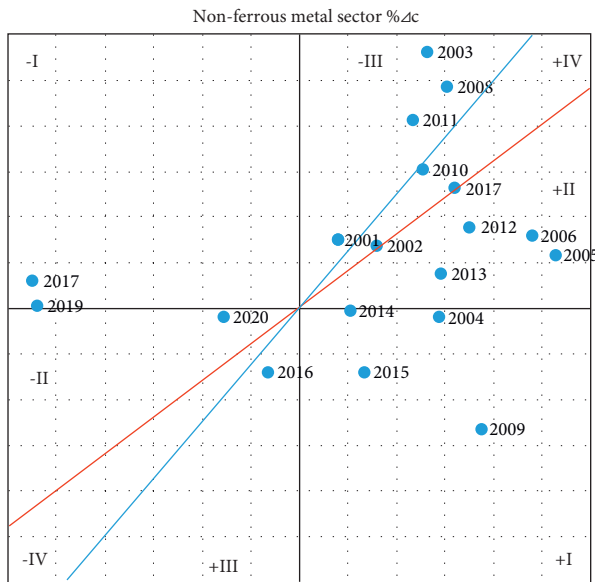


FIGURE 17: Carbon emission decoupling states of energy consumption in the nonferrous metal sector from 2001 to 2020.

decoupling model, as shown in Table 3; and the decoupling state of energy efficiency is judged according to the decoupling model, as shown in Table 4. All calculation results are shown in Table 11.

According to Figure 17, there are 9 times of decoupling between carbon emission and output value growth of the nonferrous metal sector during 2001–2020, including 4 times of strong decoupling, 4 times of weak decoupling, and 1 time of recession decoupling. There are 8 times of negative decoupling, including 3 times of strong negative decoupling, 1 time of weak negative decoupling, and 4 times of expansion negative decoupling. There are 3 times of expansion

connection. From the whole research period, most of the carbon emissions are decoupled from the growth of output value, which proves that the energy conservation and emission reduction in the nonferrous metal sector are effective, but it is not particularly prominent, especially in recent years.

As shown in Figure 18, from the perspective of time evolution characteristics, the change in decoupling state of carbon emission of the nonferrous metal sector from 2001 to 2020 is unstable, which is divided into five stages. The first stage is from 2001 to 2003. The carbon emissions are basically in the state of expansion negative decoupling, and the output value has maintained a small growth, which can be regarded as the adjustment stage. According to the data from 1999 to 2000, it should be the continuation of the previous state. The second stage is from 2004 to 2007. The carbon emissions are basically decoupled. During this period, the output value increased the most. For example, in 2005 and 2006, the output value increased by 26% and 24%, respectively. The third stage is from 2008 to 2011. The decoupling state of carbon emissions is very unstable, but during this period, the output value growth is stable and the carbon emission changes greatly. The fourth stage is from 2012 to 2016. The carbon emissions are basically decoupled, with two strong decouples, which shows that the output value has been increasing, accompanied by a small increase or even decrease in carbon emissions. The nonferrous metal sector has the best emission reduction effect at this stage. The fifth stage is 2017–2020. The carbon emissions are in a strong negative decoupling state, which shows that the output value has decreased significantly, but the carbon emissions have increased.

To further analyze the reasons for the decoupling between energy carbon emission and output value growth in the nonferrous metal sector, the relationship between carbon

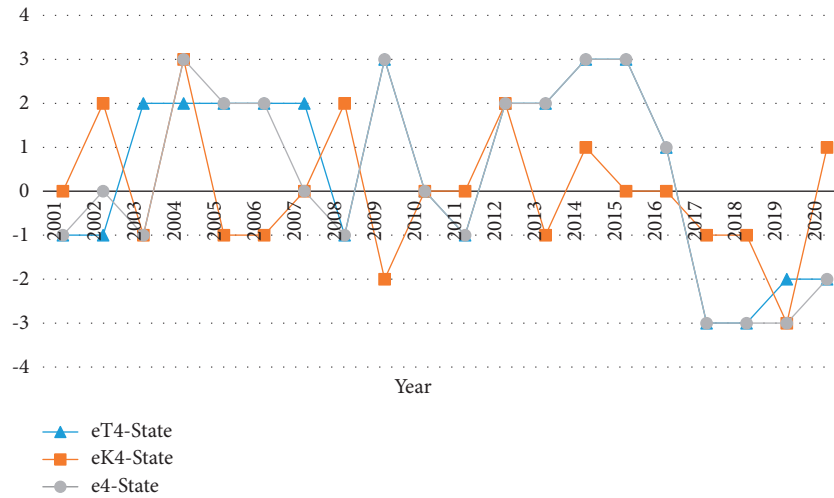


FIGURE 18: Decoupling of energy efficiency, energy structure, and carbon emission of the nonferrous metal sector from 2001 to 2020.

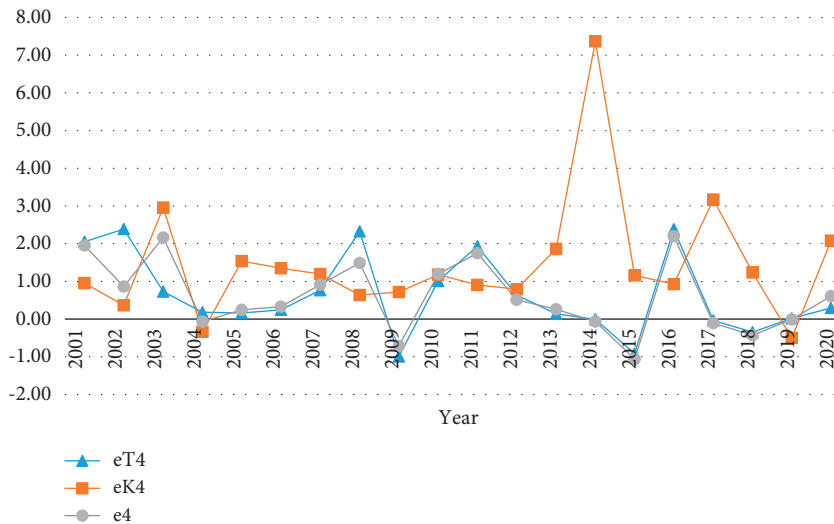


FIGURE 19: Relationship between carbon emission decoupling index and intermediate variables of the nonferrous metal sector from 2001 to 2020.

emission decoupling index e_4 and energy efficiency decoupling index e_{T4} and energy structure decoupling index e_{K4} is shown in Figure 19. According to Figure 19, the carbon emission decoupling index of the nonferrous metal sector before 2008 was jointly affected by energy efficiency and energy structure, and the fluctuation of the carbon emission decoupling index after 2008 was basically consistent with that of the energy efficiency decoupling index, indicating that the carbon emission decoupling state was determined by the energy efficiency decoupling index in this period. That is to say, the main driving factor of carbon emission reduction in the nonferrous metal sector is the energy consumption per unit output value. Therefore, energy-saving measures and improving the level of energy-saving technology are very important for carbon emission reduction in nonferrous metal sector. At the same time, it is also found that the substantial growth of output value has brought about the decoupling state of carbon emissions. Once the output value

decreases, it would lead to the negative decoupling state of carbon emissions. It can be seen that the industrial economic scale has a great impact on the efficiency of industrial production factors. Before 2016, the energy consumption per unit output value of the nonferrous metal sector as a whole showed a downward trend. From the decline of energy efficiency after 2017, it can be seen that the potential of energy efficiency to inhibit carbon emissions in the future is limited, as shown in Figure 18. The energy structure does not play a great role in carbon emission of nonferrous metals, but it has great potential to curb carbon emission through the use of new energy.

4.5. Decoupling Analysis of Carbon Emission from the Non-metallic Sector. According to the collected data of the nonmetallic sector from 2000 to 2020, this part calculates the carbon emission change rate $\% \Delta C_5$, the energy consumption

TABLE 12: Decoupling index and decoupling relationship of the nonmetallic sector from 2001 to 2020.

Year	$\% \Delta E_5$	$\% \Delta G_5$	$\% \Delta C_5$	e_{T5}	e_{T5} state	e_{K5}	e_{K5} state	e_5	e_5 state			
2001	0.09	0.06	0.09	1.43	-III	-1	1.03	+IV	0	1.48	-III	-1
2002	0.16	0.12	0.07	1.30	-III	-1	0.43	+II	2	0.55	+II	2
2003	0.12	0.03	0.17	3.87	-III	-1	1.43	-III	-1	5.55	-III	-1
2004	-0.11	0.22	-0.10	-0.49	+I	3	0.92	-IV	0	-0.46	+I	3
2005	0.08	0.13	0.04	0.62	+II	2	0.55	+II	2	0.34	+II	2
2006	0.02	0.32	0.04	0.06	+II	2	1.93	-III	-1	0.11	+II	2
2007	0.04	0.27	0.06	0.16	+II	2	1.38	-III	-1	0.22	+II	2
2008	0.49	0.27	0.38	1.84	-III	-1	0.78	+II	2	1.44	-III	-1
2009	-0.18	0.26	-0.14	-0.71	+I	3	0.79	-II	-2	-0.56	+I	3
2010	-0.03	0.26	0.00	-0.10	+I	3	-0.19	-I	-3	0.02	+II	2
2011	0.01	0.14	0.06	0.09	+II	2	4.56	-III	-1	0.40	-III	-1
2012	0.33	0.09	0.31	3.75	-III	-1	0.93	+IV	0	3.48	-III	-1
2013	-0.10	0.16	-0.10	-0.61	+I	3	1.02	-IV	0	-0.63	+I	3
2014	0.03	0.08	0.03	0.38	+II	2	0.82	+IV	0	0.31	+II	2
2015	-0.05	0.05	-0.06	-1.03	+I	3	1.12	-IV	0	-1.15	+I	3
2016	-0.05	0.01	-0.04	-3.68	+I	3	0.73	-II	-2	-2.67	+I	3
2017	-0.10	-0.26	-0.07	0.39	-II	-2	0.73	-II	-2	0.28	-II	-2
2018	0.14	-0.25	0.12	-0.55	-I	-3	0.87	+IV	0	-0.48	-I	-3
2019	-0.00	-0.01	+0.00	0.58	-II	-2	-0.02	-I	-3	-0.01	-I	-3
2020	-0.02	-0.03	0.01	0.78	-II	-2	-0.59	-I	-3	-0.45	-I	-3

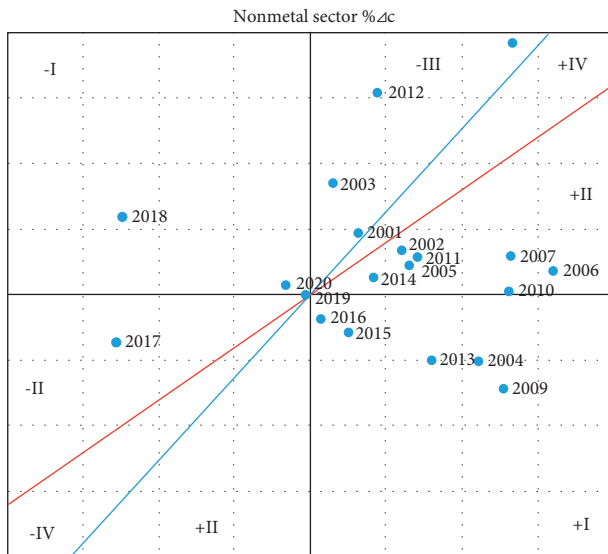


FIGURE 20: Carbon emission decoupling states of energy consumption in the nonmetallic sector from 2001 to 2020.

change rate $\% \Delta E_5$, and the industrial output value change rate $\% \Delta G_5$ and then calculates the carbon emission decoupling index e_5 , the energy structure decoupling index e_{K5} , and the energy efficiency decoupling index e_{T5} of the nonmetallic mining industry using formulas (3), (7), and (9). The decoupling state of carbon emission is judged according to the decoupling model, as shown in Table 2; the decoupling state of energy structure is judged according to the decoupling model, as shown in Table 3; and the decoupling state of energy efficiency is judged according to the decoupling model, as shown in Table 4. All calculation results are shown in Table 12.

According to Figure 20, during 2001–2020, there are 11 times of decoupling between carbon emission and output

value growth of nonmetallic sector, including 5 times of strong decoupling and 6 times of weak decoupling. There are 9 times of negative decoupling, including 3 times of strong negative decoupling, 1 time of weak negative decoupling, and 5 times of expansion negative decoupling. From the whole research period, most of the carbon emissions are decoupled from the output value growth, but there are not many advantages, which proves that the effect of energy conservation and emission reduction in the nonmetallic sector is very limited, especially the negative decoupling in recent four years.

As shown in Figure 21, from the perspective of time evolution characteristics, the annual carbon emission decoupling state of nonmetallic sector from 2001 to 2020 can be divided into three stages. The first stage is from 2001 to 2003. The carbon emissions are basically in the state of expansion negative decoupling, and the output value has maintained growth. During this period, there is a weak decoupling state. With the significant growth of output value, it can be regarded as the adjustment stage. The second stage is from 2004 to 2016. The carbon emissions are basically decoupled. In 2008 and 2011–2012, there is an expansion negative decoupling. During this period, the output value has been increasing significantly, accompanied by a small increase in carbon emissions, or even negative growth. The third stage is 2017–2020. Carbon emissions are in a strong negative decoupling state, which shows that the output value has decreased significantly, but the carbon emissions have increased.

To further analyze the reasons for the decoupling between energy carbon emission and output value growth in the nonmetallic sector, the relationship between carbon emission decoupling index e_5 and energy efficiency decoupling index e_{T5} and energy structure decoupling index e_{K5} is shown in Figure 22. According to Figure 22, the change

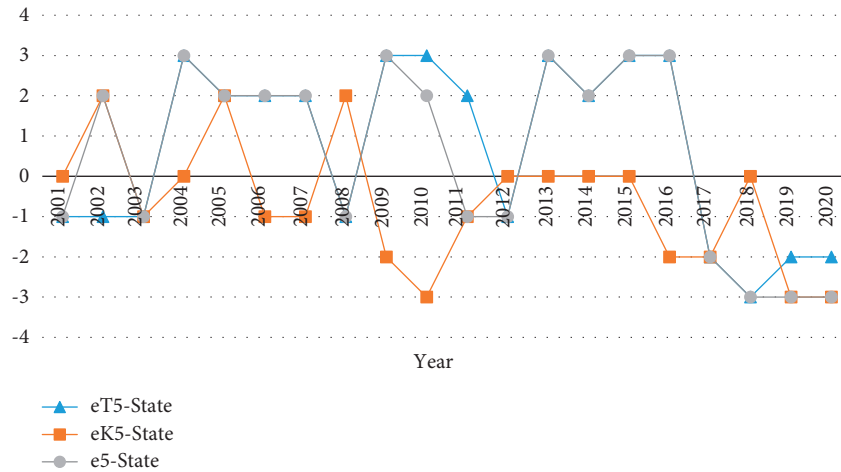


FIGURE 21: Decoupling of energy efficiency, energy structure, and carbon emission of the nonmetallic sector from 2001 to 2020.

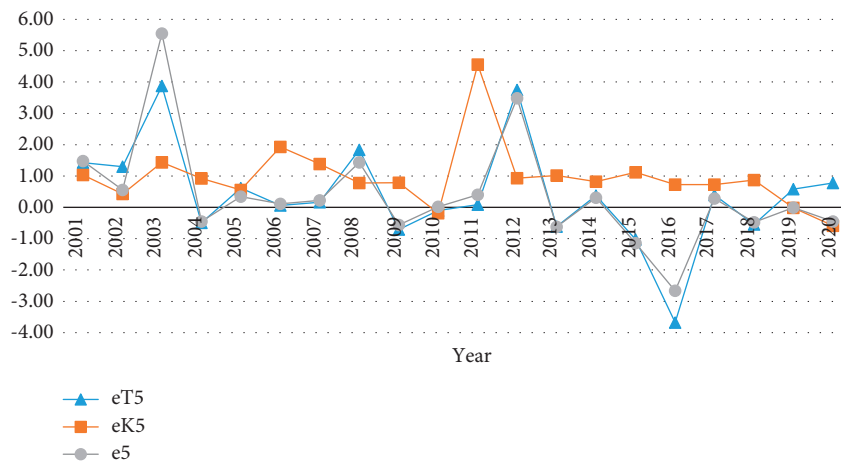


FIGURE 22: Relationship between carbon emission decoupling index and intermediate variables of the nonmetallic sector from 2001 to 2020.

trend of carbon emission decoupling index of the nonmetallic sector is basically consistent with that of energy efficiency index, except that it is affected by energy structure in individual time periods. From 2003 to 2009, the fluctuation of carbon emission decoupling index and energy efficiency decoupling index is consistent, which shows that the decoupling state of carbon emission is determined by the energy efficiency decoupling index; that is to say, the main driving factor of carbon emission reduction in the nonmetallic industry is to reduce energy consumption. In 2010–2012 and 2018–2020, the decoupling index of energy structure has a great impact on carbon emission decoupling, and energy efficiency has a greater impact on carbon decoupling index in 2013–2017. Therefore, in 2003–2009 and 2013–2017, the carbon emission reduction in the nonmetallic sector is mainly affected by energy-saving measures and energy-saving technologies. In other times, the optimization of energy structure plays a decisive role in the carbon emission reduction of the nonmetallic sector. According to the development of the nonmetallic sector, it is also found that the significant growth of output value has brought about the decoupling state of carbon emissions.

Once the output value decreases, it will lead to the negative decoupling state of carbon emissions. It can be seen that the relative carbon emission reduction effect of the whole industry is not ideal. Once the output value decreases, the energy consumption per unit output value will increase. Before 2016, the overall energy intensity of the nonmetallic sector showed a downward trend. After 2017, the energy efficiency decreased significantly. It can be seen that the potential of energy efficiency to inhibit carbon emissions is limited, as shown in Figure 21. The energy structure has not been able to well curb carbon emissions, which shows that the adjustment of energy structure is not ideal, but it may have great potential to curb carbon emissions in the future through the use of new energy.

4.6. *Decoupling Analysis of Carbon Emission in Mining Industry.* According to the collected data of the mining industry from 2000 to 2020, this part calculates the carbon emission change rate $\% \Delta C$, the energy consumption change rate $\% \Delta E$, and the industrial output value change rate $\% \Delta G$ and then calculates the carbon emission decoupling index e , the

TABLE 13: Decoupling index and decoupling relationship of mining industry from 2001 to 2020.

Year	% ΔE	% ΔG	% ΔC	e_T	e_T state	e_K	e_K state	e	e state			
2001	0.07	0.01	0.03	13.06	-III	-1	0.49	+II	2	6.40	-III	-1
2002	0.09	0.09	0.08	0.95	+IV	0	0.87	+IV	0	0.83	+IV	0
2003	0.12	0.14	0.11	0.84	+IV	0	0.93	+IV	0	0.78	+II	2
2004	0.03	0.17	0.08	0.19	+II	2	2.52	-III	-1	0.48	+II	2
2005	0.03	0.19	0.09	0.15	+II	2	3.21	-III	-1	0.49	+II	2
2006	+0.00	0.16	0.07	0.03	+II	2	16.28	-III	-1	0.47	+II	2
2007	0.08	0.18	0.12	0.42	+II	2	1.58	-III	-1	0.67	+II	2
2008	0.05	0.18	0.11	0.26	+II	2	2.41	-III	-1	0.62	+II	2
2009	0.17	0.14	0.14	1.15	+IV	0	0.85	+IV	0	0.97	+IV	0
2010	0.02	0.18	0.10	0.10	+II	2	5.83	-III	-1	0.59	+II	2
2011	0.03	0.13	0.09	0.23	+II	2	2.94	-III	-1	0.67	+II	2
2012	0.06	0.09	0.08	0.68	+II	2	1.23	-III	-1	0.84	+IV	0
2013	+0.00	0.10	0.06	0.01	+II	2	87.96	-III	-1	0.63	+II	2
2014	-0.22	0.04	-0.04	-5.44	+I	3	0.18	-II	-2	-1.00	+I	3
2015	0.02	-0.02	0.00	-1.57	-I	-3	-0.20	+I	3	0.31	+II	2
2016	-0.13	-0.05	-0.06	2.79	+III	1	0.50	-II	-2	1.40	+III	1
2017	0.06	-0.20	-0.13	-0.30	-I	-3	-2.13	-I	-3	0.64	-II	-3
2018	-0.02	-0.12	-0.08	0.18	-II	-2	3.81	+III	1	0.70	-II	-2
2019	0.03	-0.08	-0.04	-0.33	-I	-3	-1.57	+I	3	0.52	-II	-2
2020	-0.02	0.02	0.12	-1.21	+I	3	-4.74	-I	-3	5.74	-III	-1

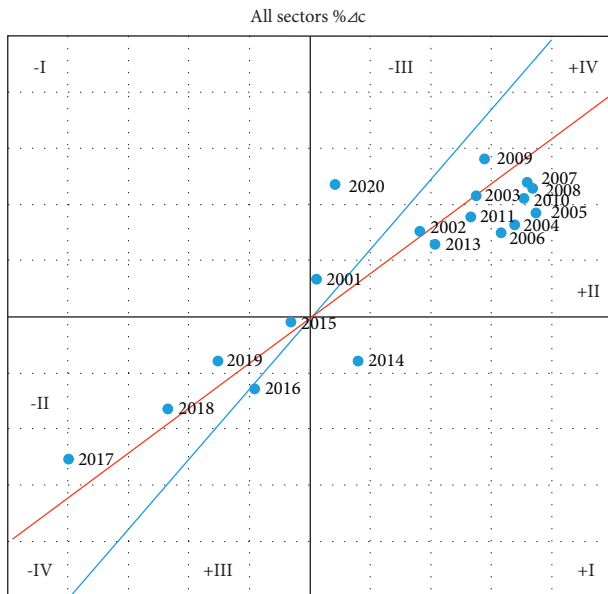


FIGURE 23: Carbon emission decoupling states of energy consumption in mining industry from 2001 to 2020.

energy structure decoupling index e_K and the energy efficiency decoupling index e_T using formulas (3), (7), and (9). The decoupling state of carbon emission is judged according to the decoupling model, as shown in Table 2; the decoupling state of energy structure is judged according to the decoupling model, as shown in Table 3; and the decoupling state of energy efficiency is judged according to the decoupling model, as shown in Table 4. All calculation results are shown in Table 13.

According to Figure 23, there are 12 decoupling states between carbon emission and output value growth of mining industry during 2001–2020, including 1 strong decoupling

state, 10 weak decoupling states, and 1 recession decoupling state. There are 5 times of negative decoupling, including 3 times of weak negative decoupling and 2 times of expansion negative decoupling. Expansion connection occurred 3 times. From the whole research period, most of the carbon emissions are decoupled from the output value growth, which proves that the carbon emission reduction in the mining industry is very effective, but there has been a continuous negative decoupling in recent years.

As shown in Figure 24, from the perspective of time evolution characteristics, the decoupling state of carbon emission of mining industry from 2001 to 2020 is relatively stable, which can be basically divided into two stages. The first stage is from 2001 to 2016, and carbon emissions are basically decoupled or linked, except for weak negative decoupling in 2001. The output value has been increasing significantly during this period, accompanied by a small increase in carbon emissions. 2002–2012 is the golden decade of China’s mining industry. Because of the strong market demand, the scale and output value of the industry have increased significantly. At the same time, under the guidance of energy conservation and emission reduction policies, the industry pays attention to reducing energy consumption, which has formed a decoupling state of carbon emissions for more than a decade. The second stage is from 2017 to 2020. The decoupling state of carbon emissions is basically negative decoupling. During this period, the output value has been negative growth, especially the output value decreased by 20% in 2017, but the decline of carbon emissions is small, resulting in negative decoupling. At the same time, China proposed the policy of supply-side reform, the market demand decreased, and the mining industry carried out the elimination reform of backward production capacity. The period is also a few difficult years for the development of the mining industry. After 2019, the market demand gradually recovered.

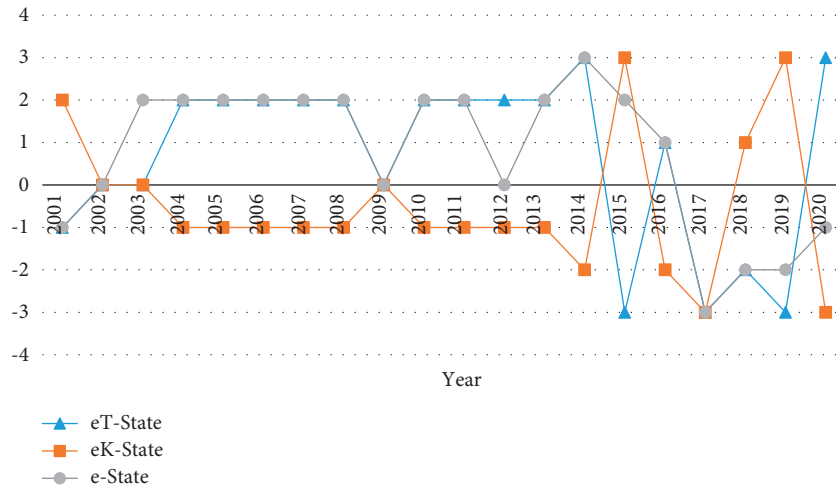


FIGURE 24: Decoupling of energy efficiency, energy structure, and carbon emission of mining industry from 2001 to 2020.

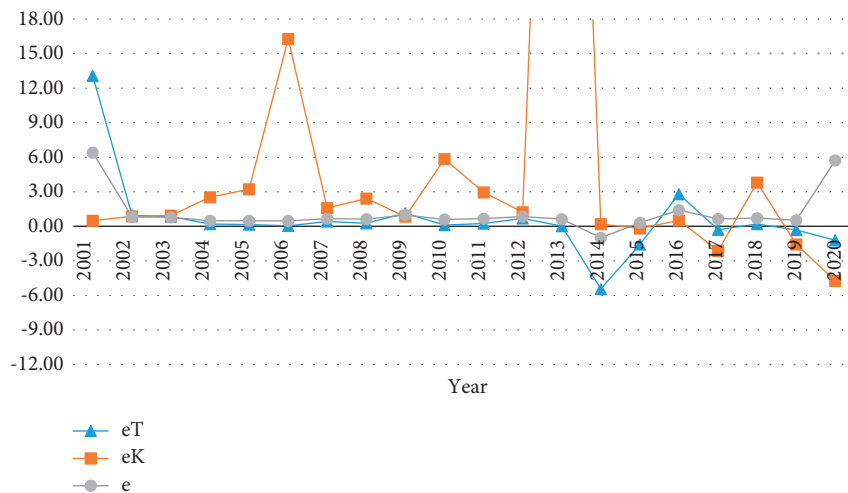


FIGURE 25: Relationship between carbon emission decoupling index of the mining industry and intermediate variables. *Note.* In Figure 25, the value of e_K in 2013 is 87.96, because it is too large than other values, so it is not shown in the figure.

To further analyze the reasons for the decoupling between energy carbon emission and output value growth in the mining industry, the relationship between carbon emission decoupling index e and energy efficiency decoupling index e_T and energy structure decoupling index e_K is shown in Figure 25. According to Figures 24 and 25, the fluctuation of carbon emission decoupling index of mining industry is basically consistent with that of energy efficiency decoupling index from 2001 to 2014, indicating that the decoupling state of carbon emission is mainly determined by energy efficiency decoupling index; that is to say, the main driving factor of carbon emission reduction in mining industry is energy efficiency. Therefore, energy-saving measures and energy utilization technology are very important for carbon emission reduction in mining industry. At the same time, in-depth analysis found that the positive and substantial growth of output value will lead to the decoupling state of carbon emissions. For example, the output value has maintained growth from 2002 to 2014, corresponding to the weak decoupling state of carbon emissions. On the contrary,

the output value decreased sharply from 2017 to 2019, corresponding to the negative decoupling state of carbon emissions. Through the above analysis, this study believes that the adjustable range of production capacity of the mining industry is very limited, the supply is inelastic, and the industry is still in the stage of economies of scale. Economic scale can improve the efficiency of production factors, including energy efficiency. Therefore, the increase in industrial output value corresponds to the improvement of energy efficiency. When the output value of mining industry decreases, the corresponding energy consumption and operating costs cannot be reduced accordingly. Since 2015, the energy structure index has a great impact on the carbon emission decoupling index and inhibits carbon emission, as shown in Figure 25. In general, the energy efficiency of mining industry is the main driving factor of carbon emission reduction, while the energy structure has a little inhibitory effect on carbon emission.

The energy efficiency of the mining industry basically showed an upward trend and was relatively stable before

2014. During this period, the improvement of energy efficiency is the main driving force of the industry's emission reduction, as shown in Figure 25. After 2015, the energy efficiency is mainly in the state of negative decoupling and fluctuates greatly. It can be seen that the resistance to the improvement of energy efficiency after 2015 is very large and cannot maintain high-energy efficiency, which also shows that the space for the continuous improvement of the energy efficiency is very limited. Therefore, the inhibitory effect of energy efficiency on carbon emissions from mining industry will be very limited in the future.

From 2001 to 2014, the energy structure of the mining industry was basically in a state of negative decoupling, which failed to inhibit carbon emissions, as shown in Figure 25. From 2015 to 2020, the decoupling state of energy structure was unstable and showed W-shaped fluctuation, but the inhibition effect of energy structure on carbon emission increased. Therefore, increasing the proportion of new energy consumption in the future will greatly curb carbon emissions, and the inhibitory effect of energy structure adjustment on carbon emissions in the future has great room for improvement.

As shown in Figure 25, the carbon emissions of the mining industry from 2002 to 2016 were decoupled and very stable. The emission reduction effect during the period is relatively prominent. It can be seen that the emission reduction measures of the whole industry are reasonable. Carbon emissions from 2017 to 2020 are in a negative decoupling state, which shows that the industrial emission reduction measures during this period are unreasonable. From 2017 to 2020, the output value decreased significantly, resulting in negative decoupling of carbon emissions. It can be seen that the whole mining industry is highly dependent on economic scale.

5. Conclusions

Through the above research, the following conclusions are drawn:

- (1) From 2002 to 2016, the carbon emission of the mining industry was basically decoupled and very stable. During the whole period, energy efficiency was the main driving factor of carbon emission reduction and had a great impact on carbon emission decoupling. During this period, the impact of energy structure on carbon emission decoupling is very small, and it cannot inhibit carbon emission. From 2017 to 2020, the carbon emission of the mining industry is basically in the state of negative decoupling. During this period, the energy structure has become the main factor to curb carbon emission.
- (2) The energy efficiency of the mining industry basically showed an upward trend from 2004 to 2014 and was relatively stable. After 2015, the energy efficiency was mainly in the state of negative decoupling and fluctuated greatly. This study believes that there is great resistance to the improvement of energy efficiency, which also shows that the space for the continuous improvement of energy efficiency is very limited, and

its inhibition effect on carbon emission in the future will also be very limited. From 2003 to 2014, the energy structure of mining industry was basically in the state of negative decoupling, which could not inhibit carbon emission and had little impact; from 2015 to 2020, the decoupling state of energy structure is unstable, but it has an inhibitory effect on carbon emissions and the impact is increasing. Therefore, this study believes that by increasing the proportion of new energy consumption, the inhibition effect of energy structure adjustment on carbon emissions will have great room for improvement in the future.

- (3) Among all subsectors, the decoupling state of carbon emissions in the coal sector is the best ideal. The energy conservation and emission reduction effect of the coal sector is the most stable, the ferrous metal mining industry is the second, and the nonferrous metal sector is the most unstable. The effect of energy conservation and emission reduction in the petroleum and natural gas sector is the least ideal. The energy efficiency is the main driving factor of emission reduction in coal sector. The decoupling of carbon emissions in other industries is mainly affected by the energy efficiency index, but in some periods, the energy structure has a great impact on the decoupling of carbon emissions.
- (4) The decoupling state of carbon emissions in the whole mining industry is closely related to the growth of output value. When the output value increases significantly, the energy efficiency is in a strong decoupling state, and the energy efficiency decreases when the output value decreases. It can be seen that economic scale and capacity concentration have a great impact on the energy efficiency of the mining industry.

Data Availability

The datasets used or analyzed during this study are available from the corresponding author on reasonable request. The original data in this study are obtained from China Energy Statistical Yearbook (2000–2020) and China Statistical Yearbook (2000–2021). For a detailed introduction, refer to “2.3 data source and data processing” and Reference [24, 25] in the paper.

Conflicts of Interest

The authors declare no conflicts of interest.

Authors' Contributions

Guangyu Jia and Lili Wei conceptualized the study and wrote, reviewed, and edited the manuscript; Lili Wei designed methodology, validated the study, and wrote the original draft preparation; Xiaohui Xu provided software; Lingyun Zhao provided resources; Lili Wei and Xiaohui Xu curated the data; and Guangyu Jia supervised the study.

Acknowledgments

This study was supported by the Shandong Social Science Planning and Research Project (Grant no. 17CJJJ09).

References

- [1] World Bank, *Mineral products for climate action: mineral consumption intensity of clean energy transformation*, World Bank, Washington, D.C., USA, 2020.
- [2] Ministry of Natural Resources, *China mineral resources report*, pp. 15–20, Geological Publishing House, Beijing, China, 2020.
- [3] First Finance and Economics, “The path, opportunities and challenges of China’s “carbon neutrality” goal in 2060,” 2020, <https://www.yicai.com/news/100843313.html>.
- [4] H. Y. Qiang and B. Gao, “Options for sustainable development of mining industry under the background of carbon neutrality,” *Natural Resources Economics of China*, vol. 34, no. 4, pp. 4–11, 2021.
- [5] OECD, *Indicators to Measure Decoupling of Environmental Pressure from Economic Growth*, OECD, Paris, France, 2002.
- [6] R. Juknys, “Transition period in Lithuania: do we move to sustainability?” *Environmental Research, Engineering and Management*, vol. 4, no. 26, pp. 4–9, 2003.
- [7] P. Tapio, “Towards a theory of decoupling: degrees of decoupling in the EU and the case of road traffic in Finland between 1970 and 2001,” *Transport Policy*, vol. 12, no. 2, pp. 137–151, 2005.
- [8] D. Gray, Anablej, L. Iiingworht, and W. Graham, *Decoupling the Link between Economic Growth, Transport Growth and Carbon Emissions in Scotland*, The Centre for Transport Policy, Robert Gordon University, Aberdeen, England, 2006.
- [9] D. Diakoulaki and M. Mandaraka, “Decomposition analysis for assessing the progress in decoupling industrial growth from CO₂ emissions in the EU manufacturing sector,” *Energy Economics*, vol. 29, no. 4, pp. 636–664, 2007.
- [10] L. C. D. Freitas and S. Kaneko, “Decomposing the decoupling of CO₂ emissions and economic growth in Brazil,” *Ecological Economics*, vol. 70, no. 8, pp. 1459–1469, 2011.
- [11] Z. Csereklyei and D. I. Stern, “Global energy use: decoupling or convergence?” *Energy Economics*, vol. 51, pp. 633–641, 2015.
- [12] M. Conte Grand, “Carbon emission targets and decoupling indicators,” *Ecological Indicators*, vol. 67, pp. 649–656, 2016.
- [13] Y. P. Zhao, Q. H. Sun, and N. Duan, “Responsive relationship between economic development and energy consumption in China: a practical research based on comparative de-link and re-link theory,” *Science Research Management*, vol. 27, no. 3, pp. 128–134, 2006.
- [14] C. M. Wang, “Decoupling analysis of China economic growth and energy consumption,” *China Population, Resources and Environment*, vol. 20, no. 3, pp. 35–37, 2010.
- [15] J. W. Peng, X. J. Huang, T. Y. Zhong, and Y. T. Zhao, “Decoupling analysis of economic growth and energy carbon emissions in China,” *Resources Science*, vol. 33, no. 4, pp. 626–633, 2011.
- [16] W. Wang, M. Li, and M. Zhang, “Study on the changes of the decoupling indicator between energy-related CO₂ emission and GDP in China,” *Energy*, vol. 128, pp. 11–18, 2017.
- [17] L. Yue and F. Li, “Empirical analysis of the Tapio decoupling of western provincial economic growth and carbon dioxide with Gansu Province as a case,” *Journal of Beijing Institute of Technology (Social Sciences Edition)*, vol. 13, no. 2, pp. 19–22, 2011.
- [18] S. Ren, H. Yin, and X. Chen, “Using LMDI to analyze the decoupling of carbon dioxide emissions by China’s manufacturing industry,” *Environmental Development*, vol. 9, pp. 61–75, 2014.
- [19] Q. Lu, H. Yang, X. Huang, X. Chuai, and C. Wu, “Multi-sectoral decomposition in decoupling industrial growth from carbon emissions in the developed Jiangsu Province, China,” *Energy*, vol. 82, pp. 414–425, 2015.
- [20] Z. Wang and L. Yang, “Delinking indicators on regional industry development and carbon emissions: Beijing-Tianjin-Hebei economic band case,” *Ecological Indicators*, vol. 48, pp. 41–48, 2015.
- [21] X. Zhou, M. Zhang, M. Zhou, and M. Zhou, “A comparative study on decoupling relationship and influence factors between China’s regional economic development and industrial energy-related carbon emissions,” *Journal of Cleaner Production*, vol. 142, pp. 783–800, 2017.
- [22] B. M. Chen and H. L. Du, “On the decoupling between cultivated land occupation and GDP growth,” *Resource Science*, vol. 28, no. 5, pp. 36–42, 2006.
- [23] J. Vehmas, J. Kaivo-oja, and J. Luukkanen, *Global Trends of Linking Environmental Stress and Economic Growth*, Turku School of Economics and Business Administration, Finland, 2003.
- [24] NBSC, *China Statistical Yearbook (2000-2021)*, China Statistics Press, Beijing, China, 2000-2021.
- [25] NBSC, *China Energy Statistical Yearbook (2000-2020)*, China Statistics Press, Beijing, China, 2000-2020.
- [26] L. L. Wei, X. W. Feng, and G. Y. Jia, “Construction and application analysis of carbon emission influence factor model of energy consumption in mining industry,” *Advances in Civil Engineering*, vol. 2021, pp. 1–12, 2021.
- [27] NDRC, *National climate change plan(2014-2020)*, NDRC, Beijing, China, 2014, <https://www.scio.gov.cn>.

Research Article

Preparation, Encapsulation, and Performance Evaluation of Ternary Phase Change Materials for Building Envelope

Hongzhi Zhu, Bin Guo , and Zhi Li

College of Hydraulic and Civil Engineering, Shandong Agricultural University, Tai'an 271018, Shandong, China

Correspondence should be addressed to Bin Guo; guobin@sdau.edu.cn

Received 27 November 2021; Revised 16 March 2022; Accepted 18 March 2022; Published 1 April 2022

Academic Editor: Guoming Liu

Copyright © 2022 Hongzhi Zhu et al. This is an open access article distributed under the Creative Commons Attribution License, which permits unrestricted use, distribution, and reproduction in any medium, provided the original work is properly cited.

Background. In order to make up for the defect that a single phase change material cannot meet the phase change temperature in a specific application field, three kinds of materials with higher phase change temperature are selected in this paper. Through the phase change material composite method, it was adopted to carry out step cooling curve test and differential scanning calorimetry (DSC) test, based on the second law of thermodynamics and the theory of phase equilibrium. DSC thermal analysis and Fourier transform infrared spectroscopy (FT-IR) characterization were carried out. The phase change diatomite was used for packaging materials and durability evaluation. The results show that when TD-MA : LA = 6.2 : 3.8, the phase transition temperature of the experimental ternary composite phase change material is 20.1°C. The adsorption of diatomite to phase change material (PCM) is only physical adsorption, and the thermal stability is good after 100 phase change cycles. The maximum mass loss rate of phase change diatomite encapsulated by phenylpropene emulsion and cement powder is only 0.65%, at last, this phase change diatomite is suitable for building envelope structure.

1. Introduction

Phase change heat storage technology is a method for energy storage by using the characteristics of phase change materials (PCMs) that can absorb or release a large amount of phase change latent heat during phase change [1]. Phase change materials are used in building envelopes to strengthen the heat preservation, heat storage, and heat insulation capabilities of the envelope structure, thus can reduce heating and air conditioning energy consumption, reduce electrical load, and ultimately achieve energy saving goals [2–7].

A single phase change material is sometimes difficult to meet the requirements of a certain field for the phase change temperature and phase change materials. Therefore, many scholars prepare composite phase change materials with the required phase change temperature by mixing two or more phase change materials [8–12]. However, there are few studies on the preparation of ternary composite phase change materials to improve the utilization rate of phase change materials. The phase change material usually needs to

be shaped and packaged before it is put into use, so as to make up for its shortcomings of low thermal conductivity such as large volume change during phase change and easy leakage. Commonly used encapsulation methods include methods of porous carriers composite, macro encapsulation, sol-gel encapsulation, microcapsule encapsulation, etc. [13–16]. C. Hasse et al. prepared phase change paraffin microcapsules and encapsulated them in the honey comb panel [17]. The experiment found no phase change material leakage in the panel. Ramakrishnan S prepared a composite phase change material with paraffin wax and expanded perlite as raw materials in which mass ratio of paraffin can reach 50% [18, 19] the experimental results show that the composite PCM has good chemical compatibility and thermal stability. Although these methods have many advantages, secondary encapsulation is still needed to improve the stability of phase change materials in the phase change cycle.

This paper aims to prepare and select ternary composite phase change materials suitable for building envelopes by using phase change materials TD, MA, LA as raw materials,

using the method of heating and melting and processing cooling curve and DSC test. Using diatomaceous Earth as a matrix to shape the phase change material and encapsulate it with a packaging material, illustrating the FT-IR characterization of the phase change material and the shaped phase change material.

2. Experiment

2.1. Experimental Materials and Instruments. Tetradecanol (TD), called myristyl alcohol, is a colorless to white waxy solid. Myristic acid (MA), a white crystalline waxy solid. Lauric acid (LA), called dodecanoic acid, a white flake or bead-like solid. The particle size of Expanded perlite (EP) is between 2 mm to 3 mm, appearing white particles, honeycomb pore structure. The particle size of diatomite (DE) is between 5 mm and 15 mm, appearing white or light yellow particles. Styrene acrylic emulsion is a thick milky liquid. Cement powder (wet with water). Magnetic heating stirrer, electronic balance, temperature acquisition instrument, temperature sensor, differential scanning calorimeter (DSC), Fourier transform infrared spectrometer (FT-IR), vacuum drying oven, refrigerated refrigerator.

2.2. Experimental Procedures and Methods

2.2.1. Theoretical Prediction of Thermophysical Properties of Ternary Composite Phase Change Materials. According to the second law of thermodynamics and phase equilibrium theory, the melting point and heat of solution formula of the eutectic phase change material can be obtained, so as to theoretically predict the eutectic temperature of the eutectic system and the proportion of corresponding components. The eutectic temperature formula and the heat of solution formula of the binary composite phase change material are as follows.

$$T_m = \frac{1}{1/T_A - R \ln X_A/H_A} \quad (1)$$

$$= \frac{1}{1/T_B - R \ln X_B/H_B},$$

$$H_m = T_m \left[\frac{X_A H_A}{T_A} + \frac{X_B H_B}{T_B} \right], \quad (2)$$

$$X_A + X_B = 1. \quad (3)$$

Among them, T_m is the melting temperature of the eutectic phase change material, K. H_m is the heat of fusion of the eutectic phase change material, J/mol, T_A , T_B , are the melting temperatures of the A and B components respectively, K. H_A , H_B , are the latent heat of phase change of A and B components, J/mol. X_A , X_B are the mole percentages of A and B components in the mixture, respectively.

In the calculation, the thermal properties of TD and MA are first brought into the above formulas (1)–(3), contributing to the eutectic point temperature of the TD-MA binary

eutectic is 304 K and the heat of solution is 198 J. Converting the calculated mole percentage to mass percentage is TD: MA = 67.4:32.6, and the TD-MA binary eutectic is combined with LA as a single component. When the mass ratio TD-MA:LA = 62.5:37.5, the eutectic point temperature of the TD-MA-LA eutectic is 295.2 K, which meets the temperature requirements of the building envelope for phase change materials.

2.2.2. Step Cooling Curve Test of Composite Phase Change Materials. In this experiment, the TD-MA binary composite phase change material is set to 9 different mass ratios (8:2, 7:3, 6:4, 4:6, 2:8), (6.8:3.2, 6.7:3.3, 6.6:3.4, 6.5:3.5) Perform step cooling curve test. Compound the obtained TD-MA binary eutectic compound with LA, and set TD-MA:LA to 6 different mass ratios (8:2, 6.3:3.7, 6.2:3.8, 6.1:3.9, 6:4, 4:6, 2:8) Continue the experiment, after that, DSC test was combined for analysis and comparison.

2.2.3. DSC Test of Composite Phase Change Material. The phase change temperature and latent heat of the composite phase change materials with different proportions were obtained by DSC test using differential scanning calorimetry.

2.2.4. Performance Characterization of Shaped Composite Phase Change Materials. The amorphous phase change materials were prepared by using diatomite as the matrix adsorption phase change material. The amorphous phase change materials before and after the phase change cycle were tested by differential scanning calorimetry. The chemical composition and structure of the fixed phase change materials before and after phase change cycle were analyzed by Fourier transform infrared absorption spectrometer.

2.2.5. Shaped Composite Phase Change Material Packaging and Durability Test. Weighing 4 parts of 20 g phase change diatomaceous Earth shaped composite phase change material, one of which is not packaged, and the other three are packaged in different packaging methods, and the thermal cycle test is performed on them, and the different packaging is evaluated by the mass loss rate cold and hot cycle durability under the material.

3. Results and Analysis

3.1. Step Cold Curve Test and Analysis. Using the SRND-CM-4PT distributed modular automatic measuring unit to perform step-cooling temperature curve test on TD-MA binary composite phase change materials and TD-MA-LA ternary composite phase change materials with different mass ratios, and collect temperature data after temperature data is collected, the time-temperature curve is drawn as shown in Figures 1–3.

It can be seen from Figure 1 that the TD-MA curve under different ratios has a transition under different mass ratios,

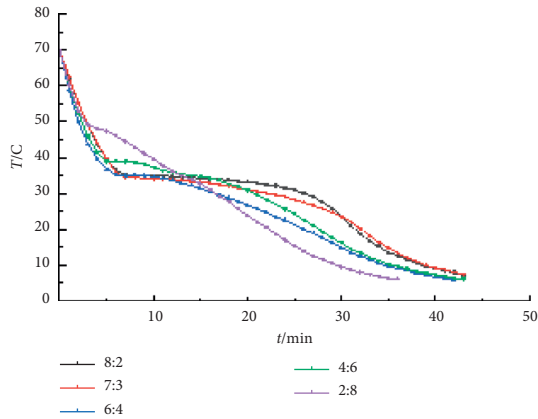


FIGURE 1: Step cooling curve of TD-MA binary composite phase change materials under different mass ratios.

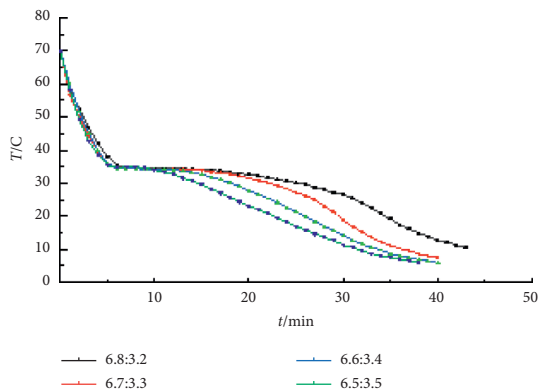


FIGURE 2: Step cooling curve of TD-MA binary composite phase change materials with different mass ratios near eutectic point.

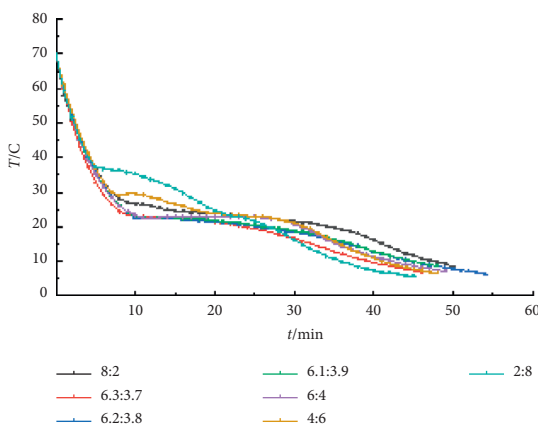


FIGURE 3: Step cooling curves of binary eutectic TD-MA and LA at different mass ratios.

indicating that the TD-MA composite phase change materials under different mass ratios have crystallized during the cooling process. Moreover, the size of the temperature plateau is different, indicating that the size of the latent heat of phase change is different. When the mass ratio TD : MA is 8 : 2, 7 : 3, 6 : 4, 4 : 6, 2 : 8, the crystallization temperature is 35.3°C, 34.7°C, 35°C, 38.7°C, and 49.0°C, respectively. The

crystallization temperature is lower at 7 : 3 and 6 : 4, and it is preliminarily judged that the eutectic point temperature appears between these two ratios.

Figure 2 shows the step cooling curves of TD-MA composite phase change materials with different ratios near the low eutectic point. It can be seen that the TD-MA composite phase change materials under the four mass ratios have crystallized during the cooling process. When the mass ratio is 6.5 : 3.5, the crystallization temperature is slightly higher and the phase transition duration is shorter, so it is excluded. The crystallization temperature of the other three ratios is close, and it is not easy to distinguish in the step cooling curve, so take these three ratios to continue the DSC test.

It can be seen from Figure 3 that the binary eutectic TD-MA and LA at different mass ratios of TD-MA-LA ternary composite phase change materials have crystallized during the cooling process. When the mass ratio TD-MA : LA is 8 : 2, 6 : 4, 4 : 6, 2 : 8, the crystallization temperature is 27.2°C, 24.4°C, 29.6°C, and 37.3°C, respectively. When the mass ratio is near the theoretically predicted eutectic point mass ratio, the crystallization temperature is the lowest and the crystallization temperature is within the comfortable temperature of the human body, roughly between 20°C and 25°C, but the difference is small and difficult to distinguish, so take TD-MA. The ratio of LA was tested by DSC at 6.3 : 3.7, 6.2 : 3.8, 6.1 : 3.9.

3.2. DSC Test Analysis of Composite Phase Change Materials.

The DSC test curves of the TD-MA binary composite phase change material near the mass ratio of the eutectic point predicted by theory are shown in Figures 4–6. The DSC test curves of the TD-MA-LA ternary composite phase change material near the mass ratio of the eutectic point predicted by theory are shown in Figures 7–9.

From Figures 4–6, it can be concluded that when the mass ratio TD : MA is 6.8 : 3.2, 6.7 : 3.3, 6.6 : 3.4, the phase transition temperature of the TD : MA binary composite phase change material is 33.4°C, 33.1°C, and 34.8°C. When the ratio of the two is 6.7 : 3.3, the TD-MA binary composite phase change material has a low eutectic point, which is 1.1°C different from the theoretical prediction, and the latent heat of phase change is 208.3 J/g, which is closed to the theoretical prediction. Therefore, take this ratio of TD-MA binary composite phase change material to continue the configuration of ternary composite phase change material.

It can be seen from Figures 7–9 that the phase transition temperature of the TD-MA-LA ternary composite phase change material with the mass ratio near the eutectic point is predicted to be around 20°C. The ternary composite phase change material when TD-MA : LA = 6.2 : 3.8 is selected as the final material required for this study. The phase change temperature is 20.1°C, and the latent heat of phase change is larger, which is 154.6 J/g. Compared with other ratios, TD-MA : LA = 6.2 : 3.8 has great advantages, suitable phase change temperature and large latent heat of phase change, which can satisfy the building envelope structure.

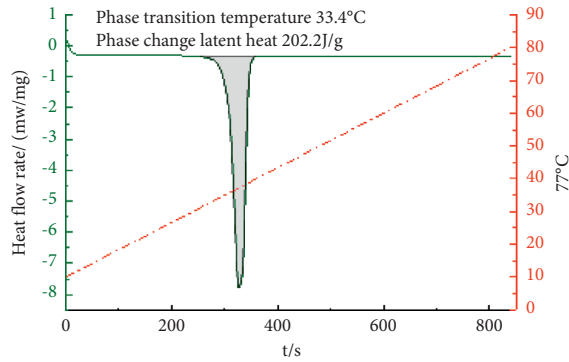


FIGURE 4: TD:MA is the DSC curve of TD-MA at 6.8:3.2.

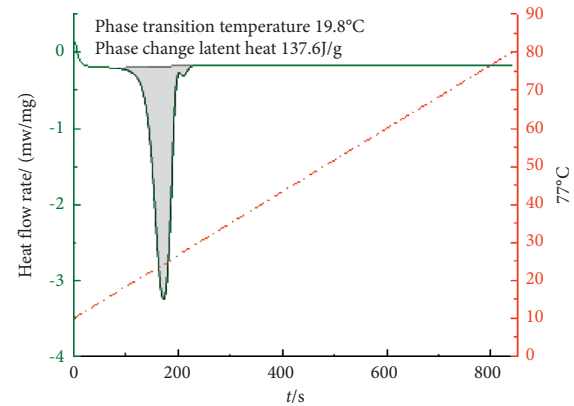


FIGURE 7: TD-MA:LA is the DSC curve of TD-MA-LA at 6.3:3.7.

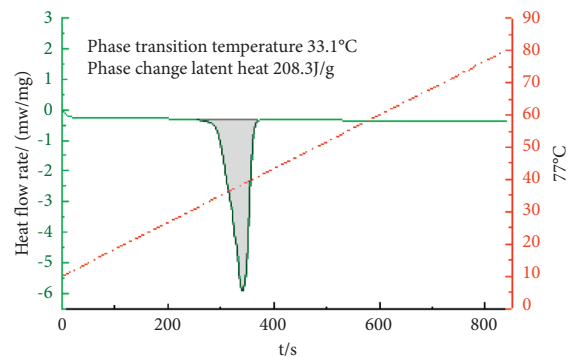


FIGURE 5: TD:MA is the DSC curve of TD-MA at 6.7:3.3.

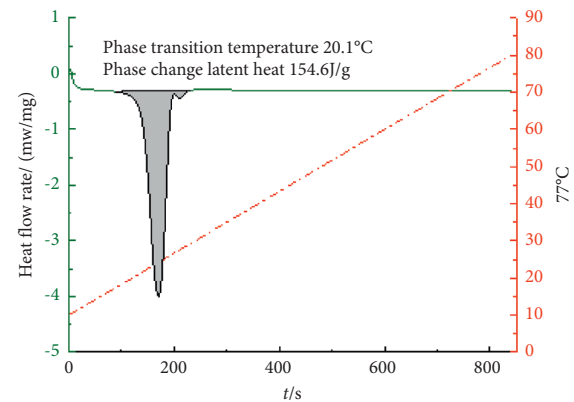


FIGURE 8: TD-MA:LA is the DSC curve of TD-MA-LA at 6.2:3.8.

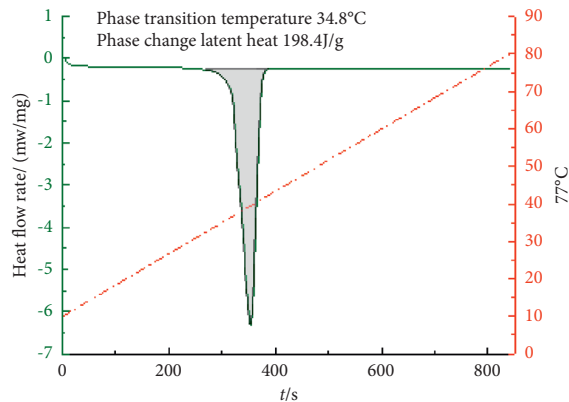


FIGURE 6: TD:MA is the DSC curve of TD-MA at 6.6:3.4.

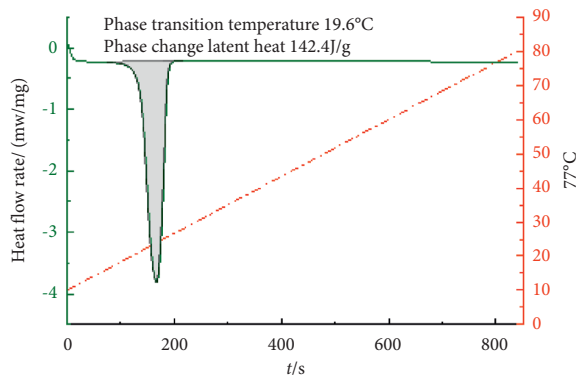


FIGURE 9: TD-MA:LA is the DSC curve of TD-MA-LA at 6.1:3.9.

3.3. FT-IR Analysis. The infrared spectra of LA, MA, TD, and TD-MA-LA eutectics measured experimentally are as shown in Figure 10. The infrared spectra of TD-MA-LA eutectic, diatomaceous Earth, and phase change diatomite are shown in Figure 11.

From Figure 10, it can be seen that the positions of the peaks in the infrared spectra of LA and MA and their strengths are similar. Observe the infrared spectra of LA. There are two characteristic absorption peaks at 2920 cm^{-1} and 2840 cm^{-1} , respectively, which are CH_3 -symmetrical stretching vibration peak, $-\text{CH}_2$ -Asymmetrical stretching vibration peak. The $\text{C}=\text{O}$ stretching vibration absorption peak appears at 1700 cm^{-1} , the $-\text{CH}_2$ - flexural vibration peak

appears at 1470 cm^{-1} , and the OH surface deformation flexural vibration peak appears at 1415 cm^{-1} . At 930 cm^{-1} and 725 cm^{-1} , the bending vibration peaks of the terminal alkenyl group CH and the $(\text{CH}_2)_{10}$ bending vibration absorption peaks appear. Observe the infrared spectrum curve of TD, the peak at 3332 cm^{-1} is the characteristic absorption peak of the OH bond vibration of alcohol and water molecules. The spectrum shows CH_3 -symmetric stretching vibration peaks and $-\text{CH}_2$ -asymmetry at 2920 cm^{-1} and

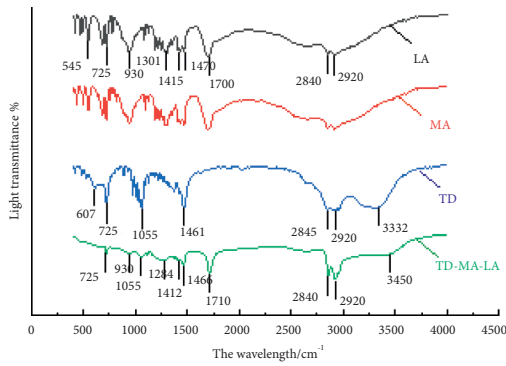


FIGURE 10: Infrared spectra of La, Ma, Td, and TD-MA-LA composite phase change materials/.

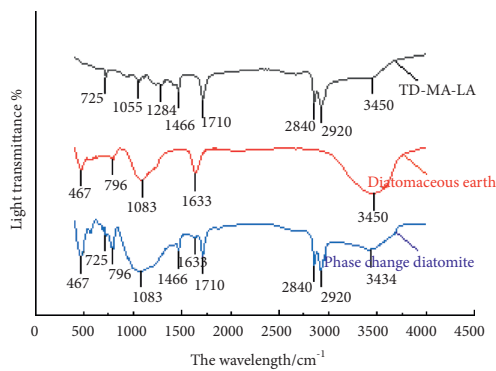


FIGURE 11: Spectrum of TD-MA-LA eutectic, diatomite and phase change diatomite.

2845 cm^{-1} . Stretching vibration peak, the peak at 1461 cm^{-1} is $-\text{CH}_2-$ flexural vibration peak, and the peak at 1055 cm^{-1} is CO stretching vibration absorption peak. Compared with the infrared spectra of LA and TD, the infrared spectra of TD-MA-LA can be seen at 3450 cm^{-1} , 2920 cm^{-1} , 2840 cm^{-1} , 1710 cm^{-1} , 1464 cm^{-1} , 1412 cm^{-1} , 1055 cm^{-1} , and 930 cm^{-1} . Corresponding characteristic absorption peaks also appeared at 725 cm^{-1} , and no new characteristic peaks were generated. Only the position of individual peaks has a slight deviation and the strength of some peaks has changed slightly, indicating that the ternary composite phase change material is only physically mixed during the preparation process, and no chemical reaction occurs.

It can be seen from Figure 11 that the O-H bond of water molecules and the Si-O-H bond stretching vibration absorption peak of diatomite appear at 3450 cm^{-1} of diatomite. Corresponding to the O-H bending vibration peak at 1633 cm^{-1} , the characteristic absorption peak at 1083 cm^{-1} is the cyclic Si-O-Si stretching vibration absorption peak, and the Si-O bending vibration absorption peak at 467 cm^{-1} . It can be seen from the infrared spectrum of the phase change diatomite that it contains all the characteristic peaks of diatomite and TD-MA-LA composite materials, and no new characteristic peaks are generated, indicating that the phase change diatomite is in the preparation only physical adsorption, no chemical reaction occurs.

3.4. DSC Characterization of Shaped Composite Phase Change Materials. The DSC curves of TD-MA-LA and phase change diatomite before and after cycling are shown in Figure 12.

It can be seen from Figure 12 that the phase change temperature of the phase change diatomite after the adsorption of the phase change material by diatomite is 20.4°C , which is 0.3°C change from previous adsorption, and the latent heat of phase change appears to be reduced to 55.9 J/g . The phase change temperature of the phase change diatomite after 100 cycles of phase change is 20.3°C , which is a change of 0.1°C from before the cycle, and the latent heat of phase change is 51.2 J/g , which is 8.4% lower than that before the cycle, showing that phase change diatomite has good thermal stability.

3.5. Analysis of Durability Results of Cooling and Heating Cycles. The mass of phase-change diatomite after encapsulation by styrene-acrylic emulsion, cement powder, styrene-acrylic emulsion+cement powder is 39.52 g , 39.27 g , and 49.61 g , respectively, and the durability of phase-change diatomaceous Earth under different packaging methods. And the test results are shown in Table 1 and Figure 13.

It can be seen from Figure 13 that the mass loss rate of phase change diatomite under the four encapsulation methods increases with the increase of the number of phase change cycles. In the unencapsulated state, the mass loss of phase change diatomaceous Earth is relatively large, and the quality is stable after about 40 phase change cycles, and the mass loss rate is about 5.1% . The effect of packaging with cement powder and styrene-acrylic emulsion is obvious, and the maximum mass loss rate About 2.1% and 1.8% respectively. It can be seen that the encapsulation method using styrene-acrylic emulsion mixed with cement powder has the best effect. The quality is close to stable after the phase change cycle is about 20 times, and the maximum mass loss rate is only about 0.65% . From experiments that the encapsulation method of styrene-acrylic emulsion and cement powder has the best durability. It can be used with building with long service life. This encapsulation method can be used to prepare phase-change energy storage aggregates and combine with building materials to prepare phase-change energy storage concrete for use in building envelopes.

4. Discussion

To make more of the phase change materials in different areas to get reasonable application more effectively, most scholars [20] will be focused on two or more composite phase change materials, in line with the principle of phase change materials of high utilization rate, this study selected three kinds of high phase transition temperature of solid liquid phase change materials for building palisade structure after through distribution, through the theoretical prediction and experimental verification, The thermal properties of the ternary composite phase change material finally

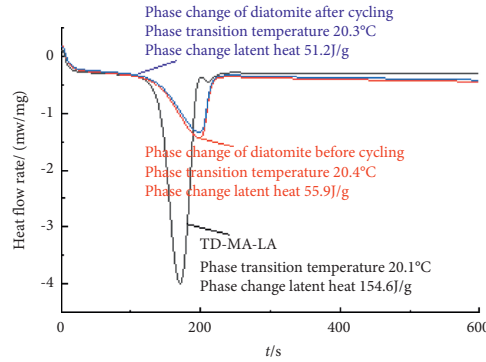


FIGURE 12: DSC curves of TD-MA-LA and phase change diatomite.

TABLE 1: Changes of mass and loss rate of phase change expanded perlite under different encapsulation methods.

Packaging materials	Cycle number	Mass/g					
		0	10	20	30	40	50
Unencapsulate	Mass/g	20.00	19.73	19.37	19.12	18.98	18.98
	Loss rate/%	0	1.4	3.2	4.4	5.1	5.1
Styrene-acrylic emulsion	Mass/g	39.52	39.34	39.24	39.16	39.16	39.16
	Loss rate/%	0	0.9	1.7	1.8	1.8	1.8
Cement powder	Mass/g	39.27	39.05	38.95	38.87	38.85	38.85
	Loss rate/%	0	1.1	1.6	2.0	2.1	2.1
Styrene-acrylic emulsion and cement powder	Mass/g	49.61	49.52	49.49	49.48	49.48	49.48
	Loss rate/%	0	0.44	0.60	0.65	0.65	0.65

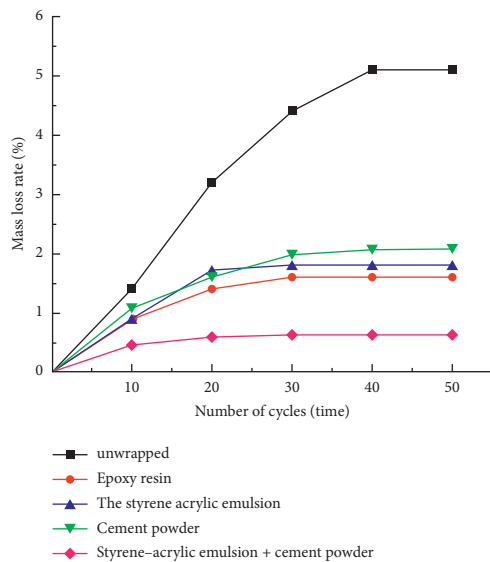


FIGURE 13: Mass loss rate of phase change expanded perlite under different encapsulation methods.

prepared meet the requirements of this study, so that the single phase change material can be reasonably utilized.

The latent heat of phase-change materials will inevitably decrease after being adsorbed by diatomite, and no new materials will be formed in the melting composite process of phase-change materials and the adsorption process of diatomite, which indicates that no chemical reaction takes

place in each component. The prepared phase-change energy storage aggregate has excellent phase-change stability. Some scholars [21–23] found that, after packaging the porous matrix material after adsorption of PCM, the leakage problem of liquid PCM would be greatly improved due to the obstruction of packaging layer on the liquid PCM. In this study, the double-packaging effect of styrene-acrylic emulsion + cement powder was very excellent. After about 10 phase transformation cycles, there was no leakage and the mass loss rate was only 0.65%. However, the problem of low adsorption rate of diatomite itself needed further study. It can be seen that how to use more phase change materials in a better way under the premise of ensuring no leakage, so as to play a greater role in phase change heat storage and release is particularly critical.

5. Conclusions

- (1) Theoretical calculation of the ternary composite phase change material TD-MA : LA = 62.5 : 37.5, the system has a eutectic point, and the eutectic point temperature is 23.2°C. Through the step cooling curve test and DSC test experiment, when TD-MA : LA = 6.2 : 3.8, the phase change temperature of the ternary composite phase change material is 20.1°C, and the latent heat of phase change is 154.6 J/g. The thermophysical properties of the final ternary composite phase change material meet the requirements for application in building envelopes.

- (2) TD, MA, LA did not undergo chemical reaction during the melting and compounding process, only physical melting and mixing. The adsorption of diatomite to the TD-MA-LA composite phase change material is only physical adsorption, and no new substances are produced during the process. The phase change latent heat of the adsorbed phase change diatomite is reduced to a certain extent, which is 55.9 J/g. The phase change temperature of diatomite is basically unchanged after the phase change cycle, the latent heat of phase change is reduced by 8.4%, and it has good thermal stability.
- (3) The cold and heat cycle durability of phase change diatomaceous Earth after encapsulation is significantly better than before encapsulation. Among them, the encapsulation method of styrene-acrylic emulsion mixed cement powder is the most excellent, with a maximum mass loss rate of only 0.65% and excellent durability.

Data Availability

The data that support the finding of this study are available from the corresponding author upon reasonable request.

Conflicts of Interest

The authors declare that they have no conflicts of interest.

References

- [1] A. S. Manirathnam, M. K. Dhanush Manikandan, R. Hari Prakash, B. K. Kumar, and M. D. Amarnath, "Experimental analysis on solar water heater integrated with Nano composite phase change material," *Materials Today Proceedings*, vol. 9, no. 1, pp. 869–921, 2020.
- [2] Y. Liu, L. Hou, Y. Yang, Y. Feng, and L. Yang, "Effects of external insulation component on thermal performance of a Trombe wall with phase change materials," *Solar Energy*, vol. 204, pp. 115–133, 2020.
- [3] J. F. Lin, "Application research of phase change materials in building Energy conservation," *Neijiang science and technology*, vol. 40, no. 4, pp. 52–53, 2019.
- [4] K. Ahmet, "Energy storage applications in greenhouses by means of phase change materials (PCMs): a review," *Renewable Energy*, vol. 13, no. 1, pp. 89–103, 1998.
- [5] T. T. Shi, X. G. Zhang, J. X. Qiao et al., "Preparation and characterization of composite phase change materials based on paraffin and carbon foams derived from starch," *Polymer*, vol. 1, pp. 123–143, 2020.
- [6] X. L. Wang, X. Cheng, D. Li et al., "Preparation a three-dimensional hierarchical graphene/stearic acid as a phase change materials for thermal energy storage," *Materials Research Express*, vol. 7, no. 9, pp. 55–60, 2020.
- [7] K. Cellat, B. Beyhan, C. Gungor et al., "Thermal enhancement of concrete by adding bio-based fatty acids as phase change materials," *Energy and Buildings*, vol. 106, no. 1, pp. 156–163, 2015.
- [8] S. L. Zhang, F. F. Chen, W. Q. Pan, S. Wang, Y. Jiang, and D. Yuan, "Development of heat transfer enhancement of a novel composite phase change material with adjustable phase change temperature," *Solar Energy Materials and Solar Cells*, vol. 210, 2020.
- [9] D. H. Jiang, X. L. Zhang, S. X. Liao, H. Fei, and Q. J. Gu, "Preparation and thermal properties of hexadecanoic acid-tetradecanol binary phase change materials," *Modern Chemical Industry*, vol. 39, no. 10, pp. 146–149, 2019.
- [10] K. Yang, M. Jiao, S. Wang, Y. Yu, D. Quan, and J. Cao, "Thermoregulation properties of composite phase change materials in high temperature environmental conditions," *International Journal of Clothing Science & Technology*, vol. 30, no. 4, pp. 507–516, 2018.
- [11] L. Gao, X. G. Sun, B. Z. Sun, D. Y. Che, and Z. Z. Liu, "Preparation and thermal properties of palmitic acid/expanded graphite/carbon fiber composite phase change materials for thermal energy storage," *Journal of Thermal Analysis and Calorimetry*, vol. 114, pp. 1–11, 2019.
- [12] P. M. Hou, J. F. Mao, R. R. Liu, F. Chen, Y. Li, and C. Xu, "Improvement in thermodynamic characteristics of sodium acetate trihydrate composite phase change material with expanded graphite," *Journal of Thermal Analysis and Calorimetry*, vol. 137, no. 4, pp. 1295–1306, 2019.
- [13] R. A. Mitran, D. Lincu, L. Buhăleanu, D. Berger, and C. Matei, "Shape-stabilized phase change materials using molten NaNO₃-KNO₃ eutectic and mesoporous silica matrices," *Solar Energy Materials and Solar Cells*, vol. 215, 2020.
- [14] T. Shi, Y. Fang, and H. X. Zhang, "Advances in the study of formalized phase change materials," *Materials bulletin*, vol. 29, no. 2, pp. 439–442, 2015.
- [15] C. Hasse, M. Grenet, A. Bontemps, R. Dendievel, and H. Sallee, "Realization, test and modelling of honeycomb wallboards containing a Phase Change Material," *Energy&Building*, vol. 43, no. 1, pp. 232–238, 2010.
- [16] S. Ramakrishnan, X. M. Wang, S. Jay, E. Petinakis, and J. Wilson, "Development of thermal energy storage cementitious composites (TESC) containing a novel paraffin/hydrophobic expanded perlite composite phase change material," *Solar Energy*, vol. 158, pp. 626–635, 2017.
- [17] W. W. Wang, X. F. Song, and Y. N. Cai, "Preparation and thermal properties of ternary fatty acid eutectic/Silicon dioxide phase change composites," *Journal of Materials Science and Engineering*, vol. 38, no. 1, pp. 68–73, 2020.
- [18] C. Li, L. Qi, and Y. L. Ding, "Carbonate salt based composite phase change materials for medium and high temperature thermal energy storage: from component to device level performance through modelling," *Renewable Energy*, vol. 140, pp. 140–151, 2019.
- [19] W. C. Li, Y. F. Cai, and T. Y. Yan, "Preparation of sodium acetate trihydrate/expanded graphite composite phase change materials and its heat storage properties," *Journal of Shanghai Jiaotong University*, vol. 54, no. 10, pp. 1015–1023, 2020.
- [20] S. Hhleln, A. Knig-Haagen, and D. Brüggemann, "Macro-encapsulation of inorganic phase-change materials (PCM) in metal capsules," *Materials*, vol. 11, no. 9, 2018.
- [21] Y. C. Zhang, Y. Wang, J. H. Zhou, Z. R. Zhang, and T. Li, "Preparation and characterization of phase change energy storage wall materials based on desulfurization gypsum," *New Building Materials*, vol. 47, no. 4, pp. 135–146, 2020.
- [22] B. Beyhan, K. Cellat, Y. Konuklu et al., "Robust micro-encapsulated phase change materials in concrete mixes for sustainable buildings," *International Journal of Energy Research*, vol. 41, no. 1, pp. 113–126, 2017.
- [23] Y. W. Wang and W. L. Li, "Preparation and properties of shaped PEG/SiO₂/graphite composite phase change thermal regenerative concrete," *Concrete & Cement Products*, vol. 3, pp. 65–69, 2020.

Research Article

Optimization of the Stirring Blade Structure of the Pumping Unit Based on the Improvement of Concrete Suction Efficiency

Shengqiang Jiang ¹, Hong Wan,¹ Guodong Cao ¹, Yuanqiang Tan,² Jingang Liu,¹ Shiping Yang,¹ Xiangwu Xiao,¹ Zhenggang Tong,³ and Quanxu Yu³

¹School of Mechanical Engineering, Xiangtan University, Xiangtan 411105, China

²Institute of Manufacturing Engineering, Huaqiao University, Xiamen 361021, China

³SANY Industrial Park, SANY Heavy Industry Co., Ltd., Changsha 411100, China

Correspondence should be addressed to Shengqiang Jiang; jsqcx@xtu.edu.cn

Received 3 December 2021; Accepted 27 January 2022; Published 25 February 2022

Academic Editor: Andreas Lampropoulos

Copyright © 2022 Shengqiang Jiang et al. This is an open access article distributed under the Creative Commons Attribution License, which permits unrestricted use, distribution, and reproduction in any medium, provided the original work is properly cited.

In this paper, a discrete element method (DEM) is used to simulate the suction process of fresh concrete in the pumping system, and the influence of the stirring blade on the suction is explored. The Hertz-Mindlin with JKR Cohesion contact model is used to establish the DEM model of fresh concrete, and the suction work is realized by an API function of DEM, and the movement of particles in the suction cylinder can be completed smoothly. The changes of the concrete flow field during the suction process are further studied, and the influence mechanism of the stirring blade on the suction process is explained. A numerical simulation scheme is designed to explore the influence of the rotation speed, installation angle, and edges distance of the stirring blade on the suction efficiency and the stirring resistance torque, and the structure of the stirring blade is optimized according to the influence law. The simulation results show that the stirring resistance torque of the optimized stirring blade is reduced without the suction efficiency of the pumping system reduced, and the stirring energy consumption of the pump suction is reduced.

1. Introduction

Fresh concrete is transported from the hopper to the pouring site along the pipeline with the help of the concrete pump truck [1]. It has the advantages of adjustable pumping height, long conveying distance, large pumping concrete quality, fast conveying speed, high efficiency, continuous operation, labor saving, and strong economy. And it is widely used in various concrete construction projects [2]. Pumping system is the core part of the concrete pump truck [3], usually located in its tail. The reciprocating motion of the piston in the conveying cylinder is powered by the hydraulic system that converts the hydraulic energy into mechanical energy. With the cooperation of the S-pipe reversing work, the concrete in the hopper is sucked into the conveying cylinder to complete the suction work, while the concrete in the conveying cylinder is pushed through the S-pipe to the output pipe to complete the push work, as shown in Figure 1. During the pumping process, the

stirring blade continuously stirs the fresh concrete in the hopper. Speeding up the flow of the fresh concrete that can ensure the fluidity of the fresh concrete in the hopper, promote the suction work, prevent the rapid solidification of the fresh concrete, and the blockage of the pipe at the bottom of the hopper. Optimizing the structural parameters of the stirring blade can improve the suction performance and reduce the energy consumption.

The actual experiments of pumping concrete are time-consuming and labor-intensive, while the numerical simulation technology can reduce the waste of resources and save the economy. In recent years, there were many numerical simulations of fresh concrete. Roussel et al. [4] roughly divided its types into three types: single-phase flow models [5–7], discrete particle flow models [8–10], and suspension flow models [11–13] and elaborated on the advantages and disadvantages of the three methods. Choi et al. [14] chose the single-phase fluid method and used

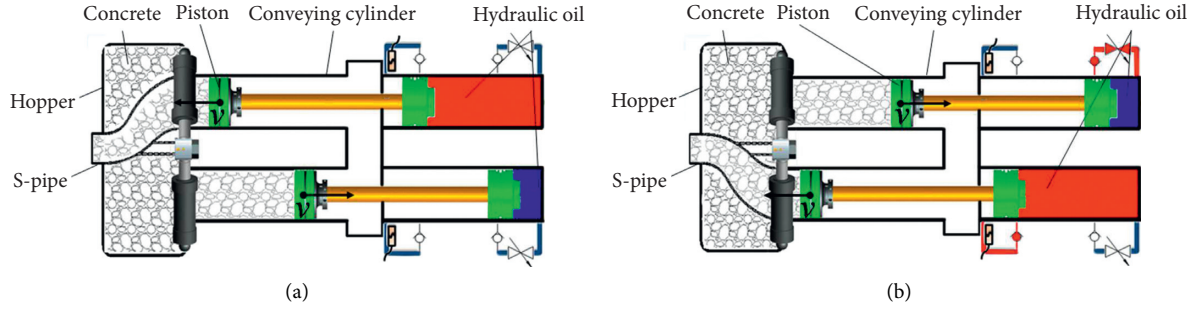


FIGURE 1: The pumping process before (a) and after (b) the S-pipe reversing work.

Fluent to solve the complex concrete flow. The experimental, analytical, and numerical results found that the behavior of the lubricating layer is similar to that of mortar in terms of rheology. Zhan et al. [15] used the DEM to numerically simulate the local pumping problem and explored the influence of a series of factors on the local pumping performance, which were related to the pipe geometry, aggregate geometry, and pumping conditions. Shengqiang et al. [16] used a computational fluid dynamics-discrete element method (CFD-DEM) coupling model to explore the influence of structural parameters and inclination angles of tapered pipes, elbows and their combinations on pressure loss, and proposed a pump truck conveying pipeline. They used a single-objective optimization method to reduce the pressure loss (about 5.45%) in the pumping process. In addition, there were a lot of work on the optimal design of pumps [17–19]. Liu et al. [20] explored the influence of the geometry of inlet guide vanes (IGVs) on the stability of centrifugal pump operation, and prerotation adjustment of IGVs effectively adjusted the operation of centrifugal pump. The researches on pumping were mostly aimed at the pumping and flow of fresh concrete in the pipeline, but the researches on the process of concrete pumping and suction are very few. At present, there is still a lack of research on the suction process of the pumping system.

In this paper, the discrete element method simulated the suction process of fresh concrete in the pumping system, and the influence of the stirring blade on the suction is explored. First, the Hertz-Mindlin with JKR Cohesion contact model is used to establish the DEM model of fresh concrete, and the mechanical behavior of the concrete particles is described. Comparison between experiments and simulations of slump flow tests and L-box tests, the feasibility of simulating the flow behavior and rheological properties of the fresh concrete is proved. The geometric structure of pumping system is simplified. The suction force of the conveying cylinder is customized by the API function of DEM to realize the suction work; therefore, the numerical simulation of the suction process is completed. Next, the changes of the concrete flow field during the suction process are further studied, the particle flow velocity at different positions is considered, and the influence mechanism of the stirring blade on suction process is explained. In addition, the numerical simulation scheme is designed to explore the influence of the rotation speed, installation angle and edges

distance of the stirring blade on the suction efficiency and the stirring resistance torque, and the structure of the stirring blade is optimized according to the influence law. Finally, verified by the results before and after optimization, the stirring resistance torque of the optimized stirring blade is reduced without the suction efficiency of the pumping system reduced, thereby the stirring energy consumption of the pump suction is reduced.

2. The Simulation of the Suction Process of the Pumping System

2.1. The Numerical Simulation Method. The discrete element method is that the discontinuous body is separated into a set of rigid elements, and the motion equation of each rigid element is solved by the method of time-step iteration, and then the overall motion shape of the discontinuous body is obtained. In the process of numerical simulation using the discrete element method, each particle in the material is used as a particle unit to establish a mathematical model, and the size and physical properties of the particle unit are given. Among them, there are two relations of contact and separation between each particle. When the contact occurs, the contact force and moment will be generated at the contact point, the magnitude of that can be calculated according to the contact mechanics model.

Hertz-Mindlin with JKR (Johnson–Kendall–Roberts) cohesion is a cohesion contact model that can model strongly adhesive systems and provide attractive cohesion forces. JKR normal force F_{JKR} , normal damping F_n^d , tangential force F_t , tangential damping F_t^d , and rolling frictional torque T_i are as follows:

$$\begin{aligned}
 F_{JKR} &= -4\sqrt{\pi\gamma E^*} \alpha^{(3/2)} + \frac{4E^*}{3R^*} \alpha^3, \\
 F_n^d &= -2\sqrt{\frac{5}{6}} \frac{\ln e}{\sqrt{\ln^2 e + \pi^2}} \sqrt{K_n m^*} V_n^{\text{rel}}, \\
 F_t &= -K_t \delta_t, \\
 F_t^d &= -2\sqrt{\frac{5}{6}} \frac{\ln e}{\sqrt{\ln^2 e + \pi^2}} \sqrt{K_n m^*} V_t^{\text{rel}}, \\
 T_i &= -\mu_r F_{JKR} R_i \omega_i.
 \end{aligned} \tag{1}$$

In the above,

$$\begin{aligned} \delta_n &= \frac{\alpha^2}{R^*} - \sqrt{\frac{4\pi\alpha}{E^*}}, \\ \frac{1}{E^*} &= \frac{1-\nu_i^2}{E_i} + \frac{1-\nu_j^2}{E_j}, \\ \frac{1}{R^*} &= \frac{1}{R_i} + \frac{1}{R_j}, \\ \frac{1}{m^*} &= \frac{1}{m_i} + \frac{1}{m_j}, \\ K_n &= 2E^* \sqrt{R^* \delta_n}, \\ K_t &= 8G^* \sqrt{R^* \delta_n}. \end{aligned} \quad (2)$$

Figure 2 shows the typical plot of JKR normal force as a function of normal overlap.

This model provides attractive cohesion forces even if the particles are not in physical contact. The maximum gap between particles with nonzero force is given by

$$\begin{aligned} \delta_C &= \frac{\alpha_C^2}{R^*} - \sqrt{\frac{4\pi\gamma\alpha_C}{E^*}}, \\ \alpha_C &= \left[\frac{9\pi\gamma R^{*2}}{2E^*} \left(\frac{3}{4} - \frac{1}{\sqrt{2}} \right) \right]^{(1/3)}. \end{aligned} \quad (3)$$

The maximum value of the cohesion force occurs when particles are not in physical contact and the separation gap is less than δ_C . The value of maximum cohesion force, called pull-out force, is given by

$$F_{J\text{pullout}} = -\frac{3}{2}\pi\gamma R^*. \quad (4)$$

Hence, the adhesion of fresh concrete is determined by the surface energy, which is the basic parameter of the Hertz–Mindlin with JKR model. The viscosity of concrete flow is characterized by the adhesion of fresh concrete.

2.2. The DEM Model of Fresh Concrete. Fresh concrete is mainly mixed by water, cement, sand, coarse aggregate (stone), and various additives (concrete water-reducing agent or concrete retarder). The mix proportions for the fresh concrete are given in Table 1. The mass ratio of mortar (water + cement + sand + water-reducing agent + retarder) to coarse-aggregate is about 1.35.

In the simulation, the fresh concrete is composed of coarse aggregate particles and mortar particles with a mass ratio of 1.35. In order to realize the feasibility of numerical simulation and the calculation efficiency, both particles are set as spheres. The diameter of mortar particles is uniformly 10 mm. According to experiments, the coarse aggregate particle size in the DEM model is normally distributed, with an average of 20 mm, a standard deviation of 5 mm, a

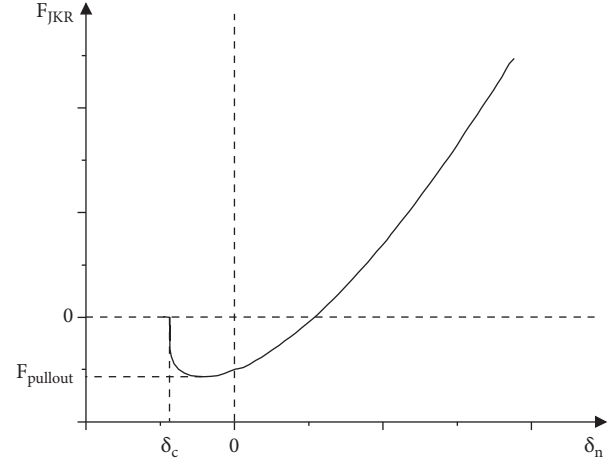


FIGURE 2: Normal force as a function of normal overlap.

minimum of 10 mm, and a maximum of 30 mm, as shown in Figure 3.

Under the hydration of cement, fresh concrete has strong adhesion. The adhesion not only exists between particles and particles but also particles and geometry. Compared with other contact models, the Hertz–Mindlin with JKR model has higher matching for fresh concrete, which has obvious cohesion effects [21]. The mechanical behaviors of fresh concrete discrete elements are described when they come into contact with each other.

2.3. The Validation of the Fresh Concrete DEM Model.

The rheological properties of fresh concrete are expressed by various standard tests, slump flow test, L-box test, and V-funnel test. In experiments, three slump tests and L-box tests were repeated, and the test results are averaged. In the simulations of slump flow tests and L-box tests, all the uncertain quantities in the DEM model of the fresh concrete were continuously adjusted so that the gap between experiments and simulations results is less than 5%. Figures 4(a) and 4(b) show the model of slump cone and L-box. Figures 4(c) and 4(d) show their dimensions.

In experiments, after the fresh concrete collapses and stabilizes naturally, the average remaining height is 77 mm, the average slump value is 223 mm, and the average expansion value is 404 mm. In the simulation, the average remaining height is 85 mm, the slump value is 215 mm, which is 3.6% different from the experiments, and the expansion value is 413 mm, which is 2.2% different from the experiments. It is not difficult to find that the simulation is very similar to the experiments by observing the vertical and horizontal shape of fresh concrete carefully from Figures 5(a) and 5(b).

In experiments, when the fresh concrete stopped flowing naturally, the fresh concrete did not flow to the end of the L-box. The average height of the front end is 219 mm, and the flow distance is 480 mm. In the simulation, the average height of the front end is 224 mm, which is 2.3% different from the experiments, and the flow distance is 498 mm, which is 3.8% different from the experiments. Figures 6(a)

TABLE 1: The mix proportions of the fresh concrete.

Water-cement ratio	Cement (kg/m ³)	Sand (kg/m ³)	Coarse aggregate (kg/m ³)	Concrete water reducing (kg/m ³)	Concrete retarder (kg/m ³)
0.42	390	900	1080	3.20	0.39

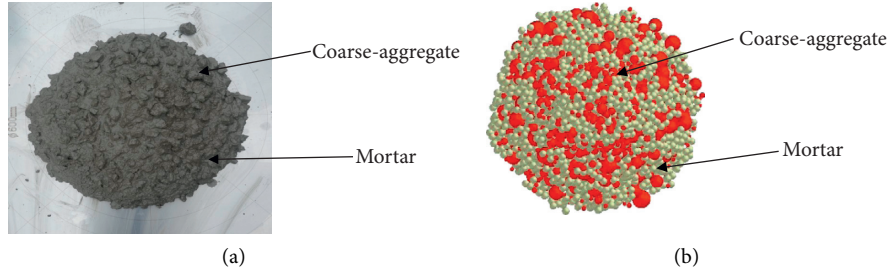


FIGURE 3: The fresh concrete in experiments (a) and simulations (b).

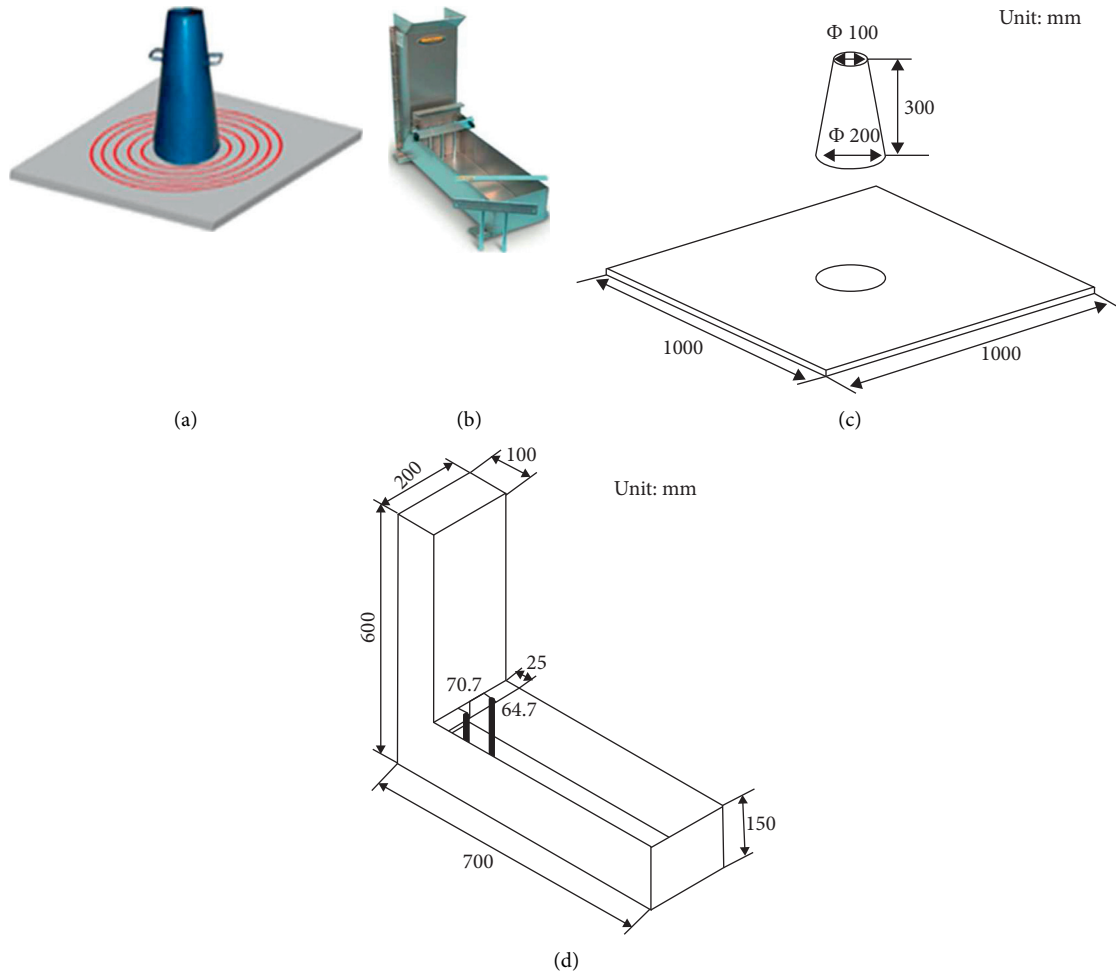


FIGURE 4: The model of the slump cone (a) and L-box (b); the dimension of the slump cone (c) and L-box (d).

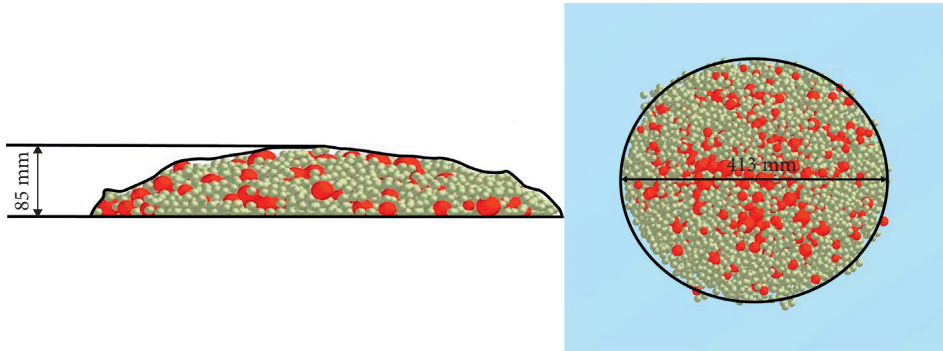
and 6(b) show that the experiments and simulations of the L-box are also very similar.

In short, the difference between the results of simulations and experiments is less than 5% for slump and L-box tests. The feasibility of simulating the flow behavior and

rheological properties of the fresh concrete is proved. The DEM model of the fresh concrete will be applied to the numerical simulation of the pumping and suction process. The surface energy of the final DEM model of fresh concrete is shown in Table 2. The time step is set as $3.80675e - 06$ s.

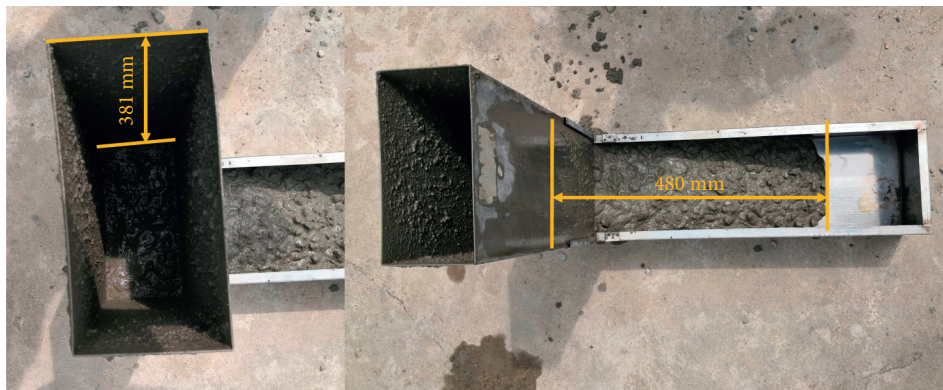


(a)

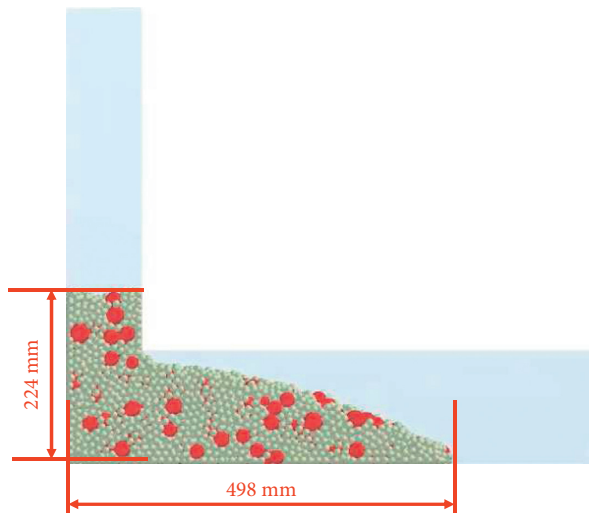


(b)

FIGURE 5: The results of slump tests in experiments (a) and simulations (b).



(a)



(b)

FIGURE 6: The results of L-box tests in experiments (a) and simulations (b).

TABLE 2: The surface energy of the final DEM model of fresh concrete.

	Coarse aggregate-coarse aggregate	Coarse aggregate-mortar	Coarse aggregate-steel	Mortar-mortar	Mortar-steel
Surface energy (J/m ²)	1	3	0.6	5	0.9

2.4. Realization of the Suction Work of the Pumping System. Pumping system is an executive mechanism to realize suction work and determine pumping performance, which is composed of pump transport mechanism, hopper, S valve, oscillating mechanism, stirring mechanism, conveying pipeline, and lubrication system. The pumping suction test device has an angle of 8° with the horizontal plane, the inner diameter of the conveying cylinder is 230 mm, and the pumping stroke is 1600 mm, as shown in Figures 7(a) and 7(b).

In the DEM numerical simulation, the main purpose is to study the interaction between particles and particles and between particles and geometric bodies. Therefore, only the geometries in direct contact with the fresh concrete particles in the pumping system need to be considered when establishing geometric models in simulation. There is a hopper, a stirring blade, a S-pipe, two conveying cylinders *L* and *R*, two concrete pistons *L* and *R*, and an in-out pipe, as shown in Figure 8.

The suction efficiency is an important performance index of the pumping system, which is calculated as follows:

$$\eta = \frac{M_1}{M_2}. \quad (5)$$

Among them, M_2 is theoretical suction mass that is the mass of the conveying cylinder completely filled with fresh concrete; M_1 is actual suction mass that is the mass of the conveying cylinder actually filled with fresh concrete during a single suction process.

The average suction efficiency is 84.6% that is measured in experiments. The theoretical suction mass is 88.9 kg, which is measured in simulation.

In experiments, the hydraulic system converts hydraulic energy into mechanical energy, which drives the concrete piston to reciprocating motion in the conveying cylinder. The fresh concrete is sucked under the combined action of atmospheric pressure and gravity and pushed by the concrete piston. The suction process is mainly due to the movement of the concrete piston, and negative pressure is formed at the position of the piston port, which is manifested as the suction effect of the conveying piston cylinder.

In DEM numerical simulation, with the help of API function, an additional particle body force is defined as suction force. The concrete particles in the area near the connecting port of the conveying piston cylinder and the hopper obtain a custom suction force to realize the suction work at the beginning of each time step. As in experiments, the pushing process is realized by using concrete piston. The suction force is in the direction of the conveying cylinder in the suction process. Its size is proportional to the mass of the particle and the parameter k , which is defined to control the size of suction force. The relevant formulas are as follows:

$$F' = F + F_{\text{suction}}, \quad (6)$$

$$F_{\text{suction}} = km.$$

In the above, F' is the resultant force of a particle at the beginning of the time step, F is the resultant force of the particle at the end of the last time step, F_{suction} is the self-defined suction force, and m is the mass of the particle.

Figure 9(a) is the numerical simulation result without adding suction force ($k=0$). The actual suction mass is 3.2 kg, and the suction efficiency is 3.60%. Figure 9(b) is the numerical simulation result with adding suction force ($k=66$). The actual suction mass is 75.2 kg, and the suction efficiency is 84.59%. The relationship between the parameter k and suction efficiency is shown as Figure 10 according to the results of multiple numerical simulations. The value of parameter k is adjusted to meet the experimental suction efficiency, which required adjustment for some conditions, including the inclination angle of the pumping system, the pumping stroke, and the speed of the piston movement during suction. In this article, the inclination angle of the pumping system is 8°, the pumping stroke is 1600 mm, and the speed of the piston movement during suction is 1 m/s. Obviously, if suction force is not added, the actual suction mass is extremely small, and the suction work is difficult to complete. After adding suction force, the suction performance of the pumping system can be revealed. When k is 66, comparing the results in simulation with the results in experiments, the difference in suction efficiency is less than 0.1%. Therefore, it is necessary to add suction force and k is 66.

In the DEM numerical simulation, the total time is 7.7 s. Fresh concrete particles were generated in the hopper from 0 to 0.5 s. The movements of geometries are shown in Table 3 from 0.5 to 7.7 s. The stirring blade rotates at a fixed speed. The S-pipe swings and commutates during the commutating period that is 0.2 s. The stroke of the conveying cylinder is 1600 mm, and the time for each suction and push is 1.6 s. There is a pumping cycle of 3.6 s, a total of 2 cycles. The numerical simulation visualization process of the second pumping cycle (4.1–7.7 s) is shown in Figure 11.

3. Analysis of Concrete Flow

3.1. The Flow Field of Concrete Particles. The particles velocity nephogram is used to represent the flow field of fresh concrete particles. In order to analyze the flow field in the pumping process, three sections A, B, and C are set up, as shown in Figure 12. Section A is perpendicular to the central axis of *Z* axis and passes through the central axis of the piston cylinder *L*. Section B is perpendicular to the central axis of *Y* axis and passes through the central axis of the stirring blade. And section C is perpendicular to the central

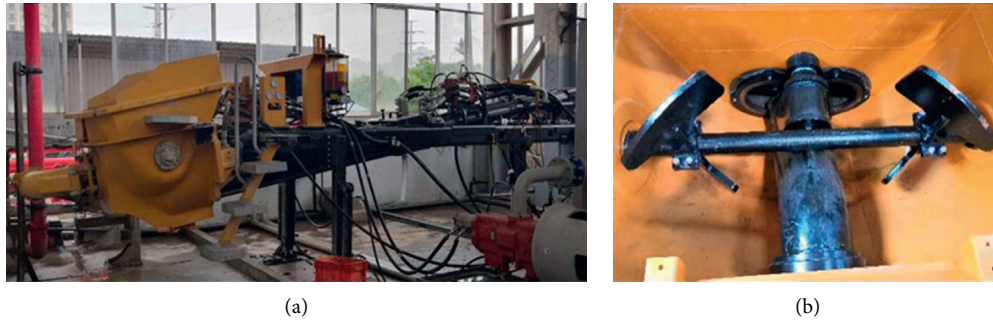


FIGURE 7: Pumping suction test device (a) and the internal situation of the hopper (b).

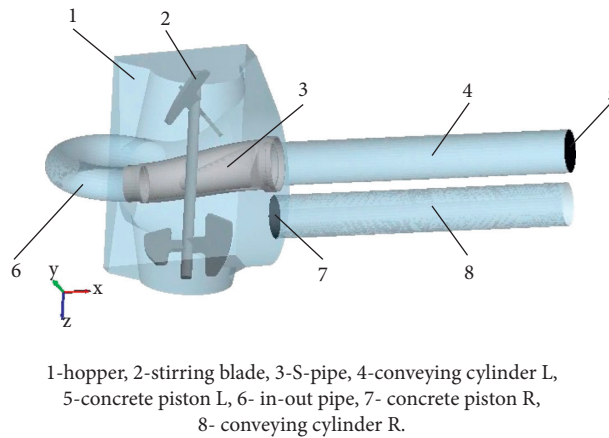


FIGURE 8: The geometries in simulation. 1-hopper, 2-stirring blade, 3-S-pipe, 4-conveying cylinder L, 5-concrete piston L, 6-in-out pipe, 7-concrete piston R, and 8-conveying cylinder R.

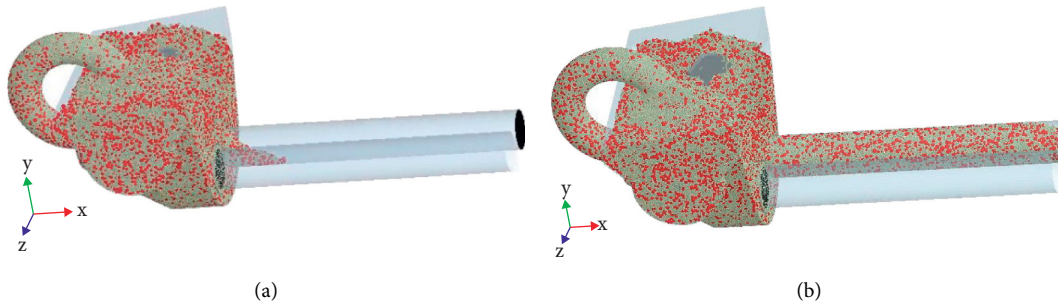


FIGURE 9: The numerical simulation results when $k=0$ (a) and $k=66$ (b).

axis of X axis and passes through the central axis of the stirring blade.

At 5.9 s, the S-pipe reversing is completed, and it is connected to the conveying cylinder R. The concrete flow rate in the swing area of the S-pipe is larger, and the concrete flow rate near the suction side of the stirring area of the stirring blade is larger than that far from the suction side.

From 5.9 to 7.5 s, the fresh concrete in the hopper is sucked into the conveying cylinder L, the S-pipe remains static, and the stirring blade keeps rotating. The concrete flow rate in the conveying cylinder L is relatively stable in the early and middle stages and decreases at the end of the suction process. The concrete flow rate in the stirring area of

stirring blade has little change. Figures 13(a)–13(d) show the concrete flow field of sections A, B, and C at 5.9 s, 6.4 s, 7 s, and 7.5 s.

From 7.5 s to 7.7 s, the conveying cylinder L stops suction, the S-pipe swings and reverses, and the stirring blade continues to rotate. The flow field in the hopper changes greatly, and the concrete flow rate away from the suction side increases affected by the reversal of the S-pipe. Figure 13(e) and 13(f) show the concrete flow field of sections A, B, and C at 7.6 s and 7.7 s.

According to the numerical simulation of the suction process, the concrete flow rate near the wall of hopper is small. The concrete flow rate in the stirring area of the

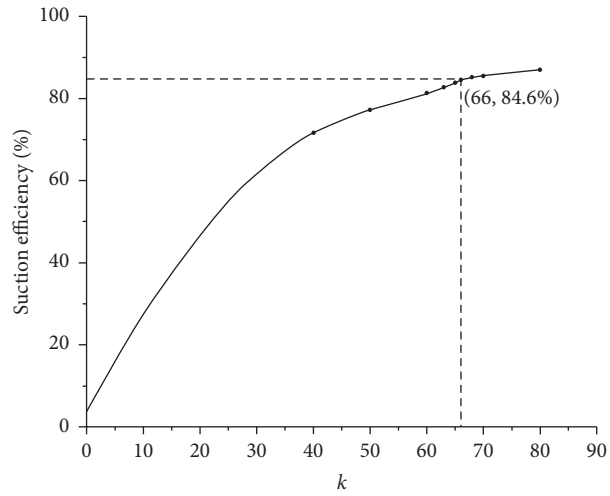


FIGURE 10: The relationship between the parameter k and suction efficiency.

TABLE 3: The movements of geometries.

Time	Stirring blade	S-pipe	Concrete piston L	Conveying cylinder L	Concrete piston R	Conveying cylinder R
0.5–2.1 s	25 r/min	0	-1 m/s	Push	1m/s	Suction
4.1–5.9 s		6.12 rad/s	0	—	0	—
2.1–2.3 s		0	1m/s	Suction	-1 m/s	Push
5.7–5.9 s		0	0	—	—	—
2.3–3.9 s		0	1m/s	Suction	-1 m/s	Push
5.9–7.5 s		0	0	—	—	—
3.9–4.1 s		-6.12 rad/s	0	—	—	—
7.5–7.7		-6.12 rad/s	0	—	—	—

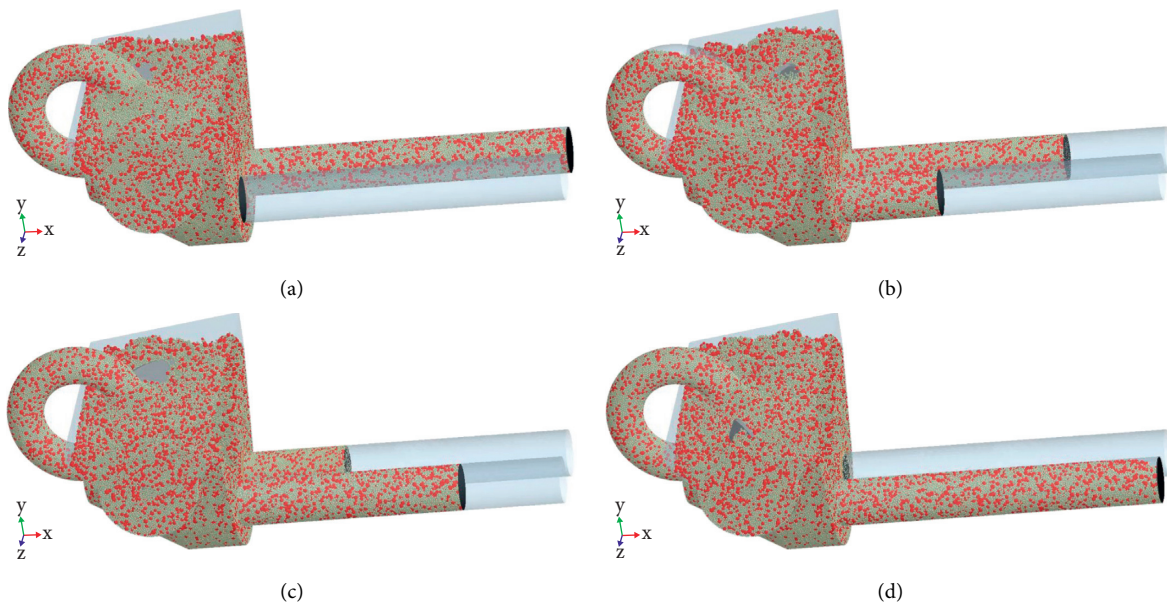


FIGURE 11: Continued.

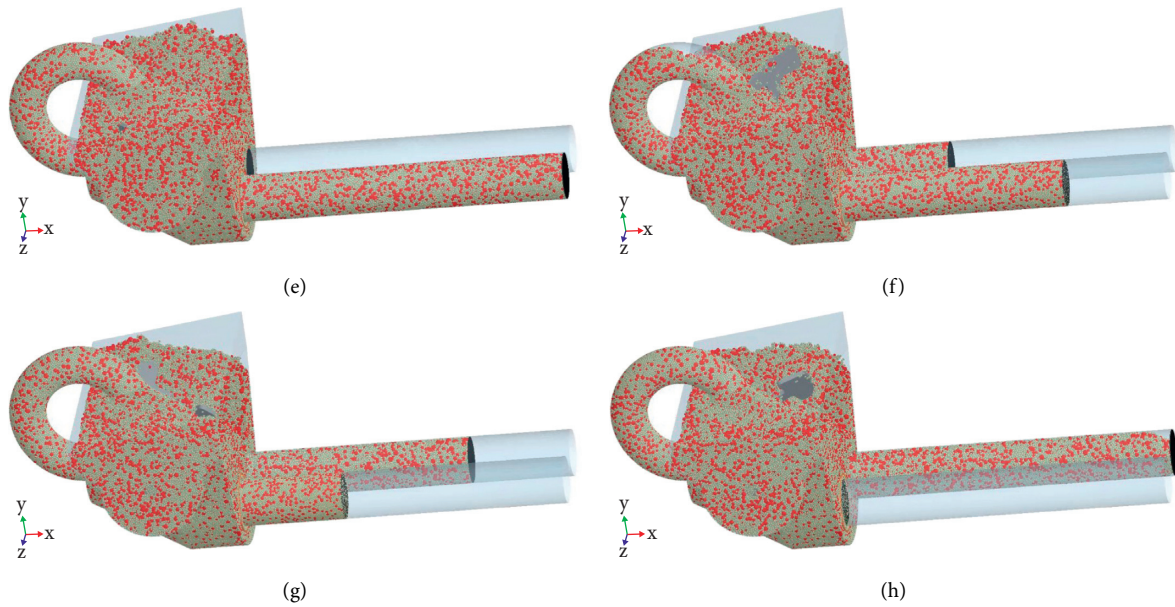


FIGURE 11: The numerical simulation visualization process of the second pumping cycle (4.1–7.7 s): (a) $t = 4.1$ s, (b) $t = 4.6$ s, (c) $t = 5.2$ s, (d) $t = 5.7$ s, (e) $t = 5.9$ s, (f) $t = 6.4$ s, (g) $t = 7$ s, and (h) $t = 7.56$ s.

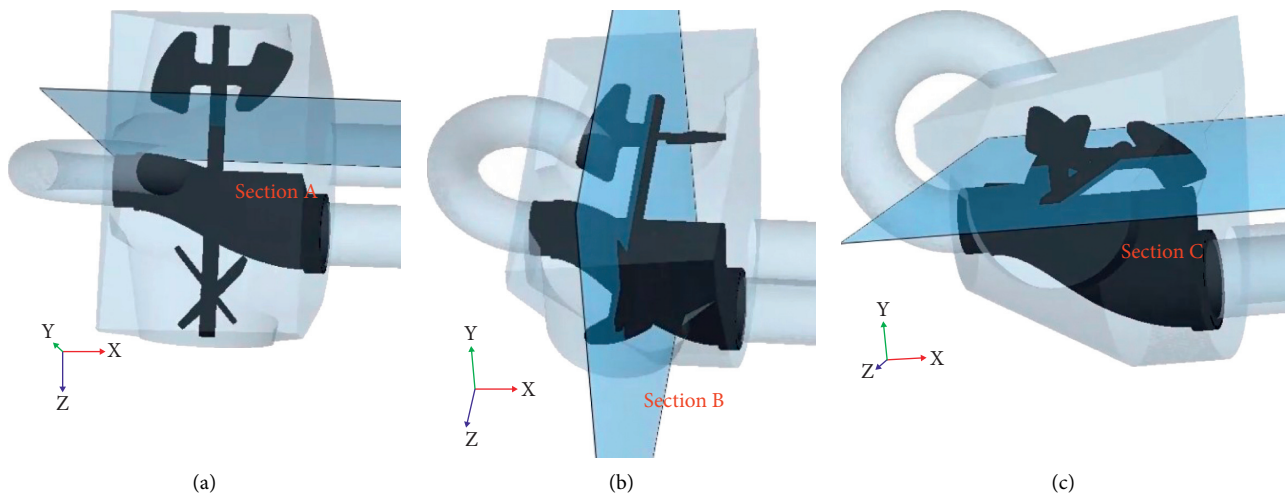


FIGURE 12: The position of sections.

stirring blade changes little. The concrete flow rate in the piston cylinder is large in the early and middle stages and is lower at the end of suction. When the S-pipe swings, the concrete flow rate in the swing area is large.

3.2. The Flow Velocity of Concrete Particles. There are 5 typical positions in the hopper, as shown in Figure 14. Position 1 is at the center of the connection between the conveying cylinder L and the hopper, which is the necessary entrance and exit to suck and push fresh concrete. Position 2 is directly below the axis of the stirring blade, which is the edge of the rotation area of the stirring blade. Position 3 is located directly above the axis of the stirring blade and close

to the shaft of the stirring blade, which is an area where the stirring blade cannot be swept. Position 4 is below the discharge end of the S-pipe, which is the area on the nonsuction side and close to the hopper wall in the hopper. Position 5 is located below the connection between the S-pipe and the conveying cylinder R , which is the suction side and near the hopper wall area in the hopper. Each position has a virtual grid for counting the concrete particle velocity, which the size is $60\text{ mm} \times 60\text{ mm} \times 60\text{ mm}$. The center coordinates of grids are shown in Table 4.

Statistics of the concrete particle velocity at 5 locations, the change of particle velocity at different locations with time, and the average particle velocity are shown in Figure 15. The change cycle of the particle velocity at position 1

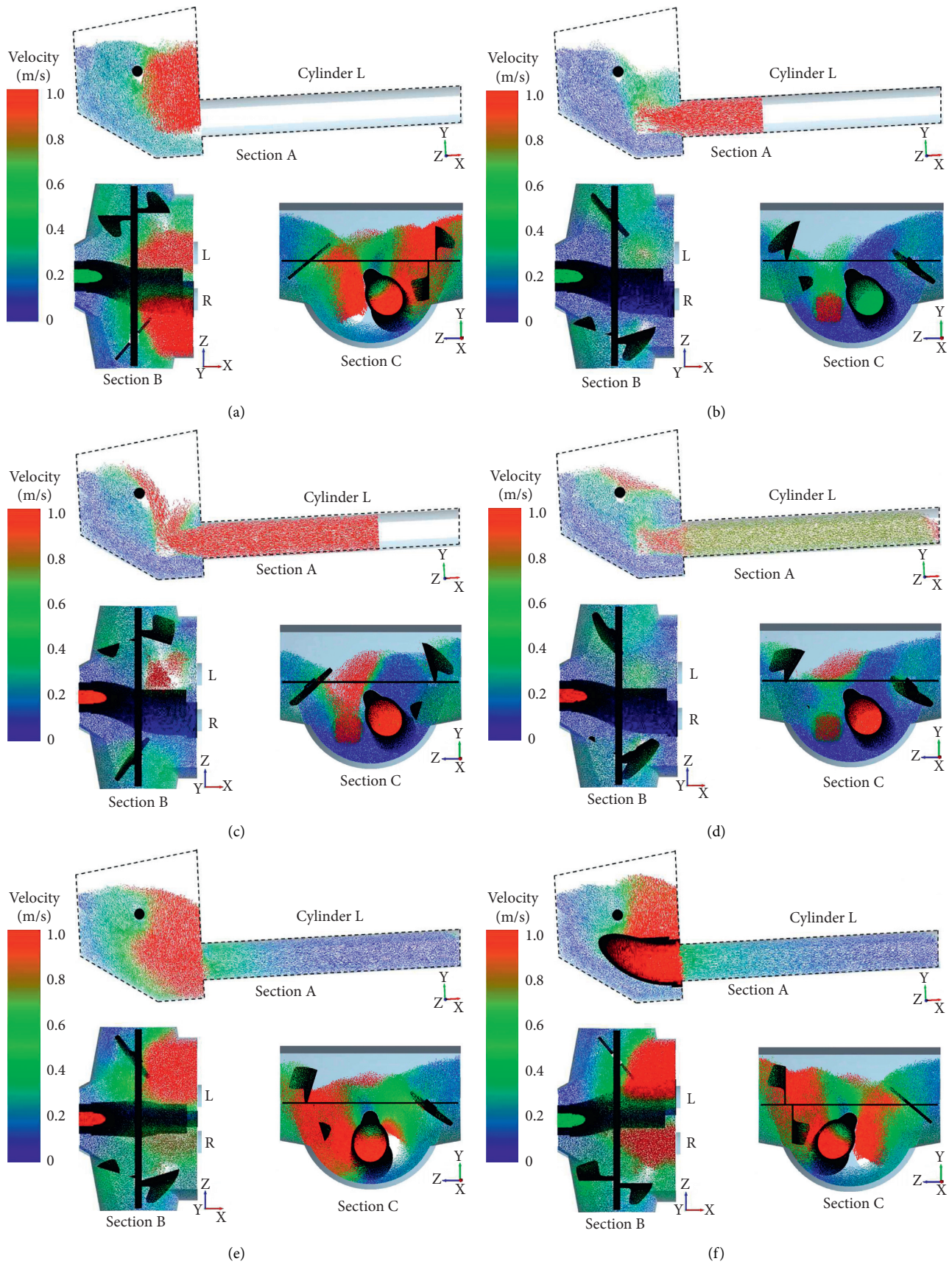


FIGURE 13: The concrete flow field of sections A, B, and C at different times: (a) $t = 5.9$ s, (b) $t = 6.4$ s, (c) $t = 7$ s, (d) $t = 7.5$ s, (e) $t = 7.6$ s, and (f) $t = 7.7$ s.

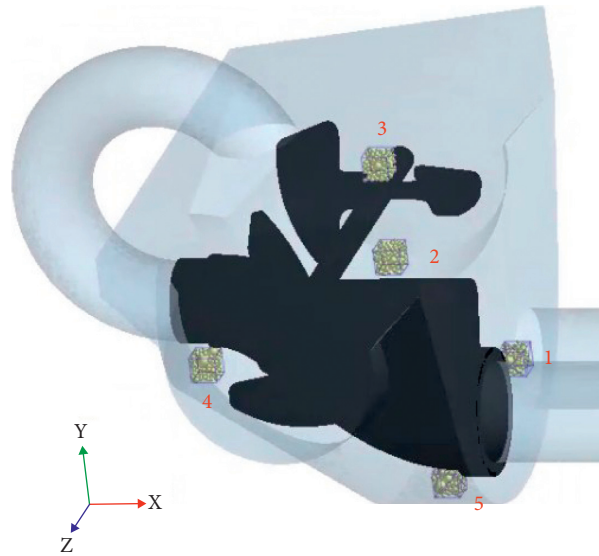


FIGURE 14: Five typical positions.

TABLE 4: The center coordinates of grids.

Position	X	Y	Z
1	347.5	-210	-147.5
2	0	-70	-400
3	0	160	-550
4	-337.5	-160	0
5	250	-380	147.5

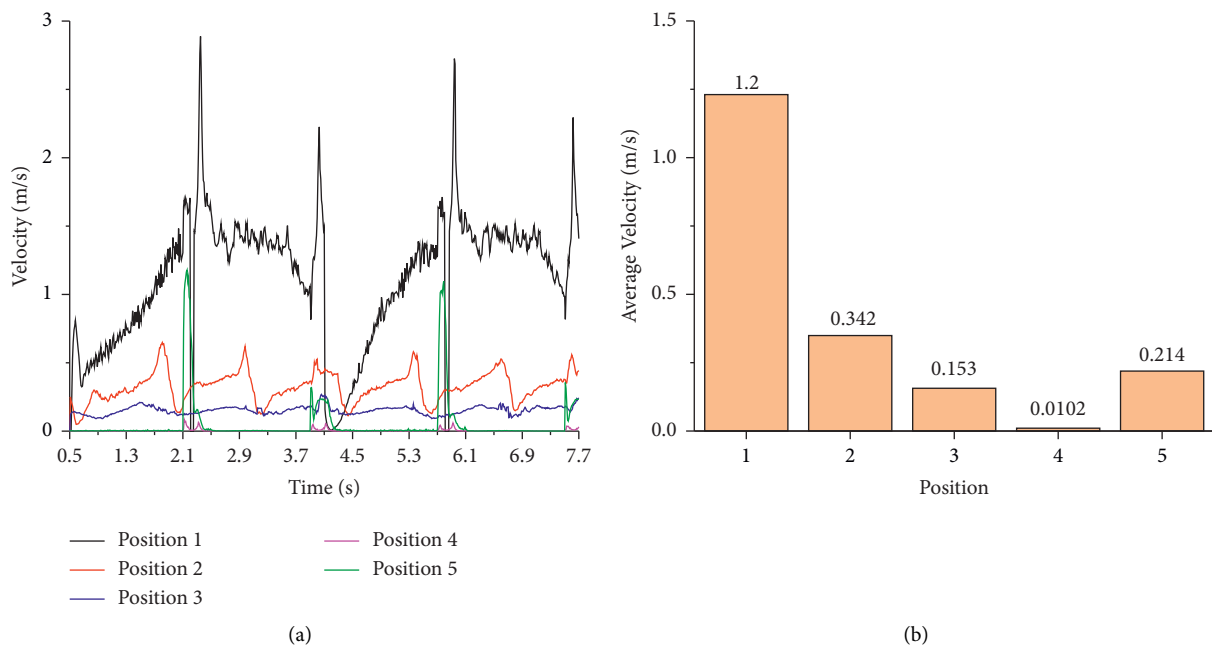


FIGURE 15: The change of particle velocity with time (a) and the average particle velocity at different locations (b).

is the same as the pumping cycle. The particle velocity fluctuates greatly during the reversing phase of the S-pipe (2.1–2.3 s, 3.9–4.1 s, 5.7–5.9 s, 7.5–7.7 s), including the maximum value. It is relatively stable in the early and

middle stages and has a slow downward trend at the end of suction. It is shown that the particle flow velocity caused by the reversal of the S-pipe is greater than that caused by the suction. The change of particle velocity in position 2 is

related to the rotation of the stirring blade, and the velocity always reaches the maximum when the stirring blade is swept. Position 3 particle velocity changes very little. The particles of position 4 and position 5 are driven only when the S-pipe is reversing, and the particle velocity can be ignored at other times. When the S tube reverses, the particle velocity of position 4 is small while that of position 5 is large. During the whole pumping process, the average particle velocity of the 5 positions is 1, 2, 5, 3, 4 in descending order.

In terms of the particle flow velocity, the particle flow caused by the reversing work of the S-pipe is the largest, followed by the particle flow caused by the suction work of the conveying cylinder, and the particle flow caused by the stirring work of the stirring blade is the smallest. The particle flow velocity near the hopper wall near the suction side is larger than that far from the suction side. The S-pipe swinging time is short, and the stirring blade has a greater auxiliary effect on the suction work in a long time.

Figure 16 is the flow trajectory of concrete particles near the stirring blade on the suction side. During the suction process, the concrete particles near the axis of the stirring blade form an obvious circulation under the continuous stirring of the stirring blade. The concrete particles near the suction port of the conveying cylinder and above the suction port of the piston cylinder in the hopper continuously flow into the conveying cylinder.

All in all, the stirring work makes the concrete particles in the hopper form an annular flow field around the stirring axis, ensuring the flow performance of the fresh concrete, and transporting concrete particles to the suction port of the conveying piston cylinder, thereby the suction of pumping system is promoted.

4. The Influence of the Stirring Blade Parameters

4.1. The Numerical Simulations. The stirring blade is composed of a stirring axis and four blades, which two blades are distributed at both ends of the axis. In the initial model of the stirring blade, the blade does not open holes, the angle between the blade plane and the axis (installation angle α) is 40° , and the stirring blade rotates at a constant speed of 25 r/min (rotation speed n) when working, as shown in Figure 17. In the following, the blade will be opened with a hole, in which the edges distance d refers to the distance between the inner and outer edges, as shown in Figure 18.

In this paper, the rotation speed n , the installation angle α , and the edges distance d of the stirring blade are considered as influencing factors that each factor is set to 4 levels. The suction efficiency η of the pumping suction process and the stirring resistance torque T_M of the stirring blade are considered as indicators to explore the influence on the suction process. The single-factor comparison scheme is designed, which included a total of 10 simulations, as shown in Table 5. Among them, only the rotation speed is changed in simulations 1, 2, 3, 4; only the installation angle is changed in simulations 2, 5, 6, 7; only the edges distance d is changed in simulations 2, 8, 9, 10.

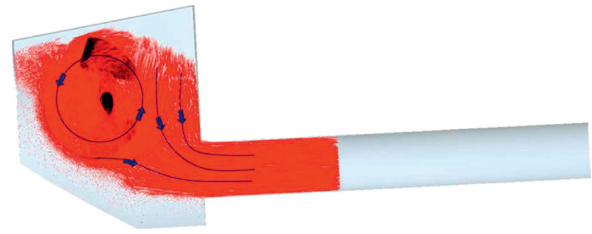


FIGURE 16: The flow trajectory of concrete. Particles near the stirring blade on the suction side.

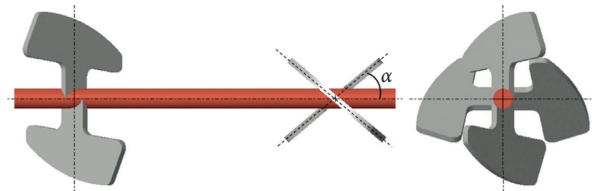


FIGURE 17: The initial model of the stirring blade.

4.2. Results of Simulations. Figure 19 is the variation of the stirring resistance torque with time from the results of simulations. The change of the resistance torque of the mixing blade T_M is periodic and the period is 1.8 s which is the sum of the single suction time and the single S-pipe reversing time. The stirring resistance torque always fluctuates greatly during the S-pipe reversing period, which reaches the peak value at the beginning, and reaches the valley value at the end. The increase and decrease of the stirring resistance torque at different rotation speeds are occurred at the different time, while the trends of stirring resistance torque with different installation angles and different edges distances are the same.

First, the influence of the rotation speed of the stirring blade on pump suction is revealed by comparing the results of simulations 1, 2, 3, and 4, as shown in Figure 20(a). As the rotation speed increases, the suction efficiency η increases and the average of stirring resistance torque \bar{T}_M increases. Second, the influence of the installation angle of the stirring blade on pump suction is revealed by comparing the results of simulations 2, 5, 6, and 7, as shown in Figure 20(b). As the installation angle a increases, the suction efficiency is almost unchanged and the average of stirring resistance torque decreases. Third, the influence of the edges distance d of the stirring blade on pump suction is revealed by comparing the results of simulations 2, 8, 9, and 10, as shown in Figure 20(c). Compared with the base blade, the suction efficiencies of three perforated blades are slightly reduced, and they are almost the same. In addition, the average stirring resistance torque of the perforated blades is greatly reduced. As the edges distance decreases, the opening area increases, and the average of stirring resistance torque decreases.

The rotation speed has a great influence on the suction efficiency, while the installation angle and the edges distance have almost no influence on the suction efficiency. Moreover, with the increase of the rotation speed, installation

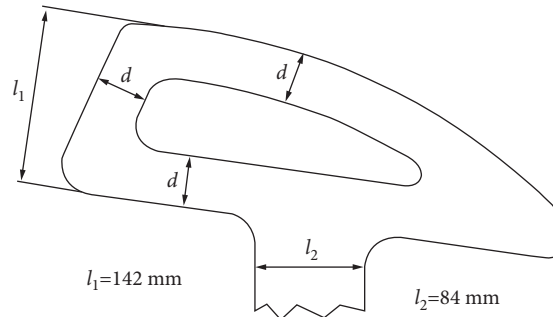


FIGURE 18: The blade with a hole.

TABLE 5: The single-factor comparison scheme.

No.	Edge distance d (mm)	Installation angle α ($^\circ$)	Rotation speed n (r/min)
1	—	40	20
2	—	40	25
3	—	40	30
4	—	40	35
5	—	35	25
6	—	45	25
7	—	50	25
8	50	40	25
9	40	40	25
10	30	40	25

“—” means that the mixing blade does not perforate.

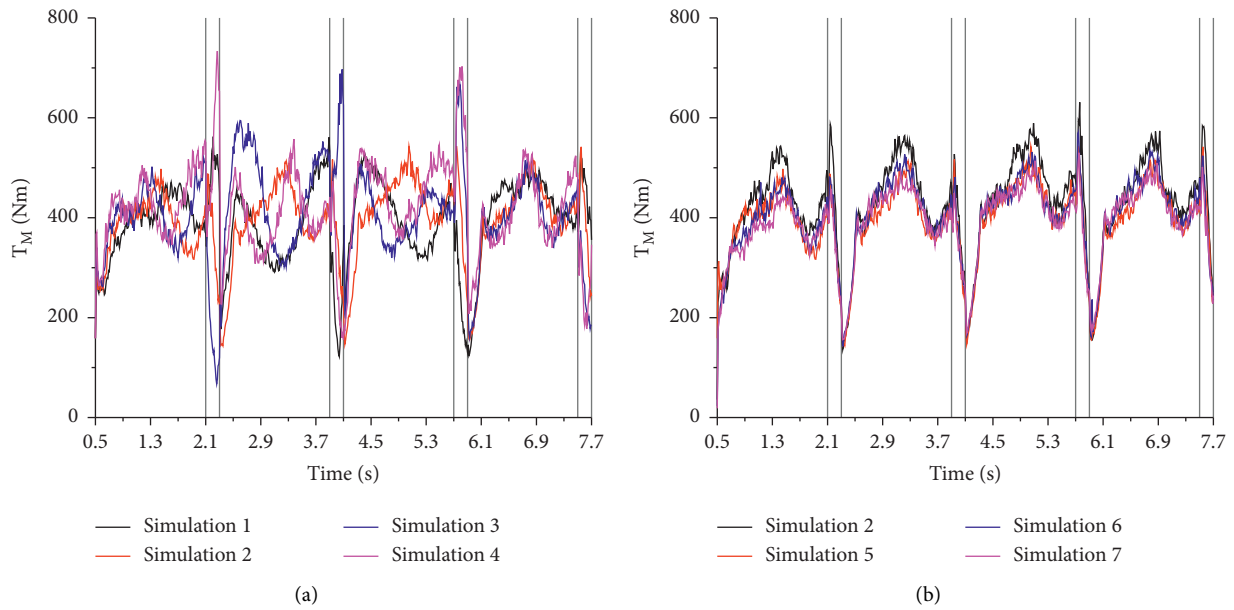


FIGURE 19: Continued.

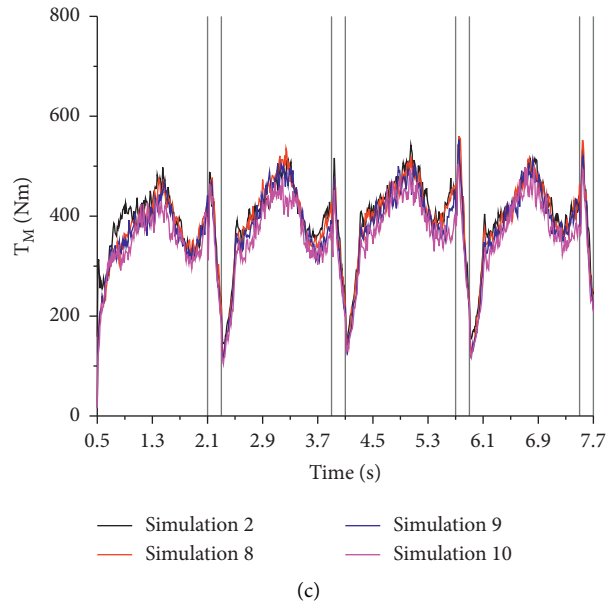


FIGURE 19: The variation of the stirring resistance torque with time.

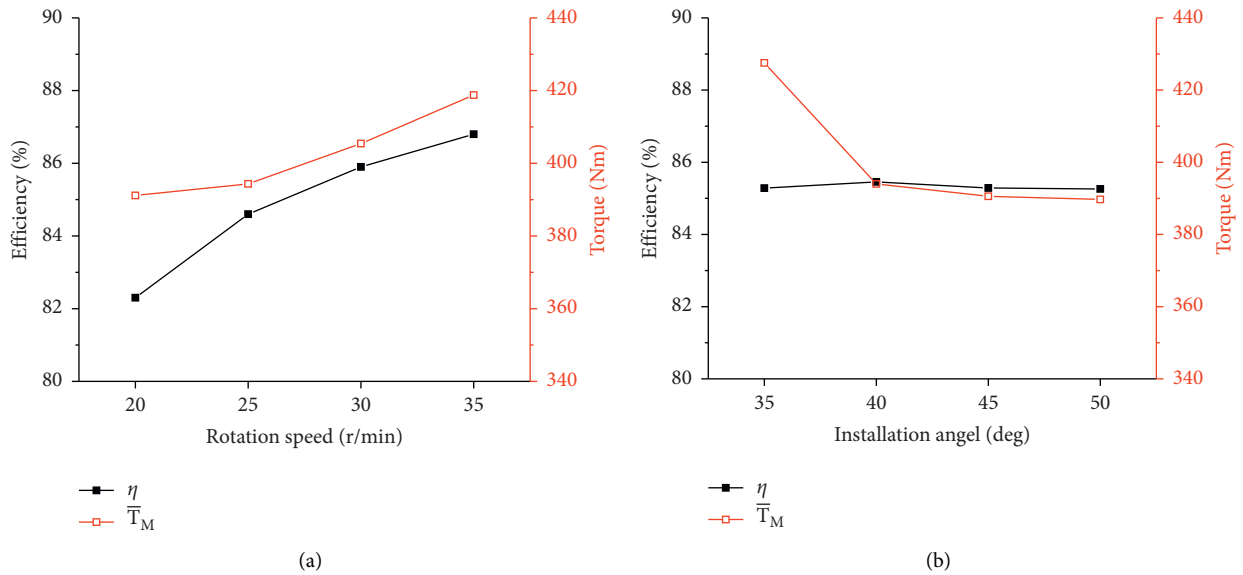


FIGURE 20: Continued.

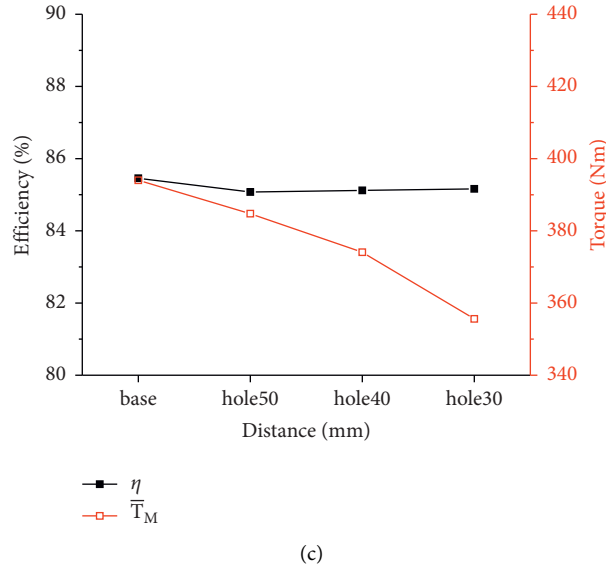


FIGURE 20: The influence of the rotation speed (a), installation angle (b), and edge distance (c) of the stirring blade on the pump suction.

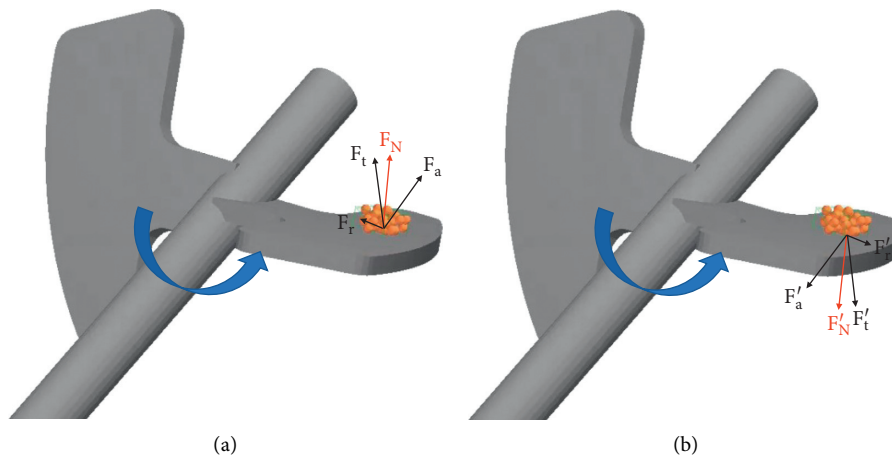


FIGURE 21: The force analysis of the concrete particles' unit (a) and the blade unit (b).

angle, and edges distance, the stirring resistance torque of the stirring blade increases.

4.3. The Influence Mechanism of the Stirring Blade Parameters.

The interaction between the stirring blade and the concrete particles is mainly generated the point where they directly collide with each other. Concrete particles in direct collision with stirring blades are divided into many particle units. Through the force analysis of any one of the concrete particle units, this unit is mainly driven by the normal force F_N of the blade. Correspondingly, the stirring blade unit is mainly subjected to the resisting force F_N' of concrete particles, which is opposite to the normal force F_N of the blade, as shown in Figure 21. The resisting force F_N' is decomposed into the radial force F_r' pointing to the stirring axis, the axial force F_a' parallel to the stirring axis, and the tangential force F_t' tangent to the rotation direction of the stirring axis. The

relationship between tangential force F_t' and resisting force F_N' is shown in formula (7). The radial force and axial force are parallel to the rotation direction of the stirring blade, which does not hinder the rotation of the stirring blade. The stirring resistance torque is mainly the synthesis of the torque of the tangential force of each stirring blade unit to the stirring blade axis. Therefore, the stirring resistance torque mainly comes from the tangential force.

$$F_t' = F_N' \cos \alpha. \tag{7}$$

Changing the rotation speed is mainly to change the resisting force. With the increase of rotation speed, the resisting force increases, so the stirring resistance torque increases. The installation angle is changed, and the tangential force changes accordingly, as shown in formula (7). The larger the installation angle α , the smaller the tangential force and the smaller the stirring resistance torque. When

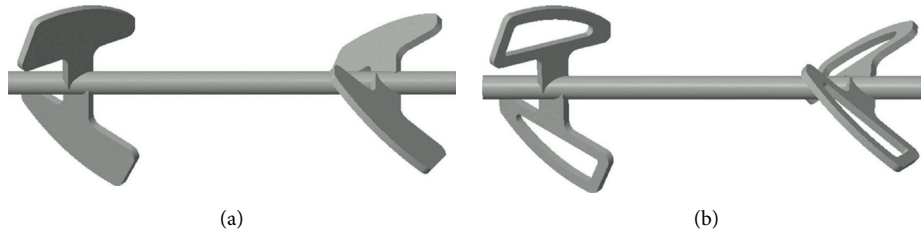


FIGURE 22: The (a) initial stirring blade and (b) optimized stirring blade.

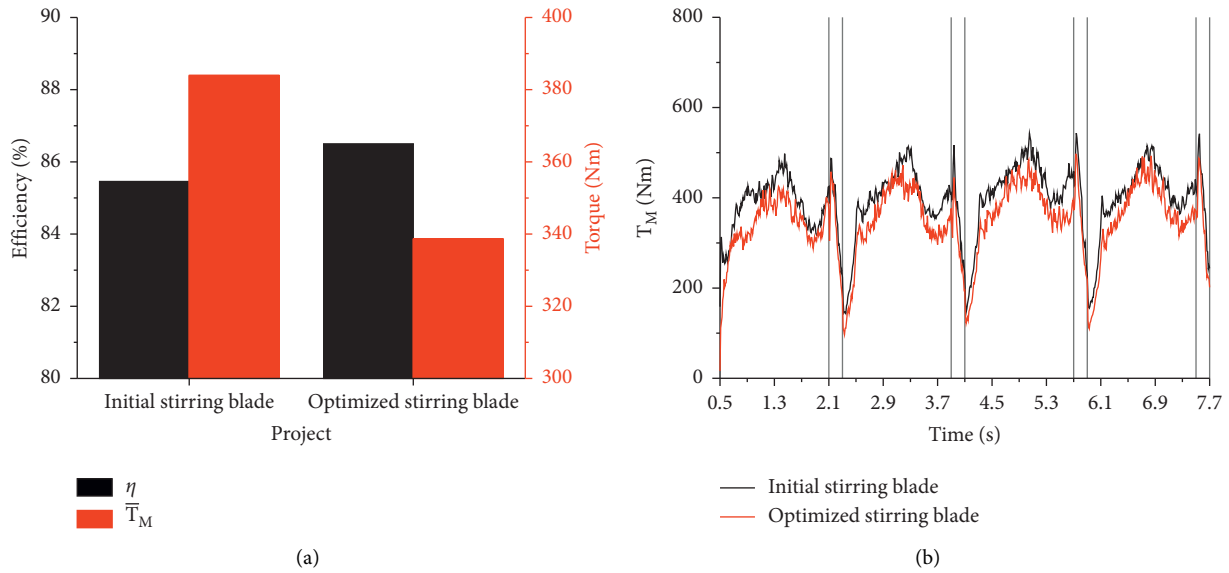


FIGURE 23: The simulation results of the initial stirring blade and the optimized stirring blade.

the stirring blade is opened a hole, the area of the stirring blade is changed with the edges distance d . With the decrease of the edges distance, the area of the blade decreases, and the units of the stirring blade decreases, so the stirring resistance torque decreases. These rules are consistent with the simulation results.

5. Optimization

In order to reduce the stirring energy consumption of the stirring blade without reducing the suction efficiency, the structure of the initial stirring blade is optimized. The installation angle is improved from 40° to 50° and the blade is opened with a hole which the edges distance is 30 mm, as shown in Figure 22.

The pumping suction with the optimized stirring blade is simulated compared with the initial stirring blade. The simulation results are shown in Figure 23. After optimization, the trend of the stirring resistance torque is unchanged, the suction efficiency is increased by 1.22%, and the stirring resistance torque of the mixing blade is reduced by 11.8%. It is consistent with the expectation which reduces the stirring energy consumption of the stirring blade without reducing the suction efficiency.

6. Conclusions

The DEM model of fresh concrete was established. The gap between experiments and simulations results of slump flow tests and L-box tests was less than 5%, so the feasibility of simulating the flow behavior and rheological properties of the fresh concrete was proved.

The geometric structure of pumping system was simplified. The suction force of the conveying cylinder was customized by the API function of DEM to realize the suction work. The difference of suction efficiency in experiments and simulations was less than 0.1%. Therefore, the numerical simulation of the suction process was completed and feasible.

The concrete particles flow during the suction process was further studied. In terms of the particle flow velocity, the particle flow caused by the reversing work of the S-pipe was the largest, followed by the particle flow caused by the suction work of the conveying cylinder, and the particle flow caused by the stirring work of the stirring blade was the smallest. The stirring blade made the concrete particles in the hopper form an annular flow field around the stirring axis, so the suction of pumping system was promoted.

In addition, the influence of the stirring blade was explored. The rotation speed had a great influence on the

suction efficiency, while the installation angle and the edges distance had almost no influence on the suction efficiency. Moreover, with the increase of the rotation speed, installation angle, and edges distance, the stirring resistance torque of the stirring blade increased.

An optimized stirring blade was established and compared with the initial stirring blade. After optimization, the suction efficiency was increased by 1.22%, and the stirring resistance torque of the mixing blade was reduced by 11.8%. The stirring energy consumption of the stirring blade was reduced without the suction efficiency reduced.

Data Availability

The data used to support the findings of this study are available from the corresponding author upon request.

Conflicts of Interest

The authors declare that they have no conflicts of interest.

Acknowledgments

This work was supported by the Natural Science Foundation of Hunan Province (2021JJ20009, 2020JJ5541, 2020JJ5538, 2019GK4025, and 2019JJ20015) and the NSFC projects of China (52075465 and 11772135). The authors are grateful for the financial support for this research.

References

- [1] Y. Wu, W. Li, and Y. Liu, "Fatigue life prediction for boom structure of concrete pump truck," *Engineering Failure Analysis*, vol. 60, pp. 176–187, 2016.
- [2] S.-J. Lee, I.-S. Chung, and S.-Y. Bae, "Structural design and analysis of CFRP boom for concrete pump truck," *Modern Physics Letters B*, vol. 33, no. 14n15, Article ID 1940033, 2019.
- [3] A. L. Wang, Z. Q. Shi, C. X. Yuan, and Y. Q. Hu, "Optimal design of concrete pumping displacement control," *Advanced Materials Research*, vol. 1586, pp. 238–242, 2012.
- [4] N. Roussel, M. R. Geiker, F. Dufour, L. N. Thrane, and P. Szabo, "Computational modeling of concrete flow: general overview," *Cement and Concrete Research*, vol. 37, no. 9, pp. 1298–1307, 2007.
- [5] M. Cremonesi, L. Ferrara, A. Frangi, and U. Perego, "Simulation of the flow of fresh cement suspensions by a Lagrangian finite element approach," *Journal of Non-newtonian Fluid Mechanics*, vol. 165, no. 23, pp. 1555–1563, 2010.
- [6] S. Tichko, J. Van De Maele, N. Vanmassenhove et al., "Numerical simulation of formwork pressure while pumping self-compacting concrete bottom-up," *Engineering Structures*, vol. 70, pp. 218–233, 2014.
- [7] E. Secrieru, W. Mohamed, S. Fataei, and V. Mechtcherine, "Assessment and prediction of concrete flow and pumping pressure in pipeline," *Cement and Concrete Composites*, vol. 107, Article ID 103495, 2020.
- [8] H. Hoornahad and E. A. B. Koenders, "Simulating macroscopic behavior of self-compacting mixtures with DEM," *Cement and Concrete Composites*, vol. 54, pp. 80–88, 2014.
- [9] V. Mechtcherine and S. Shyshko, "Simulating the behaviour of fresh concrete with the Distinct Element Method - d," *Cement and Concrete Composites*, vol. 55, pp. 81–90, 2015.
- [10] H. Ji, J. Caiyun, L. Yue et al., "Simulation of motion behavior of concrete in pump pipe by DEM," *Advances in Civil Engineering*, vol. 2021, Article ID 3750589, 16 pages, 2021.
- [11] G. Lu, K. Wang, and T. J. Rudolph, "Modeling rheological behavior of highly flowable mortar using concepts of particle and fluid mechanics," *Cement and Concrete Composites*, vol. 30, no. 1, pp. 1–12, 2007.
- [12] Y. Tan, H. Zhang, D. Yang, S. Jiang, J. Song, and Y. Sheng, "Numerical simulation of concrete pumping process and investigation of wear mechanism of the piping wall," *Tribology International*, vol. 46, no. 1, pp. 137–144, 2011.
- [13] M. S. Choi, Y. J. Kim, and J. K. Kim, "Prediction of concrete pumping using various rheological models," *International Journal of Concrete Structures and Materials*, vol. 8, no. 4, pp. 269–278, 2014.
- [14] M. Choi, N. Roussel, Y. Kim, and J. Kim, "Lubrication layer properties during concrete pumping," *Cement and Concrete Research*, vol. 45, pp. 69–78, 2013.
- [15] Y. Zhan, J. Gong, Y. Huang, C. Shi, Z. Zuo, and Y. Chen, "Numerical study on concrete pumping behavior via local flow simulation with discrete element method," *Materials*, vol. 12, no. 9, 2019.
- [16] J. Shengqiang, C. Xiaodong, C. Guodong et al., "Optimization of fresh concrete pumping pressure loss with CFD-DEM approach," *Construction and Building Materials*, vol. 276, 2021.
- [17] M. Liu, L. Tan, and S. Cao, "Theoretical model of energy performance prediction and BEP determination for centrifugal pump as turbine," *Energy*, vol. 172, 2019.
- [18] M. Liu, L. Tan, Y. Xu, and S. Cao, "Optimization design method of multi-stage multiphase pump based on Oseen vortex," *Journal of Petroleum Science and Engineering*, vol. 184, no. C, 2020.
- [19] X. Wenyang and T. Lei, "Design method of controllable velocity moment and optimization of pressure fluctuation suppression for a multiphase pump," *Ocean Engineering*, vol. 220, 2020 (prepublish).
- [20] M. Liu, L. Tan, and S. Cao, "Influence of geometry of inlet guide vanes on pressure fluctuations of a centrifugal pump," *Journal of Fluids Engineering*, vol. 140, 2018.
- [21] K. L. Johnson, K. Kendall, and A. D. Roberts, "Surface energy and the contact of elastic solids," *Proceedings of the Royal Society of London - Series A: Mathematical and Physical Sciences*, vol. 324, no. 1558, pp. 301–313, 1971.

Research Article

Numerical Simulation Research on Cutting Rock with a PDC Cutter Assisted by an Impact Force

Yong Wang , Hongjian Ni , Ruihe Wang, Bin Huang, Shubin Liu, and Heng Zhang

School of Petroleum Engineering, China University of Petroleum (East China), Qingdao 266580, China

Correspondence should be addressed to Hongjian Ni; nhj_upc@126.com

Received 29 October 2021; Revised 13 December 2021; Accepted 17 December 2021; Published 7 January 2022

Academic Editor: Guoming Liu

Copyright © 2022 Yong Wang et al. This is an open access article distributed under the Creative Commons Attribution License, which permits unrestricted use, distribution, and reproduction in any medium, provided the original work is properly cited.

Extensive studies have been carried out on cutting rock with a PDC cutter, but cutting rock assisted by impact force is rarely studied. In this paper, cutting rock using conical and cylindrical PDC cutters assisted by impact force were researched with the explicit dynamic model. The laws of cutting rock using a cylindrical cutter assisted by impact force are the same as those of a conical cutter. There are thresholds of impact frequency and amplitude when they are single variables. When impact frequency is lower than the threshold frequency, the impact frequency is the dominant frequency in the frequency spectrum of weight on bit (WOB), and the amplitude of dominant frequency and removal volume decreases with the increase of impact frequency. When the impact frequency is higher than the threshold frequency, there is no dominant frequency in the frequency spectrum of WOB, and the removal volume behaves the same. When the impact force is lower than the threshold amplitude, there is no dominant frequency in the frequency spectrum of WOB, and it does not affect the removal volume but the removal volume is positively correlated with the impact amplitude. When the impact amplitude is higher than the threshold amplitude, the removal volume is also positively correlated with the impact amplitude, and the removal volume assisted by low-frequency (20 Hz and 40 Hz) impact force is higher. The frequency threshold and amplitude threshold of the conical cutter are smaller than those of the cylindrical cutter. Although the cutting depth and removal volume of the conical cutter are lower than those of the cylindrical cutter, the amplifications of cutting depth and removal volume of the conical cutter are higher than those of the cylindrical cutter when assisted by impact force.

1. Introduction

In the process of oil and gas exploration, there are some problems such as low rate of penetration (ROP), short pure drilling time and long drilling cycle in hard rock, and abrasive formation with poor drillability. In view of the above problems, many indoor tests and field applications of a conical PDC cutter have been carried out, and good results have been achieved [1–5].

Durrand et al. [6] first carried out the research on the conical PDC cutter. The indoor test results show that the conical cutter has better friction resistance, impact resistance, and heat resistance than the cylindrical cutter. Field tests show that it is more suitable for hard rock with high WOB, larger rock debris, and lower crushing specific energy. Sun and Zou [7] have carried out laboratory experiments on

the conical cutter. They found that when the inclination angle is 20–25°, the cutting force and specific energy are the minimum, and the crushing efficiency is at the highest. Azar et al. and German et al. [3, 8] applied the hybrid bit in high hardness carbonate rock formation, the footage increased by 29%–190%, the ROP increased by 62%–157%, and the weight on bit decreased by 26%. Conical bit and hybrid bit have great potential and application prospects in prolonging bit life and improving ROP.

Impact force can restrain downhole vibration and improve bit life. Wang and Lehnhoff [9] used the finite element method to simulate the cutting formation process in the two-dimensional rock cutting process. The material nonlinearity and geometric nonlinearity of rock are considered in the model. Han et al. [10] used the Mohr–Coulomb model to simulate the rock failure process assisted by the impact force,

and the failure forms mainly include compression failure caused by stress wave, tensile failure caused by stress wave reflection, and fatigue failure caused by stress cyclic loading. Zhao et al. [11] obtained the relationship between the length of the intermediate crack, lateral crack, and radial crack and the amplitude of load and the impact velocity of load by studying the experiment of indenter pressing into rock. Zhao et al. [12] studied the characteristics of rock intrusion with a single cutter by rock breaking theory and experiment. Their results show that the increase of static pressure and impact energy can improve the cutting force and increase the rock removal volume. A certain preload can reduce the fracture toughness and hardness of the rock material and increase the crushing volume of rock. Increasing the impact frequency and reducing the impact distance can greatly improve the cutting depth in brittle and hard rock.

There are extensive research studies and applications of the impact force on the cylindrical PDC cutter [13–19]. There are also some experiments and field applications of the conical cutter [7, 20], but there is no research on the conical cutter and the cylindrical cutter cutting rock assisted by the impact force. Therefore, the research on the cutting rock law of conical and cylindrical cutters assisted by the impact force is beneficial to expand the application of the conical PDC cutter and further improve drilling efficiency. In this paper, based on the explicit dynamic method, the effect of the impact force on the conical cutter and cylindrical cutter cutting rock is studied with the Holmquist–Johnson–Cook model.

2. Holmquist–Johnson–Cook Model

In the case of high strain, high strain rate, and high pressure, Holmquist et al. [21] proposed the Holmquist–Johnson–Cook (HJC) model, and the equivalent strength equation of the model includes hydrostatic pressure, strain rate, and damage. The model is divided into three

parts: the strength model, the damage model, and the constitutive model.

2.1. Strength Model. The strength model is described as follows:

$$\sigma^* = [A(1 - D) + BP^{*N}] (1 + C \ln \dot{\epsilon}^*), \quad (1)$$

where the standard equivalent stress $\sigma^* = \sigma/f'_C$ and $\sigma^* < S_{\max}$, σ is the actual equivalent stress, f'_C is the quasistatic uniaxial compressive strength, and S_{\max} is the upper limit of standard equivalent stress; D is the damage ($0 \leq D \leq 1$); $P^* = P/f'_C$ is the standard pressure (P is the actual pressure); $\dot{\epsilon}^* = \dot{\epsilon}/\dot{\epsilon}_0$ is the dimensionless strain rate ($\dot{\epsilon}$ is the actual strain rate, and $\dot{\epsilon}_0 = 1S^{-1}$ is the reference strain rate); C is the strain rate coefficient; A is the standard viscosity coefficient; B is the standard pressure hardening coefficient; and N is the pressure hardening index.

2.2. Damage Model. The damage model is expressed as follows:

$$D = \sum \frac{\Delta \epsilon_p + \Delta \mu_p}{\epsilon_p^f + \mu_p^f}, \quad (2)$$

where $\epsilon_p^f + \mu_p^f = D_1 (P^* + T^*)^{D_2} \geq EF_{\min}$, D_1 and D_2 are the constants, $T^* = T/f'_C$, T is the maximum hydrostatic pressure that the material can withstand, and EF_{\min} is the plastic strain limit of the material failure. The damage is accumulated by an equivalent strain, which includes the equivalent plastic strain $\Delta \epsilon_p$ and the plastic volume strain $\Delta \mu_p$.

2.3. Constitutive Model. The constitutive model can be divided into three stages: linear elastic stage (equation (3)), transitional stage (equation (4)), and compaction stage (equation (5)).

$$P = K\mu (-T(1 - D) \leq P \leq P_{\text{crush}}), \quad (3)$$

$$\begin{cases} P = \frac{(\mu - \mu_{\text{crush}})(P_1 - P_{\text{crush}})}{(\mu_p - \mu_c)} + P_{\text{crush}} \text{ (uploading)} \\ P = P_0 - [(1 - F)K + FK_{\text{lock}}](\mu_0 - \mu) \text{ (unloading)} \end{cases} \quad (P_{\text{crush}} \leq P \leq P_{\text{lock}}), \quad (4)$$

$$\begin{cases} P = K_1 \bar{\mu} + K_2 \bar{\mu}^2 + K_3 \bar{\mu}^3 \text{ (uploading)} \\ P = K_1 \bar{\mu} \text{ (unloading)} \\ \bar{\mu} = \frac{\mu - \mu_{\text{lock}}}{1 + \mu_{\text{lock}}} \end{cases} \quad (P_{\text{lock}} < P). \quad (5)$$

In the linear elastic stage, P_{Crush} and μ_{crush} are the corresponding stress and volume strain in the uniaxial compression stress experiment.

In the transitional stage, the pores in the material are gradually squeezed out, resulting in plastic volumetric strain. In this stage, the unloading curve is different from the

loading curve, and it will follow the interpolation path of the adjacent region.

In the compaction stage, the pores are completely extruded. Therefore, the standard volume strain rate μ can be calculated from the current density ρ and the initial density ρ_0 , $\mu = \rho/\rho_0 - 1$. The constants (K_1 , K_2 , and K_3) are the material constants without porosity. The locked volume strain rate μ_{lock} can be calculated from the particle density ρ_{grain} of the material, $\mu_{lock} = \rho_{grain}/\rho_0 - 1$.

3. Numerical Model

The cutting rock process of the conical cutter is simulated in this paper, and the effect of the impact force on the cutting process is studied. In simulations, assumptions are as follows: (1) the material of the cutter is rigid; (2) the rotary motion of the PDC cutter is simplified to a linear motion; and (3) the rock material has no initial confining pressure and initial damage. To improve the calculation speed, the symmetrical plane boundary condition is used to halve the model. The width, length, and height of the rock sample are 15 mm, 70 mm, and 20 mm, respectively. We use the hexahedral mesh for the rock sample, as shown in Figure 1. A fine mesh with an average element size of 0.20 mm is used for the top 10 mm of the sample, while a course with an average element size of 1 mm is used for the bottom 10 mm of the sample. The above physical model is meshes as shown in Figure 1, in which the cutter is a rigid material, and the rock material is the HJC model. The model parameters are listed in Table 1. To simulate the influence of bit inertia on the rock breaking process, the average value of bit mass on a single tooth is applied to a cutting tooth, which is 5 kg.

The diameter of the conical cutter is 13 mm, and the apex angle is 75°. The radius of the cone tip is 2 mm. The diameter of the cylindrical cutter is 13 mm, and the radius of the chamfered corner is 0.5 mm. The geometric dimensioning of the cutter is shown in Figure 2, where w is the WOB and v is the cutting speed.

4. Simulation Results and Analysis

Due to the influence of bit inertia and bit rock contact stiffness, the impact force exerted on the bit cannot be directly transmitted to the bit rock contact surface. Therefore, the frequency and amplitude of the impact force are the important factors affecting the rock-breaking efficiency. To express the axial impact force, the WOB equation can be expressed as follows: where k is the impact frequency, p is the impact amplitude, and w_0 is the static value of WOB. The conical cutter and the cylindrical cutter were firstly used to simulate the process of cutting rock assisted by the impact force. The static WOB is 900 N, the cutting speed is 0.8 m/s, the impact frequency is 20 Hz, and the impact amplitude is 1000 N. The equivalent stress cloud is shown in Figure 3, in which the PDC cutter is hidden. The unit of stress in the figure is MPa. The rock stress decay direction with the cylindrical tooth is perpendicular to the cutting tooth surface, and the maximum stress appears on the contact surface between the cylindrical cutter and rock. The equivalent stress of rock cutting by the

conical tooth is mainly affected by the spherical cone, the attenuation direction is inclined downward, and the maximum stress only appears in the contact area between the spherical cone tip and rock. The equivalent stress of rock cutting by the conical cutter is mainly affected by the spherical cone tip; the stress decay direction is perpendicular to the sphere of the cone; the maximum stress of rock only appears in the contact area with the spherical cone.

$$w = w_0 + p(1 + \sin 2 k\pi t), \quad (6)$$

4.1. Influence of Impact Frequency. This section studies the influence of frequency of the impact force on rock cutting by the conical cutter and the cylindrical cutter. The impact amplitude is set to 1000 N.

Figure 4 shows the effect of frequency of impact forces on the WOB frequency spectrum. In the WOB frequency spectrum of the cylindrical cutter, there is no significant dominant frequency when there is no impact. The dominant frequencies of WOB are 20 Hz and 40 Hz and the amplitudes are 620 N and 600 N when the frequencies of the impact force are 20 Hz and 40 Hz, respectively. But there is no main frequency when the impact frequency reaches or even exceeds 60 Hz. In the WOB frequency spectrum of the conical cutter, there is no significant dominant frequency when there is no impact. The dominant frequencies of WOB are 20 Hz and 40 Hz and the amplitudes are 680 N, 640 N, and 420 N, respectively, when the frequencies of the impact force are 20 Hz, 40 Hz, and 60 Hz. But there is no main frequency when the impact frequency reaches or even exceeds 60 Hz. The comparison shows that the impact force has a more significant effect on the main frequency of the conical cutter. The impact at the dominant frequency will inevitably affect the WOB on the cutter.

Figure 5 shows the effect of the impact force frequency on the average WOB. When the impact frequency is 20 Hz, the average WOB on the cylindrical cutter increases by 102% compared with that without impact, and the average WOB on the conical cutter increases by 82%. As the impact frequency increases, the average WOB decreases rapidly. When frequencies are higher than 60 Hz, the average WOB on the cylindrical cutter and that on the conical cutter are almost the same, increasing by 70% compared with those without the impact. Impact force has a greater impact on the dominant frequency of the conical cutter, resulting in a higher average WOB on the conical cutter.

Impact force affects the WOB and will inevitably affect the cutting depth. Figure 6 shows the cutting depth-time curves of the cylindrical cutter and conical cutter at different impact frequencies. When there is no impact, the cutting depth of the cylindrical cutter is more stable than the conical cutter. When the impact frequency is 20 Hz and 40 Hz, the fluctuation of the cutting depth of the cylindrical cutter is very large, and the maximum value is 2 mm. When the impact frequency is not less than 60 Hz, the cutting depth of the cylindrical cutter is relatively stable, but it has a significant increase compared with that without impact.

When there is no impact, the cutting depth of the conical cutter fluctuates greatly. When impact frequency is 20 Hz, the

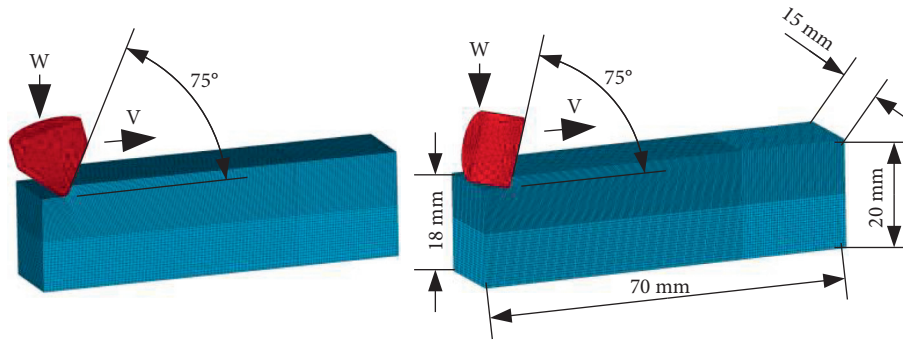


FIGURE 1: Finite element model of cutting rock.

TABLE 1: Parameters of the finite element model.

Parameter/unit	Value
A	0.79
B	1.6
N	0.61
C	0.007
f_c'/GPa	0.048
S_{max}	7
D_1	0.04
D_2	1
EF_{min}	0.01
P_{crush}/GPa	0.016
μ_{crush}	0.001
K_1/GPa	85
K_2/GPa	-171
K_3/GPa	208
μ_{lock}	0.1
P_{lock}/GPa	0.8
T/GPa	0.004
G/GPa	14.86
$\rho/kg/m^3$	2440
$J/Kg\cdot K$	654

A : standard viscosity coefficient; B : standard pressure hardening coefficient; N : pressure hardening index; C : strain rate coefficient; f_c' : quasi-static uniaxial compressive strength; S_{max} : the upper limit of standard equivalent stress; D_1 : constant; D_2 : constant; EF_{min} : plastic strain limit of material failure; P_{crush} : stress in the uniaxial compression stress experiment; μ_{crush} : volume strain in the uniaxial compression stress experiment; K_1 , K_2 , and K_3 : material constant without porosity; μ_{lock} : locked volume strain rate; P_{lock} : locked stress; T : the maximum hydrostatic pressure that the material can withstand; G : the shear modulus; ρ : density of rock; and J : specific heat capacity.

cutting depth fluctuation increases rapidly. When the impact frequency increases to 40 Hz, the fluctuation of cutting depth is 1.5 mm. When the impact frequency exceeds 40 Hz, the cutting depth fluctuation decreases. The fluctuation of cutting depth of the cylindrical teeth is larger, but the curve of the conical cutter is smoother.

Figure 7 shows the average cutting depth and removal volume of the cylindrical cutter and the conical cutter at different impact frequencies. For the cylindrical cutter, the average cutting depth without impact is 1.57 mm and the removal volume is 0.563 g. When the impact frequency is 20 Hz, the average cutting depth is 3.2 mm and the removal volume is 1.48 g, which increase by 105% and 162%, respectively. When the impact frequency increases to 60 Hz, the average cutting depth and removal volume decrease to 2.8 mm and 1.28 g,

respectively. When the impact frequency reaches 60 Hz, the average cutting depth and removal volume are 2.7 mm and 1.2 g, respectively.

For the conical cutter, the average cutting depth is 1.7 mm and the removal volume is 0.28 g when there is no impact force. When the impact frequency is 20 Hz, the average cutting depth and removal volume are 2.8 mm and 0.61 g, respectively, increasing by 64% and 117%. When the impact frequency increases to 40 Hz, the average cutting depth and removal volume decrease to 2.5 mm and 0.53 g. When the impact frequency is 60 Hz, the average cutting depth and removal volume are 2.46 mm and 0.5 g, respectively, which increase by 44% and 78% compared with those without the impact force. The impact frequency continues to increase, while the average cutting depth and removal volume remain unchanged.

Therefore, when the amplitude of the impact force is given, there is an upper threshold for the impact frequency. In this paper, the frequency threshold of the cylindrical cutter and the conical cutter is 60 Hz. The impact force has two components: the fluctuation component and the mean component of the impact force. The mean component increases the average WOB, and the fluctuation component leads to the impact fragmentation of rock. The fluctuation component of the impact force acts on cutting teeth and rock, and the inertia of cutter also occupies a part of the fluctuation component. The higher the frequency is, the more fluctuation component occupied by the inertia of cutter. Impact fragmentation of rock occurs only when the fluctuation component applied to the rock is greater than a certain value. When the impact amplitude is constant and the frequency increases, the fluctuation component of the impact force becomes smaller, and the fluctuation component occupied by the inertia of cutter increases. It results in a lower fluctuation component acting on the rock. With the increase of frequency, the impact fragmentation will disappear when the impact component on rock decreases to a certain value.

4.2. Influence of Impact Amplitude. To study the effect of impact amplitude on the rock breaking process of high and low-frequency impact forces, the rock breaking process of impact forces at 20 Hz and 100 Hz with different impact amplitudes was simulated.

Figure 8 shows the effect of the impact amplitude on the WOB frequency spectrum. When the cylindrical cutter is assisted by the impact force at 20 Hz, there is no dominant

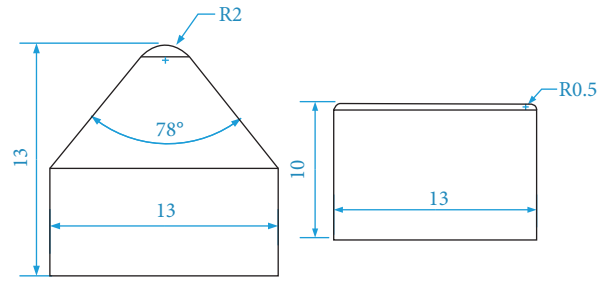


FIGURE 2: The geometric dimensioning of the cutter.

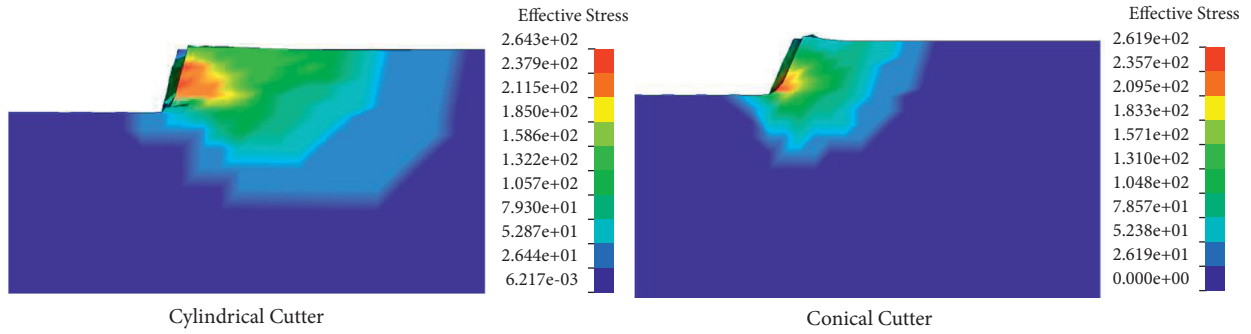


FIGURE 3: Equivalent stress cloud.

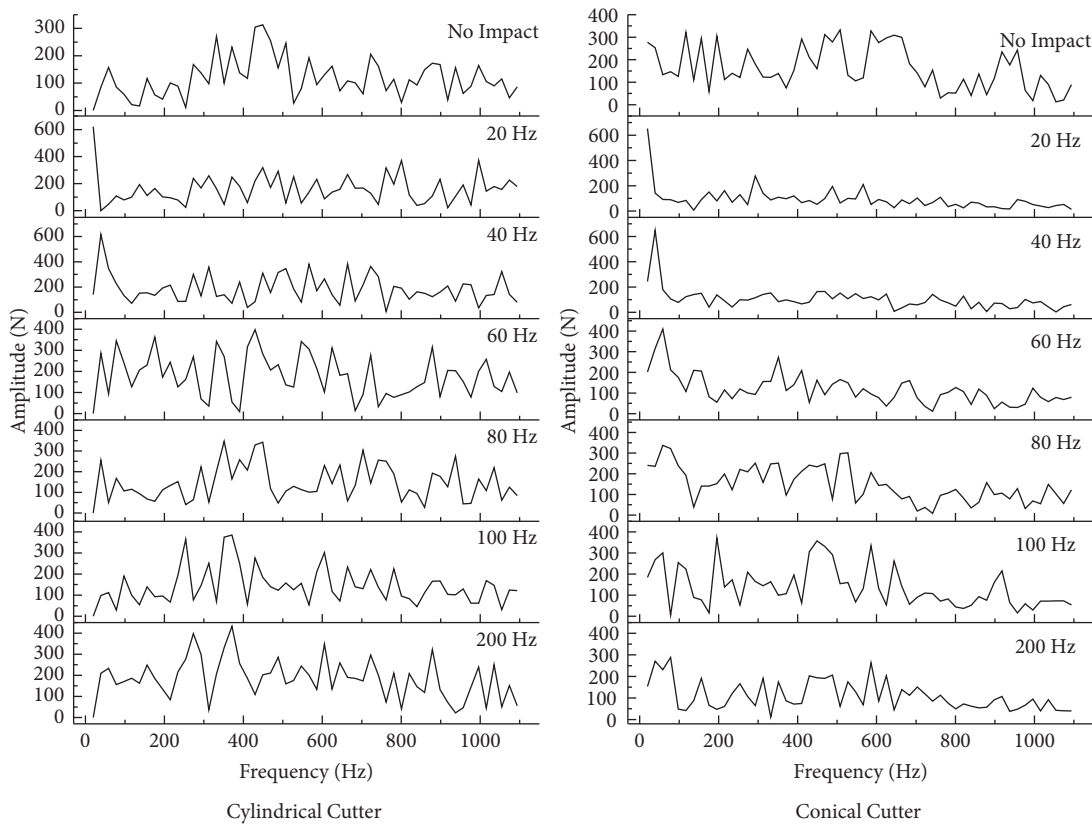


FIGURE 4: WOB frequency spectrum.

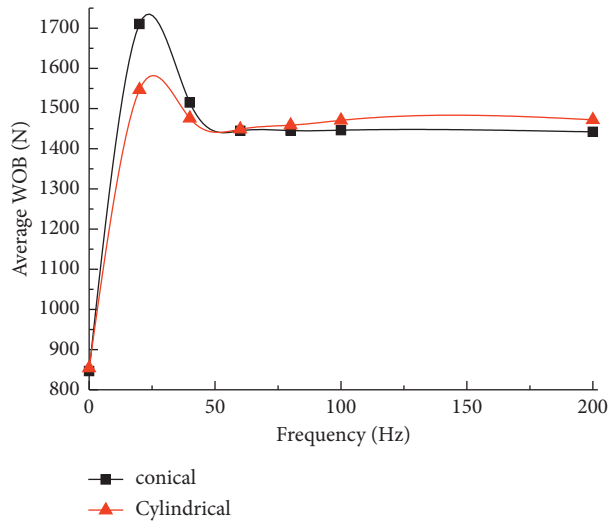


FIGURE 5: The effect of impact frequency on average WOB.

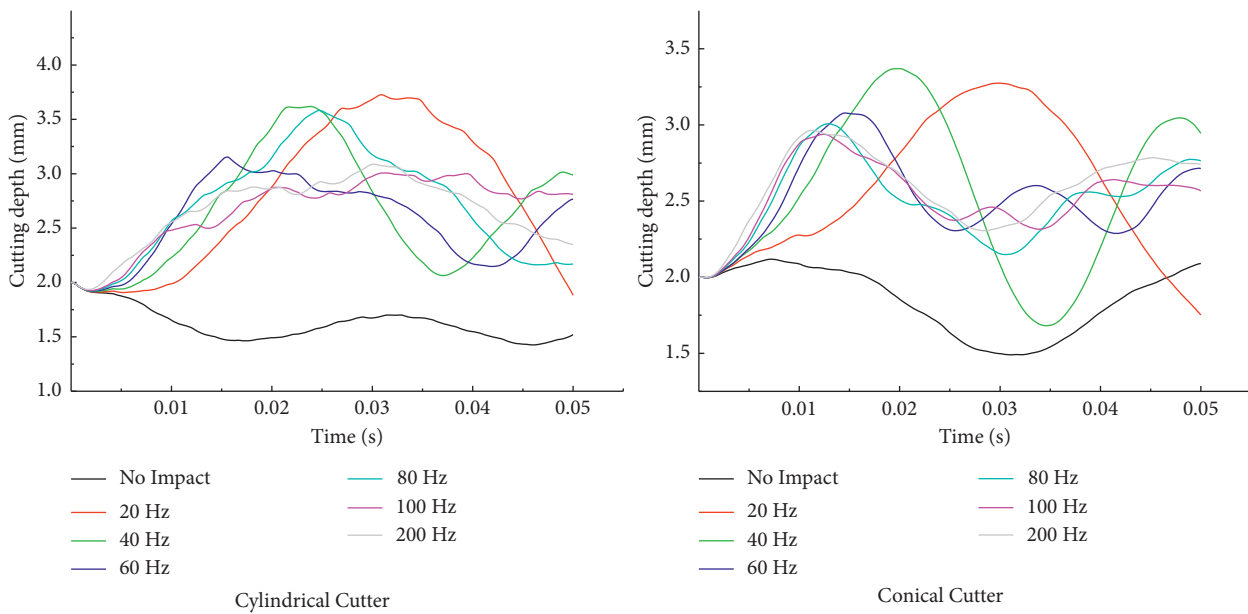


FIGURE 6: Cutting depth-time curve.

frequency if the impact amplitude is less than 600 N. When the amplitude of the impact force increases to 800 N, 20 Hz becomes the dominant frequency, and the amplitude at the dominant frequency is 450 N. When the impact amplitude is 1000 N, the main frequency is 20 Hz and the amplitude increases to 600 N. There is no dominant frequency when the frequency of impact force is 100 Hz.

When the conical cutter is assisted by the impact force at 20 Hz, there is no dominant frequency in the WOB frequency spectrum if the impact amplitude is less than 400 N. When the amplitudes of impact force are 600 N, 800 N, and 1000 N, the dominant frequency is 20 Hz and the amplitudes at 20 Hz are 270 N, 450 N, and 600 N, respectively. WOB at 100 Hz impact force always has no dominant frequency.

There is no dominant frequency when the frequency of impact force is 100 Hz.

The dominant frequency of the cylindrical cutter and the conical cutter only appears when the amplitude of impact force is higher than the threshold. The thresholds for the cylindrical cutter and the conical cutter are 600 N and 400 N, respectively.

The average WOB curves for the cylindrical cutter and the conical cutter assisted by the impact force are shown in Figure 9. When the cylindrical cutter is assisted by the impact force at 100 Hz, the average WOB increases linearly if the amplitude of the impact force is between 0 and 400 N. When the impact amplitude exceeds 400 N, the growth rate of average WOB decreases with the increase of the impact

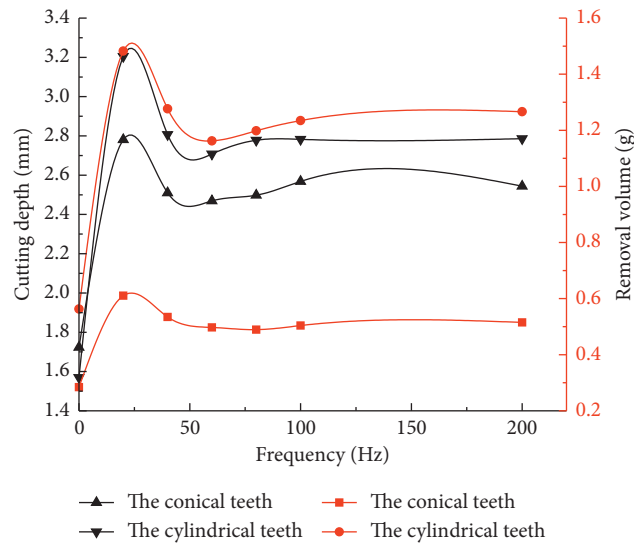


FIGURE 7: Cutting depth and removal volume.

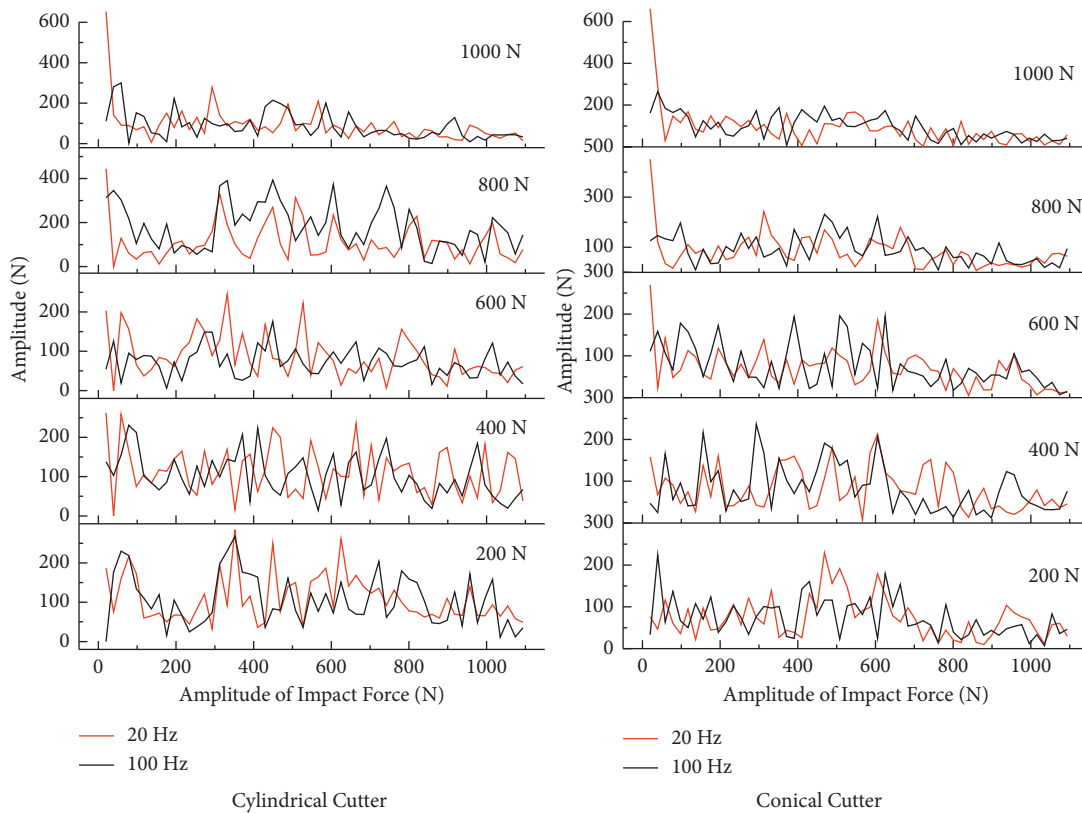


FIGURE 8: WOB frequency spectrum.

amplitude. When the impact frequency is 20 Hz and the impact amplitude is 0–400 N, the average WOB increases linearly. When the impact amplitude is 400–1000 N, the average WOB increases linearly with the increase of the impact amplitude, but the growth rate becomes higher. When the impact amplitude is 1000 N, the average WOB is 1540 N if the impact frequency is 20 Hz, and the average

WOB is 1350 N if the impact frequency is 100 Hz. The former is 14% higher than the latter.

When the impact amplitude is 0–200 N, the average WOB of the conical cutter at 20 Hz is the same as that at 100 Hz. When the impact amplitude is greater than 200 N, the average WOB increases almost linearly, but the growth rate of the former is larger. When the impact amplitude is

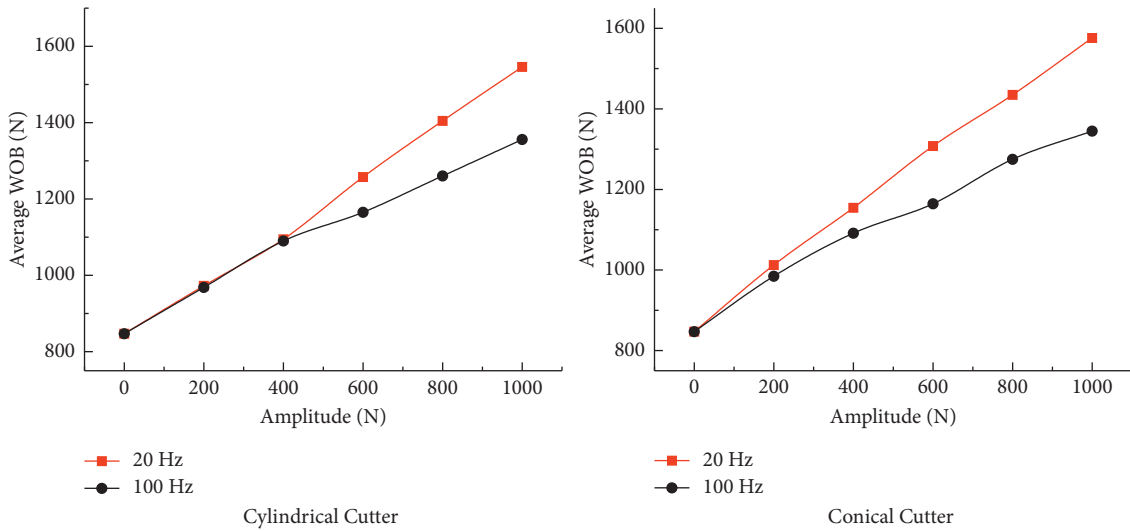


FIGURE 9: The effect of impact amplitude on average WOB.

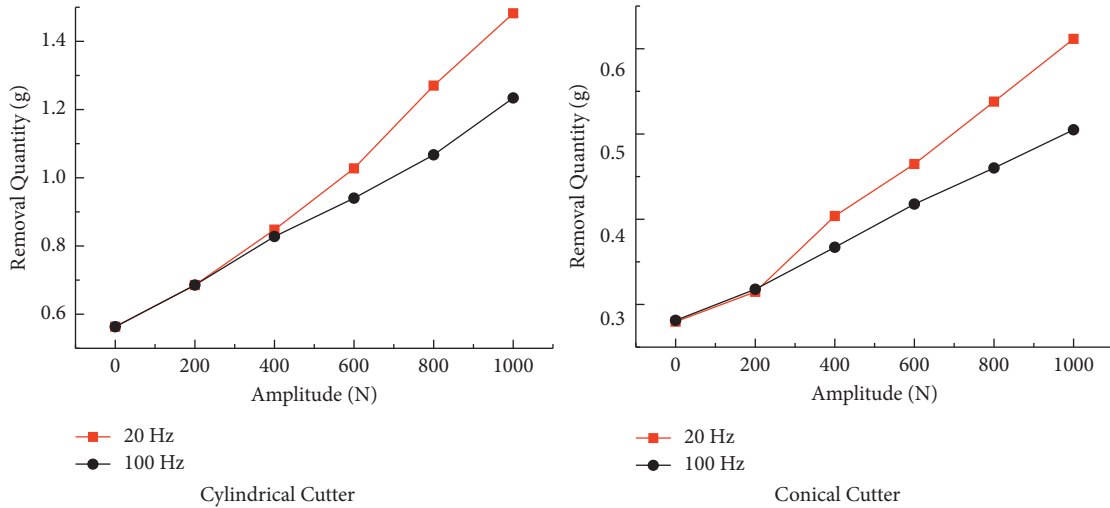


FIGURE 10: The effect of impact amplitude on removal volume.

1000 N, the average WOB is 1570 N if the impact frequency is 20 Hz, and that is 1340 N if the impact frequency is 100 Hz. The former is 17% higher than the latter.

Figure 10 shows the effect of the impact amplitude on removal volume. When the amplitude of the impact force is 0–400 N, the removal volume at 20 Hz is the same as that at 100 Hz and increases linearly with the increase of the impact amplitude. When the amplitude of the impact force exceeds 400 N and the impact force is at 20 Hz, the removal volume of the cylindrical cutter increases linearly and the growth rate is higher; but when the impact force is at 100 Hz, the removal volume of the cylindrical cutter decreases. When the impact force is 1000 N and impact frequency is 20 Hz and 100 Hz, the removal volume is 1.48 g and 1.23 g, respectively. The former is 20% higher than the latter.

When the amplitude of the impact force is 0–200 N and impact frequency is 20 Hz and 100 Hz, respectively, the removal volume of the conical cutter is the same. When the

impact amplitude is greater than 200 N, there is a linear relationship between the removal volume of the conical cutter and the impact amplitude. But the growth rate of the removal volume is greater when the impact frequency is 20 Hz. When the impact amplitude is 1000 N and the frequency is 20 Hz and 100 Hz, the removal volume is 0.61 g and 0.50 g, respectively, and the former is 22% higher than the latter.

5. Conclusion

This paper identifies the main effects of the impact force on the rock-breaking process of the conical PDC cutter. The research points out that there is an upper threshold for the impact frequency and a lower threshold for the impact amplitude. The frequency threshold of both cylindrical cutter and conical cutter is 60 Hz, and their impact amplitude threshold is 400 N and 200 N, respectively.

- (1) When the impact frequency is lower than the threshold frequency, the impact force leads to a large peak value at the impact frequency in the WOB frequency spectrum, and the average WOB and removal volume increase significantly. But with the increase of impact frequency, the removal volume decreases rapidly.
- (2) When the impact frequency is higher than the threshold, the peak value in the WOB frequency diagram decreases greatly, and the average WOB remains unchanged.
- (3) When the impact amplitude is higher than the threshold value, the peak value in the frequency spectrum is the impact frequency.
- (4) Although the cutting depth and removal volume of the conical cutter are lower than those of the cylindrical cutter, the amplifications of cutting depth and removal volume of the conical cutter are higher than those of the cylindrical cutter.

Data Availability

The raw data can be provided if requested.

Conflicts of Interest

The authors declare that they have no conflicts of interest.

Acknowledgments

This work was sponsored by the Major Science and Technology Project of the CNPC under Grant ZD2019-183-005.

References

- [1] Y. Sun, D. Zou, Y. Guo, C. Xiuping, and Yi Yang, "Design and field application of plow-cutting PDC bit," *Oil Drilling & Production Technology*, vol. 38, no. 1, pp. 53–56, 2016.
- [2] Y. B. Benalouane, S. Mokrani, S. Ziani, and Z. Djamel, "Impregnated bits design and optimization: an iterative method for improving drilling performances. case study: hassi messaoud cambrian reservoir in Algeria," in *Proceedings of the SPE/IADC Middle East Drilling Technology Conference and Exhibition*, 2011.
- [3] M. Azar, A. White, S. Segal, and S. Velvaluri, "Pointing towards improved PDC bit performance: innovative conical shaped polycrystalline diamond element achieves higher ROP and total footage," in *Proceedings of the SPE/IADC Drilling Conference*, 2013.
- [4] R. Hempton, C. Copeland, G. Cox, and C. Faught, "Innovative conical diamond element bits drill back-to-back tight curves in one run, improving economics while reducing risk in avalon shale play, New Mexico," in *Proceedings of the SPE Liquids-Rich Basins Conference-North America*, 2015.
- [5] V. Radhakrishnan, A. Chuttani, F. Anggrani, and H. Nan, "Conical diamond element technology delivers step change in directional drilling performance," in *Proceedings of the IADC/SPE Asia Pacific Drilling Technology Conference*, 2016.
- [6] C. Durrand, M. Skeem, and D. Hall, "Thick PDC, shaped cutters for geothermal drilling: a fixed cutter solution for a roller cone drilling environment," in *Proceedings of the 44th US Rock Mechanics Symposium and 5th US-Canada Rock Mechanics Symposium*, American Rock Mechanics Association, Salt Lake City, UT, USA, 2010.
- [7] Y. X. Sun and D. Y. Zou, "Experimental study on force of stinger cutter breaking rock," *Applied Mechanics and Materials*, vol. 727-728, pp. 406–410, 2015.
- [8] V. German, M. Pak, M. Azar, and S. Bits, "Conical diamond element bit sets new performance benchmarks drilling extremely hard carbonate/chert formations, perm region Russia," in *Proceedings of the SPE/IADC Drilling Conference and Exhibition*, 2015.
- [9] J.-K. Wang and T. Lehnhoff, "Bit penetration into rock-a finite element study," in *Proceedings of the International Journal of Rock Mechanics and Mining Sciences & Geomechanics Abstracts*, 1976.
- [10] G. Han, M. Bruno, and M. B. Dusseault, "Dynamically modelling rock failure in percussion drilling; proceedings of the Alaska Rocks 2005," in *Proceedings of the 40th US Symposium on Rock Mechanics (USRMS)*, American Rock Mechanics Association, Anchorage, AK, USA, June 2005.
- [11] F. Zhao, X. Li, F. Tao, and S. Xie, "Theoretical analysis and experiments of rock fragmentation under coupling dynamic and static loads," *Chinese Journal of Rock Mechanics and Engineering*, vol. 24, no. 8, pp. 1315–1320, 2005.
- [12] F. Zhao, X. Li, and F. Tao, "Research on experiments of brittle rock fragmentation by combined dynamic and static loads," *Rock and Soil Mechanics*, vol. 26, no. 7, pp. 1038–1042, 2005.
- [13] X. Zhu, H. Luo, and Y. Jia, "Numerical analysis of air hammer bit drilling based on rock fatigue model," *Chinese Journal of Rock Mechanics and Engineering*, vol. 31, no. 4, pp. 754–761, 2012.
- [14] T. Lin, Z. Lian, Y. Meng, and B. Yang, "Finite elements method study on dynamic rock breaking in air drilling," *Chinese Journal of Rock Mechanics and Engineering*, vol. 27, no. S2, pp. 3592–3596, 2008.
- [15] Y. Jing, X. Yuan, L. Jiang, and H. Zhang, "Numerical simulation and field experimental study on rock breaking in high speed rotating percussion drilling," *Journal of China University of Petroleum (Edition of Natural Science)*, vol. 43, no. 1, pp. 75–80, 2019.
- [16] S. Ziani, S. Fetayah, A. Boudebza, B. Mohammed Miloud, B. Yacine, and M. Fatah, "Percussion performance drilling motor delivered extreme cost saving in hard and abrasive formation in Ahnet Basin, Algeria," in *Proceedings of the IADC/SPE Drilling Conference and Exhibition*, 2018.
- [17] X. Zhu and J. Liu, "Rock breaking and ROP rising mechanism of rotary-percussive drilling technology," *Acta Petrolei Sinica*, vol. 39, no. 2, pp. 216–222, 2018.
- [18] S. Li, W. Li and T. Yan, "A study on the rock breaking mechanism of drill bits under combined loads and field applications," *Journal of Vibration and Shock*, vol. 36, no. 16, pp. 51–55+112, 2017.
- [19] X. Zhu and W. Liu, "The rock breaking and ROP rising mechanism for single-tooth high-frequency torsional impact cutting," *Acta Petrolei Sinica*, vol. 38, no. 5, pp. 578–586, 2017.
- [20] R. Brown and B. Meckfessel, *Improving marcellus Shale Performance Using Pdc Bits with Optimized Torque Management Technology, Cutting Structure Aggressiveness and Unique Roller Cone Steel Tooth Cutting Structures*, SPE Eastern Regional Meeting, OnePetro, 2010.
- [21] T. J. Holmquist, G. R. Johnson, and W. H. Cook, "A computational constitutive model for concrete subjected to large strains, high strain rates, and high pressures," in *Proceedings of the 14th Int symposium on ballistics*, pp. 561–600, Quebec city, Canada, 1993.

Research Article

Quantitative Characterization of Overburden Rock Development Pattern in the Goaf at Different Key Stratum Locations Based on DEM

Xiaoqiang Zhang , Bolin Hu, Jiaying Zou, Chuandong Liu, and Yuanfan Ji

College of Environment and Resources, Xiangtan University, North Second Ring Road, Yuhu District, Xiangtan, Hunan 411100, China

Correspondence should be addressed to Xiaoqiang Zhang; kdyoung@126.com

Received 10 November 2021; Revised 27 November 2021; Accepted 30 November 2021; Published 14 December 2021

Academic Editor: Guoming Liu

Copyright © 2021 Xiaoqiang Zhang et al. This is an open access article distributed under the Creative Commons Attribution License, which permits unrestricted use, distribution, and reproduction in any medium, provided the original work is properly cited.

The overburden rock mining fissures are the main cause of coal spontaneous combustion, gas pooling, and mine water inrush caused by goaf air leakage. Rapid and accurate determination of the development and evolution law of mining fissures have great significance for the application of coal spontaneous combustion prevention and control, gas disaster prevention and control, and water damage prevention and control measures. In this paper, a preliminary judgment of the development height of the water-conducting fracture zone is made based on the theoretical analysis, and the physical model size of the numerical simulation is determined according to its judgment result. It is judged that the development height of its water-conducting fracture zone is between 49 and 64.2 m, which is in line with the actual results. Based on this, a three-dimensional solid model was established in PFC (Particle Flow Code) software to analyze the fissure development pattern of the overburden rock and the development height of the water-conducting fracture zone when the main key stratum of the rock seam is in different positions by simulating the excavation process of the coal seam. The results show that when the main key stratum is located in the “original crack belt boundary,” the development of water-conducting fracture zone is significantly inhibited; when the main key stratum is located in the “original caving zone,” the water-conducting fracture zone is fully developed, and the crack belt finally develops to the top of the model. In order to verify the accuracy of the numerical simulation, similar material simulation experiments were performed under the same scheme. The results are consistent with the numerical simulation conclusions, effectively verifying the accuracy of the numerical simulation. Finally, the extraction of porosity of the goaf was carried out based on numerical simulation, and the permeability zoning of the goaf was performed; the results show that the development of the water-conducting fracture zone has a significant influence on the permeability of the mining area, and the more fully developed the fissure is, the greater is its permeability. In this paper, the fissure development law in the goaf under different key strata is explored by various research strata, and the results show a good consistency, which provides a scientific basis for the prevention and control of disasters such as water inrush and coal and gas outburst in mines, and provides theoretical guidance for safe mining.

1. Introduction

As shallow coal seam is mined out and shallow coal resources are gradually depleted, deep mining will become the new normal for coal resource mining in China [1]. However, as the depth of mining increases, the original stress field caused by the impact of mining is destroyed and the process of stress redistribution becomes more and more intense in the mining area [2–5]. The goaf will form bending

subsidence belt, crack belt, and caving zone in the vertical direction [6]. The degree of fissure development of mining overburden rock within different belt heights is not the same, thus having an important impact on gas enrichment zone, coal spontaneous combustion distribution, roof water inrush, etc. [7–10]. Problems such as coal and gas protrusion and roof water emergence caused by mining fissures seriously affect the efficiency and safety of mining [11]. Reasonable and effective characterization of overburden rock

fissure development in the mining area is an important guide to improve the targeting and effectiveness of gas disaster and coal spontaneous combustion disaster in the mining area. At present, Ma et al. have done a detailed study on the development of fissures in overburden rock and overburden aquifer in the goaf, the failure pattern, mechanisms of the stress regime, and deformation behaviors and other directions, which accurately reveals the damage mechanism of overburden under complex stress [12–15]. Tu and Liu [16] researched the formation, development, closure, and variation of cracks in the roof of the coal seam, and the influence of coal mining. They also described the range of fissure development. Cheng et al. [17] used the mathematical model of gas outflow and gas transport at the working face and COMSOL finite element software to simulate the gas transport pattern in the overburden rock fissure area under the influence of mining. The results show that the development of overburden rock fissure area is influenced by mining. The fissure area is connected to form a trapezoidal platform structure. Cao and Li [18] used the discrete element software UDEC and the multiphysics software COMSOL to simulate the gas transport pattern of the mining fissure above the goaf. The results show that as the working face advances, the overburden rock in the mining area gradually form a trapezoidal mining fissure network, and the size of the fissure network increases with the advancing distance of the working face; compared with the gas transport in the overburden rock, the flow of mining-induced gas in the fissure network is much larger. In addition, the overburden rock above the mined coal seam is not uniformly endowed, and there are key strata in the mined overburden rock, which is one or more stratum of the harder, thicker, high elastic modulus, and high tensile strength rock in the mined overburden rock, which play a major role in controlling the local or global rock stratum of the fissure development pattern of the whole goaf [19]. The deformation characteristics of the key stratum is an important factor affecting the transport behavior of the overburden rock, and the study of the breaking law and collapse characteristics of the key stratum is the key to solving serious mine disasters such as coal and gas outburst and rock burst [20–23]. The above-mentioned studies have analyzed and studied the fissure development pattern of overburden rock by different means, effectively analyzing and characterizing the deformation characteristics of overburden rock fissures under different mining environments, and deepening the understanding of overburden rock fissure development law; they did not consider the key layer as a factor.

The location of the key stratum has a significant influence on the development of mining fissures, and many scholars have conducted a lot of empirical and theoretical studies on coal mining overburden rock damage and the height of mining overburden rock fissure development. On this basis, Xu et al. [24] studied the influence of the vertical distance between the key stratum and coal seam on the development of water-conducting fracture zone, and concluded that when this distance is less than a certain critical value, the fissure will develop to the top of the rock seam, which complements the prediction formula of water-

conducting fracture zone in the regulation (The “Regulation” here refers to the “Buildings, water bodies, railroads and main shaft coal pillar retention and coal compression mining regulations.”). Liu et al. [25] used physical and numerical simulations to study the effect of the presence of key stratum on the movement of overburden rock at the fully mechanized mining workplace, and the results showed that the presence of overburden key stratum is crucial for coal mining, especially for the upper section of a single key stratum. When the upper coal seam key stratum does not exist, a stable masonry structure is formed after mining. Stable stacked layers are easily formed at the bottom of the coal seam. Li et al. [26] analyzed the mechanical characteristics and effects of key stratum fragmentation during the excavation of oversized mining face, and the results showed that the inferior key stratum is easily broken to form a cantilever beam structure instead of a stable articulated structure. When the inferior key stratum is broken, it will induce the breakage of the main critical layer and further trigger the periodic breakage of the underlying layer. Li et al. [27] used UDEC numerical simulation software to analyze the effect of the breakage of the compound key stratum on the overburden rock and ground pressure, and the results showed that the inferior key stratums affected by mining all exhibited sliding instability and could not form a stable body-beam structure after the breakage and collapse. Guo and Yang [28] improved the traditional key stratum calculation method and established a mechanical model of the structural load-bearing characteristics of the interlayer key stratum under the ultra-thick coal seam, and verified the calculation of this method, and the result calculation is consistent with the engineering reality, which is of great significance to the determination of the key stratum for the mining of ultra-thick coal seam under the mining void area. The above studies investigated the effects of single and compound key stratum on the overburden rock movement under different mining conditions, but none of them considered the effect of the change of key stratum position on the development of crack belt in the same coal seam.

Therefore, this paper takes into account the quantitative characterization of mining overburden rock fissures and the key stratum location factor, and adopts theoretical analysis, physical experiment, and numerical simulation methods to conduct an in-depth study on the quantitative characterization of mining overburden rock fissure development height by the location of the main key stratum of overburden rock. And, on the basis of numerical simulation, the porosity between the rock formation and the goaf is derived, and the permeability zoning is carried out according to the porosity to guide the key prevention area of mine water inrush, in order to achieve the effect of preventing and controlling water inrush.

2. Method

2.1. Preliminary Judgment of the Upper Height Limit of Water-Conducting Fracture Zone Development. The overlying strata are deformed by the upper load. Due to its

own physical properties, the rock formation does not break immediately, but the middle of the rock formation sinks and the rock formation is elongated. When the tensile stress on the rock formation exceeds its own tensile strength, vertical fissure will appear in the rock formation until it completely penetrates the rock formation. Considering the bending and sinking of the overlying strata as a subsidence basin, as shown in Figure 1, the middle end of the subsidence basin is approximately horizontal, while the two ends are bending and deforming sections, and the tensile deformation occurring in the overlying strata mainly occurs in the bending and deforming sections. After the deformation of the rock formation, fissures of different forms will appear in the rock formation, and the nature of the fissures determines its hydraulic conductivity. We can use the rock stretching rate ε to express the degree of rock stretching, that is, the ratio of the length of the rock after stretching to the original length. The amount of tensile deformation of rock formation is a comprehensive parameter reflecting two factors of fissure density and width of rock formation, and there is a direct causal relationship between the gas conduction performance of fractured rock formation and the amount of tensile deformation at the level of rock formation. As the rock formation increases in height, there is finally a rock formation with smaller stretching rate, so that the upper and lower rock layers cannot be penetrated, and the development height of water-conducting fracture zone reaches the upper limit.

In the curve section at the edge of the sinking basin of the rock formation, the tensile rate ε of the neutral layer before and after the bending deformation of the rock formation can be expressed as:

$$\varepsilon = \frac{(l_1 - l_0)}{l_0}, \quad (1)$$

where l_0 is the length of the straight line section before the bending and deformation of the rock formation and l_1 is the arc length of the curved section after the bending and deformation of the rock formation.

Assuming that the vertical distance from the neutral layer of the rock to the coal seam is h , the limit angle δ_0 , the full extraction angle ψ , and according to the geometric relationship in Figure 2, we can obtain: $l_0 = AE + EF = h \cdot (\cot \delta_0 + \cot \psi)$. Approximate that $\psi' = \delta'_0 = (\psi + \delta_0)/2$, it is assumed that two circular arcs with equal radius and arc length and opposite curvature direction can be fitted by two segments, and set the arc angle to ϕ , radius of r , then the length of the curve at the edge of the sunken basin l_1 is:

$$l_1 = \frac{2r \cdot \phi \cdot \pi}{180}. \quad (2)$$

As shown in Figure 3, the geometric relationship by $\triangle OOM$ gives:

$$(2r)^2 = (r + (r - w_0))^2 + l_0^2, \quad (3)$$

$$\phi = \arcsin \frac{l_0}{2r}.$$

So:

$$r = \frac{w_0^2 + l_0^2}{4w_0}, \quad (4)$$

$$\phi = \arcsin \frac{2w_0 \cdot l_0}{w_0^2 + l_0^2},$$

where w_0 is the maximum sinking of rock layer; m is the mining thickness of coal seam; and q is the rock subsidence coefficient.

The subsidence coefficient q of the rock formation in the conductive fracture zone is generally greater than the surface subsidence coefficient q_0 , subsidence coefficient at coal seam roof $q = 1$; therefore, the coefficient of rock subsidence at the layer height h is:

$$q = 1 - (1 - q_0) \cdot \frac{h}{H}, \quad (5)$$

H is the burial depth of coal seam.

Combined with the above analysis, the calculation steps of rock stretching rate ε are [28]:

- (1) Calculation of the rock subsidence coefficient

$$q = 1 - (1 - q_0) \cdot \frac{h}{H}. \quad (6)$$

- (2) Calculation of the w_0 , l_0 :

$$\begin{cases} w_0 = m \cdot q, \\ l_0 = h \cdot (\cot \delta'_0 + \cot \psi'). \end{cases} \quad (7)$$

- (3) Calculation of the arc angle ϕ and length of sinking basin bottom l_0 :

$$\begin{cases} \phi = \arcsin \left[\frac{2w_0 \cdot l_0}{(w_0^2 + l_0^2)} \right], \\ l_1 = \frac{(w_0^2 + l_0^2) \cdot \phi \cdot \pi}{(180 \cdot 2w_0)}. \end{cases} \quad (8)$$

- (4) Calculation of tensile rate ε :

$$\varepsilon = \frac{(l_1 - l_0)}{l_0}. \quad (9)$$

The overlying strata of 7435 workings of the Kongzhuang coal mine belongs to medium-hard strata, and the following values are assigned to the medium-hard roof rock formation: $q = 0.7$, $\cot \delta' = \cot \psi' = 0.577$; from the calculation steps of the tensile rate of the rock formation, the calculation of the tensile rate of each rock formation was carried out, and some of the results are shown in Table 1.

Table 1 shows that the tensile rate is maximum at J4 rock formation with 20.63%, which indicates that large deformation occurred due to overloading of J4 rock formation, while the upper rock formation, J5 rock formation, deformed less under the support of J4 rock formation with a

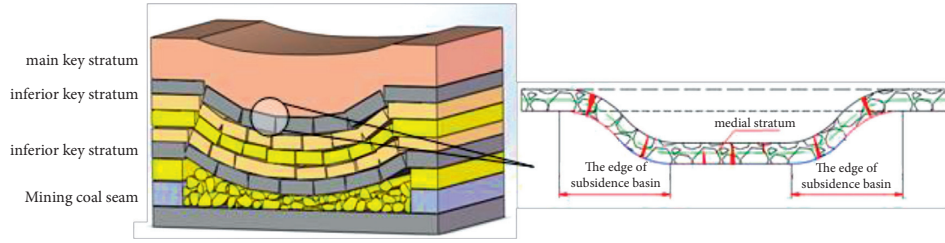


FIGURE 1: Sketch map of rock stratum's tensile deformation.

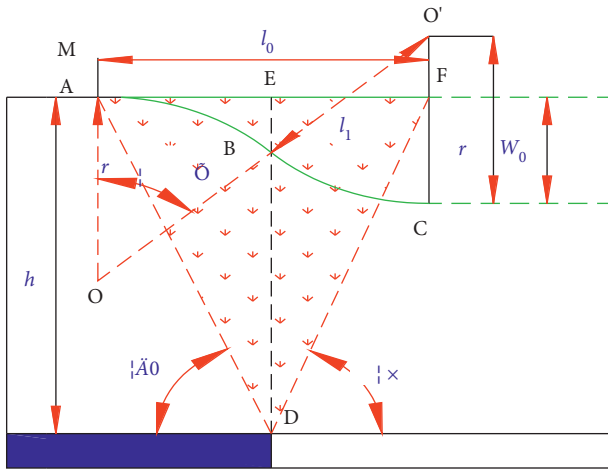


FIGURE 2: Geometric model of rock stratum bending and subsidence.

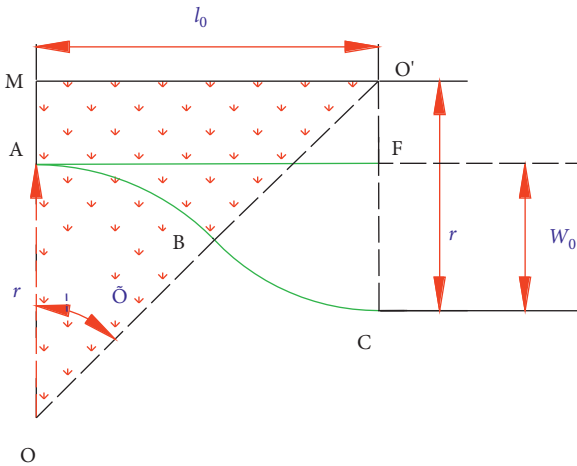


FIGURE 3: Geometrical relationship of model.

tensile rate of 5.83%. When the tensile rate is calculated to the J10 rock formation, the tensile rate of the J10 rock formation is 0.34%, and the tensile rate of the J10 rock formation varies widely with the tensile rate between the upper and lower rock formation, which means that the inflection point of the tensile rate is considered to have been reached.

So far, it can be preliminarily determined that the development height of water-conducting fracture zone in 7435 working face of the Kongzhuang coal mine is between 49 and 64.2 m (developed to J10-J11 layer number rock formation),

and the tensile rate of J10 rock formation and J11 rock formation are 0.24% and 0.34%, respectively.

2.2. Similar Material Simulation Experiment

2.2.1. Modeling of Similar Materials.

Similar material model is a model based on the principle of similarity theory, using materials with similar mechanical properties to the prototype, and scaled down to a certain scale with reference to the actual geological conditions. Extraction is carried out on the model according to similar ratios, and the actual site conditions are analyzed and inferred by observing the deformation and damage of the model. In this paper, based on the actual parameters of 7435 working face of the Kongzhuang coal mine and the existing experimental conditions, the similar ratios of each parameter were determined, as shown in Table 2. The experiment material aggregate is screened river sand (particle size in 0.1–0.35 mm), and auxiliary materials are gypsum, calcium carbonate, mica, etc. The coal rock layer materials in the simulation experiment are designed strictly according to the similar ratio of volume weight and similar ratio of stress.

Based on the determined similarity ratios, the corresponding parameters of the similarity model can be obtained (Table 3).

The experiment equipment adopts a two-dimensional physical similar material simulation test bench. The length, width, and height of the maximum two-dimensional model of the experiment bench are 1.9 m × 0.22 m × 1.5 m, respectively, and the effective height is 1.4 m. Figure 4 shows the schematic diagram of similar material model lying, and the parameters in the figure are all obtained by converting the working surface of 7435 in Kongzhuang as the engineering background according to the geometric similarity ratio.

The strength of similar materials is an important factor to ensure the accuracy of the experimental results. Therefore, we conducted single axis compressive strength and uniaxial tensile strength. The calculation formula of single axis compressive strength and uniaxial tensile strength of coal rock is:

$$R_c = \frac{P}{A}, \tag{10}$$

$$R_t = \frac{2P}{Dt \pi}$$

TABLE 1: Physical parameters and tensile rate of each rock formation.

Layer number	Lithology	Strata thickness/m	Vertical height from coal seam roof/m	Tensile rate (%)
J17	Mudstone	5.3	100.6	0.11
J16	Sandstone	11.4	89.2	0.11
J15	Mudstone	4.5	84.7	0.13
J14	Sandstone	6.8	77.9	0.16
J13	Fine sandstone	5.6	72.3	0.18
J12	Medium grain sandstone	3.0	69.3	0.21
J11	Mudstone	5.1	64.2	0.24
J10	Sandy mudstone	15.2	49	0.34
J9	Mudstone	11.1	37.9	0.63
J8	Post office box stone	4.2	33.7	0.99
J7	Mudstone	5.8	27.9	1.43
J6	Medium grain sandstone	7.2	20.7	2.62
J5	Sandy mudstone	5.0	15.7	5.83
J4	Medium grain sandstone	6.7	9	20.63
J3	Sandy mudstone	3.0	6	2.81
J2	Coal seam	6.0	0	
J1	Post office box stone	26.6	22.3	

TABLE 2: Similarity ratio of each parameter.

Ratio of similitude	Value
Similarity ratio of geometric	1 : 150
Similarity ratio of volume weight	1 : 0.66
Similarity ratio of time	1 : 12
Similarity ratio of stress	1 : 225

TABLE 3: Prototype and comparison of similar model parameters.

Layer number	Lithology	Actual thickness/m	Actual volume weight/kN/m ³	Model thickness/cm	Volume weight of model thickness/g/cm ³	Model total thickness/cm
J17	Mudstone	5.3	24.0	3.5	1.4	88.1
J16	Sandstone	11.4	23.8	7.6	1.6	84.6
J15	Mudstone	4.5	24.0	3.0	1.4	77.0
J14	Sandstone	6.8	23.8	4.5	1.6	74.0
J13	Fine sandstone	5.6	23.3	3.7	1.6	69.5
J12	Medium grain sandstone	3.0	25.2	2.0	1.6	65.8
J11	Mudstone	5.1	24.0	3.4	1.4	63.8
J10	Sandy mudstone	15.2	24.3	10.1	1.6	60.4
J9	Mudstone	11.1	24.0	7.4	1.4	50.3
J8	Post office box stone	4.2	23.3	2.8	1.5	42.9
J7	Mudstone	5.8	24.0	3.8	1.4	40.1
J6	Medium grain sandstone	7.2	25.2	4.8	1.6	36.3
J5	Sandy mudstone	5.0	24.3	3.3	1.6	31.5
J4	Medium grain sandstone	6.7	25.2	4.4	1.6	28.2
J3	Sandy mudstone	3.0	24.3	2.0	1.6	23.7
J2	Coal seam	6.0	20.8	4.0	1.4	21.7
J1	Post office box stone	26.6	22.3	17.7	1.5	17.7

R_c is the single axis compressive strength, MPa; R_t is the uniaxial tensile strength, MPa; P is the magnitude of load, N; D is the diameter of coal rock specimen, cm; and t is the height of coal rock specimen, cm.

The single axis compressive strength of some rock masses were obtained and are shown in Table 4.

The strength test results showed that the maximum error of the single axis compressive strength of the rock layer was

3.24% and the minimum error was only 0.23%, and the similar material proportioning scheme used was reasonable.

2.2.2. Experimental Scheme. In order to verify the influence of different key stratum locations on the development of water-conducting fracture zone, three physical experiment scenarios were established according to the actual conditions

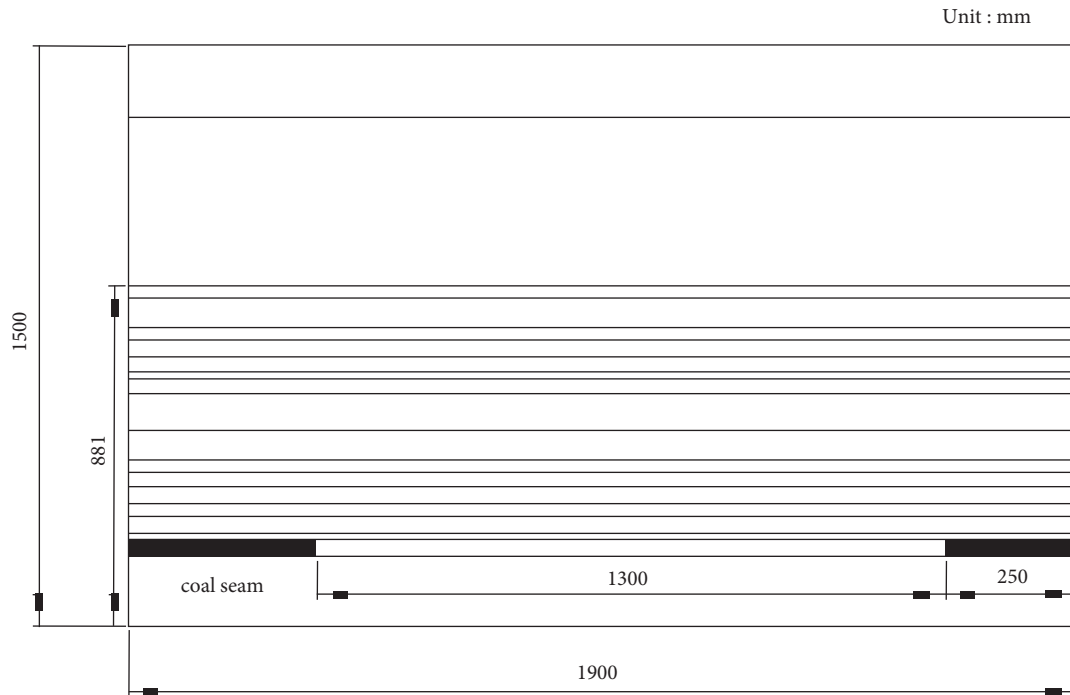


FIGURE 4: Schematic drawing of similar material model.

TABLE 4: Results of uniaxial compressive strength of partially tested rock.

Layer number	Lithology	Single axis compressive strength/MPa	Theoretical value of materials	Empirical value/kPa	Error/%
J12	Medium grain sandstone	48.93	215.29	214.06	0.57
J11	Mudstone	42.15	185.46	187.53	1.10
J10	Sandy mudstone	56.43	248.29	251.34	1.21
J9	Mudstone	51.73	227.70	222.03	2.55
J8	Post office box stone	75.11	330.48	327.85	0.80
J7	Mudstone	32.09	141.19	141.53	0.23
J6	Medium grain sandstone	33.48	147.31	146.12	0.81
J5	Sandy mudstone	27.15	119.46	117.7	1.49
J4	Medium grain sandstone	30.07	132.30	133.07	0.57
J3	Sandy mudstone	23.23	102.21	99.00	3.24

of 7435 working face in the Kongzhuang coal mine. Scheme 1 is the prototype of 7435 working face of the Kongzhuang coal mine, whose main key stratum J16 rock formation is located outside the water-conducting fracture zone. Scheme 2 is the prototype of 7435 working face of the Kongzhuang coal mine, and without considering the influence of other conditions, only the position of J16 rock formation in the rock formation is changed, so that it is located in the upper part of the prototype water-conducting fracture zone, and the key stratum is redetermined, and it is ensured that the “J16 rock formation sandstone” is still the main key stratum in the overlying strata after the change. Similarly, the main key stratum J16 of scheme 3 is located within the prototype caving zone. In this way, three similar material simulation test scenarios were designed based on the actual conditions at the 7435 working face of the Kongzhuang coal mine, with the main key stratum outside the “crack belt,” the main key

stratum at the “original crack belt boundary,” and the main key stratum within the “original caving zone.” The three locations selected had significant variability (Figure 5), and these three test schemes were discussed respectively. According to the key stratum judgment method, the position of each key stratum of the three test schemes is judged, as shown in Table 5.

In particular, it should be noted that all rock formation and their markings involving 7435 working face in this paper are the same in all three scenarios to which the rock formation and markings correspond, and the markings have no relationship with the location. That is to say, the marking of all strata follows the marking of scheme 1, and scheme two and three are no longer remarked. For example, the main key stratum “J16 sandstone” is marked as J16 in all three scenarios, and the corresponding markings of other rock layers are not changed.

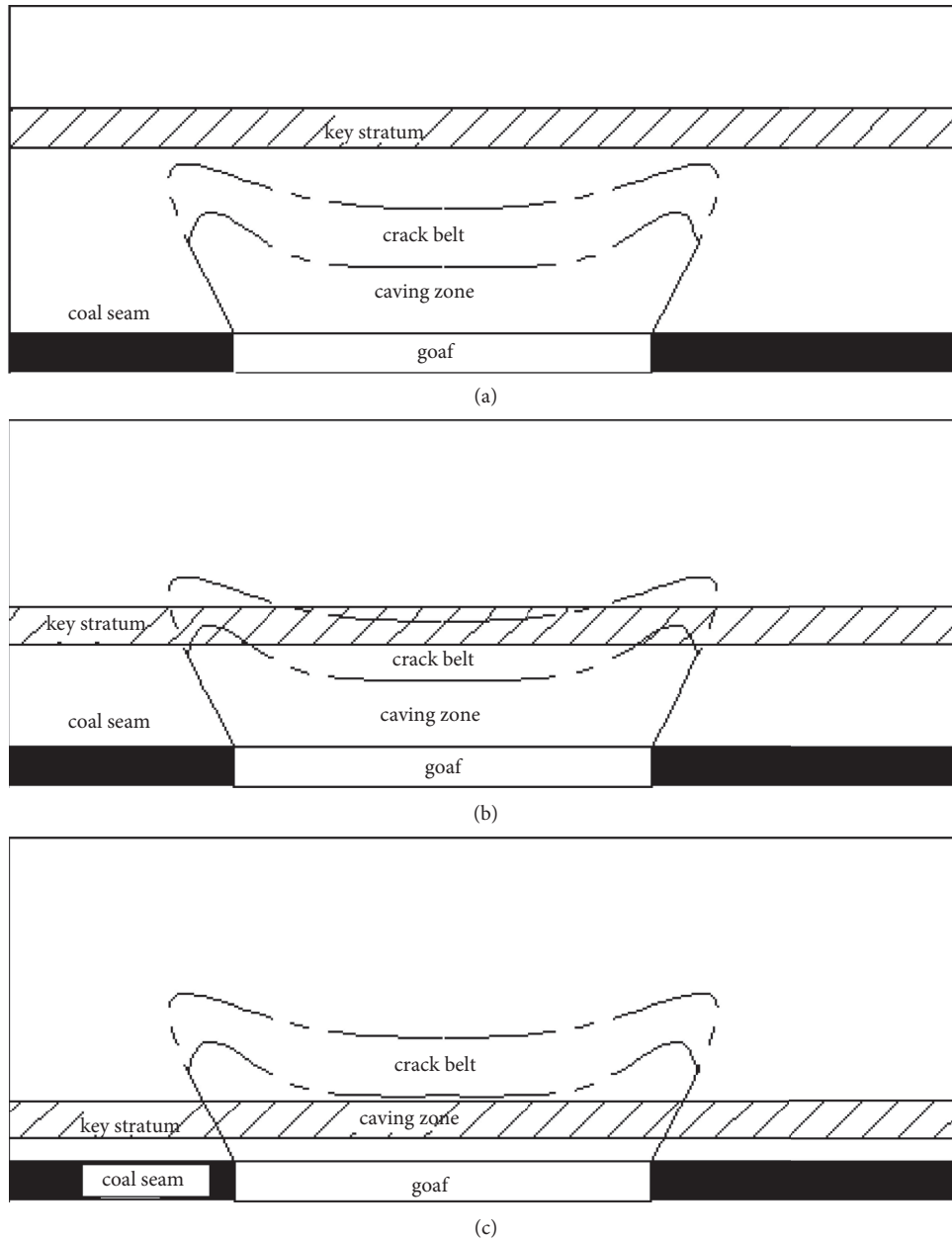


FIGURE 5: Test plan design: (a) the main key stratum is located in the “original crack belt”; (b) the main key stratum is located in the “original crack belt boundary”; (c) the main key stratum is located in the “original caving zone”.

TABLE 5: The key stratum positions of each experimental scheme.

Scheme		Scheme 1	Scheme 2	Scheme 3
Coal seam	Height mining	6	6	6
Inferior key stratum 1	Thickness	6.7	6.7	6.7
	Thickness from coal seam	9.7	9.7	9.7
Inferior key stratum 2	Thickness	7.2	7.2	—
	Thickness from coal seam	21.9	21.9	—
Inferior key stratum 3	Thickness	11.1	—	—
	Thickness from coal seam	43	—	—
Compound key stratum	Thickness	15.2	—	15.2
	Thickness from coal seam	58.2	—	69.9
Main key stratum	Thickness	11.4	11.4	11.4
	Thickness from coal seam	94.6	54.4	26.1

2.3. PFC Numerical Simulation

2.3.1. Modeling. According to the actual geological conditions of 7435 working face of the Kongzhuang coal mine, the numerical simulation of the whole process of working face mining was carried out by using step excavation method to study the law of roof collapse and porosity change during the mining process of each scheme, ignoring the factors such as rock joint fissures and inter-rock faults, and considering only the development of overburden rock fissures caused by mining. After the preliminary judgment of the height of the water-conducting fracture zone, the model size of the physical model was determined to more accurately reflect the fissure development pattern of the rock formation during actual mining. After calculation, the size of the simulated mining model was determined as 285 m (length) \times 33 m (width) \times 132.2 m (height), and the numerical simulation model shown in Figure 6 was established by adopting the key stratum location scheme with similar material simulation experiments.

2.3.2. Boundary Conditions and Solution Parameters. The contact model between particle units includes contact stiffness model, sliding model, and bond model, and the bond model can be divided into contact bond model and parallel bond model, and the parallel bond model is more suitable for the simulation of coal rock, so the parallel bond model is chosen in this paper. For the simplicity of data analysis and the clarity of subsequent result analysis, several layers of measurement circles are uniformly arranged throughout the model (Figure 7), and the measurement circles can be locally encrypted in the range of caving zone and crack belt. We emphasized and improved the description of the boundary conditions, and the completed description was rewritten as, "In order to simulate the coal seam excavation process, the following boundary conditions were added to the model: the upper boundary is a free boundary, and the vertical load is applied to the top of the model to simulate the self-weight of the upper rock mass, so as to reflect the collapse and breakage process of the overburden rock; the left and right boundaries restrict the horizontal movement and allow the movement along the vertical direction, so as to reflect the mining process of the working face; the bottom boundary restricts the movement in the vertical direction and allows the horizontal movement, that is, the left and right boundaries fix the x -axis and the bottom boundary fixes the y -axis."

In order to get more realistic simulation results, it is necessary to ensure the consistency of physical properties between the simulation object and the real object. Therefore, we use the mechanical parameters of each rock seam and coal seam as the boundary conditions of the calculation, in order to realistically reflect the deformation and breakage of the coal seam and overlying strata during the excavation process.

3. Result and Analysis

3.1. Analysis of Overburden Rock Movement Pattern. After coal mining, the movement of overlying strata is an important factor causing coal mine collapse and water inrush. Consequently, it is urgent to explore, analyze, and summarize the law of overlying strata movement to prevent water inrush disasters in coal mines. In order to compare the dynamic process of caving subsidence of overlying strata along with the advancing of working face in each scheme, the subsidence displacement of the luminous sheet after the collapse of the rock formation at different mining stages was counted by means of a scale; the rightmost side of the image represents the initial boundary line of mining, and the relationship between the pushing position of working face and roof collapse in different mining stages is drawn (Figures 8–10).

It can be seen that the measuring points in each scheme increase with the increase of the mining distance of the working face, and the subsidence value increases in the transverse and vertical directions, with the overburden rock closer to the mining coal seam, the strata affected by the abutment pressure, and the fissure development experiencing the compaction-closure stage. The smaller the separation space, the more stable the rock formation is. With the continuous forward mining of the working face, the overall shape of the caving strata near the mining coal seam presents an inverted ladder type, and the fissure development form of the strata far from the mining coal seam presents a funnel type. These two different subsidence patterns indicate two different fissure development characteristics. The rock formation close to the mining coal seam is completely broken under the action of supporting pressure, and large variation in rock subsidence values. With the process of stress recovery, the rock formation is gradually compacted and the subsidence amplitude value tends to decrease; the rock formation far away from the coal seam mainly occurs by bending deformation, and the small spacing of the longitudinal separation does not allow the rock to break and no longitudinal fissures are developed.

Three schemes of overburden rock migration present different characteristics; in Scheme 1, as the mining distance increases, the overlying strata will continue to collapse and damage, and the scope of influence will gradually expand. In the initial stage of mining, the overlying collapsed strata will have a smaller influence. As the periodic pressure continues, the scope of impact increases, with the most obvious contrast between Scheme 1 and Scheme 2. After the fourth periodic pressure, the subsidence range of the measurement point did not change significantly in Scheme 2 by the role of the key stratum, and the influence range of the first periodic pressure was one layer, and from the fifth periodic pressure to the eighth periodic pressure, although the mining distance of the working face increased greatly, the fissure development height of the overlying rock did not change significantly; in Scheme 3, after the fourth periodic pressure, the top plate

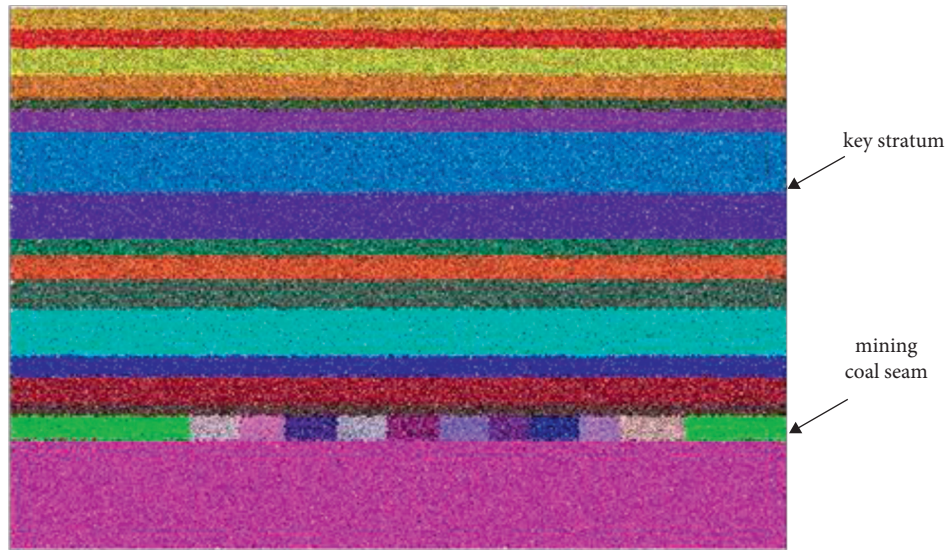


FIGURE 6: PFC particle flow numerical simulation mining model.

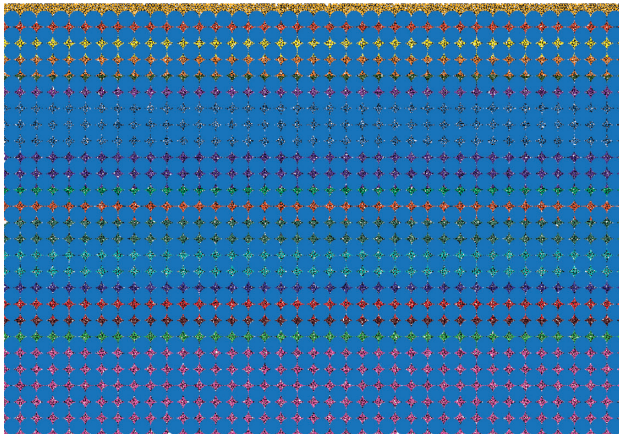


FIGURE 7: Measurement of circular layout.

collapse breaking speed increased significantly, and the water-conducting fracture developed rapidly upward, and even developed to the top of the model after the eighth water-conducting fracture.

3.2. Influence of Different Key Stratum Locations on the Development Height of Water-Conducting Fracture Zone.

By predicting and verifying the development height of water-conducting fracture zone under different key stratum positions through numerical simulation methods and similar material simulation experiments, the simulated excavation process fissure development of three schemes is compared and analyzed to recognize the development height of water-conducting fracture under different key stratum reserve conditions. In similar material simulation experiments, the height range of the development of water-conducting fracture zone in the overlying strata is represented by trapezoidal diagrams, and the influence on different rock formations is marked by colored lines, (1) represents the model before excavation, (2) represents immediate roof

collapse, (3) represents the initial collapse of the main roof, (4) represents the first periodic pressure, (5) represents the second periodic pressure, (6) represents the third periodic pressure, (7) represents the fourth periodic pressure, (8) represents the fifth periodic pressure, and (9) represents the eighth periodic pressure. Due to the simulation of similar materials, the simulated overburden rock collapse results are subjectively influenced by people, the development size of fissures and the spacing of separation are judged with unstable errors, and only parameters such as the pressure step of the top plate and the collapse height of the top plate can be preliminarily analyzed, and it is more difficult to carry out the precise division of the development height of the water-conducting fracture zone. Therefore, we compare and verify the numerical simulation results with the fissure development height of similar material simulation experiments, which can not only verify the realism of its numerical simulation but also further make a more accurate judgment and summary of the water-conducting fracture zone development height and development law in similar material simulation experiments.

3.2.1. Analysis of Simulated Experimental Results for Similar Materials

(1) *Analysis of the Development of the Water-Conducting Fracture Zone in Scheme 1.* J16 rock formation is the main key stratum with a vertical distance of 82.9 m from the working face; J4, J6, and J9 are the three inferior key strata; and J10 and J9 are compound key strata. Clear “three zones” can be formed after the collapse of overlying strata (Figure 11). The development height of the water-conducting fracture zone shows a linear growth trend with the advance of the working face, when the fissure development reaches the lower part of inferior key stratum, the J10–J12 rock formation produces the phenomenon of separation, but the vertical fissure stagnates, which is

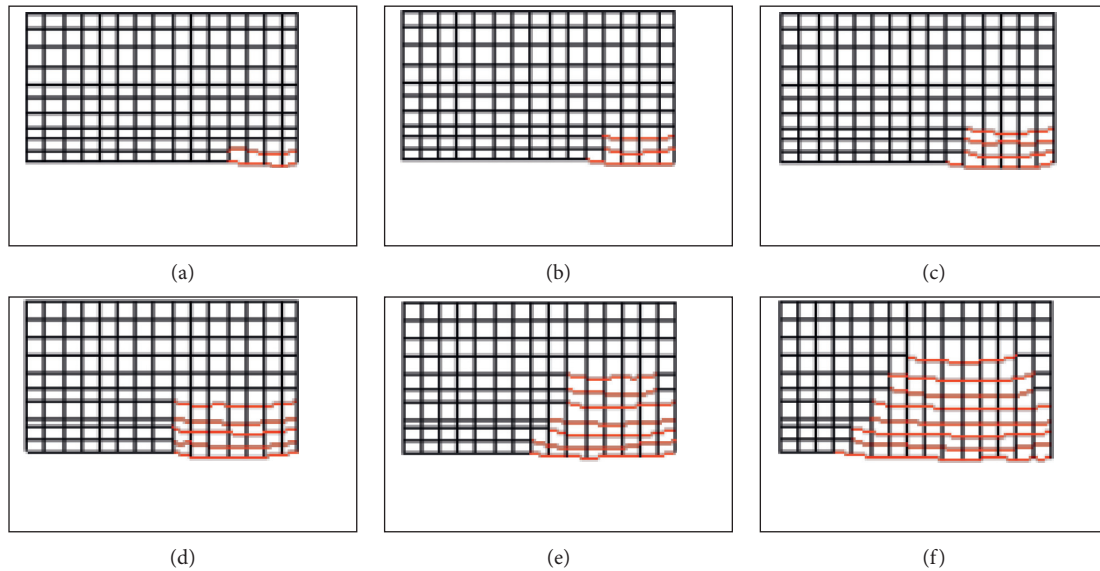


FIGURE 8: Subsidence map of measuring point with working face of scheme 1. (a) The first periodic pressure. (b) The second periodic pressure. (c) The third periodic pressure. (d) The fourth periodic pressure. (e) The fifth periodic pressure. (f) The eighth periodic pressure.

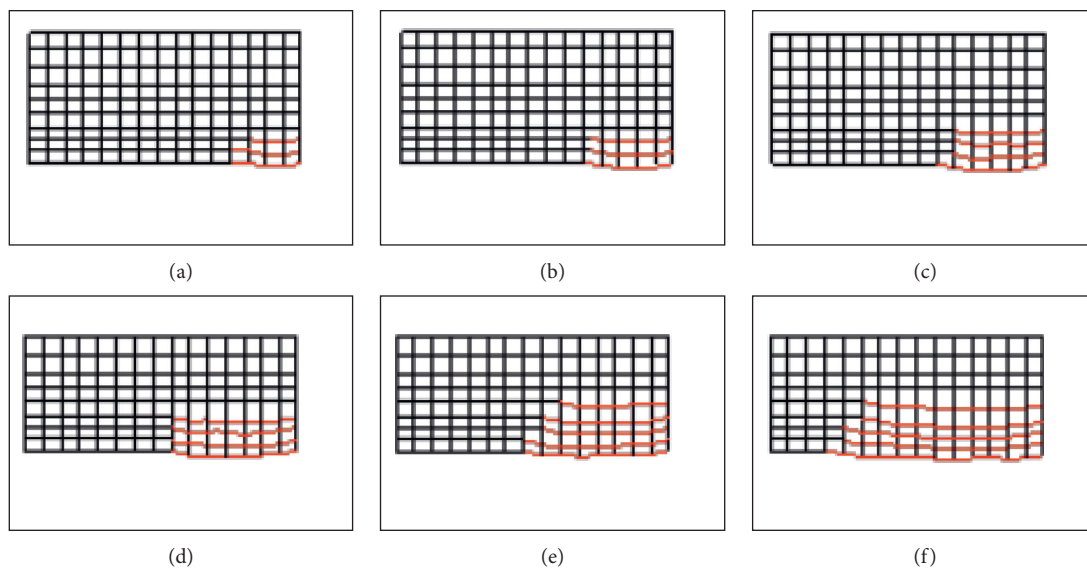


FIGURE 9: Subsidence map of measuring point with working face of scheme 2. (a) The first periodic pressure. (b) The second periodic pressure. (c) The third periodic pressure. (d) The fourth periodic pressure. (e) The fifth periodic pressure. (f) The eighth periodic pressure.

because the inferior key stratum plays the role of local control of the rock formation. However, as the working face continues to advance, when the pressure of the upper rock formation exceeds the tensile strength of the inferior key stratum itself, the inferior key stratum also breaks, forming a caving zone, which is mainly composed of the collapse of J3, J4, and J5 rock formation, with a height of nearly 14 m. The water-conducting fracture zone finally develops to the lower part of the compound key stratum, that is, the lower part of the J9-J10 rock formation, and the highest place of fissure development is about 58 m from the mining working face.

(2) *Analysis of the Development of the Water-Conducting Fracture Zone in Scheme 2.* The main key stratum J16 is 42.9 m from the working face, which is about 7.2 times the mining height, and J4 and J6 are two inferior key strata. There is no obvious bending and sinking zone after the collapse of the overlying strata (Figure 12). The phenomenon at the early stage of excavation is similar to scheme 1, but as the working face advances, the fissure affects J9 rock formation and its upper neighbor J16 rock formation, but no through fissure is formed in J16, which is due to the fact that the main key stratum is the most controlling rock formation

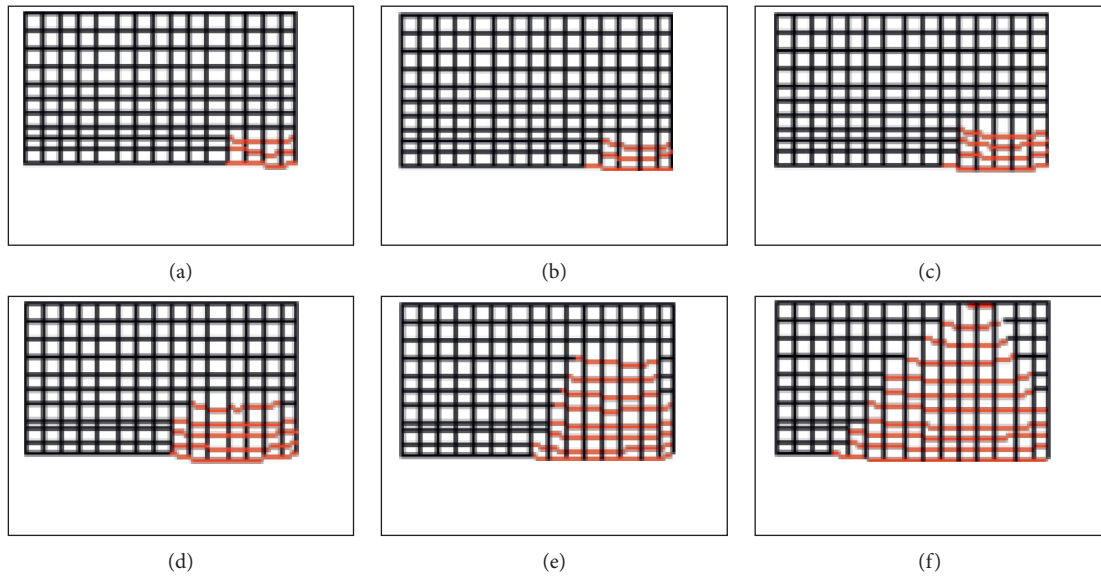


FIGURE 10: Subsidence map of measuring point with working face of scheme 3. (a) The first periodic pressure. (b) The second periodic pressure. (c) The third periodic pressure. (d) The fourth periodic pressure. (e) The fifth periodic pressure. (f) The eighth periodic pressure.

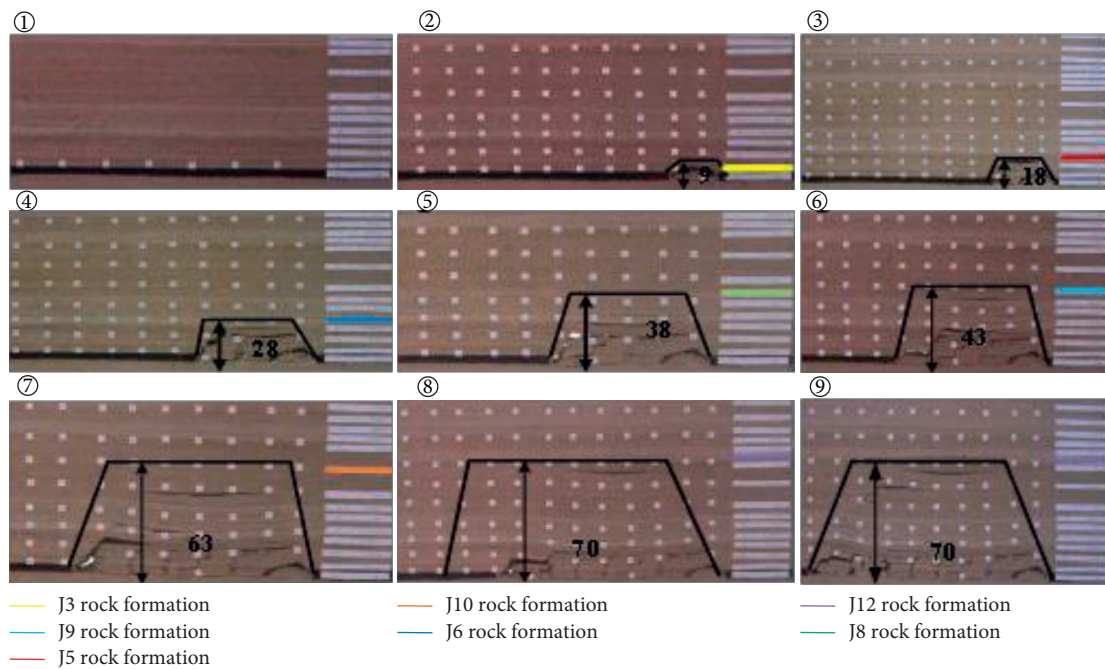


FIGURE 11: Development height of water conducting fracture zone of scheme 1.

in the overlying strata, which plays a key role in controlling the development of the whole crack belt and effectively inhibits the upward growth of the crack belt. The final development height of the water-conducting fracture zone stagnates at around 49 m, which is about 8.2 times of the mining height, indicating that when the main key stratum is located at the “original crack belt boundary,” the fissure development height can be effectively suppressed.

(3) Analysis of the Development of the Water-Conducting Fracture Zone in Scheme 3. The vertical distance of the main

key stratum from the working face is 14.6 m. Only J4 is an inferior key stratum, and J10 and J16 are compound key strata. Compared to Scheme 1 and Scheme 2, the lateral length and longitudinal height of the crack belt reaches the maximum (Figure 13). At the early stage of mining, the collapse of the overlying strata is similar to the previous two groups of tests, but when the water-conducting fracture zone develops between J4 rock formation and J5 rock formation, the development speed of the fissure is suppressed and maintained at a height of 14–17 m above the working face for a certain period of time, the height development of the

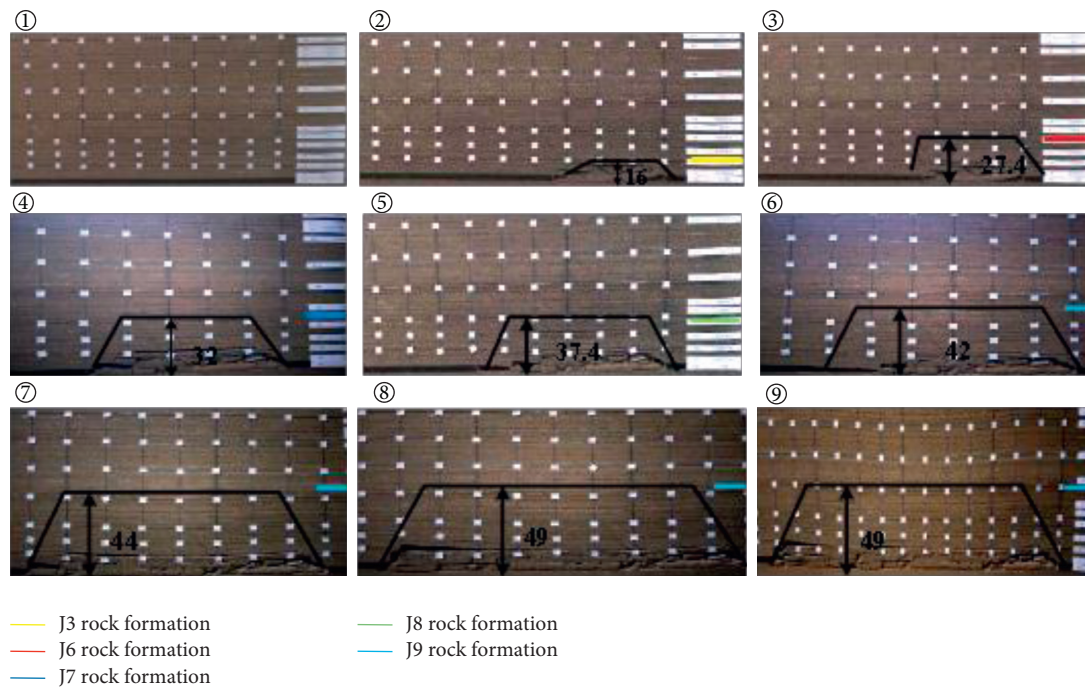


FIGURE 12: Development height of water-conducting fracture zone of scheme 2.

water-conducting fracture zone is obviously controlled by the effect of the upper J16 key stratum, and the water-conducting fracture zone develops slowly. However, as the working face continues to advance, when mining to 55 m, that is, the actual mining is up to 82.5 m, after the third periodic pressure occurs in the working face, the J16 key stratum breaks down and the water-conducting fracture zone gets a faster development rate; at this time, obvious longitudinal fissures can be found in the upper rock formation. It can be seen that when the main key stratum is located in the “caving zone,” it is easy to break down and collapse; there will be a period of rapid development of water-conducting fracture zone, which is extremely unfavorable to mine due to water damage prevention and control, and will also have some impact on surface subsidence.

3.2.2. Analysis of Numerical Simulation Results

(1) *Analysis of the Development of the Water-Conducting Fracture Zone in Scheme 1.* Based on the analysis of the numerical simulation results (Figure 14), it is obtained that: In the initial excavation, that is, when the working face advances 20 m, the main roof has no collapse phenomenon; when the working face advances to 33 m, the main roof has a preliminary collapse, and the working face comes to pressure for the first time. When the excavation reached 50 m, the upper roof collapsed and the working face came under pressure periodically, and it was accompanied by the separation of J5 rock formation and J6 rock formation. When the working face was advanced to

65 m, the separation gap between J5 rock formation and J6 rock formation was further enlarged, and the second periodic collapse of the roof occurred. When the working face continued to advance to 86 m, the J5 rock formation collapsed completely. When the working face continued to advance to 105 m, the J6 rock formation and J7 rock formation became separated and affected the J7 rock formation and J8 rock formation. The working face continued to advance to 134 m, the fifth periodic pressure appeared in the goaf, and the J9 and J10 rock formations appeared to bend and sink. When the working face advances to 165 m, the compacted stability zone in the middle of the goaf gradually increases. When the working face advances to 180 m, the compacted stability zone increases significantly under the upper support pressure, and the development height of water-conducting fracture zone stagnates under the J10 rock formation, but its density increases. This simulation result is basically the same as the rock collapse pattern of similar material simulation experiments.

(2) *Analysis of the Development of the Water-Conducting Fracture Zone in Scheme 2.* Based on the analysis of the numerical simulation results (Figure 15), it is obtained that: The collapse of the top plate of Scheme 2 is not much different from Scheme 1 in the early stage of mining. When the working face advanced to 65 m, the upper roof completely collapsed, J5 rock formation had broken, and J6 rock formation acted as an inferior key stratum without deformation. When the working face continues to advance to 86 m, the J6 rock formation was bent and deformed, the water-conducting fracture zone developed to the J10 rock layer, and a small separation gap appears

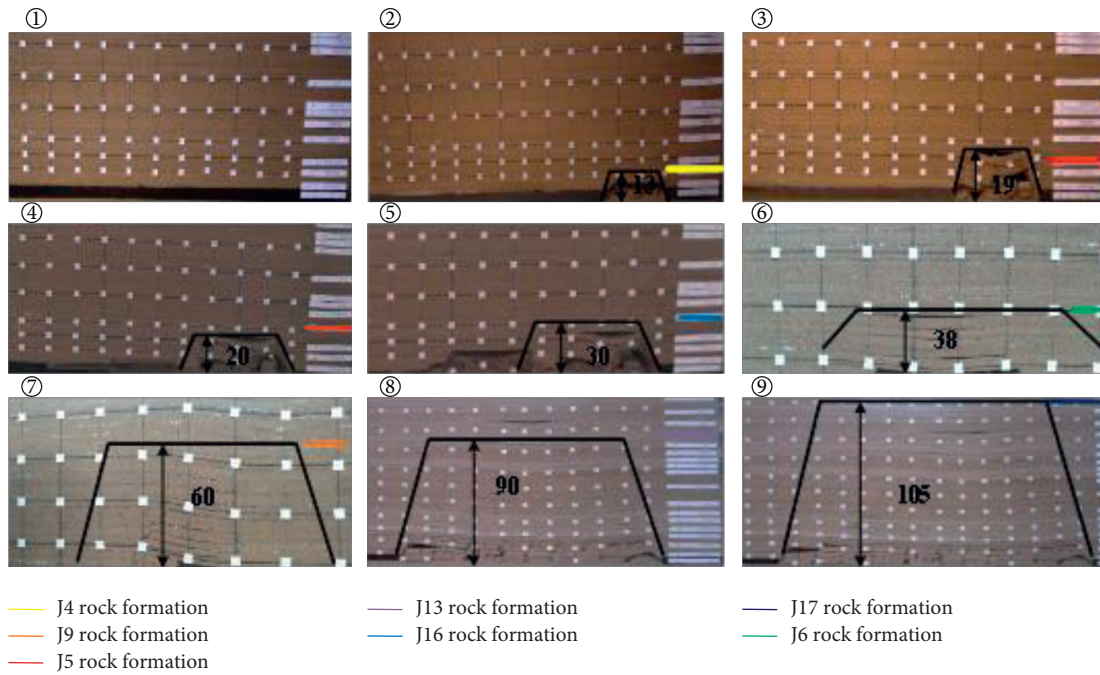


FIGURE 13: Development height of water-conducting fracture zone of scheme 3.

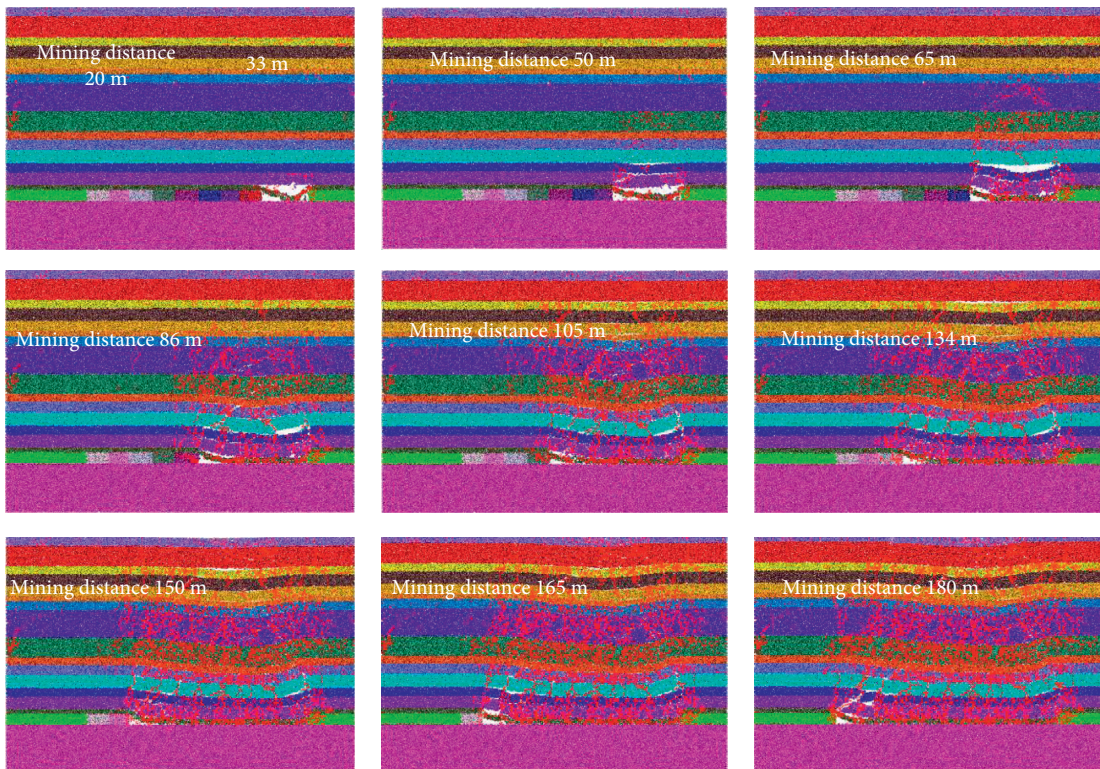


FIGURE 14: Caving characteristics of mining overlying rock of scheme 1.

between the J9 and J10 rock formations. When the working face continued to 105 m, longitudinal fissures in the overburden rock developed rapidly but could not penetrate the J16 rock formation. The working face

continues to move forward, due to the controlling effect of the main key stratum J16 rock formation, and the transverse fissure has increased significantly after development, but the longitudinal fissure was stagnant.

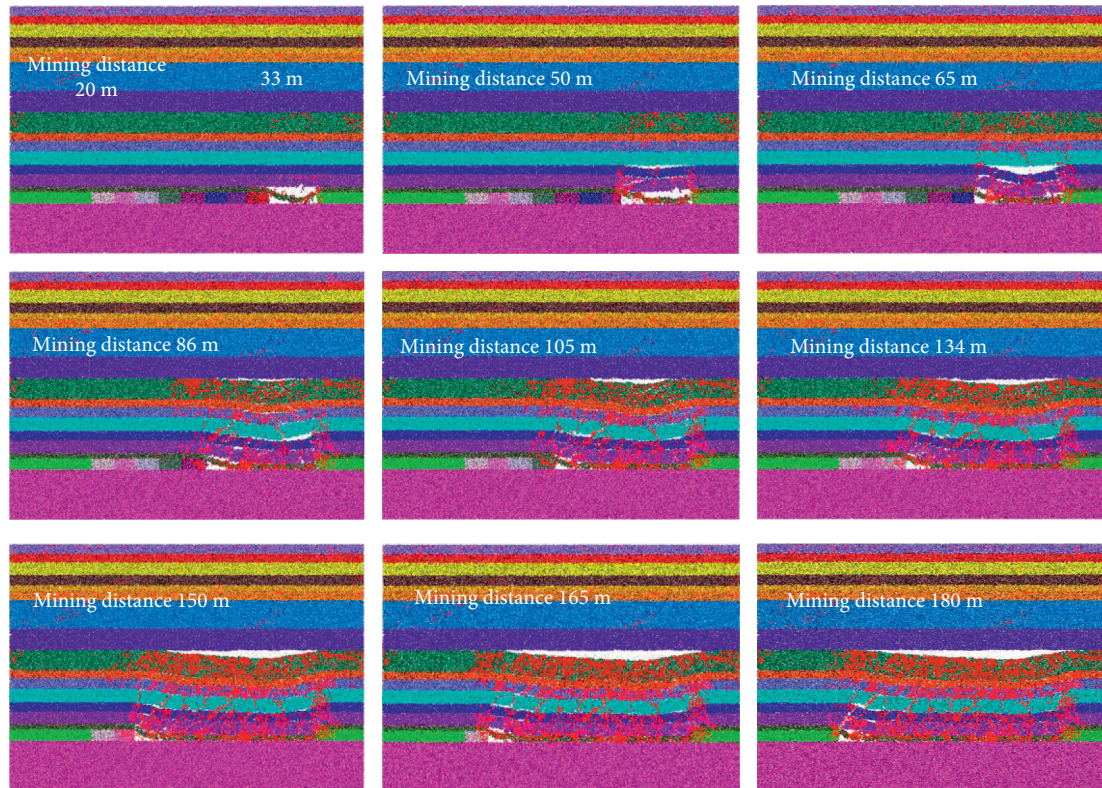


FIGURE 15: Caving characteristics of mining overlying rock of scheme 2.

(3) *Analysis of the Development of the Water-Conducting Fracture Zone in Scheme 3.* Based on the analysis of the numerical simulation results (Figure 16), it is obtained that: The collapse of the top plate in Scheme 3 is basically the same as Scheme 1 and Scheme 2 when mining to 20 m and 33 m, which indicates that the ability of the overburden rock to withstand the action of the upper pressure is not obvious at the early stage of mining, and the collapse of the overburden rock and the evolution of fissures only appear as obvious changes with the advancement of the working face. When the working face had advanced to 50 m, the J5 rock formation began to break and became separated from the J6 rock formation. When the working face advanced to 65 m, the J5 rock formation was completely broken and the main key stratum, J6 rock formation, started to break. As the working face continues to advance, the main key stratum, J6 rock formation, is completely broken, the water-conducting fracture zone is well developed, the horizontal and vertical fissures are gradually expanded, and the water-conducting fracture zone finally develops to the top of the rock formation.

3.2.3. Permeability Zoning of the Goaf. Coal seam mining is a process in which the original stress balance of the coal rock is disrupted and restabilized. In this process, the change of stress will not only lead to the generation of new fissures in the coal rock but also lead to the expansion and expansion or contraction and closure of the original fissures in the coal rock. And, these fissures in different forms provide channels

for water and gas to move from low-porosity position to high-porosity position, and because some of the vertical fissures have the function of up and down conduction, leading to water or gas protrusion at the working face, which endangers mine safety.

Therefore, it is important to classify the permeability performance of each area according to the size of permeability to prevent and control water damage and gas protrusion in mines and to ensure mine safety. Therefore, using the feature that the PFC^{2D} numerical simulation method can directly extract the model porosity data, the regions are divided into strong permeability zone, permeability zone, separation zone, and compacted stability zone according to the porosity size (Figures 17–19).

Figures 18 and 19 show the permeability zoning of Scheme 2 and Scheme 3. Relative to Scheme 1, both Scheme 1 and Scheme 2 have the same four zones, but their impact areas and the morphology of each zone are different. It can be seen that the strong permeability zone and the permeability zone of Scheme 1 and Scheme 2 are both in the adjacent area behind the working face, and their heights do not differ much, which indicates that this is the key area for prevention when mining operations are carried out. However, in terms of the size of the compacted stability zone and the separation zone, Scheme 2 reflects a larger area of influence than Scheme 1, and its large compacted stability zone is more conducive to coal mining safety. In addition, although the separation zone of Scheme 2 is larger, its overall morphology presents a more obvious elongated shape, and from a longitudinal perspective, its smaller longitudinal

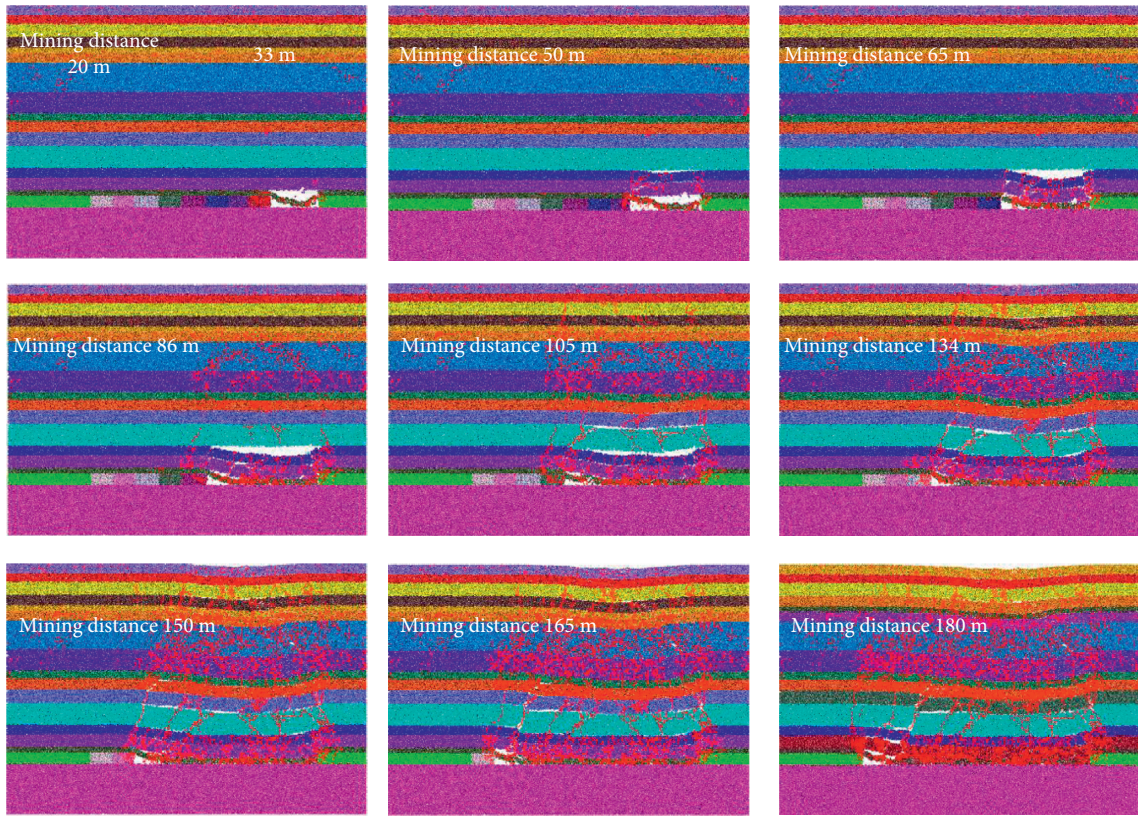


FIGURE 16: Caving characteristics of mining overlying rock of scheme 3.

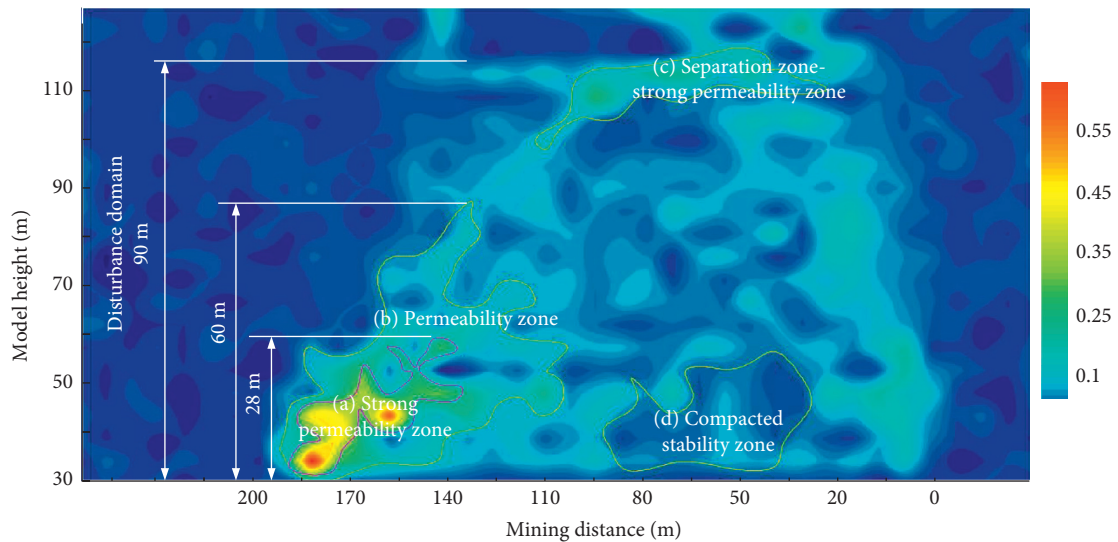


FIGURE 17: Permeability zoning in goaf when excavated to 190 m of scheme 1. The porosity distribution of scheme 1 is shown in Figure 17, and the permeability zone is divided into four regions. (a) Strong permeability zone , the porosity rate in this area is generally greater than 0.25, mainly due to the coal gangue accumulation holes and vertical fissures of rock collapse, and dynamic changes with the advance of the working face, which can directly affect the working face. (b) Permeability zone , the porosity of this area is between 0.1 and 0.35, and it is mainly composed of vertical fissures, and the influence range can reach 60 m in the vertical direction, and if the above contains aquifer, it may directly affect the working surface. (c) Separation zone , the porosity of this area is 0.25–0.35, mainly composed of separation lateral fissures, which may become a water storage space if the rock formation contains water, but has less impact on the working surface. (d) Compacted stability zone , the porosity of this area is generally below 0.1, mainly because the coal gangue in the goaf is compacted under the action of the load above, and the stress is gradually recovered by the stress-relaxation area, resulting in the reduction of porosity. The water conductivity of this area is weak and has little influence on the working face.

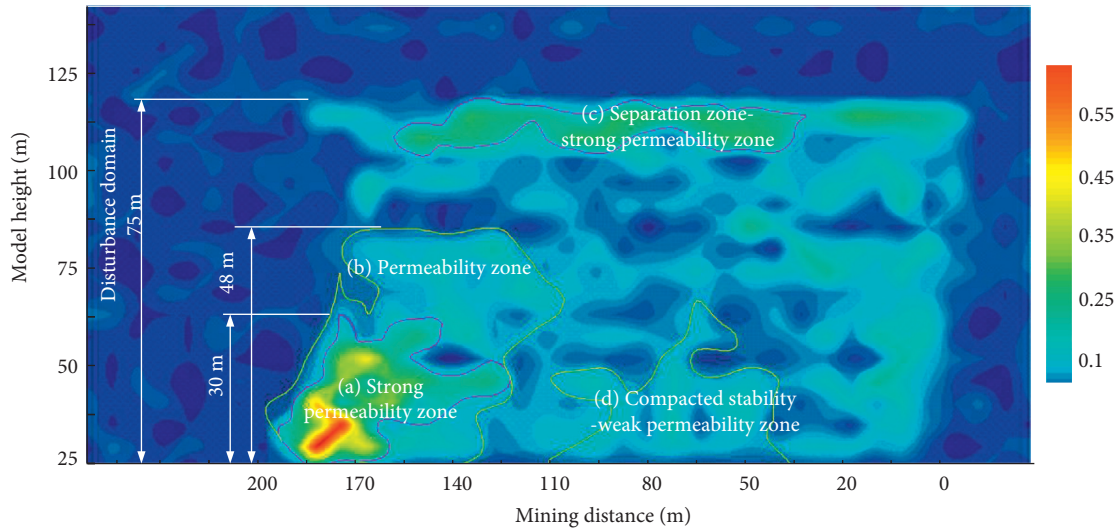


FIGURE 18: Permeability zoning in goaf when excavated to 190 m of Scheme 2.

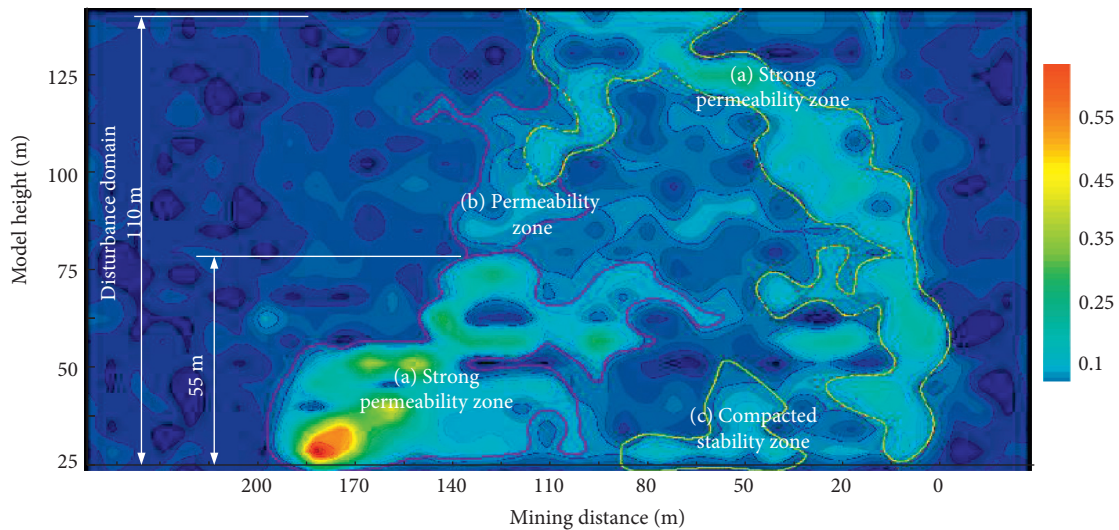


FIGURE 19: Permeability zoning in goaf when excavated to 190 m of Scheme 3.

length poses greater difficulties for communication between aquifers compared to the morphology of the delaminated zone of Scheme 1.

Scheme 3 does not contain a separation zone because the vertical distance between the key stratum and the working face is too small, resulting in the development of fissures to the top of the model, and because overall movement occurs above the key stratum after it breaks. It is worth noting that, compared with Scheme 1 and Scheme 2, the strong permeability zone of Scheme 3 is extremely wide, with a large distribution on both sides of the entire working face, and directly through the upper and lower rock formations, which will directly lead to the water inrush in the working face if it contains an aquifer. In fact, this is also due to the premature breakage of the main key stratum, while the mechanical properties of the other key strata determine if their support is not sufficient to control the overall rock deformation, thus leading to the development of fracture

zones on the top of the formation. When mining under such working conditions, strict measures should be taken to prevent and control water surges in order to ensure mining safety.

4. Conclusion

In this paper, using the 7435 working face of the Kongzhuang coal mine as a prototype, the transport and breaking law of overlying strata under different key strata were explored by means of theoretical analysis, and similar material simulation experiments, numerical simulation, and the development height of its water-conducting fracture zone was predicted and judged. And, on the basis of numerical simulation, the porosity values were extracted and the permeability zoning of the goaf was classified by its results. The main conclusions obtained are as follows:

- (1) Based on the theoretical analysis, a preliminary judgment was made on the development height of the water-conducting fracture zone. It is judged that the development height of the water-conducting fracture zone is 49–64.2 m, which is consistent with the actual results. The model size of the numerical simulation experiment is also determined.
- (2) An experimental model of similar material simulation was established based on the similarity principle, the effect of the development height of its water-conducting fracture zone was studied by changing the position of the main key stratum, and the fissure development pattern of its overburden rock was analyzed. The results show that when the main key stratum is located outside the “original crack belt,” the highest fissure development is about 58 m from the mining face, which is about 10 times the mining height; when the main key layer is in the position of the “original crack belt boundary,” the final development height of the water-conducting fracture zone is stagnant at around 49 m, which is about 8.2 times of the mining height; when the main key stratum is in the position of the “original caving zone,” the water-conducting fracture zone finally develops to the top of the model.
- (3) A three-dimensional physical model was established in PFC based on the height of the water-conducting fracture zone determined by theoretical analysis, and numerical simulations were carried out for coal seam mining under different main key strata to analyze the overburden rock fissure development pattern and predict the development height of the water-conducting fracture zone. The results show that the prediction results of numerical simulation can very well match with the experimental results of similar material simulation, which proves the accuracy and precision of numerical simulation results.
- (4) Based on the calculation results of numerical simulation, the porosity data of the goaf and the permeability zoning were extracted. The results show that when the main key stratum is located in the “original crack belt boundary,” the area of its compacted stability zone is the largest and the height of the permeability zone is small, which is conducive to production safety; when the main key stratum is located in the “original caving zone,” the area of its compacted stability zone is smaller, but the area of the strong permeability zone is the largest and penetrates to the top of the model, so when mining under such working conditions, it should do a good job of strict measures to prevent water surges to ensure mining safety.

In this paper, numerical simulations and similar material simulation experiments are mainly used to investigate the development height of water-conducting fracture zone and porosity distribution under different key strata locations, and preliminary results are obtained. However, further research is needed to combine the research results with

practical applications, and further research is conducted in conjunction with practical applications. In addition, since the experimental object selected for this study is only limited to the Kongzhuang coal mine, in order to test the conclusions of this paper, we will increase the number of experimental samples and repeat the conclusions of this study by combining the research data from several coal mines, in order to obtain universal laws and better guide the safe mining work in coal mines.

Data Availability

The data used to support the findings of this study are included within the article.

Conflicts of Interest

The authors declare that they have no conflicts of interest.

Acknowledgments

This work was supported by the Natural Science Foundation of China (Grant No. 51804270), the Natural Science Foundation of Hunan Province (Grant No. 2020JJ5547), and the Research Fund of Hunan Provincial Department of Education (Grant No. 19C1745).

References

- [1] A. Kidybinski and J. Dubinski, *Strata Control in Deep Mines*, Rouledge, England, UK, 1990.
- [2] E. J. Sellers and P. Klerck, “Modelling of the effect of discontinuities on the extent of the fracture zone surrounding deep tunnels,” *Tunnelling and Underground Space Technology*, vol. 15, no. 4, pp. 463–469, 2000.
- [3] Q. Qian and S. Li, “A review of research on zonal disintegration phenomenon in deep rock mass engineering,” *Chinese Journal of Rock Mechanics and Engineering*, vol. 27, pp. 1278–1284, 2008.
- [4] Q. Jiang, X. T. Feng, J. Chen, K. Huang, and Y. L. Jiang, “Estimating in-situ rock stress from spalling veins: a case study,” *Engineering Geology*, vol. 152, no. 1, pp. 38–47, 2013.
- [5] S. Yin, J. Zhang, and D. Liu, “A study of mine water inrushes by measurements of in situ stress and rock failures,” *Natural Hazards*, vol. 79, no. 3, pp. 1961–1979, 2015.
- [6] T. Liu, “Influence of mining activities on mine rockmass and control engineering,” *Journal of China Coal Society*, vol. 20, 1995.
- [7] Q. Qu, J. Xu, and M. Qian, “Study on influences of key strata movement on gas emissions of adjacent layer,” *Chinese Journal of Rock Mechanics and Engineering*, vol. 26, no. 7, pp. 1478–1484, 2007.
- [8] J. Yang and Y. Luo, “Enhanced subsurface subsidence prediction model incorporating key strata theory,” *Mining, Metallurgy & Exploration*, vol. 38, no. 2, pp. 995–1008, 2021.
- [9] X. Miao, X. Cui, J. a. Wang, and J. Xu, “The height of fractured water-conducting zone in undermined rock strata,” *Engineering Geology*, vol. 120, no. 1–4, pp. 32–39, 2011.
- [10] P. Xu, M. Zhang, Z. Lin, Z. Cao, and X. Chang, “Additional stress on a buried pipeline under the influence of coal mining subsidence,” *Advances in Civil Engineering*, vol. 2018, Article ID 3245624, 16 pages, 2018.

- [11] H. Yanli, Z. Jixiong, A. Baifu, and Z. Qiang, "Overlying strata movement law in fully mechanized coal mining and backfilling longwall face by similar physical simulation," *Journal of Mining Science*, vol. 47, no. 5, pp. 618–627, 2011.
- [12] D. Ma, J. Zhang, H. Duan et al., "Reutilization of gangue wastes in underground backfilling mining: overburden aquifer protection," *Chemosphere*, vol. 264, Article ID 128400, 2021.
- [13] D. Ma, J. Wang, X. Cai et al., "Effects of height/diameter ratio on failure and damage properties of granite under coupled bending and splitting deformation," *Engineering Fracture Mechanics*, vol. 220, Article ID 106640, 2019.
- [14] D. Ma, S. Kong, Z. Li, Q. Zhang, Z. Wang, and Z. Zhou, "Effect of wetting-drying cycle on hydraulic and mechanical properties of cemented paste backfill of the recycled solid wastes," *Chemosphere*, vol. 282, Article ID 131163, 2021.
- [15] H. Wu and D. Ma, "Fracture response and mechanisms of brittle rock with different numbers of openings under uniaxial loading," *Geomechanics and Engineering*, vol. 25, pp. 481–493, 2021.
- [16] M. Tu and Z. Liu, "Research and application of crack development in mining seam roof," *Coal Science and Technology*, vol. 30, no. 7, pp. 54–56, 2002.
- [17] C. Cheng, X. Cheng, R. Yu, W. Yue, and C. Liu, "The law of fracture evolution of overlying strata and gas emission in goaf under the influence of mining," *Geofluids*, vol. 2021, Article ID 2752582, 16 pages, 2021.
- [18] J. Cao and W. Li, "Numerical simulation of gas migration into mining-induced fracture network in the goaf," *International Journal of Mining Science and Technology*, vol. 27, no. 4, pp. 681–685, 2017.
- [19] M. Qian, X. Mao, and J. Xu, "Key strata theory in strata control," *Journal of China Coal Society*, vol. 21, no. 3, pp. 225–230, 1996.
- [20] Y. Liang, B. Li, and Q. Zou, "Movement type of the first subordinate key stratum and its influence on strata behavior in the fully mechanized face with large mining height," *Arabian Journal of Geosciences*, vol. 12, no. 2, p. 31, 2019.
- [21] J. Ju and J. Xu, "Structural characteristics of key strata and strata behaviour of a fully mechanized longwall face with 7.0m height chocks," *International Journal of Rock Mechanics and Mining Sciences*, vol. 58, pp. 46–54, 2013.
- [22] J. Ju, J. Xu, and Q. Wang, "Cantilever structure moving type of key strata and its influence on ground pressure in large mining height workplace," *Journal of China Coal Society*, vol. 36, pp. 2115–2120, 2011.
- [23] J. Xu, X. Wang, W. Liu, and Z. Wang, "Effects of primary key stratum location on height of water flowing fracture zone," *Chinese Journal of Rock Mechanics and Engineering*, vol. 28, pp. 380–385, 2009.
- [24] J. Xu, W. Zhu, and X. Wang, "New method to predict the height of fractured water-conducting zone by location of key strata," *Journal of China Coal Society*, vol. 37, pp. 762–769, 2012.
- [25] Y. Liu, Q. Qi, and A. Wang, "Influence of valleys terrain on pressure of fully mechanized working faces in shallow coal seams," *Shock and Vibration*, vol. 2021, Article ID 8880041, 11 pages, 2021.
- [26] M. Li, J.-x. Zhang, Y.-l. Huang, and R. Gao, "Measurement and numerical analysis of influence of key stratum breakage on mine pressure in top-coal caving face with super great mining height," *Journal of Central South University*, vol. 24, no. 8, pp. 1881–1888, 2017.
- [27] J. Li, Y. Huang, J. Zhang, M. Li, M. Qiao, and F. Wang, "The influences of key strata compound breakage on the overlying strata movement and strata pressure behavior in fully mechanized caving mining of shallow and extremely thick seams: a case study," *Advances in Civil Engineering*, vol. 2019, Article ID 5929635, 11 pages, 2019.
- [28] G. Guo and Y. Yang, "The study of key stratum location and characteristics on the mining of extremely thick coal seam under goaf," *Advances in Civil Engineering*, vol. 2021, Article ID 8833822, 9 pages, 2021.

Research Article

Analysis of Plastic Zone and Pressure Variance Features of Surrounding Rock of High-Altitude Macker Tunnel: A Case Study in Jiagluling Macker Tunnel in Qinghai

Xiaojun Ma,¹ Hongyan Guo ,^{2,3} Juyi Hu,² Shuang Cai ,² Liang Cheng,² and Danfeng Zhang¹

¹Qinghai Communications Construction Management Co. Ltd., Xining, Qinghai, 810003, China

²China Merchants Chongqing Communications Technology Research & Design Institute Co. Ltd., Chongqing 400067, China

³Chongqing University, Chongqing 400044, China

Correspondence should be addressed to Hongyan Guo; 717692502@qq.com and Shuang Cai; caishuang@cmhk.com

Received 16 September 2021; Accepted 13 October 2021; Published 21 October 2021

Academic Editor: Guoming Liu

Copyright © 2021 Xiaojun Ma et al. This is an open access article distributed under the Creative Commons Attribution License, which permits unrestricted use, distribution, and reproduction in any medium, provided the original work is properly cited.

Due to the special mechanical properties of macker rock, problems may be caused easily if the pressure of the surrounding rock calculated from the standard empirical equation is used in the structural design of tunnel support, such as obviously insufficient bearing capacity of the support structure, large deformation, and collapse. Taking the Jiagluling Macker Tunnel in Gonghe-Yushu Highway as an example, the distribution pattern of plastic zone of the surrounding rock and the calculation method and reasonable values of pressure of the surrounding rock are studied in this paper, by means of theoretical analysis, numerical computation, and field measurement data. The results show that the elastic-plastic analysis method is suitable for the pressure of the surrounding rock of macker tunnel. The influence radius of the plastic zone of the surrounding rock can be 32 m, and the lateral pressure of the surrounding rock of the tunnel is equivalent to the vertical pressure. In the absence of test conditions and measured data, the pressure of the surrounding rock can be approximately 0.83 MPa for the purpose of design of tunnel support structure. This conclusion provides technical support for projects in similar conditions.

1. Introduction

In China's Western Development Program, the buildup of a convenient transportation system is the necessity for economic development and social progress in the western region and the improvement of land traffic network also requires expansion of transportation infrastructure into naturally severe, high-latitude, and high-altitude cold regions. With the rise of construction of railways and highways in Tibetan region, increasing attention from the engineering community has been paid to the construction technology for tunnels in high-altitude and cold areas. Jiagluling Tunnel in Gonghe-Yushu Highway is a typical high-altitude macker tunnel in cold region. Due to lack of understanding of the mechanical properties of the surrounding rock of high-altitude macker [1], the distribution pattern of the plastic zone of the surrounding rock [2, 3], the variation law of the

pressure of the surrounding rock, and the reasonable values of the pressure of the surrounding rock are unclear when the tunnel support structure is designed, thus resulting in engineering problems occurring in the process of tunnel construction, such as large deformation, extrusion and collapse of the surrounding rock, uplift of tunnel bottom, cracking of support structure, and deformation and damage of lining.

The majority of domestic studies on macker tunnel focus on mechanical properties, deformation rules and deformation mechanism of the surrounding rock [4], instability failure mechanism, and engineering treatment measures [5]. For example, Na Qicai et al. conducted indoor remodeling of rock sample according to natural density and water content of the rock and obtained mechanical parameters of rock by means of indoor direct shear compression test, value range of elastic modulus through conversion of modulus of compression, and

accurate value of elastic modulus with the help of numerical inverse analysis [6]. Based on measured data regarding construction monitoring of the surrounding rock of the Shazizhi Macker Tunnel in western Zhengzhou, Wang Cheng et al. analyzed the variances of the surrounding rock of a macker tunnel in layered structure over time and proposed corresponding variance equations [7]. Through statistical analysis of field measured data, working face sketching, and application of theories about engineering geology and structural mechanics, Tian Siming analyzed the deformation and damage mechanism of high-geostress macker, discussed the impact of bedded rock and soft rock strata on the stability of tunnel surrounding rock, and revealed the mechanical mechanism of deformation and damage of high-geostress macker [8]. Teng Junyang et al. found through their study that heaving floor of a macker tunnel is caused by a combination of factors including low intensity of tunnel surrounding rock [9], softening and hydraulic pressure effect of groundwater on the surrounding rock, and rheology of macker [10]. However, there is little research on reasonable values of pressure of the surrounding rock of the macker tunnel [11, 12], which is very disadvantageous to engineering design.

Therefore, starting from the actual situation of the construction of Jiagluling Tunnel in Gonghe-Yushu Highway, this paper studies the values of pressure of the surrounding rock of Jiagluling Macker Tunnel, and it is intended to provide a basis and technical support for the design of similar projects.

2. Project Overview

Jiagluling Tunnel, as a typical high-altitude permafrost highway tunnel in cold region, is located in the Gonghe-Yushu (Jiegu) Highway along National Route 214 and its entrance and exit are more than 4,300 m above sea level. The left line of the tunnel is 2925 m long, and the right line is 2845 m long, as shown in Figure 1(a). Tunnel excavation revealed that the surrounding rock is mainly composed of green-gray and gray-black silty macker and slate interbedded with a small amount of thin-medium-thickness quartzite, crystalline limestone, and sand slate. Silty macker and slate, classified as soft rock, are in thin-very thin silty structure and have poor silty calcareous cementation performance, as shown in Figure 1(b). Their bedding surface is quite prone to cracking. They are easily softened in case of contact with water and are heavily influenced by weathering. Interstratigraphic folds and small compression faults are developed, joint fissure is well developed, and rock mass is more fractured, fragmentary, and lamellar.

Due to extrusion of macker, after tunnel excavation and early support placement, daily average deformation rate stays at 10–30 mm and accumulative maximum deformation reaches 40–80 cm. Moreover, such engineering problems as early support cracking, invasion limit, collapse of the surrounding rock on the working surface, inverted arch, heaving floor, and secondary lining cracking are accompanied, and these problems result in extremely heavy engineering risk, significant construction difficulty, and up to 6 years of the construction period.

3. Methodology

Now, the common test methods for the distribution range of plastic zone of the surrounding rock mainly include acoustic wave method, multipoint displacement meter method [7], seismic wave method, geological radar method, and advanced borehole camera technology [13, 14]. Finally, in combination with actual construction situation of Jiagluling Tunnel, the acoustic wave method and multipoint displacement meter method are used to test the broken rock zone of the surrounding rock and conducting contrastive analysis [15].

3.1. Test of Plastic Zone of Surrounding Rock

3.1.1. Test Principle

(1) *Acoustic Wave Method.* The acoustic wave method is a widely accepted and well-developed test method for broken rock zone of the surrounding rock and its feasibility has been proven by a large number of engineering practices. Its test principle is that acoustic wave travels in rock and its velocity will fall with the development of fracture in rock mass, the decrease in density, and the increase in acoustic impedance. On the contrary, if the rock mass has good integrity, heavy stress, and large density, the propagation velocity of the acoustic wave should also be significant, as shown in Figure 2. As a result, for the surrounding rocks of the same nature, high measured acoustic wave velocity indicates better integrity of the surrounding rock and low velocity indicates the presence of fissure in the surrounding rock and damage to the surrounding rock. An acoustic wave tester is used to measure the acoustic wave velocity values of rocks at different depths from the surface of the surrounding rock and depth and acoustic wave velocity curves are drawn. Then, the thickness of the broken rock zone of the surrounding rock in the lane under test is inferred according to related geological data.

(2) *Multipoint Displacement Meter Method.* Many multipoint displacement meters are generally used in the coal production process to obtain large sets of monitoring data, to study the stability of lane surrounding rock or the displacement inside the surrounding rock. Analysis of these sets of monitoring data can also bring us to the range of thickness of the broken rock zone of the surrounding rock. A multipoint displacement meter is used to measure the rock displacement variation at different depths in the surrounding rock. According to the curve of time-varying displacement measured by displacement meter, the convergence of rocks at different depths in the surrounding rock toward drift can be derived. The larger displacement variation with time indicates that the rock mass within the range of this position is fractured. Therefore, through analysis of the displacement and time variation of different points, the broken rock zone and the slightly disturbed zone can be identified, as shown in Figure 3.

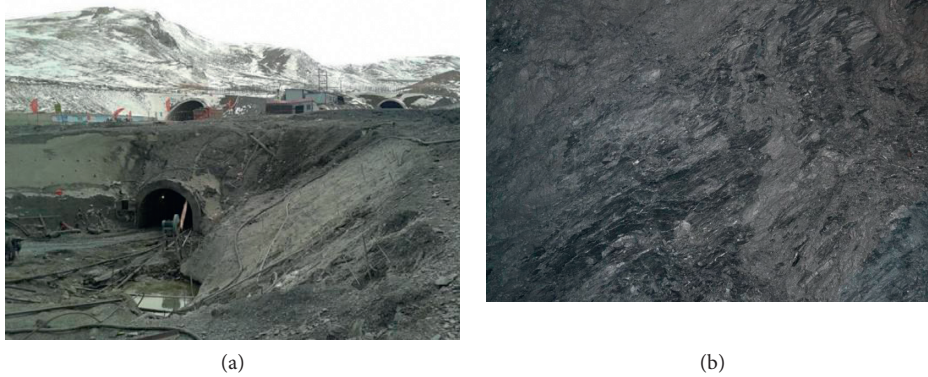


FIGURE 1: Jiangluling Tunnel. (a) Cross section of the tunnel entrance. (b) Photo of the surrounding rock at tunnel entrance face.

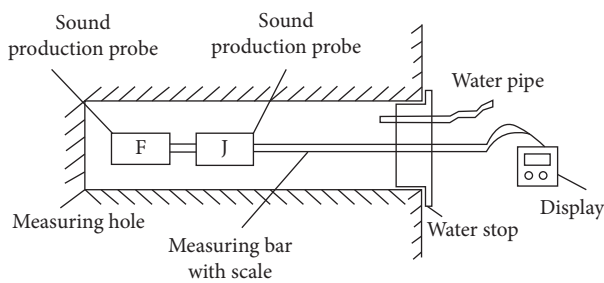


FIGURE 2: Principle of acoustic wave test.

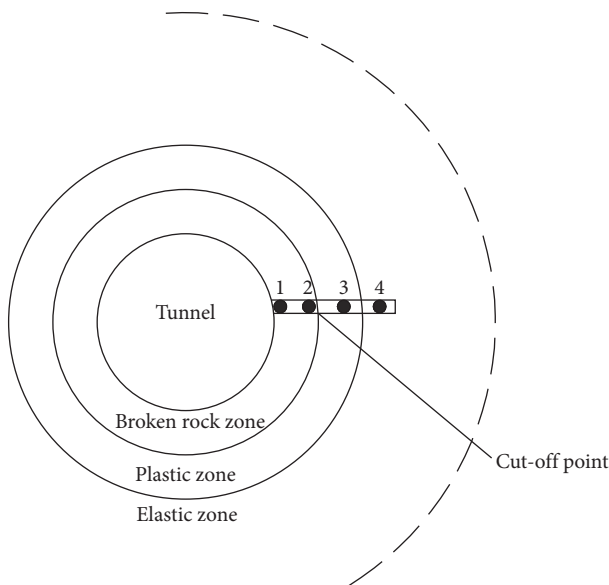


FIGURE 3: Test principle of multipoint displacement meter method.

3.1.2. *Test Scheme.* Six survey sections are arranged in Jiangluling Tunnel according to the on-site construction conditions and geological conditions of the surrounding rock, including two for left and right portals at the entrance and one for left and right portals at the exit, respectively, which are ZK330 + 875, ZK330 + 897, ZK331 + 625, YK330 + 847, YK330 + 855, and YK331 + 475 in turn. Because the vaults are not easy for irrigation and grouting, 4

measuring points are arranged on each section, which are left and right haunches and left and right side walls in turn, as shown in Figure 4(a).

Down-the-hole drilling is used at each measuring point, with a hole depth of 8-9 m and an aperture of 120 mm, as shown in Figure 4(b). After drilling, the acoustic wave test (Figure 5) is adopted, and then the multipoint displacement meter (Figure 6) is embedded for long-term monitoring. By comparing and analyzing the test results of the two different methods, the distribution range of the plastic zone of the surrounding rock of the macker tunnel is obtained.

3.2. *Stress Test of Surrounding Rock.* The surrounding rock is tested by embedding a pressure cell between the steel support and the surrounding rock so that the contact pressure between the surrounding rock and the primary support is analyzed. Six survey sections are arranged according to the on-site construction conditions and geological conditions of the surrounding rock, including two for left and right portals at the entrance and one for left and right portals at the exit, respectively, which are ZK330 + 875, ZK330 + 897, ZK331 + 625, YK330 + 847, YK330 + 855, and YK331 + 475 in turn. There are 5 measuring points on each section, namely, vault, left and right haunches, and left and right side walls, as shown in Figure 7.

4. Results and Discussions

4.1. Test Results and Discussion on Plastic Zone of Surrounding Rock

4.1.1. *Analysis of Results from Acoustic Wave Test.* The acoustic wave method is an instant test, which can only give the loosening condition of the surrounding rock in the current test state. By analyzing the variation pattern of acoustic wave propagation velocity in the surrounding rock at different depths after primary supporting, the influence range of the surrounding rock and the distribution range of the plastic zone of the surrounding rock can be determined. Because water column coupling is required between the probe and surrounding rock during acoustic wave test, it is easy for holes at measuring points 2 and 3 to collapse, and it is difficult to effectively block water. Therefore, only

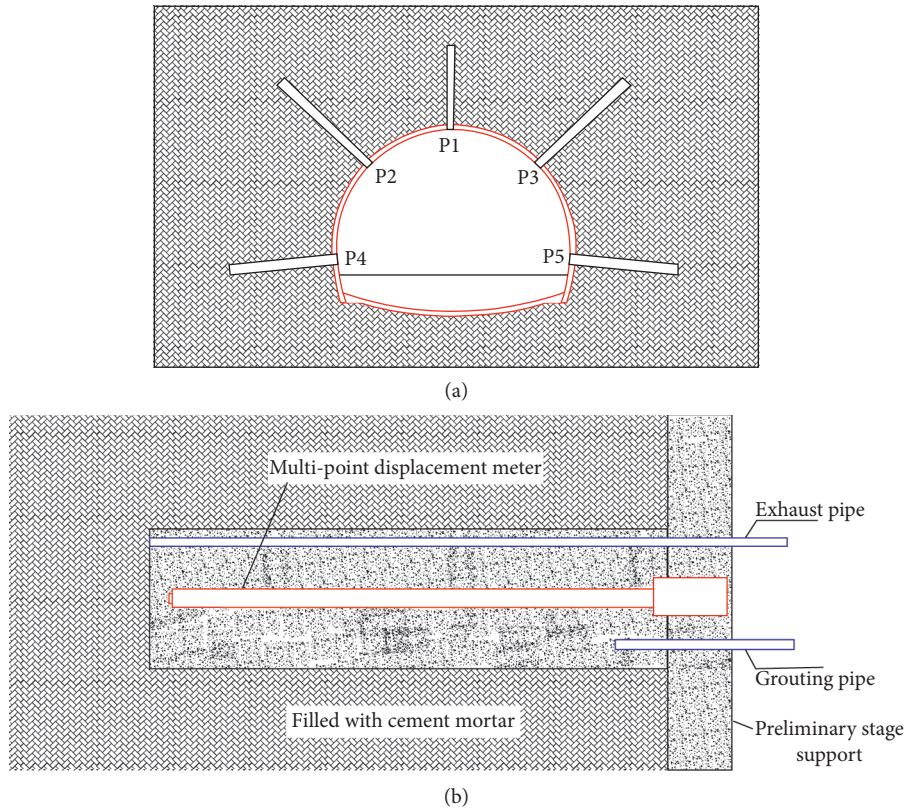


FIGURE 4: Layout of section measuring points and installation method of multipoint displacement meter. (a) Layout of measuring points, the borehole depth $L = 8.0$ m and aperture $\Phi 70$ mm. (b) Multipoint displacement meter installation diagram, the borehole depth $L = 8.0\text{--}9.0$ m and aperture $\Phi 120$ mm.



FIGURE 5: YL-LCT broken rock zone tester (Shanghai Y-Link Engineering and Technology Co., Ltd., China).

measuring points 1 and 4 are subjected to acoustic wave test. As the test results on the left and right sides are symmetrical and similar, the test results on one side (as shown in Figure 8) are given below to determine the distribution range of the plastic zone of the surrounding rock.

It can be derived from Figure 8 that, within the range of 0–8 m from the primary supporting free face of the macker tunnel, the acoustic wave propagation velocity



FIGURE 6: Multipoint (4-point) displacement meter (Shandong Heng'an Electronic Technology Co., Ltd., China).

was rather low, and the wave velocity error fell between 0.8 and 1.6 km/s. The figure also shows a trend of slow increase, which indicates that, with the deepening of the tunnel depth, the density of the surrounding rock increases, and the degree of the surrounding rock affected by excavation decreases gradually. However, the wave velocity error did not change suddenly but increased slowly, and the wave velocity error in the deep layer was slightly higher than that in the shallow layer, which

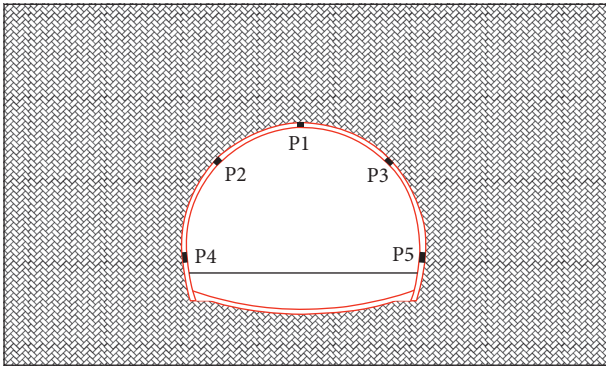


FIGURE 7: Layout of stress measuring points of the surrounding rock, the borehole depth $L = 8.0$ m and aperture $\Phi 70$ mm.

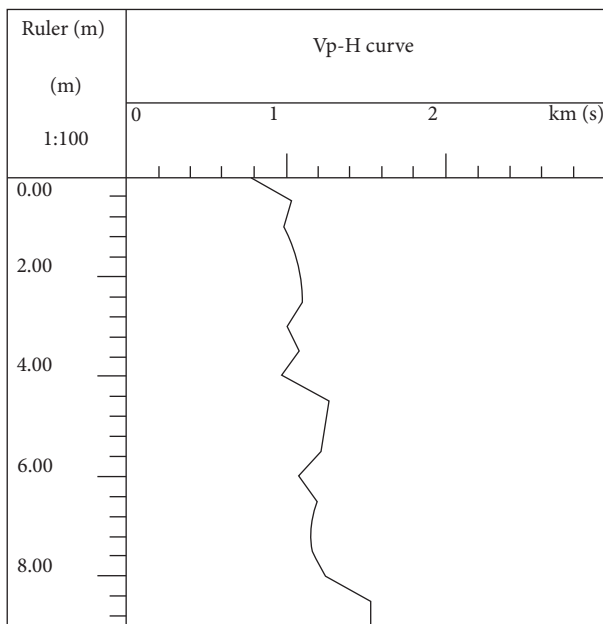


FIGURE 8: Variation pattern of wave velocity error with depth of measuring point.

means that the surrounding rock of the macker tunnel was greatly affected within the test depth (8 m), where plastic deformation occurred; that is, the distribution range of plastic zone of the surrounding rock of the macker tunnel was not less than 8 m.

4.1.2. Analysis of Test Results from Multipoint Displacement Meter Method. The multipoint displacement method is to use a multipoint displacement meter to measure the rock displacement variation at different depths in the surrounding rock. According to the curve of displacement measured by displacement meter, the convergence of rocks at different depths in the surrounding rock toward drift can be derived. The larger displacement variation with time indicates that the rock mass within this position is cracked. Therefore, through analysis of the displacement and time variation of different points, the broken rock zone and the slightly disturbed zone can be identified. Four-point

displacement meters with a length of 8.0 m are embedded at the test points of each test section on-site for long-term monitoring. In order to facilitate comparative analysis, the monitoring results of the same test point are also taken for analysis, as shown in Figure 9.

As shown in Figure 4, the displacement of the deep part of the surrounding rock decreases with the increase of depth. However, after tunnel excavation, the axial displacements of four measuring points (2 m, 4 m, 6 m, and 8 m) in the surrounding rock relative to the free face of the surrounding rock are very small. The monitoring data show that the deformation of the surrounding rock reaches 60–80 cm after tunnel excavation, which means that, after tunnel excavation, the relative displacement between the surrounding rock and surface within 8 m around the tunnel is close to 0; that is, the surrounding rock shrinks inward at the same time within 8 m around the tunnel. Then, it shows that the plastic zone distribution range of the Jiangluling Macker Tunnel is larger than 8 m, which is consistent with the results measured with the acoustic wave method.

4.1.3. Discussion. According to the results of the two test methods, the plastic zone radius of the surrounding rock in the Jiangluling Macker Tunnel is greater than 8 m, which is demonstrated by numerical analysis as follows. Calculation and analysis are conducted with FLAC3D software. Numerical calculation and analysis mode is shown in Figure 10 and mechanical parameters regarding the surrounding rock are obtained through laboratory experiment, as shown in Table 1.

As shown in Figure 11(a), after the excavation of the macker tunnel, the plastic zone of the surrounding rock is distributed in X shape with a large reverse distribution range, and the yield range of the surrounding rock is 14–38 m. After tunnel excavation, the radius of the area where the shear strain of the surrounding rock is greater than 0.01 is 15–32 m. Based on the two analysis results, the distribution range of the plastic zone of the surrounding rock in the Jiangluling Macker Tunnel is 15 m in a horizontal direction and 32 m in a numerical direction (Figure 11(b)). Therefore, during the calculation of the pressure of the surrounding rock in the macker tunnel, the influence radius of the plastic zone of the surrounding rock can be 32 m, and then the empirical formula or theoretical formula can be used for calculation.

4.2. Surrounding Rock Stress Test Results and Discussion

4.2.1. Test Results. The test results of typical sections are extracted to draw the law of variation in pressure of the surrounding rock with time and the cross-sectional drawing of the surrounding rock pressure spatial distribution, as shown in Figures 12 and 13, respectively.

The results of the test and analysis on the pressure of the surrounding rock in the Jiangluling Tunnel show the following:

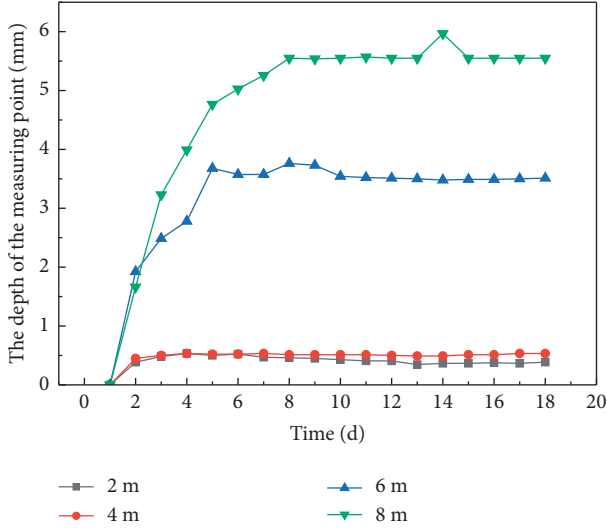


FIGURE 9: Law of variation in the surrounding rock displacement with time at different depths.

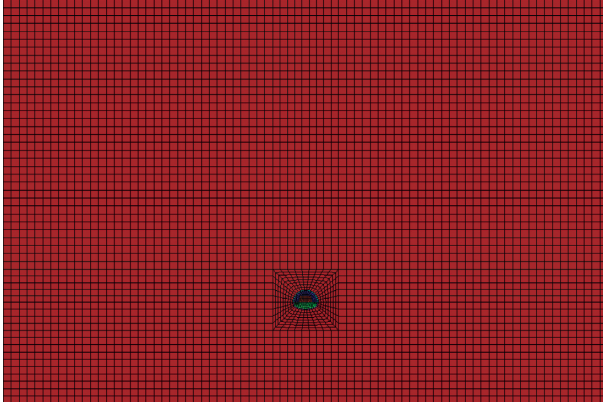


FIGURE 10: Numerical calculation and analysis model.

TABLE 1: Mechanical parameters value of the surrounding rock.

S. no.	Parameter name	Symbol	Unit	Value
1	Density	ρ	kg/m ³	2593
2	Water content	ω	%	3.78
3	Elastic modulus	E	GPa	0.201
4	Poisson ratio	ν	—	0.28
5	Cohesion	c	KPa	88.94
6	Angle of internal friction	φ	°	29.46

- (1) As shown in Figure 12, the law of variation in pressure of the surrounding rock in the macker tunnel can be divided into three stages: rapid growth, slow growth, and stabilization, which correspond to three nodes of the surrounding rock excavation, inverted arch construction, and secondary lining construction in turn.
- (2) As shown in Figure 13, the lateral pressure of the macker tunnel is basically equivalent to the vertical pressure, and the pressure of the surrounding rock is evenly distributed around the tunnel. The pressure of

the surrounding rock is 0.4–0.8 MPa, and the lateral pressure coefficient is approximately 1.0.

4.2.2. *Discussion.* At present, the study of tunnel surrounding rock is mainly divided into two research directions of empirical formula method and theoretical calculation method [16], of which the empirical formula method is a widely used and mature method to determine the pressure of the surrounding rock [10]. It is a summary of experience based on numerous practical engineering data and put forward according to different surrounding rock grades; it is convenient for engineers and technicians to obtain the magnitude and distribution mode of the pressure of the surrounding rock conveniently and quickly. The empirical formula method can be roughly divided into two categories, of which the first category is based on Platts theory, Terzaghi theory, and the form of $q = \gamma h$ Chinese standard method [17] with difference only lying in the difference of equivalent thickness h . This category, with a single influencing factor, is easy to use, but the calculated results are quite different from the actual situation. The second category is the index type formula based on Q or RMR classification system. Taking into consideration the influence of many factors, this type of formula has great progress compared with the former [2, 18]. However, due to the consideration of more indexes, the selection of these indexes has great subjectivity. As one of the methods to determine the pressure of the surrounding rock, the theoretical calculation is developed based on elastic-plastic theory and computer technology, including the theoretical formula method and numerical calculation method [19]. The theoretical formula method is mainly based on the circular tunnel model, including several elliptical tunnels, most of which are deep-buried traffic tunnels or circular roadways with high geostress, strong compression, and large deformation. The representative theoretical formulas mainly include Caquot plastic zone broken-rock pressure formula [20] (formula (1)), Fenner formula [13] (2), modified Fenner formula [21] (3), and Kastner formula.

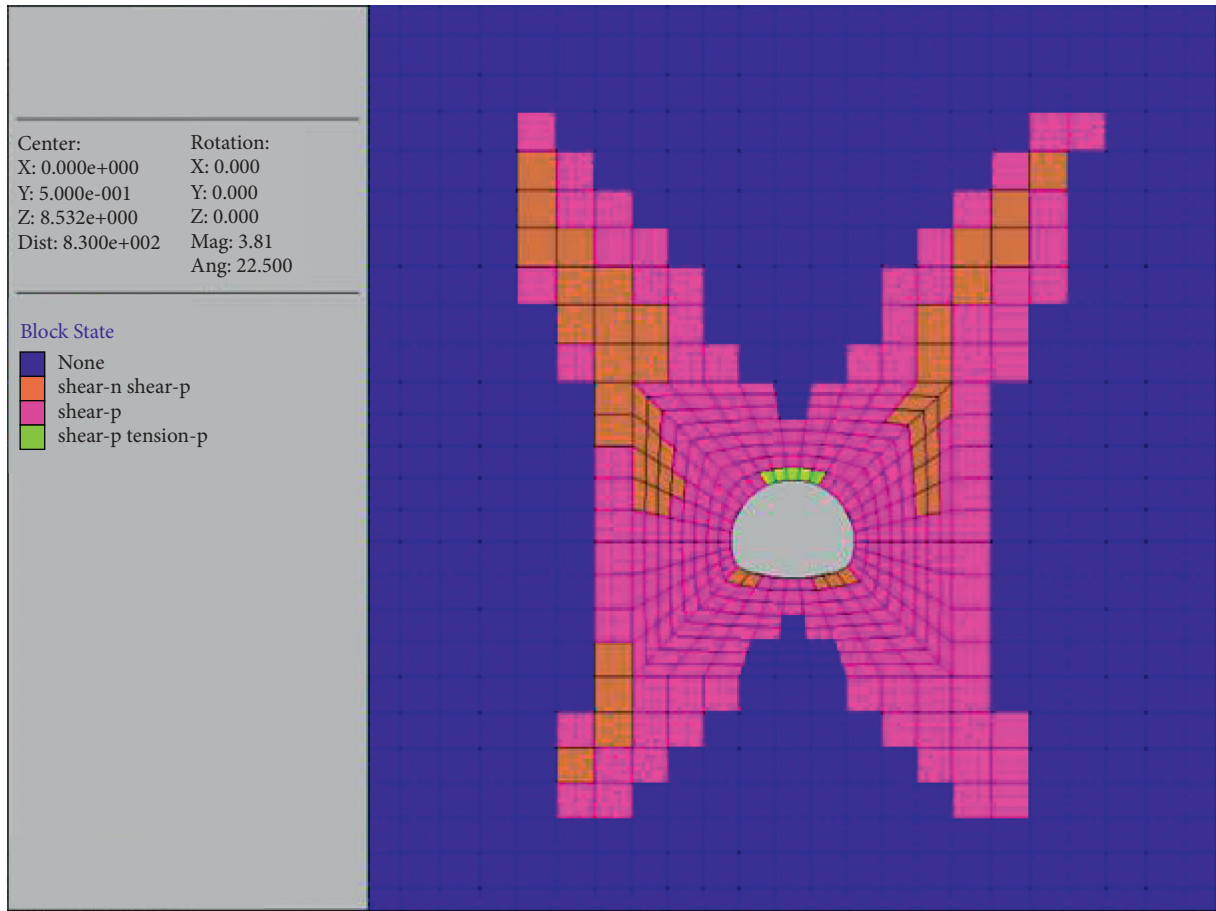
$$p = c \cdot \cot \varphi \left[\left(\frac{r_0}{R} \right)^{\xi-1} - 1 \right] + \frac{r \cdot r_0}{\xi - 2} \left[1 - \left(\frac{r_0}{R} \right)^{\xi-2} \right], \quad (1)$$

where p is the broken-rock pressure of plastic zone; c is the cohesive force of rock mass; φ is the angle of internal friction of rock mass; R is the radius of plastic ring; ξ is the plasticity coefficient; r_0 is the cavern radius; γ is the bulk density of rock mass.

$$p = [c \cdot \cot \varphi + p_0 (1 - \sin \varphi)] \left(\frac{r_0}{R} \right)^{2 \sin \varphi / (1 - \sin \varphi)} - c \cdot \cot \varphi, \quad (2)$$

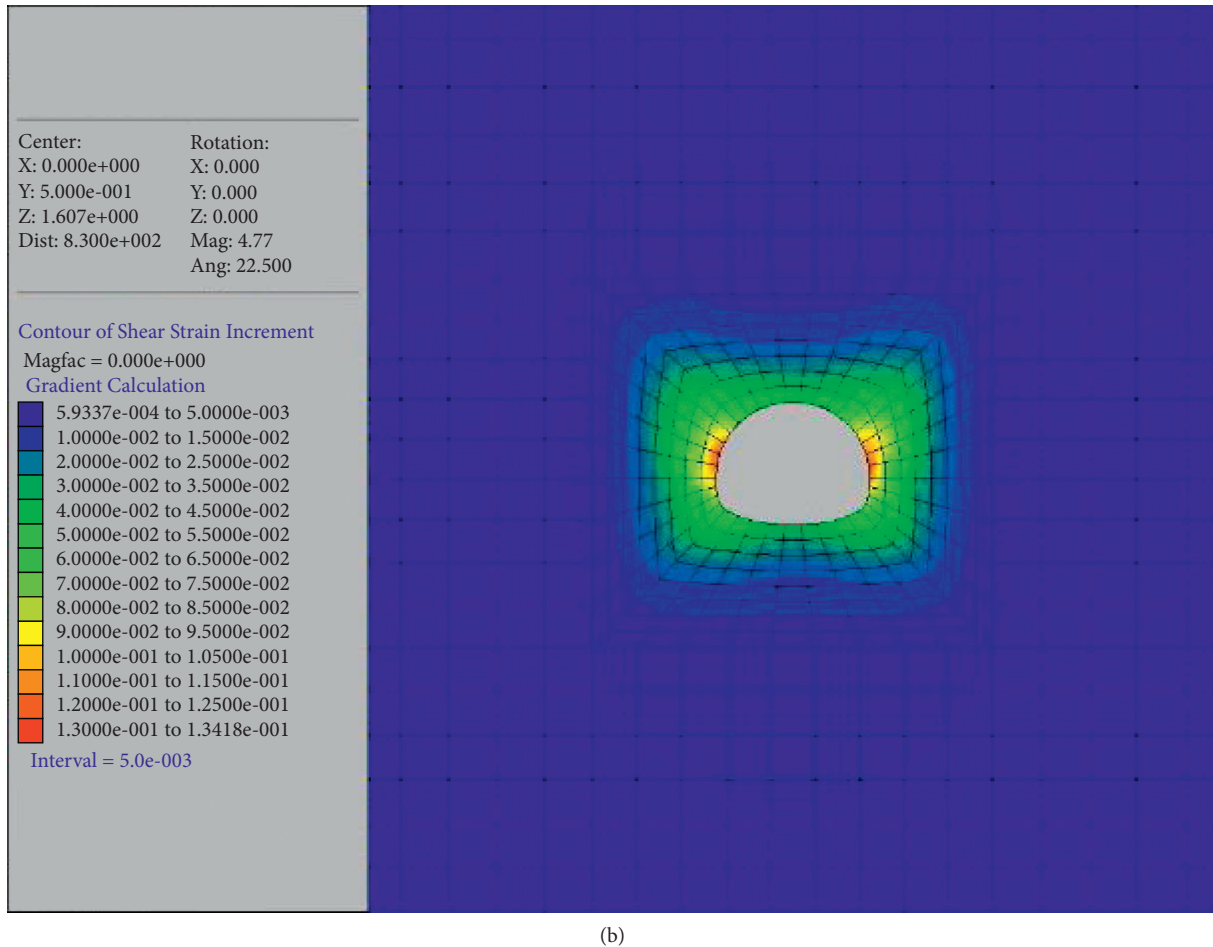
$$p = (c \cdot \cot \varphi + p_0) (1 - \sin \varphi) \left(\frac{r_0}{R} \right)^{2 \sin \varphi / (1 - \sin \varphi)} - c \cdot \cot \varphi. \quad (3)$$

In formulas (2) and (3), p is the deformation pressure of the surrounding rock acting on structure; p_0 is the original geostress; other parameters are the same as above.



(a)

FIGURE 11: Continued.



(b)

FIGURE 11: Numerical analysis results of the plastic zone radius of the surrounding rock in Jiangluling Macker Tunnel. (a) Distribution diagram of the plastic zone of the surrounding rock. (b) Distribution diagram of shear strain of the surrounding rock.

From the perspective of theoretical research results of the pressure of the surrounding rock, the key index of deep-buried tunnel affecting the pressure of the surrounding rock is equivalent to loose layer thickness or plastic zone radius of surrounding rock. It is more reasonable to study the pressure of the surrounding rock in a macker tunnel as a kind of strong-extrusion and large-deformation tunnel by the elastic-plastic analysis method. The key of the study is to analyze the plastic zone of the surrounding rock in a macker tunnel and obtain a reasonable radius of the plastic zone of the surrounding rock.

The monitoring data of some typical large-deformation tunnels in China have been investigated. The monitoring results of the pressure of the surrounding rock are statistically compared and analyzed. The selected tunnels mainly include Baojiashan Tunnel, Wushaoling Tunnel, Xiangshan Tunnel, Humaling Tunnel, and Qingshashan Tunnel. The above 5 tunnels have large-deformation problems during construction, and the pressure of the surrounding rock in corresponding sections is monitored. The test and analysis results of the pressure of the surrounding rock in each tunnel are shown in Table 2.

The comparative analysis results of the pressure of the surrounding rock in the above five tunnels show the following:

- (1) The above tunnels are all surrounding rocks of Class V or Class VI, with large deformation of soft rock existing in the tunnel construction process, which is similar to the Jiangluling Macker Tunnel with certain reference significance in the test results of the pressure of the surrounding rock. As far as lithology is concerned, the lithology of the Wushaoling Tunnel and Qingshashan Tunnel is closer to that of the Jiangluling Tunnel, with a greater reference value [22].
- (2) The pressure of the surrounding rock in the tunnel is relatively high, ranging from 0.4 MPa to 1.1 MPa, which is higher than the calculation result of the empirical formula in the code. At the same time, the lateral pressure and vertical pressure of the surrounding rock of the tunnel are almost equal, and the lateral pressure coefficient is close to 1.0, which is quite different from that of the relevant code [23].

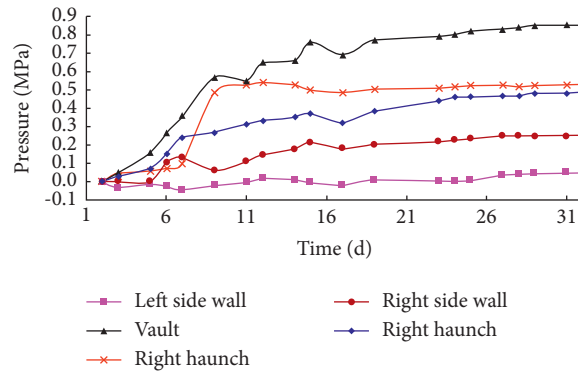


FIGURE 12: Law of variation in pressure of the surrounding rock in typical cross-section tunnel with time.

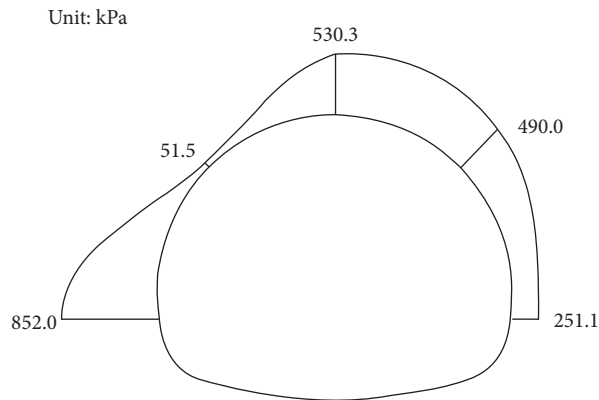


FIGURE 13: Cross-sectional diagram of the spatial distribution of pressure of the surrounding rock in a typical cross-section tunnel.

TABLE 2: Results of test on pressure of the surrounding rock in similar projects.

S. no.	Tunnel name	Tunnel category	Characteristics of rock mass in pressure test section of the surrounding rock	Maximum pressure of the surrounding rock (MPa) (location)
1	Baojiashan Tunnel	Highway tunnel	Weak and broken rock mass	0.44 (haunch)
2	Wushaoling Tunnel	Railway tunnel	Fault crushing zone, phyllite	0.60 (vault)
3	Xiangshan Tunnel	Railway tunnel	Large deformation of soft rock	0.41 (vault)
4	Humaling Tunnel	Highway tunnel	Water-rich silt-fine sandstone	0.53 (sidewall)
5	Qingshashan Tunnel	Highway tunnel	Regional fault, phyllite	1.06 (sidewall)

From three aspects of empirical formula, theoretical analysis, and field measurement, the pressure of the surrounding rock in the Jiangluling Macker Tunnel has been studied. Now, the results of the 3 methods are compared and analyzed. For the empirical formula method, the Code for Design of Highway (Railway) Tunnel and the Specification for Design of Hydraulic Tunnel are adopted to calculate in accordance with the surrounding rock of Class V, with the tunnel excavation width of $B = 13.0$ m, the tunnel excavation height of $H = 10.5$ m, and the lateral pressure coefficient of 0.389. For the theoretical formula, the Caquot plastic zone broken-rock pressure formula is adopted, with the plastic

zone radius of 32 m and the comparative analysis results shown in Table 3.

As shown in Table 3, the results calculated according to the empirical formula recommended by the code are obviously small for the macker tunnel, and those calculated according to the theoretical formula method are close to those of field measurement, which are slightly larger than the field measurement values. In other words, the pressure of the surrounding rock in the Jiangluling Macker Tunnel can be obtained by the Caquot plastic zone broken-rock pressure formula or field measurement. Under the condition where there are no accurate mechanical parameters of the

TABLE 3: Results of comprehensive comparative analysis.

Pressure of the surrounding rock	Empirical formula method		Theoretical formula method	
	Code for design of highway (railway) tunnel	Specification for design of hydraulic tunnel	Caquot plastic zone broken-rock pressure formula	Field measurement
Vertical pressure (MPa)	0.31	0.10	0.83	0.703
Horizontal pressure (MPa)	0.13	0.03	0.83	0.625

surrounding rock and the field test conditions are not available, the vertical pressure and pressure of the surrounding rock in the macker tunnel can be 0.83 MPa, and the support structure design can be carried out.

5. Conclusion

- (1) For the macker tunnel, one of the tunnels with strong extrusion and large deformation, the elastic-plastic analysis method is more reasonable to study the pressure of the surrounding rock, and the reasonable radius of the plastic zone of the surrounding rock is the key to study with the theoretical formula method.
- (2) After the excavation of the macker tunnel, the plastic zone of the surrounding rock is distributed in X shape with a wide distribution range, and the radius of the area where the shear strain of the surrounding rock is greater than 0.01 is 15–32 m. Therefore, the influence radius of the plastic zone of the surrounding rock can be 32 m when calculating the pressure of the surrounding rock in the macker tunnel.
- (3) The variation law of pressure of the surrounding rock in a macker tunnel can be divided into three stages of rapid growth, slow growth, and stabilization. The lateral pressure is basically equivalent to the vertical pressure of the surrounding rock and is uniformly distributed.
- (4) The pressure of the surrounding rock in the Jiangluling Macker Tunnel is recommended to be obtained by the Caquot plastic zone broken-rock pressure formula or field measurement. The vertical pressure and pressure of the surrounding rock in the macker tunnel can be 0.83 MPa if there are no accurate mechanical parameters of the surrounding rock and the field test conditions are not available.
- (5) On-site testing and numerical analysis methods are used in this paper to provide the values of pressure of the surrounding rock of a high-altitude macker highway tunnel. However, since not all actual engineering conditions are covered, these methods are now merely applicable to tunnels of this project. They can be used as a reference for similar projects and the subsequent projects can be further guided through verification and optimization of a large number of similar projects.

Data Availability

The data used to support the findings of this study are available from the corresponding author upon request.

Conflicts of Interest

The authors declare that they have no conflicts of interest.

Acknowledgments

This paper was jointly funded by the Qinghai Transportation Science and Technology Project (no. 2020–01) and the Science and Technology Project of the Transportation Department of Guizhou Province (no. 2020-122-031).

References

- [1] J. Teng and J. Tang, “Mechanism analysis of floor heave in layered carbonaceous shale tunnel,” *Journal of Railway Science and Engineering*, vol. 14, no. 1, pp. 110–116, 2017.
- [2] X. Mo, “Determination of the design pressure and stand-up time for primary support,” *China Civil Engineering Journal*, vol. 35, no. 1, pp. 62–67, 2002.
- [3] W. Hui, Z. Peng-qiang, Z. Wen-juan, and T. Hong-ming, “Application of a combined supporting technology with U-shaped steel support and anchor-grouting to surrounding soft rock reinforcement in roadway,” *Journal of Central South University*, vol. 25, pp. 1240–1250, 2018.
- [4] L. Song, Y. Zhang, and M. Yu, “Unified solution for elasto-plastic analysis of pressure tunnel,” *Engineering Mechanics*, vol. 15, no. 4, pp. 57–61, 1998.
- [5] H. Feng, C. Cw, C. Baj, D. Yh, D. Ng, and E. Wg, “Instability mechanism of shallow tunnel in soft rock subjected to surcharge loads,” *Tunnelling and Underground Space Technology*, vol. 99, Article ID 103350, 2020.
- [6] Q. Na, H. Guo, J. Hu, and S. Cai, “Surrounding rock mechanical parameters test and back analysis of carbonaceous shale tunnel,” *Chinese Journal of Underground Space and Engineering*, vol. 12, no. S2, pp. 504–509, 2016.
- [7] L. Li and Z. Tan, “Characteristic and mechanism research for large deformation problem in squeezing-shattered soft rock tunnel,” *Chinese Journal of Rock Mechanics and Engineering*, vol. 37, pp. 3593–3603, 2018.
- [8] C. Wang, M. Ding, and L. I. Qiang, “Study on deformation laws of carbonaceous shale tunnel in western hubei province,” *Chinese Journal of Underground Space and Engineering*, vol. 3, no. S2, pp. 1442–1444, 2007.
- [9] Z. J. Chen, “The mechanical problems for the long-term stability of underground galleries,” *Chinese Journal of Rock Mechanics and Engineering*, vol. 1, no. 1, pp. 1–20, 1982.
- [10] G. Liu, Y. Xiao, and J. Zhu, “Overview on theoretical calculation method of broken rock zone,” *Journal of China Coal Society*, vol. 46, no. 1, pp. 46–56, 2021.
- [11] W. Fan, Y. M. Hong, Y. W. Shi, and P. Sun, “The unified solution of the plastic relaxed pressures computing of surrounding rockmassess,” *Journal of Xi’an Engineering University*, vol. 25, no. 1, pp. 33–36, 2003.
- [12] J. Liu, C. Xie, and J. Rao, “Calculation model and influencing factors of surrounding rock loosening pressure for tunnel in

- fold zone,” *Advances in Civil Engineering*, vol. 2021, no. 1, pp. 1–15, Article ID 6678511, 2021.
- [13] P. Li, F. Wang, L. Fan, H. Wang, and G. Ma, “Analytical scrutiny of loosening pressure on deep twin-tunnels in rock formations,” *Tunnelling and Underground Space Technology*, vol. 83, no. JAN, pp. 373–380, 2019.
- [14] Y. X. Song, X. Y. Jia, and Y. Q. Zhu, “Study on vertical earth pressure calculation of metro tunnel,” *Rock and Soil Mechanics*, vol. 28, no. 10, pp. 2240–2244, 2007.
- [15] X. U. Kun, Z. J. Wang, M. Xiang-Lei, and C. S. Sun, “Research on detection technology for deep tunnel surrounding rock loose circle and numerical simulation analysis,” *Rock and Soil Mechanics*, vol. 34, pp. 464–470, 2013.
- [16] S. Alija, J. Torrijo, and M. Quinta Ferreira, “Geological engineering problems associated with tunnel construction in karst rock masses: the case of Gavarres tunnel (Spain),” *Engineering geology amsterdam*, vol. 157, pp. 103–111, 2013.
- [17] S. Tian, “Deformation mechanism of black batt with high stress in Baozhen tunnel,” *Journal of Beijing Jiaotong University*, vol. 37, no. 1, pp. 21–26, 2013.
- [18] F. Huang, H. H. Zhu, Q. S. Li, and E. P. Li, “Field detection and theoretic analysis of loose circle of rock mass surrounding tunnel,” *Rock and Soil Mechanics*, vol. 37, no. S1, pp. 145–150, 2016.
- [19] Z. Wang, Z. Liu, W. Ma, S. Shi, and L. Bu, “Calculation method of underground cavern loosening pressure based on limit analysis using Upper-Bound theory and its engineering application[J],” *Mathematical Problems in Engineering*, vol. 2020, pp. 1–18, Article ID 5096931, 2020.
- [20] M. Ahmed and M. Iskander, “Evaluation of tunnel face stability by transparent soil models,” *Tunnelling and underground space technology incorporating trenchless technology research*, vol. 27, no. 1, pp. 101–110, 2015.
- [21] Q. Zeng, E. Wang, and S. Wang, “Comparison between plastic radius around a circular opening derived from Hoek-Brown failure criterion and calculated through modified fenner formula,” *Journal of Shenyang Jianzhu University(Natural Science)*, vol. 24, no. 6, pp. 933–938, 2008.
- [22] M. Cai, P. K. Kaiser, H. Morioka et al., “FLAC/PFC coupled numerical simulation of AE in large-scale underground excavations,” *International Journal of Rock Mechanics and Mining Sciences*, vol. 44, no. 4, pp. 550–564, 2007.
- [23] Q. Xu, Y. Li, J. Lu, and L. Zhang, “The use of surrounding rock loosening circle theory combined with elastic-plastic mechanics calculation method and depth learning in roadway support[J],” *PLoS One*, vol. 15, no. 7, Article ID e0234071, 2020.